Diffusions électronique élastique et inélastique dans le graphène étudiées par le transport micro-onde et le bruit.

Andreas Betz

ÉCOLE NORMALE SUPÉRIEURE

Département de Physique

THÈSE de DOCTORAT de L'UNIVERSITÉ PARIS VI

Spécialité : Physique de la matière condensée

présentée par

Andreas BETZ

Pour obtenir le titre de
DOCTEUR de l'UNIVERSITÉ PARIS VI

Sujet de la thèse :

Elastic and inelastic scattering in graphene studied by microwave transport and noise

Soutenue le ..... devant le jury composé de :

M.	Tero Heikkilä	Rapporteur
M.	Vincent Bouchiat	Rapporteur
M.	Francesco Mauri	Examinateur
M.	Daniel Neumaier	Examinateur
M.	Bernard Plaçais	Co-directeur de thèse
M.	Jean-Marc Berroir	Directeur de thèse

"This is graphene. *Let's call him Mister G."*

The Simple Show for the Graphene Flagship Initiative[1]

[1] *http://www.graphene-flagship.eu/GF/Videos.php*

Abstract

This thesis discusses the elastic and inelastic scattering in monolayer graphene, investigated by means of microwave carrier dynamics and noise.

We study in a first part the high frequency properties of graphene field-effect transistors on different substrates. Particular interest lies in the figures of merit like e.g. the transit frequency f_T, defining the transistor's current amplification capabilities, and the transconductance g_m representing its gate sensitivity. High values are obtained for both parameters in GHz measurements. We find in particular that these figures remain substantial even in miniaturised devices.

We introduce top-gated graphene field-effect capacitors as a probe of the elastic scattering mechanisms in graphene. Employing similar techniques as in the transistor experiments, we are able to directly access the diffusion constant D and its dependence on carrier density. The latter is the signature of the scattering mechanism present in the graphene sheet. Our novel GHz experiments reveal a constant transport scattering time as a function of energy which is in disagreement with conventional theoretical predictions, but supports the random Dirac mass disorder mechanism.

Furthermore, we study inelastic scattering of charge carriers by acoustic phonons in graphene which is among the first realisations of such an experiment in a genuine two-dimensional geometry. A broadband cryogenic noise thermometry setup is used to detect the electronic fluctuations, the current noise, from which we extract the average electron temperature T_e as a function of Joule power P. At high bias we find $P \propto \Sigma T_e^4$ as predicted by theory and which is the tell-tale sign of a 2D phonon cooling mechanism. From a heat equation analysis of data in a broad bias range, we extract accurate values of the electron-acoustic phonon coupling constant Σ. Our measurements point to an important effect of lattice disorder in the electron-phonon energy relaxation.

Acknowledgements

My journey into the world of fundamental science - and in particular into carbon flatland - started in late 2007 when I had the opportunity to prepare my Diplomarbeit at the Laboratoire Pierre Aigrain. I am especially grateful for all the support and help I received during that time from my supervisors Christoph Strunk and Bernard Plaçais.
At my return to the LPA a year later - now as a PhD candidate - it felt as if I hadn't left and could continue to work in the encouraging and friendly atmosphere that is characteristic of the LPA. I hope that many more students can experience this in the future. First and foremost, I would like thank my supervisors Jean-Marc Berroir and Bernard Plaçais, who always had an open ear and time for discussion, despite their numerous other obligations. They took my ideas and concerns seriously and taught me all the necessary skills of a good scientist. Many thanks also go to Emiliano in his role as unofficial supervisor and friend. Thanks to Emiliano's great support and guidance over the first two years of my thesis I have achieved plenty more than I expected. SungHo has taken his place for the remainder of my three year stay. I had the pleasure to work in a very friendly and cordial atmosphere created by my colleagues, the current and former members of the P13 and GH labs, Matthieu, Erwann, Jeremie, Dora, Vincent, Gwendal, Takis, François, Thomas, Cheryl, Adrien, Julien and Lorenz. Thanks to all of you for all the great moments, running sessions in the Jardin du Luxembourg, after work beers and countless other things. I would also like to thank the engineering and electrical service of the LPA, as there are Pascal, David, Anne and Philipp, for their good work and continuous support, as well as Didier and his team. Thank you also to Olivier, François/René and Thierry in the cryo department for keeping the helium flowing, even during times of shortage. In the clean room I could always depend on Michael's and José's help if things didn't quite go as expected. Furthermore, I would like to say thank you to Anne and Fabienne for their administrative services.
I am grateful to Christoph M., Christoph V., David B., Fabien, Benjamin H., Nico, Sukhy, Josh, Carole, Claude, Pierrick, Benjamin L. and all other members of the LPA for their support, discussions and guidance. A thank you also goes to my interns David T., Andreas I., Danijela M., Christian B. It has been a pleasure working with you.
Furthermore, I thank Henri H. from the IEMN for his efforts within the Migraquel projects and Aurelie, Jorge and Annick L. for their help on hBN substrates, as well as Saint Gobain for the supply of high quality hBN. Thank you to Jean-Noel F. and Marc G. for their support and guidance.
Last but but not least, I would like to thank Clara and my family for their continuous love and support. In times when things seemed grey and hopeless you have picked me up and helped me find a positive view again. Thank you so much!

Contents

1 Introduction **1**

1.1 Graphene: description and properties . . . 11
1.1.1 Atomic structure . . . 11
1.1.2 Electronic properties . . . 12
1.1.3 Dirac fermions in graphene . . . 17
1.1.4 Consequences of Dirac equation in graphene . . . 19
1.1.5 Density of states . . . 21
1.1.6 Charge carrier mobility . . . 22
1.1.7 Other related materials . . . 23
1.1.8 Differences between MLG and 2D semiconductors . . . 25
1.2 Phonon modes in graphene . . . 26
1.3 Electronics in mesoscopic systems . . . 28
1.3.1 Length scales of mesoscopic systems . . . 28
1.3.2 Transport in mesoscopic graphene . . . 28
1.3.3 Noise in mesoscopic systems . . . 30
1.4 Single charge detection . . . 33
1.4.1 Single-electron transistors . . . 35
1.4.2 Quantum-point-contact transistors . . . 36
1.4.3 Carbon nanotube transistors . . . 36
1.4.4 Sub-nanosecond charge detection in graphene transistors . . . 37

2 Fabrication of graphene devices **39**

2.1 Obtaining graphene layers . . . 39
2.1.1 Exfoliation . . . 39
2.1.2 Chemical Vapour Deposition . . . 40
2.2 Manual stacking of thin layers: Wedging transfer . . . 42
2.3 Device fabrication . . . 44
2.3.1 Substrate preparation . . . 45
2.3.2 Deposition and localisation . . . 45
2.3.3 GHz adapted coplanar waveguide . . . 46

3 Microwave graphene field-effect transistors **53**

3.1 Single charge detection in CNT nano-FETs . . . 56
3.2 Important concepts and formulas . . . 57
3.2.1 DC characteristics of graphene FETs . . . 57
3.2.2 RF characteristics of graphene FETs . . . 61
3.2.3 Current gain and characteristic frequencies . . . 64

3.3 Experimental techniques . . . 67
3.3.1 Device fabrication . . . 68
3.3.2 Experimental setup . . . 72
3.4 Results . . . 74
3.4.1 Graphene-on-sapphire micro-transistor . . . 75
3.4.2 Graphene-on-SiO_2 nano-transistor . . . 79
3.5 Synopsis and conclusion . . . 84

4 Probing elastic scattering in a graphene field-effect capacitor 87
4.1 Important concepts and formulas . . . 89
4.1.1 Quantum capacitance - electron compressibility . . . 90
4.1.2 Boltzmann equation and transport scattering time . . . 93
4.1.3 Mechanisms of diffusion in graphene . . . 94
4.2 Working principle of a graphene field-effect capacitor . . . 100
4.2.1 2-terminal design . . . 101
4.2.2 Evanescent waves in a capacitor . . . 102
4.3 Experimental techniques . . . 105
4.3.1 Device fabrication . . . 105
4.3.2 Experimental setup . . . 106
4.4 Results and discussion . . . 107
4.4.1 Admittance spectra . . . 107
4.4.2 Conductivity and gate capacitance . . . 111
4.4.3 Diffusion coefficient $D(\epsilon)$ . . . 115

5 Electronic noise and phonon cooling in graphene 119
5.1 Important concepts and formulas . . . 120
5.1.1 Phonons in graphene . . . 120
5.1.2 Electron-acoustic phonon coupling in graphene . . . 121
5.1.3 Heat equation in presence of acoustic phonon cooling . . . 127
5.1.4 Noise in diffusive graphene devices . . . 128
5.2 Hot electrons and electronic noise experiments . . . 134
5.2.1 Measurement techniques . . . 134
5.2.2 Metals . . . 135
5.2.3 Two-dimensional electron gases . . . 136
5.2.4 Carbon nanotubes . . . 136
5.2.5 Graphene . . . 138
5.3 Experimental techniques . . . 139
5.3.1 Device fabrication . . . 139
5.3.2 Sample holder . . . 141
5.3.3 Cryogenic setup . . . 142
5.3.4 Conversion from voltage to current noise spectral density . . . 147
5.3.5 DC characterisation . . . 148
5.3.6 Experimental investigation of electron-acoustic phonon cooling . . . 149
5.4 Results and discussion . . . 150
5.4.1 DC characteristics . . . 151
5.4.2 Current noise spectra . . . 152
5.4.3 Electron temperature T_e . . . 153

5.4.4 Raman verification of cold phonon hypothesis 155
5.4.5 Acoustic phonon coupling constant Σ 157
5.4.6 Fano factor analysis 162
5.4.7 Deviations from the T^4 law at low carrier densities 164
5.5 Synopsis and conclusion 167

6 Outlook: An RF-GFET based sub-nanosecond single charge detector 169

A Appendix - Hexagonal Boron Nitride "Très BN" 173
A.1 Characterisation of hexagonal boron nitride 173

B Appendix - Admittance of a 1-dimensional distributed line 175

C Appendix - Tunnel junction fabrication 177

D Appendix - Solution of the heat equation in presence of acoustic phonon cooling 179

E Appendix - Full current noise spectra 183

F Appendix - Electron temperature in representation T^5/P 185

Bibliography 187

Chapter 1

Introduction

In 2010 the Nobel prize in physics was awarded to K. Novoselov and A. Geim from the University of Manchester for *"groundbreaking experiments regarding the two-dimensional material graphene"* [1]. In their seminal 2004 paper "Electric Field Effect in Atomically Thin Carbon Films" [2] and its follow-up [3] they were able to not only obtain atomically thin carbon layers (coined *graphene* by Boehm et al. in 1986 according to [4]), but also to demonstrate that the carriers in this new, purely two-dimensional material behave like massless Dirac fermions. This new 2D material had been described theoretically long before the initial experimental discovery, but it was only after the aforementioned publications that the "graphene gold rush" [5] truly began: Thanks to the easy technique of obtaining graphene layers by repeated peeling with ordinary adhesive tape, many laboratories - including ours, the Laboratoire Pierre Aigrain - begun research into the film of hexagonally arranged carbon atoms. Prior techniques like the first chemical exfoliation by Boehm et al. in 1962 [6] or epitaxial growth from silicon carbide wafers [7] pioneered at Georgia Tech University require more equipment and knowledge than the simple exfoliation method. The result of any of the above ways of obtaining graphene is a unique material: Graphene is the first 2D crystal of atomic thickness, while still being stronger than e.g. steel; it conducts electricity better than most other conventional conductors; being one atom thin, it is transparent to light [1] and also bendable while still keeping its unique properties.

It is especially graphene's high conductivity combined with the Dirac fermion nature of its charge carrier that has sparked the interest for this work: Use graphene to realise a sub-nanosecond single charge detector. Although the actual device has not been built yet, we present in the following key elements needed to predict the capabilities of said detector and facilitate its design.

[1] Note that even though monolayer graphene is transparent to light it is also quite absorbing at 2.8% per layer.

We will begin this thesis by introducing the general properties of monolayer graphene (MLG), in particular its atomic structure and the resulting linear energy dispersion. The latter is obtained from a tight binding approximation and allows us to calculate further properties of interest, as e.g. the density of states and charge carrier concentration [8, 9]. It is the linear dispersion relation that will lead to the description of charge carriers in MLG in the framework of the Dirac equation. To point out MLG's peculiarity among related materials, we will compare its properties especially to the ones of two-dimensional electron gases (2DEGs) in semiconductor heterostructures. We will then briefly introduce the different types of phonons in graphene [10], before we continue with the description of electronic fluctuations in mesoscopic conductors. Of special interest here is the so-called *shot noise* that arises from the granularity of charge carriers [11, 12]. The chapter concludes with an overview over the state-of-the-art of single electron detection: The main principles and devices, like e.g. single electron transistors (SETs) [13] or carbon nanotube field-effect transistors (CNT-FETs) [14], are presented, as well as a short description of necessary conditions to be met for sub-nanosecond single charge detection in graphene based detectors.

In chapter 2 we present the main principles of the nano-fabrication of our devices. The samples are generally made from exfoliated graphene, employing the famous micro-cleaving technique developed by the Manchester group [2]. Electric contacts and high frequency waveguides are patterned by means of electron-beam (e-beam) lithography followed by a metallisation step. If required the graphene flakes can be tailored into a desired shape using e-beam lithography and reactive ion etching. Depending on the sample design and purpose, the samples are either back- or top-gated. In the first case, doped silicon is chosen as substrate separated from the graphene channel by a silicon oxide layer. In the top-gate design the gate electrode is formed by means of e-beam lithography after the deposition of a thin AlOx dielectric layer. Furthermore, we present in this chapter a wet transfer technique developed at Delft university [15] that allows us to produce stacks of thin exfoliated layers.

Chapters 3 to 5 finally contain the experimental results we could obtain in the areas of radio-frequency graphene field-effect transistors (RF-GFETs), elastic scattering mechanisms probed in a graphene field-effect capacitor (GFEC) and last but not least inelastic scattering of charge carriers and acoustic phonons in graphene. We will start each topic by introducing the necessary formulas and concepts and the device specific fabrication details. Then, we will present our experimental results and analyse them with respect to expected behaviour introduced beforehand. In the paragraphs below we will give a short overview over the main results included in this work.

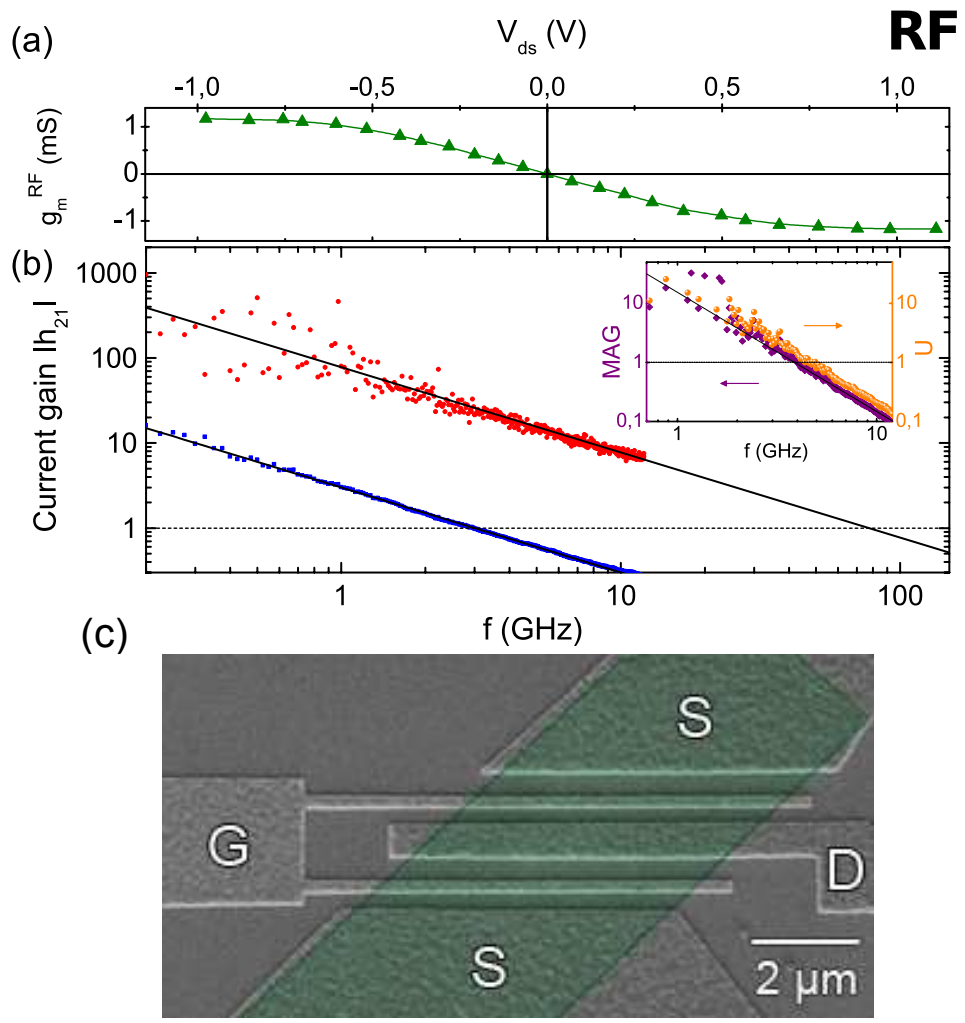

FIGURE 1.1: GHz characteristics of sapphire RF-GFET. a) RF transconductance as function of V_{ds} at $V_g = -4.3$ V. b) Current gain as function of frequency at $V_{ds} = -1.1$ V and $V_g = -5.2$ V, Blue squares show raw data with $f_T \sim 3$ GHz, red dots correspond to de-embedded data with $f_T \sim 80$ GHz. The inset displays the maximum available gain (MAG) and the unilateral power gain U as function of frequency. The solid line in (b) and the inset indicates a $1/f$ dependence. c) Scanning electron microscope picture of sample GoS. The graphene layer is highlighted in green.

Microwave graphene field-effect transistors We start off with a study of the high frequency comportment of RF-GFETs. Two types of samples are investigated: The first is a graphene micro-transistor on sapphire substrate [16], the second a graphene nano-transistor on Si/SiO_2. Both samples are top-gated with a thin AlOx dielectric layer separating the electrode from the channel. Electric contacts are made from Pd, ensuring low interface resistance. Each transistor is situated in a 50 Ω adapted waveguide allowing for precise scattering parameter measurements in the GHz range. Both transistors are characterised at DC and RF using a GHz adapted probe station and suitable

de-embedding technique. We focus on the RF-GFETs transconductance $g_m = dI_{ds}/dV_g$, i.e. the sensitivity of current with respect to changes in gate potential, and the so-called transit frequency $f_T = g_m/(2\pi C_g)$ (here, C_g represents the gate capacitance) marking the limit of current gain. Figs. 1.1(a) and 1.2(a) display the RF transconductance in the graphene-on-sapphire (GoS) and graphene-on-SiO_2 (GoSiO) samples, respectively. For the first we find $g_m^{RF}/(2WV_{ds}) \simeq 0.14$ mSμm^{-1}V^{-1} outperforming its DC counterpart, which is not commonly seen in RF-GFETs and attributed to the fully insulating sapphire substrate removing most parasitic contributions. Normalised to voltage and unit area we obtain a maximum RF transconductance of $g_m^{RF,max} \simeq 1$ mSV$^{-1}\mu$m^{-1} for sample GoSiO, which is close to the maximum reported value for graphene at high frequencies (see table 3.2) and closing in on Si and II-V structures [17].

As mentioned before, the second most interesting figure of merit of our RF-GFETs is the transit frequency f_T. It is the frequency at which the current gain $|H_{21}|$ becomes unity and marks the end of a transistor's current amplification capabilities [18]. In sample GoS we measure $f_T \simeq 80$ GHz close to the estimated value using g_m^{RF} and C_g (see Fig. 1.1(b)). The gate length here is $L_g = 200$ nm. It can be shown that $f_T \propto L_g^{-2}$ (for channel diffusion limited devices [19]), i.e. that reducing L_g remains an option for further increase of f_T. Despite L_g being a crucial element in the design of RF-GFETs, also the charge carrier mobility μ_c and the channel width W play a major role in the transistors RF behaviour. We investigate the effect of scaling on g_m and f_T in the GoSiO sample, which has a smaller channel width than GoS as well as a smaller gate length ($L_g = 110$ nm). Its transit frequency remains below the one of GoS, but still at a high level of $f_T \simeq 17$ GHz (see Fig. 1.2(b)). This result is of particular interest with respect to the establishing of graphene based sub-nanosecond single charge detectors, where a low current noise $S_I \propto W$ is needed. A short outlook on possible ways to improve RF-GFET properties concludes the chapter.

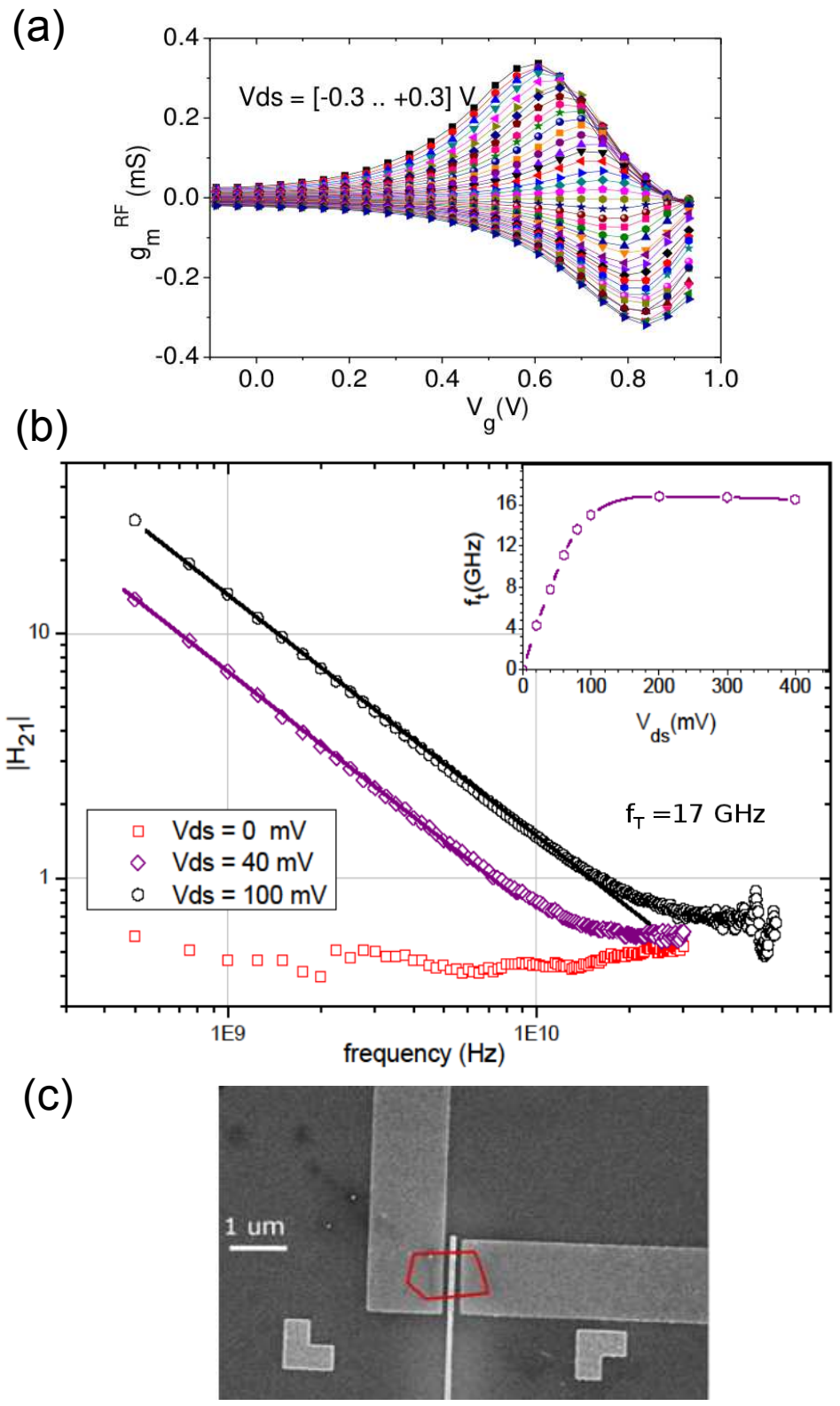

FIGURE 1.2: a) Maximum RF transconductance as function of gate voltage in sample GoSiO. Different colours correspond to different bias voltages in the range $V_{ds} = [-0.3, \ldots, 0.3]V$. b) Current gain $|H_{21}|$ as a function of frequency in graphene-on-SiO_2-FET. Different colours correspond to different drain-source voltages. The inset shows the evolution of the transit frequency f_T with drain-source voltage. c) Scanning electron microscope picture of sample GoSiO. The graphene layer is outlined in red.

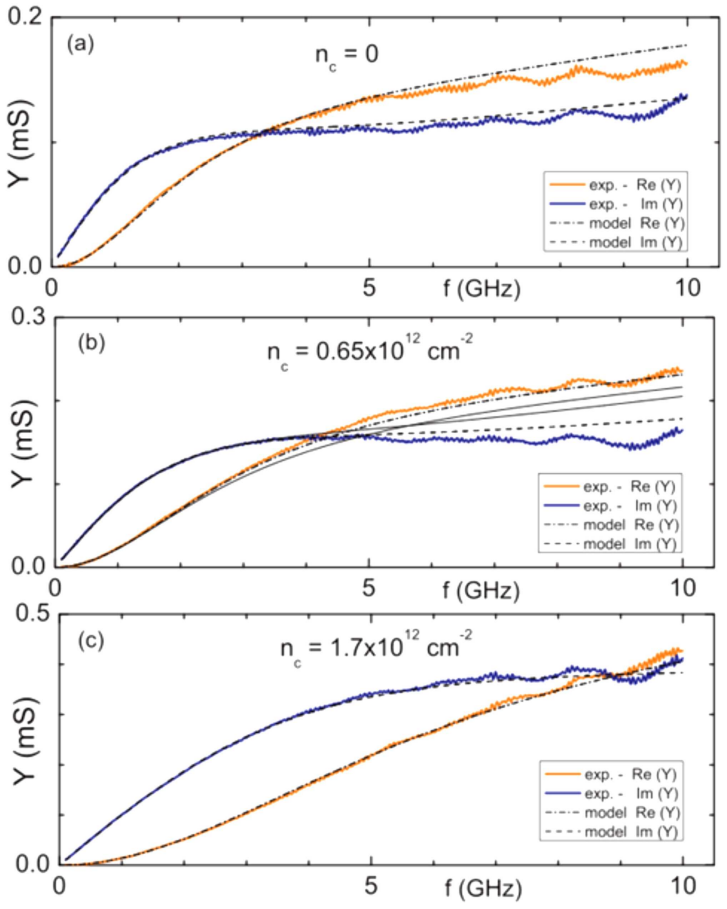

FIGURE 1.3: Admittance spectra of sample E9-Zc as function of frequency for three different carrier densities. The spectra are accurately fitted using the 1D distributed line model (dashed black lines) and an access resistance $R_a = 0.15R_g$. Omitting R_a, one obtains a slight mismatch of the fit at high frequencies as indicated by the solid lines in panel (b).

Probing elastic scattering in a graphene field-effect capacitor In chapter 4 we investigate the elastic scattering of carriers in MLG. The existing theoretical proposals are numerous [20] and outlined in the beginning of this part, following an introduction of the quantum capacitance C_Q, which describes the effect of quantum corrections to the overall capacitance of a device. We add a new facet to the subject by directly accessing the diffusion coefficient D in a graphene field-effect capacitor (GFEC) [21]. Contrary to the more usual three terminal devices comprising drain, source and back-gate, our samples are two-terminal structures: A very thin AlOx dielectric separates the graphene channel from the top-gate, the latter allowing both to control the Fermi energy and to probe the AC admittance parameters Y. It is the thin dielectric (~ 8 nm) and the small density of states that allow us to take advantage of the quantum capacitance and its energy dependence, $C_Q \propto \epsilon_F$ at $T = 0$ K and $C_Q = C_Q(\epsilon, T)$ at $T \neq 0$ K. We are able to probe simultaneously conductivity σ and capacitance C_Q via the complex admittance

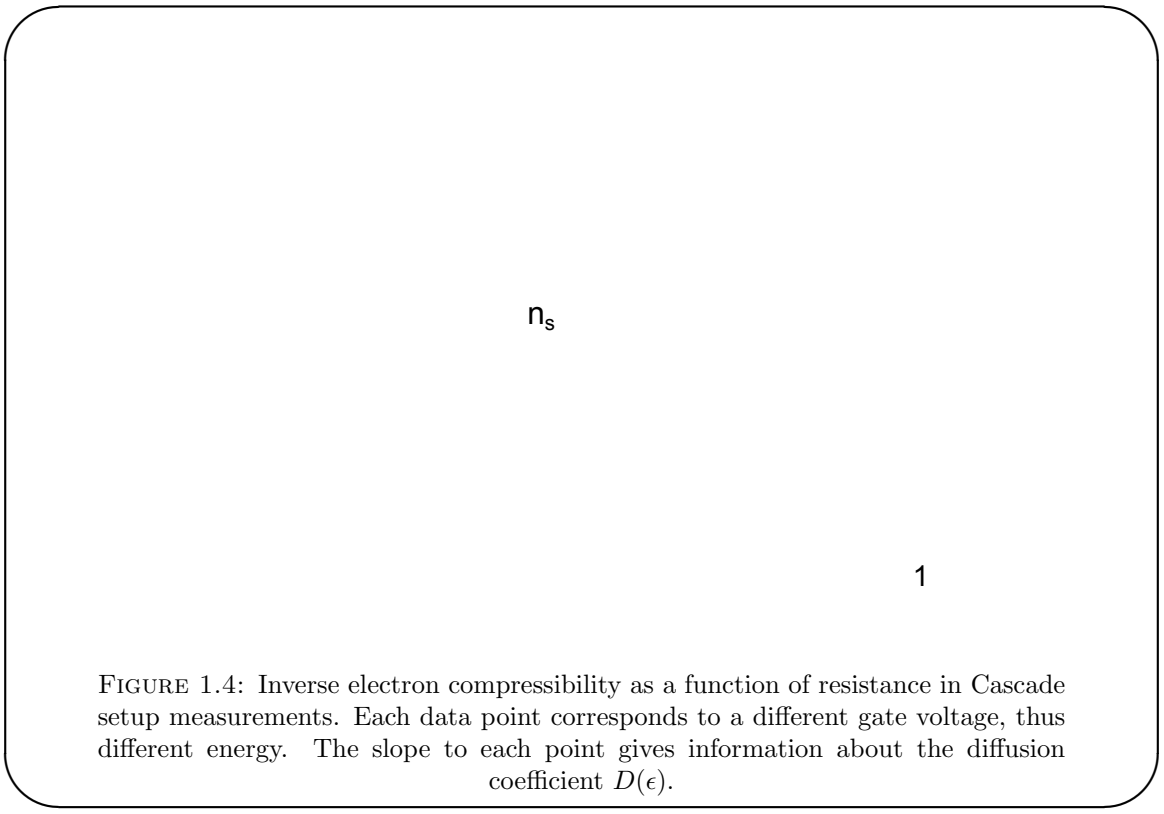

FIGURE 1.4: Inverse electron compressibility as a function of resistance in Cascade setup measurements. Each data point corresponds to a different gate voltage, thus different energy. The slope to each point gives information about the diffusion coefficient $D(\epsilon)$.

parameters in a GHz probe station setup and using appropriate de-embedding analogue to the one employed in chapter 3. The forward AC admittance signal Y_{21} exhibits a high frequency behaviour reminiscent of an evanescent wave effect in planar conductors: After the crossover of real and imaginary part of the complex admittance, we obtain $\Re(Y_{21}) = \Im(Y_{21})$ (see Fig. 1.3). The complete spectrum, including crossover and high frequency evanescent wave signature, can be modelled by a 1-dimensional distributed line of RC parts [21]. The hitherto calculated Y_{21} carries in its low frequency development separately σ and C_Q in the real and imaginary part, respectively. Using the so-called *Einstein relation* $\sigma(\epsilon) = C_Q(\epsilon)D(\epsilon)$ we can then directly extract the diffusion coefficient and transport scattering time τ_{tr} from our experiments; τ_{tr} is the average time needed to reverse the carriers direction of movement. In MLG the Fermi velocity $\nu_F = const.$ and thus we can directly convert to τ_{tr} via $D = \nu_F^2 \tau_{tr}/2$. We find values of D in accord with reported estimates, but differ in the conclusion on the main scattering mechanism. In contrast to other experiments, our measurements show that in the energy range investigated here, $\epsilon \simeq$ 0–230 meV, the diffusion coefficient is independent of energy (see Fig.1.4) and therefore also $\tau_{tr}(k_F) = const.$ This result may be explained by the so-called random Dirac mass disorder mechanism, where carriers locally acquire a finite mass, $m*(r) \neq 0$, while on the average $< m* >= 0$, as usual in MLG [22]. Alternative explanations could be a particular form of ripples or an admixture of several more conventional mechanisms. Experiments probing diffusion in MLG generally find a

sublinear dependence of σ on carrier concentration n_s; in our case $\sigma \propto \sqrt{n_s}$. Another more application oriented result of our GFEC experiments concerns the afore mentioned crossover of $\Re(Y_{21})$ and $\Im(Y_{21})$: Its frequency $\omega_c = \frac{\pi^2\sigma}{2C'_{geo}L^2} + \frac{\pi^2 D}{2L^2}$ exceeds the Thouless frequency $\omega_{Thouless} = D/L^2$ which has the effect that ω_c stays finite even at the charge neutrality point (CNP). In other words, even at the CNP the probing 1D wave can penetrate the gate region. Therefore RF-graphene devices show no critical slowing down even at neutrality.

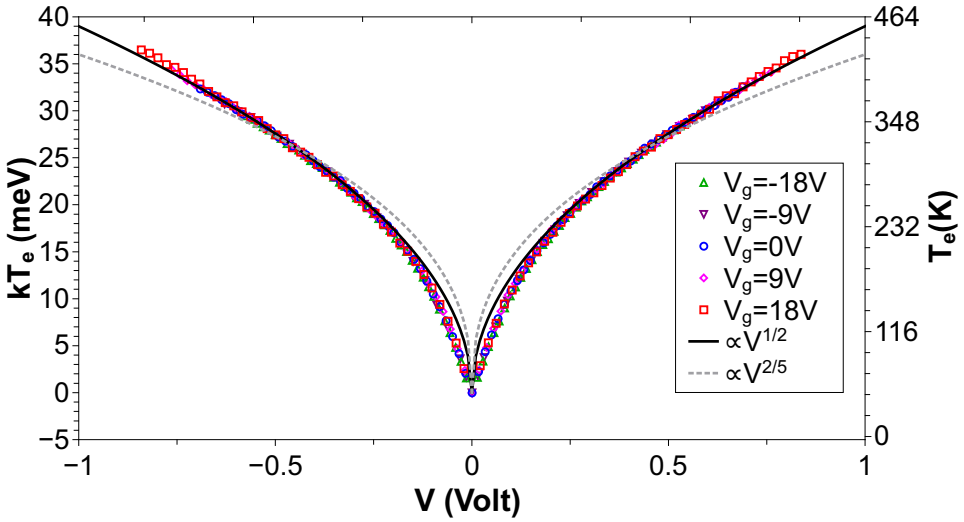

FIGURE 1.5: Electronic temperature in sample BN1 as function of voltage bias for a set of gate voltages. $T_e = S_I V/(4k_B I)$ is deduced from the $S_I(V)$ and $I(V)$ data shown in Fig. 5.18(c) and (b). Unlike $S_I(V)$, $T_e(V)$ is nearly independent of gate voltage and closely follows the $T_e \propto \sqrt{V}$ law (black solid line) expected for 2D phonons. A $T_e \propto V^{2/5}$ law (grey dashed line) is also plotted to highlight the difference with a standard 3D-phonons mechanism. Deviations are observed at low bias where a $T_e \propto V$ behavior is found.

Electronic noise and phonon cooling in graphene Finally in chapter 5, we present a study of the electronic noise and cooling of hot carriers by acoustic phonons (APs) in graphene. We detail further the description of phonons, which we will initiate in chapter 1, followed by an introduction to the temperature dependence of electron-acoustic phonon cooling in 2 dimensions. It will reveal that in graphene the crossover between regimes takes place at the so-called Bloch-Grueneisen temperature T_{BG} as opposed to normal 2D systems, where the Debye temperature Θ_D is the natural scale [23]. The different scale is a result of the small Fermi surface of graphene, thus a direct consequence of the linear energy dispersion, vanishing at the K, K' points. We will also discuss the electron-AP cooling in graphene at high and low carrier density [24]; in the first case, where the MLG is metallic, one expects a cooling power $Q = LW\Sigma(T_e^4 - T_{phonon}^4)$. Here, L, W are the samples length and width, respectively, Σ is the electron-AP coupling

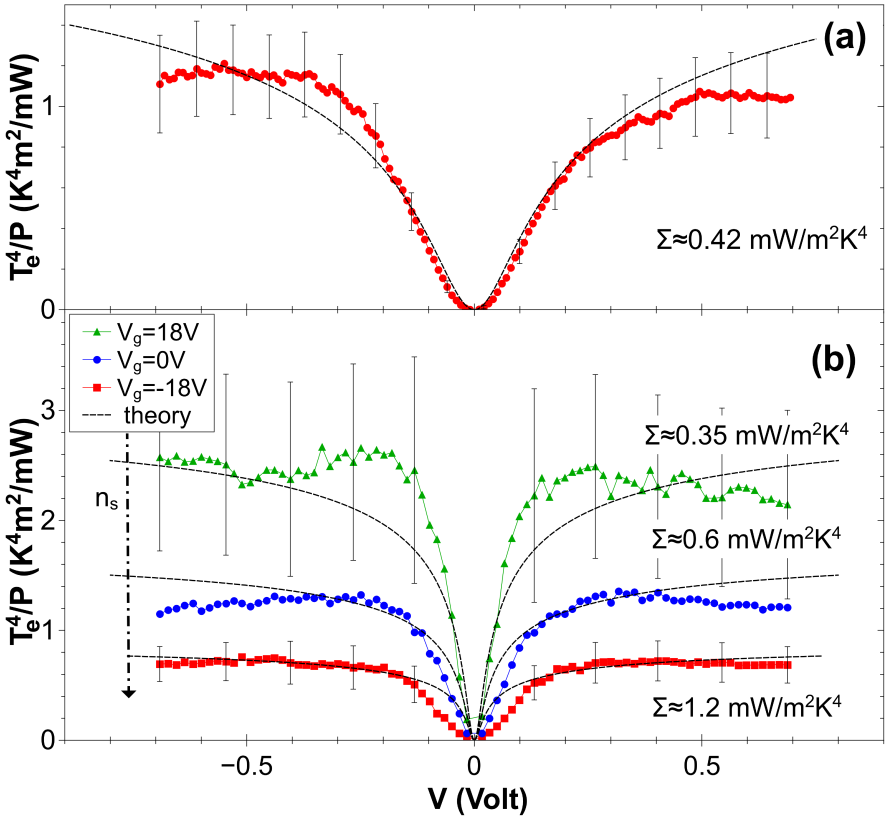

FIGURE 1.6: (a) and (b): Electron temperature of sample CVD1 (a) and BN1 (b) plotted as $T_e^4(V)/P$, where P is the Joule heating per unit area, $P = V^2/RLW$. The plateau at high bias is at a value $T_e^4/P \simeq 1/\Sigma$. The dip at low V is due to electron heat diffusion to the leads. Dashed lines are one-parameter fits with Σ as free parameter.

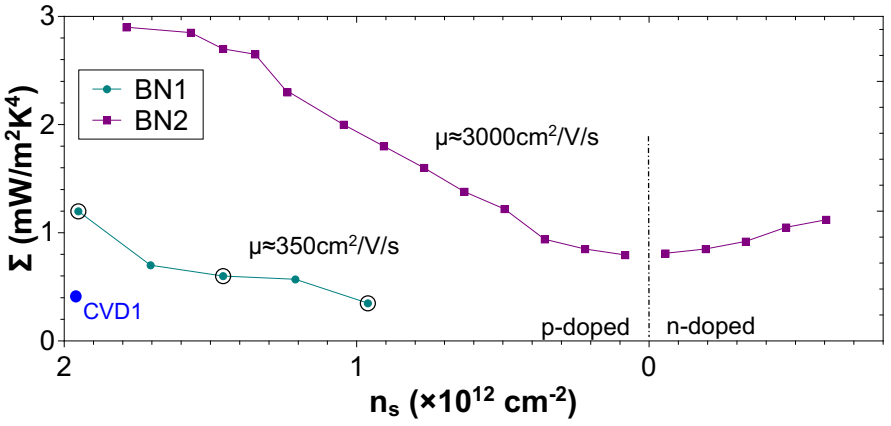

FIGURE 1.7: Σ as function of carrier density n_s for samples BN1 and BN2. The value of CVD1 is displayed as an indicator.

constant and T_e, T_{phonon} are the average electron and phonon temperature. Such a T^4 dependence is therefore one of the tell-tale signs of a two-dimensional electron-phonon

interaction, in contrast to a T^5 (T^3) law for a 3D (1D) phonon system. In addition to $Q \propto T^4$, hot carriers and cold phonons are further signatures of the expected 2D mechanism, as Σ is predicted to be much smaller than the coupling of phonons to the cold substrate. Experimentally the average electron temperature can be extracted from noise measurements [25], where an incoming Joule power $P = V^2/(LWR)$ heats the carriers and a heat balance with the phonon cooling establishes. Here, $R \equiv V/I$. Using precise calibration we obtain T_e from the current noise $S_I = 4k_BT_e/R$, where R is the sample's differential resistance. The investigated samples are backgated graphene FETs (GFETs), either on Si/SiO_2 or on hBN substrates. The latter is fabricated by means of a wet transfer technique introduced in chapter 2. Measurements take place at liquid helium temperature (4 K) and involve a GHz bandwidth amplification line. We find that in the investigated bias range, which is chosen small enough to discard the contribution of optical phonons, T_e is well fitted by $\sqrt{V}$ (see Fig. 1.5). This confirms the 2D phonon cooling mechanism. Furthermore, as can be seen from Fig. 1.5, the carriers remain much hotter than the bath. Also, we confirm the cold phonon hypothesis via "in situ" Raman spectroscopy. In order to highlight the carrier density dependence of the electron-AP cooling and to analyse data further including the electron heat diffusion to the leads, we plot data as T_e^4/P (Fig. 1.6). Using the solution of the heat equation

$$\frac{L_o}{2R}L^2\frac{d^2T^2(x)}{dx^2} = -\frac{V^2}{R} + LW\Sigma\left(T^4 - T_{phonon}^4\right) \tag{1.1}$$

where L_o is the Lorentz number, we accurately fit the average electron temperature with Σ as only free parameter [26]. In Fig. 1.7 we display Σ as a function of carrier density. At a reference density $n_s = 10^{12}$ cm^{-2} predictions for the coupling between carriers and the longitudinal acoustic branch of 2D phonons [24] are still several times bigger than values extracted from our experiments. However, using the carrier mobility μ_c as indicator for the amount of lattice disorder, our findings suggest an effect of lattice disorder on the electron-AP coupling. Further experimental and theoretical investigation is needed to clarify this topic.

At the end of this chapter we present recent measurements showing deviations from the $P \propto T^4$ law towards the charge neutrality point: A $P \propto T^3$ dependence arises which might be explained by a supercollision mechanism including two-phonon processes or phonon-impurity scattering [27]. Supercollisions are rare events that play a negligible role in electron scattering but show up strongly in the the electron energy relaxation close to neutrality.

At the end of this thesis, we briefly review the different charge detection devices introduced priorly in chapter 1 and estimate the single charge detection capabilities of a similar device based on MLG. A sub-nanosecond single charge detector design proposal

based on the knowledge acquired during the previous chapters and utilising quantum Hall edge channels in MLG and an RF-GFET capacitively coupled to the former completes this section.

Let us however first of all introduce graphene, its atomic and electronic properties, as well as general concepts and formulas important for this work.

1.1 Graphene: description and properties

1.1.1 Atomic structure

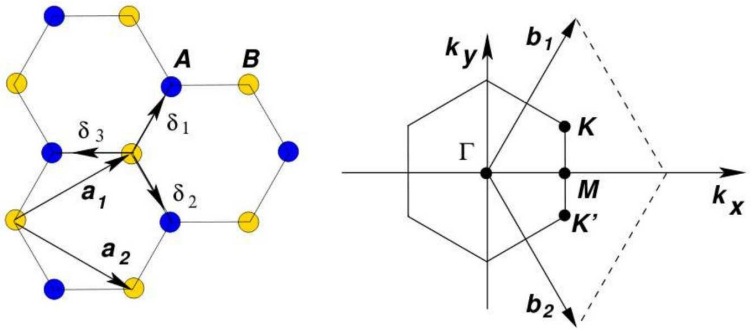

FIGURE 1.8: **Left:** Graphene lattice, made of two inter-penetrating triangular lattices (a1 and a2 are the lattice unit vectors and i ,i=1,2,3, are the nearest neighbour vectors); **Right:** Corresponding Brillouin zone. The Dirac cones are located at the K and K' points. From Castro Neto et al. [28].

MLG is a two-dimensional lattice of carbon atoms arranged in a honeycomb like shape. The atoms are equally distanced giving the honeycomb a side length of $a_{C-C} \simeq 1.42\mathring{A}$. Although exhibiting a certain symmetry, the resulting lattice is not Bravais, but a superposition of two Bravais sub-lattices, formed by atoms of type A and B as shown in Fig. 1.8. For each sub-lattice the real space unit vectors are given by

$$\mathbf{a_1} = \left(\frac{3a}{2}, \frac{\sqrt{3}a}{2}\right) \quad , \quad \mathbf{a_2} = \left(\frac{3a}{2}, -\frac{\sqrt{3}a}{2}\right) \tag{1.2}$$

and in reciprocal space, also defining the fist Brillouin zone,

$$\mathbf{b_1} = \left(\frac{2\pi}{3a}, \frac{2\pi}{\sqrt{3}a}\right) \quad , \quad \mathbf{b_2} = \left(\frac{2\pi}{3a}, -\frac{2\pi}{\sqrt{3}a}\right) \tag{1.3}$$

with $a = \sqrt{3} \cdot \mathrm{a_{C-C}}$. Although the honeycomb lattice is not a Bravais one in itself, one can construct a Bravais lattice taking a base of two carbon atoms (one from each

sub-lattice). Then, the unit vectors remain the same as for the sub-lattices. In the reciprocal lattice we define four high symmetry points K, K′ , M and Γ, which are the corners of the first Brillouin zone, its centre and the middle of the connection between two neighbouring atoms. Their importance will reveal later. Last but not least, there is a third set of vectors which we will use in the following paragraphs:

$$\delta_{\mathbf{1}} = \left(\frac{a}{2}, \frac{\sqrt{3}a}{2}\right) \quad , \quad \delta_{\mathbf{2}} = \left(\frac{a}{2}, -\frac{\sqrt{3}a}{2}\right) \quad , \quad \delta_{\mathbf{3}} = (-a, 0) \tag{1.4}$$

Hybridisation of orbitals The electron configuration of a single C atom is $1s^2 2s^2 2p^2$. Due to a very small energy separation between $2s$ and $2p$ the hybridisations sp, sp^2 or sp^3 can arise. In the case of graphene, it is sp^2 with three orbitals arranged in the graphene plane at 120 ° to each other. These σ-bonds bind the C atoms in plane, whereas the fourth, unaffected orbital can form a covalent π-bond to the next plane. The electronic properties are mostly depending on the π electrons, since the σ-bonds are far from the Fermi level.

1.1.2 Electronic properties

Graphene's astonishing properties arise from its planar nature and the hexagonal arrangement of its atoms. In the following we will give a short theoretical description of the tight-binding approach in graphene in nearest-neighbour approximation. This will be helpful in the following parts where we will briefly study several other important implications arising from graphene's particular structure: the linear energy dispersion, the linear density of states and the massless charge carriers. A more detailed description can be found e.g. in [29] and references therein.

1.1.2.1 Tight-binding approach

In the tight-binding approach one assumes first of all that at each node in a lattice the potential is mainly given by the on-site atom and all corrections $\Delta U(\mathbf{r})$, establishing the full periodicity, are small. Secondly, in order to satisfy Bloch's theorem [30], one constructs the eigenfunctions of the Hamiltonian as a linear combination of atomic wave functions [9]:

$$\Psi(\mathbf{r}) = \sum_{\mathbf{R}} e^{i\mathbf{k}\cdot\mathbf{R}} \phi(\mathbf{r} - \mathbf{R}) \tag{1.5}$$

Note that in the general description of a tight-binding model the above mentioned function $\phi(\mathbf{r})$ is not necessarily an atomic wave function but can usually be written as a linear combination of a small number of such.

Since graphene contains two atoms per unit cell, the description above has to be slightly modified. The wave function has two components, to take into account the sub-lattices A and B [8]:

$$\Psi_{\mathbf{k}}(\mathbf{r}) = a_{\mathbf{k}}\Psi^A_{\mathbf{k}}(\mathbf{r}) + b_{\mathbf{k}}\Psi^B_{\mathbf{k}}(\mathbf{r}) \tag{1.6}$$

$$= \frac{1}{\sqrt{N}}\sum_{\mathbf{R}_l} e^{i\mathbf{k}\cdot\mathbf{R}_l}\left[a_{\mathbf{k}}\Phi(\mathbf{r}-\mathbf{R}^A_l) + b_{\mathbf{k}}\Phi(\mathbf{r}-\mathbf{R}^B_l)\right] \tag{1.7}$$

Here $\mathbf{R}^{A/B}_l$ is a lattice vector in sub-lattice A or B, N the number of unit cells and the $\Phi(\mathbf{r})$ the wave functions of the $2p_z$ orbitals. The origin of the Bravais lattice is chosen to coincide with an atom of sub-lattice A.

We can now turn to solving the Schrödinger equation $H\Psi_{\mathbf{k}} = \epsilon_{\mathbf{k}}\Psi_{\mathbf{k}}$ by multiplying it from the left with $\Psi^\dagger_{\mathbf{k}}$ [9]:

$$\Psi^\dagger_{\mathbf{k}} H \Psi_{\mathbf{k}} = \epsilon_{\mathbf{k}}\Psi^\dagger_{\mathbf{k}}\Psi_{\mathbf{k}} \tag{1.8}$$

$$\left(a^\dagger_{\mathbf{k}}, b^\dagger_{\mathbf{k}}\right) H_{\mathbf{k}} \begin{pmatrix} a_{\mathbf{k}} \\ b_{\mathbf{k}} \end{pmatrix} = \epsilon_{\mathbf{k}} \left(a^\dagger_{\mathbf{k}}, b^\dagger_{\mathbf{k}}\right) S_{\mathbf{k}} \begin{pmatrix} a_{\mathbf{k}} \\ b_{\mathbf{k}} \end{pmatrix} \tag{1.9}$$

Above $H_{\mathbf{k}}$ is the Hamiltonian matrix

$$H_{\mathbf{k}} = \begin{pmatrix} \Psi^{A\dagger}_{\mathbf{k}} H \Psi^A_{\mathbf{k}} & \Psi^{A\dagger}_{\mathbf{k}} H \Psi^B_{\mathbf{k}} \\ \Psi^{B\dagger}_{\mathbf{k}} H \Psi^A_{\mathbf{k}} & \Psi^{B\dagger}_{\mathbf{k}} H \Psi^B_{\mathbf{k}} \end{pmatrix} \tag{1.10}$$

$$\tag{1.11}$$

and $S_{\mathbf{k}}$ the wave function overlap matrix

$$S_{\mathbf{k}} = \begin{pmatrix} \Psi^{A\dagger}_{\mathbf{k}} \Psi^A_{\mathbf{k}} & \Psi^{A\dagger}_{\mathbf{k}} \Psi^B_{\mathbf{k}} \\ \Psi^{B\dagger}_{\mathbf{k}} \Psi^A_{\mathbf{k}} & \Psi^{B\dagger}_{\mathbf{k}} \Psi^B_{\mathbf{k}} \end{pmatrix} \tag{1.12}$$

Finally, computing $\det\left(H_{\mathbf{k}} - \epsilon^\lambda_{\mathbf{k}} S_{\mathbf{k}}\right) = 0$ yields the eigenvalues $\epsilon^\lambda_{\mathbf{k}}$ or energy bands. There are as many bands as there are atoms per unit cell, thus $\lambda = 1, 2 = \pm$ in the case of MLG. In the end one obtains the energy dispersion relation

$$\epsilon^\lambda_{\mathbf{k}} = \frac{2\epsilon_0 - \epsilon_1 \pm \sqrt{(-2\epsilon_0 + \epsilon_1)^2 - 4\epsilon_2\epsilon_3}}{2\epsilon_3} \tag{1.13}$$

with

$$\epsilon_0 = H_{\mathbf{k}}^{AA} S_{\mathbf{k}}^{AA} \tag{1.14}$$

$$\epsilon_1 = S_{\mathbf{k}}^{AB} H_{\mathbf{k}}^{BA\dagger} + H_{\mathbf{k}}^{AB} S_{\mathbf{k}}^{BA\dagger} \tag{1.15}$$

$$\epsilon_2 = H_{\mathbf{k}}^{AA\,2} - H_{\mathbf{k}}^{AB} H_{\mathbf{k}}^{AB\dagger} \tag{1.16}$$

$$\epsilon_3 = S_{\mathbf{k}}^{AA\,2} - S_{\mathbf{k}}^{AB} S_{\mathbf{k}}^{AB\dagger} \tag{1.17}$$

$$\tag{1.18}$$

$$H_{\mathbf{k}}^{ij} = \Psi_{\mathbf{k}}^{i\dagger} H \Psi_{\mathbf{k}}^{j} \quad , \quad S_{\mathbf{k}}^{ij} = \Psi_{\mathbf{k}}^{i\dagger} \Psi_{\mathbf{k}}^{j} \tag{1.19}$$

1.1.2.2 Nearest neighbour approximation

The computation of the eigenstates can be simplified by considering only nearest neighbours (nn) to a given atom on e.g. sub-lattice A. All 3 nearest neighbours are then of type B. We defined $\delta_{\mathbf{i}} = \mathbf{R}^{B_i} - \mathbf{R}_l^A$ (see Eq.(1.4)) and calculate the off-diagonal Hamiltonian elements

$$H_{\mathbf{k}}^{AB} = t \sum_j e^{i\mathbf{k}\cdot\delta_{\mathbf{j}}} = t\gamma_{\mathbf{k}} \tag{1.20}$$

Here, t is the nn hopping energy, or transfer integral, of $\simeq 2.8$ eV [28] and is due to the perturbation ΔV of the single carbon Hamiltonian by the surrounding atoms: $t \equiv \int d^2r \Phi^{(A)\dagger}(\mathbf{r}) \Delta V \Phi^{(B)}(\mathbf{r} + \delta_{\mathbf{3}})$. $\Phi^{(j)}(\mathbf{r})$ is the orbital wave function with respect to sub-lattice j. Recent calculations show that an extension to next-nearest neighbours (nnn), thus then of the same sub-lattice, can be omitted since $t_{nnn} \simeq 0.1$ eV [31]. Owing to symmetry, we also have $H_{\mathbf{k}}^{AA} = H_{\mathbf{k}}^{BB}$ and $H_{\mathbf{k}}^{AB} = H_{\mathbf{k}}^{BA\dagger}$. Restricting calculations to nn, the diagonal elements of $H_{\mathbf{k}}^{ij}$ yield

$$H_{\mathbf{k}}^{ii} = \Psi_{\mathbf{k}}^{i\dagger} H \Psi_{\mathbf{k}}^{i} = \epsilon_{2p_z} \tag{1.21}$$

which will be our energy reference, i.e. $\epsilon_{2p_z} \equiv 0$.

Since the wave functions are assumed to be normalised we find the diagonal overlap elements $S_{\mathbf{k}}^{ii} = 1$. The off-diagonals contribute a phase factor as $H_{\mathbf{k}}^{AB}$ above:

$$S_{\mathbf{k}}^{nm} = \Psi_{\mathbf{k}}^{n\dagger} \Psi_{\mathbf{k}}^{m} \cdot \gamma_{\mathbf{k}} \tag{1.22}$$

The electrons accounting for transport are, as mentioned previously, those of the $2p_z$ orbitals. These are perpendicular to the sheet, i.e. the spatial extension into the x-y-plane is very small and we can therefore neglect the off-diagonal elements of $S_{\mathbf{k}}$.

1.1.2.3 Electronic band structure

The *nn* considerations above greatly simplify equation (1.8) and the energy dispersion (1.13). It reduces now to

$$\epsilon^{\lambda}_{\mathbf{k}} = \pm t\sqrt{1 + 4cos\left(\frac{\sqrt{3}k_x a}{2}\right)cos\left(\frac{3k_y a}{2}\right) + cos^2\left(\frac{\sqrt{3}k_x a}{2}\right)} \tag{1.23}$$

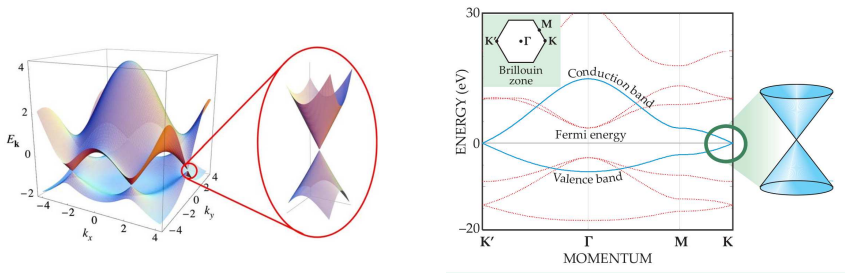

FIGURE 1.9: left: Energy dispersion of graphene monolayer. From Castro Neto et al [28]. right: Band structure of MLG. From Geim and MacDonald [32]

The energy vanishes at two inequivalent points [29]

$$\mathbf{K} = \left(\frac{2\pi}{3a}, \frac{2\pi}{3\sqrt{3}a}\right) \quad , \quad \mathbf{K}' = \left(\frac{2\pi}{3a}, -\frac{2\pi}{3\sqrt{3}a}\right) \tag{1.24}$$

They are the corners of the first Brillouin zone and are responsible for one of the remarkable properties of MLG: valence and conduction band cross. As a consequence, graphene is often referred to as a semi-metal or zero-gap semiconductor. The band structure, or energy dispersion, of MLG obtained from Eq.(1.23) is shown in Fig. 1.9. $\mathbf{K}$ and $\mathbf{K}'$ are also-called Dirac points or charge neutral points. They come in pairs due to time-reversal symmetry ($\epsilon_{-\mathbf{k}} = \epsilon_{\mathbf{k}}$) and give rise to a two-fold, so-called *valley degeneracy* of the zero-energy states.

Low energy linearisation Fig.1.9 already points out one major feature of the graphene energy dispersion: the conical shape in the vicinity of the Dirac points and the dependence on the two-dimensional wave-vector $\mathbf{k}$. Before we start the low energy linearisation, it is useful to define an effective tight-binding Hamiltonian matrix with the previously obtained results:

$$H_{\mathbf{k}} = \begin{pmatrix} 0 & t\gamma_{\mathbf{k}} \\ t\gamma^{\dagger}_{\mathbf{k}} & 0 \end{pmatrix} \tag{1.25}$$

This highlights again the necessity of including both sub-lattices in the description by using the spinors

$$\Psi_{\mathbf{k}}^{\lambda} = \begin{pmatrix} a_{\mathbf{k}}^{\lambda} \\ b_{\mathbf{k}}^{\lambda} \end{pmatrix} \tag{1.26}$$

In order to describe the low energy excitations in graphene, i.e. electronic excitations close to the Fermi level, one has to investigate the states in close vicinity to the Dirac points $\mathbf{K}$ and $\mathbf{K}'$. There, we define the displacement of the wave vector from the charge neutrality point $\mathbf{K}^{(\prime)}$:

$$\mathbf{q} = \mathbf{k} - \mathbf{K}^{(\prime)} \qquad \mid \mathbf{q} \mid \ll \mathbf{K} \sim 1/a \tag{1.27}$$

For the ease of calculation, we will consider a lattice rotated by 90 ° with respect to the one shown in Fig.1.8 and shift $\mathbf{K}$ and $\mathbf{K}'$ [2].

From the effective Hamiltonian (1.25) one immediately recognises that $\gamma_{\mathbf{k}}$ is the entity to be expanded in the low energy linearisation.

$$\gamma_{\mathbf{k}} \simeq \left(1 + i(\frac{\sqrt{3}a}{2}q_x + \frac{a}{2}q_y)\right) e^{i\frac{2\pi}{3}} + \left(1 + i(-\frac{\sqrt{3}a}{2}q_x + \frac{a}{2}q_y)\right) e^{-i\frac{2\pi}{3}} + (1 - i(aq_y)) \tag{1.28}$$

$$= -\frac{3a}{2}\left(q_x + iq_y\right) \tag{1.29}$$

for $\mathbf{K}$ and for $\mathbf{K}'$ analogously

$$\gamma_{\mathbf{k}} = \frac{3a}{2}\left(q_x - iq_y\right) \tag{1.30}$$

The above is achieved with the help of $sin(\pm 2\pi/3) = \pm\sqrt{3}/2$ and $cos(\pm 2\pi/3) = -1/2$. Introducing the *valley isospin* $\xi = \pm$, where $+$ denotes $\mathbf{K}$ and $-$ $\mathbf{K}'$, we can then reformulate (1.25)

$$H_{\mathbf{q}}^{\xi} = \xi \begin{pmatrix} 0 & -\frac{3}{2}ta(q_x + iq_y) \\ \frac{3}{2}ta(q_x - iq_y) & 0 \end{pmatrix} = \xi\hbar\nu_F(q_x\sigma^x + \xi q_y\sigma^y) \tag{1.31}$$

where we defined the ***Fermi velocity***

$$\nu_F = \frac{3ta}{2\hbar} \simeq 10^6 \text{ m/s} \tag{1.32}$$

and use the Pauli matrices

$$\sigma^x = \begin{pmatrix} 0 & 1 \\ 1 & 0 \end{pmatrix} \quad \text{and} \quad \sigma^y = \begin{pmatrix} 0 & -i \\ i & 0 \end{pmatrix} \tag{1.33}$$

[2] $\mathbf{K}^{(\prime)} = \left(\pm\frac{4\pi}{3\sqrt{3}a}\ ,\ 0\right)$ and $\delta_{\mathbf{1}} = \left(\frac{\sqrt{3}a}{2}, \frac{a}{2}\right)$, $\delta_{\mathbf{2}} = \left(\frac{-\sqrt{3}a}{2}, -\frac{a}{2}\right)$, $\delta_{\mathbf{3}} = (0, -a)$

The energy dispersion (1.23) then reads

$$\epsilon^{\lambda}_{\mathbf{q},\xi=\pm} = \lambda\hbar\nu_F \mid \mathbf{q} \mid \tag{1.34}$$

which is now linear in wave vector $\mathbf{q}$ for small deviations from the neutrality points (see Fig.1.9). Here, $\lambda = +$ denotes the conduction and $\lambda = -$ the valence band. Note also that although both neutrality points have the same energy dispersion, charge carriers on different sub-lattices will propagate with a phase shift in $\mathbf{k}$ space of $\phi_{\mathbf{q}} = arctan\left(\frac{q_y}{q_x}\right)$. Also, the *Fermi velocity* introduced above has been experimentally verified by [3].

Introducing a four-spinor representation of the wave function

$$\Psi_{\mathbf{k}} = \begin{pmatrix} \psi^A_+ \\ \psi^B_+ \\ \psi^B_- \\ \psi^A_- \end{pmatrix} = \frac{1}{\sqrt{2}} \begin{pmatrix} 1 \\ \lambda e^{i\phi_{\mathbf{k}}} \\ 1 \\ -\lambda e^{i\phi_{\mathbf{k}}} \end{pmatrix} \tag{1.35}$$

we can further reformulate the effective Hamiltonian to

$$H_{\mathbf{q}} = \hbar\nu_F \begin{pmatrix} \boldsymbol{\sigma}\cdot\mathbf{q} & 0 \\ 0 & -\boldsymbol{\sigma}\cdot\mathbf{q} \end{pmatrix} = \hbar\nu_F \boldsymbol{\alpha}\cdot\mathbf{q} \tag{1.36}$$

where

$$\boldsymbol{\alpha} = \begin{pmatrix} \boldsymbol{\sigma} & 0 \\ 0 & -\boldsymbol{\sigma} \end{pmatrix} \quad \text{and} \quad \boldsymbol{\sigma} = (\sigma^x, \sigma^y) \tag{1.37}$$

The off-diagonals zeros in Eq. (1.36) indicate the independence of the energy dispersion cones around the points $\mathbf{K}$ and $\mathbf{K}'$. We will therefore consider only one cone in the applied sections of this work and take into account the two-fold degeneracy by a simple factor 2.

1.1.3 Dirac fermions in graphene

The effective tight-binding Hamiltonian (1.36) is reminiscent of the Dirac equation in 2 dimensions for particles without mass. We cannot give a full introduction to the Dirac equation here and refer the interested reader thus to e.g. [33].

1.1.3.1 Dirac equation in 2D

In two dimensions one needs three mutually anti-commuting objects α_1, α_2 and β satisfying the Clifford algebra, which are in this case identified as the Pauli matrices

$$\sigma^x = \begin{pmatrix} 0 & 1 \\ 1 & 0 \end{pmatrix} \quad \sigma^y = \begin{pmatrix} 0 & -i \\ i & 0 \end{pmatrix} \quad \sigma^z = \begin{pmatrix} 1 & 0 \\ 0 & -1 \end{pmatrix}. \tag{1.38}$$

Hence one obtains the 2D Hamiltonian

$$H^{2D} = c\,\boldsymbol{\sigma} \cdot \mathbf{p} + mc^2\sigma^z \quad \text{where} \quad \boldsymbol{\sigma} = (\sigma^x, \sigma^y) \tag{1.39}$$

Substituting the speed of light c by the Fermi velocity ν_F and assuming zero mass, this is of the same form as the effective tight-binding Hamilitonian (1.31) at the point $\mathbf{K}'$. An equally valid choice in the Clifford algebra in 2D is $\alpha_1 = -\sigma^x$, $\alpha_2 = -\sigma^y$ and $\beta = -\sigma^z$ which then gives the Hamiltonian for $\mathbf{K}$.

1.1.3.2 Band, valley and chirality

Note that in the general Dirac equation $\boldsymbol{\sigma}$ describes the physical spin of a particle. In the case of graphene, $\boldsymbol{\sigma}$ describes the *sub-lattice isospin*, as introduced in Eq.(1.36). It is of importance for transport experiments since $\boldsymbol{\sigma}$ is intimately related the band index and $\boldsymbol{\sigma}||\mathbf{q}$. In terms of application of the Dirac equation, an often used operator is the

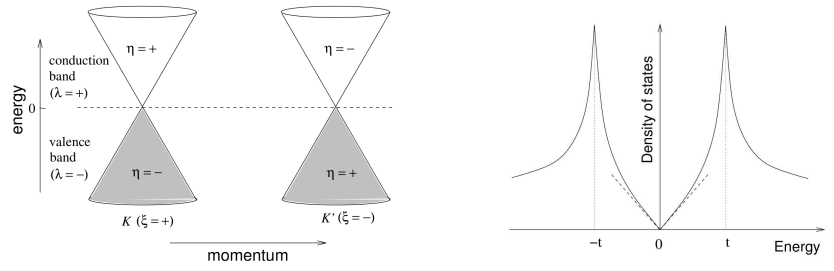

FIGURE 1.10: Left: Relation between band index λ, valley isospin ξ, and chirality η in graphene. From M. Goerbig [9]. Right: Sketch of the density of states in graphene in *nn*-approximation. The dashed lines indicate the density of states obtained in the low energy linearisation. From M. Goerbig [9].

helicity: It is the projection of the spin onto the direction of propagation of the particle

$$h_{\mathbf{p}} = \frac{\mathbf{p} \cdot \boldsymbol{\sigma}}{|\,\mathbf{p}\,|} \tag{1.40}$$

with eigenvalues $\eta = \pm$. In the absence of mass, thus e.g. approximately for neutrinos, $h_{\mathbf{p}}$ commutes with the Dirac Hamiltonian and η is a good quantum number. Since, as mentioned above, in the case of graphene $\boldsymbol{\sigma}$ refers to sub-lattice isospin $h_{\mathbf{p}}$ is also-called *chirality* operator and commutes with the effective Hamiltonian in Dirac representation. We can therefore reformulate (1.36)

$$H_{\mathbf{p}}^{\xi} = \xi \mid \mathbf{p} \mid h_{\mathbf{p}} \tag{1.41}$$

taking into account the $\mathbf{K}$, $\mathbf{K}'$ valley degeneracy via the *valley isospin* $\xi = \pm$. The band index λ (see also (1.23)) describing valence and conduction band is fully determined by chirality and valley isospin:

$$\lambda = \eta \cdot \xi \tag{1.42}$$

It is displayed in Fig.1.10.

1.1.4 Consequences of Dirac equation in graphene

1.1.4.1 Massless charge carriers

Eq.(1.34) also highlights another of graphene's surprising properties: The square root dependence on charge carrier density of the carrier mass. This can easily be seen from the semi-classical definition of the cyclotron mass [30]

$$m^{\star} = \frac{\hbar^2}{2\pi}\frac{\partial A_{\mathbf{k}}(\epsilon)}{\partial \epsilon} = \frac{\hbar^2}{2}\frac{\partial \mid \mathbf{q}\mid^2}{\partial \epsilon} = \frac{\sqrt{\pi n_s}}{\nu_F} \tag{1.43}$$

where $A_{\mathbf{k}}$ is the cross section of the Dirac cone in $\mathbf{k}$ space. Owing to the near-vanishing charge carrier density close to the Dirac point, we find massless quasi-particles as charge carrier in graphene, in contrast to a constant mass $m^{\star}$ for conventional free electrons. Novoselov et al. demonstrated that in MLG $m^{\star} \to 0$ [3] for p and n-type carriers. It is in particular this massless character, which justifies the name *Dirac quasi-particle* and leads to a high charge carrier mobility.

If the sub-lattice symmetry is broken, e.g. in case of a potential difference between A and B sites, carriers become massive again. As discussed in chapter 4, a potential difference u between the sub-lattices would create a bandgap of the same spacing at $k = 0$: $\epsilon = \pm\sqrt{u^2 + \hbar^2\nu_F^2 k^2}$. Hence $m^{\star} \neq 0$ even at $k = 0$ [29].

The vanishing mass makes graphene favourable for high frequency applications, similar to the low $m^{\star}$ in GaAs and InGaAs heterostructures, as it will result in a high carrier mobility [34].

1.1.4.2 Klein tunnelling and absence of backscattering

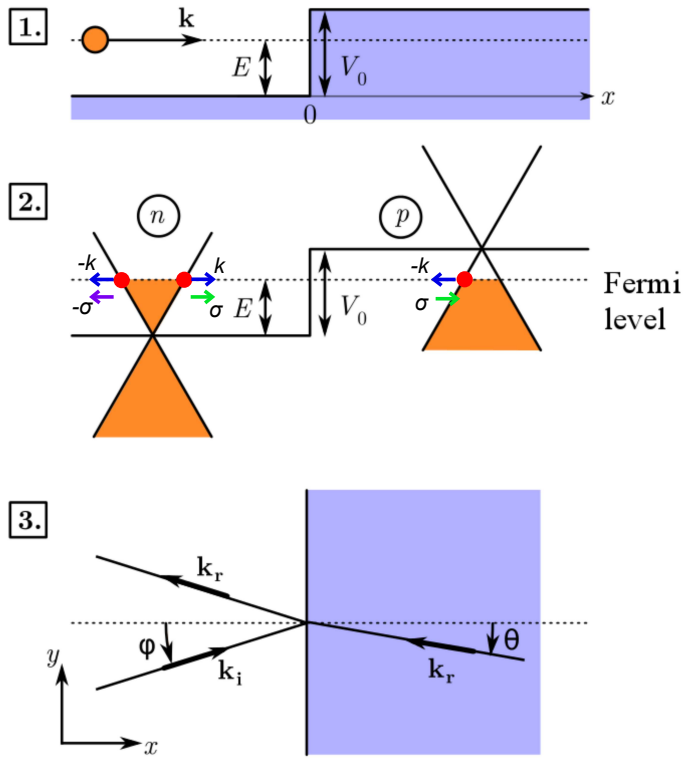

FIGURE 1.11: 1) Carrier incident on a barrier of height V_0. 2) Bandstructure in the p–n junction. The Fermi levels are uniform and aligned. Filled zones represent occupied states. 3) Geometric overview of the reflection of the incident wave on the barrier. Adapted from D. Torrin [35].

In quantum mechanics one finds the probability of particles travelling through a potential barrier to be decreasing exponentially with the barriers height. In the case of relativistic particles however, and we shall here for simplicity restrict the description to electrons, a counter-intuitive effect takes place, the so-called *Klein tunneling*. Here, the transmission probability rises with rising potential step, reaching unity for an infinitely high barrier. This can be explained by the fact that while a potential is repulsive for electrons it is at the same time attractive for positrons, thus creating positron states inside the barrier. The greater the barrier height, the greater also the possibility of alignment between electron and positron state energies, thus the greater the transmission probability. This phenomenon has been first described by Klein [36] in 1924 and coined *Klein paradox*. Although discussed widely, the Klein paradox could not be observed experimentally before the discovery of MLG [37]. Now, thanks to the Dirac nature of carriers in MLG, Klein tunnelling and related effects can be studied. We will however not go into detail on the subject of e.g. Veselago lens or triangular gated graphene [35] here, but focus on the consequences of Klein tunnelling on the electron transport.

It is generally found, both theoretically and experimentally (see e.g. [38] and [39] as well as ([29] and references therein), that carriers incident upon e.g. a p–n junction in MLG are transmitted perfectly if coming in normal to the boundary. For angles $\phi \geq 0$, a transmission probability D depending on ϕ is found: $D(\phi) = cos^2\phi$. This can be understood in terms of chirality of carriers and the conservation of the pseudo-spin. In order for backscattering to occur, $\mathbf{k}$ needs to reverse to $-\mathbf{k}$. At the same time chirality will change (see Fig. 1.11(2)) which leads to a vanishing probability of reflection. For finite angles of incidence, the situation is sketched in Fig. 1.11(3) and one obtains the aforementioned angle dependent transmission probability.
The absence of backscattering upon a potential barrier has consequences especially for the electronic transport: Even at low carrier concentration, where electron-hole inhomogeneities are likely to create random p–n junctions, these barriers remain transparent to the carriers. The high carrier mobility achievable in graphene devices is thus closely related to this absence of backscattering.
Despite Klein tunnelling being a promising subject, we will not exploit its effects in this work, as it requires high purity graphene samples that allow for the device to work in close vicinity of the charge neutral point. The samples presented during this thesis are limited by chemical potential fluctuations of the order of several meV. New fabrication techniques recently introduced at the LPA may allow investigation of this interesting subject in the near future.

1.1.5 Density of states

The density of states (DOS) $\rho(\epsilon)$ is a representation of the number of quantum states N per $\mathbf{k}$-space unit area S in the vicinity of the energy level ϵ [9, 30]:

$$\rho(\epsilon) = \frac{1}{S}\frac{\partial N}{\partial \epsilon} \tag{1.44}$$

In the two dimensional MLG one finds the number of states e.g. for the conduction band (i.e. $\lambda = +$)

$$N^+ = g \sum_{\mathbf{k}\,,\, k \leq \epsilon/\hbar\nu_F} \simeq gS \int_0^{k(\epsilon)} \frac{kdk}{2\pi} \tag{1.45}$$

and thus for the DOS of the full (positive and negative) energy range

$$\rho(\epsilon) = \frac{g}{2\pi}\frac{k(\epsilon)}{\partial\epsilon/\partial k} = \frac{2 \mid \epsilon \mid}{\pi(\hbar\nu_F)^2} \tag{1.46}$$

where we have used the inverted low energy linearisation of the dispersion relation (1.34) and $g = 4$ due to the 2-fold valley degeneracy and the electron spin.

Therefore, as also depicted in Fig.1.10 for the full DOS calculated by Hobson and Nierenberger [40], the DOS is linear in energy and vanishes at the Dirac point. This is in strong contrast to conventional 2D metals, where the DOS is constant. We will use the energy dependence of the DOS in our experiments on GFECs (chapter 4).

Density of charge carriers Integrating the DOS over the whole energy range up to the Fermi level one finds the density of charge carriers (DOCC)

$$n_s = \int_0^\infty \rho(\epsilon) f(\epsilon) d\epsilon = \frac{\epsilon_F^2}{\pi(\hbar\nu_F)^2} \tag{1.47}$$
$$f(\epsilon) = \left(1 + e^{\frac{\epsilon-\epsilon_F}{k_B T}}\right)^{-1}$$

where $f(\epsilon)$ is the Fermi-Dirac distribution. The right hand side of Eq. (1.47) is the valid solution for zero temperature. The DOCC will reach typical values of $n_s = 10^{11}$–10^{13} cm^{-2} in MLG devices. The lower limit is limited by fluctuations in ϵ_F

For the ease of calculus we can now express the Fermi energy as function of the charge carrier concentration:

$$\epsilon_F = \hbar\nu_F k_F = \hbar\nu_F\sqrt{\pi n_s} = 116.3 \text{ meV} \cdot \sqrt{\tilde{n_s}} \tag{1.48}$$
$$k_F \simeq 1.77 \cdot 10^6 \sqrt{\tilde{n_s}}$$
$$\tilde{n_s} = \frac{n_s}{10^{12}}$$

with n_s in units of cm^{-2}.

1.1.6 Charge carrier mobility

A property vital for graphene applications and frequently cited in favour of MLG is its high room temperature carrier mobility μ_c. It relates the conductivity σ to the carrier density n_s and is generally a measure of how quickly carriers move in a material under the influence of an electric field E. From the definition in terms of drift velocity [30]

$$\nu_d = \mu_c E \tag{1.49}$$

and the current density

$$j = n_s e \nu_d \tag{1.50}$$

we can immediately obtain the desired formula

$$\sigma = n_s e \mu_c \tag{1.51}$$

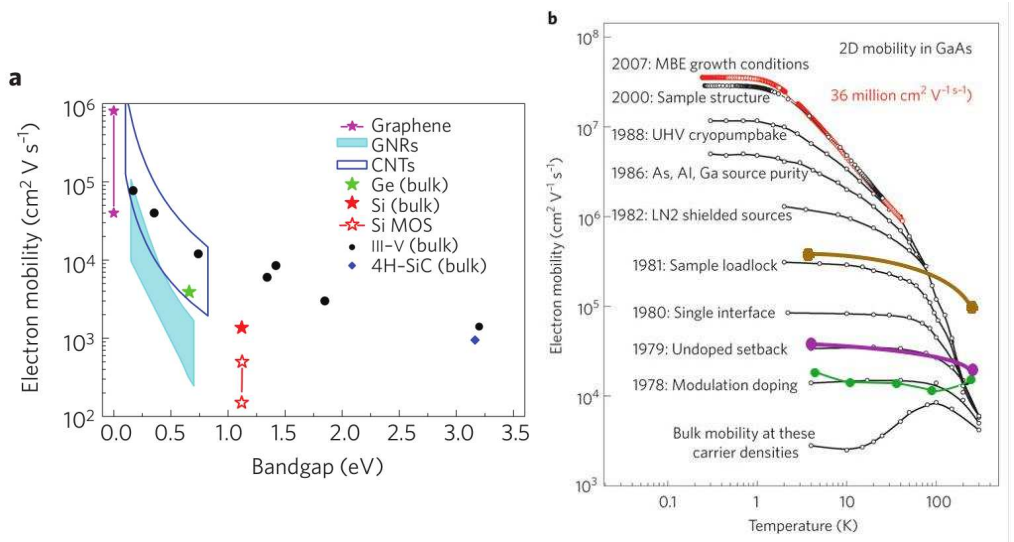

FIGURE 1.12: a) Electron mobility versus bandgap in different materials at low electric fields. From F. Schwierz [41]. b) Comparison of charge carrier mobilities in GaAs/GaAlAs hetero structures and graphene. Blue and red dots: Evolution of GaAs mobilities over the years. Adapted from Schlom et al. [42]. Additional solid lines are experimental graphene mobilities: green) CVD graphene on hBN [43]. magenta) Exfoliated graphene on hBN [44]. brown) Exfoliated graphene encapsulated in hBN [45]

Given the right choice of substrate and dielectric, room temperature mobilities of the order of 10^5 $cm^2V^{-1}s^{-1}$ can be achieved in MLG devices. As can be seen from Fig. 1.12(b) values are still well below record mobilities in e.g. GaAs heterostructures at low temperatures. However, experiments [41, 43–45] show that MLG mobilities can already reach considerable values of several 10^5 $cm^2V^{-1}s^{-1}$ and most notably that μ_c remain high even at room temperature, contrary to its semiconductor counterparts, where μ_c decreases rapidly with increasing temperature. Record values for MLG are achieved in pure systems, e.g. in MLG encapsulated in hexagonal boron nitride (see description below) or in suspended graphene devices. Typical mobilities of MLG devices on Si/SiO_2 are of the order of 10^3–10^4 $cm^2V^{-1}s^{-1}$ at room temperature. For a more detailed comparison see [41] and references therein.

1.1.7 Other related materials

Besides the monolayer of graphite, there are several related materials, each with their own astounding properties.

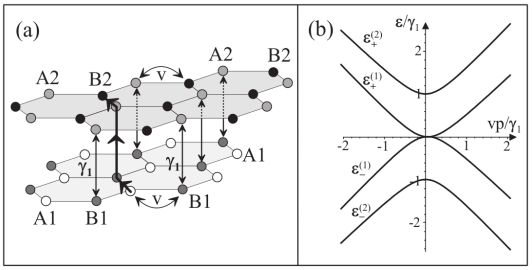

FIGURE 1.13: (a) schematic of the bilayer lattice containing four sites in the unit cell: A1 (white circles) and B1 (grey) in the bottom layer, and A2 (grey) and B2 (black) in the top layer. (b) schematic of the low energy bands near the K point obtained by taking into account intra-layer hopping, B1A2 interlayer coupling, A1B2 interlayer coupling and zero layer asymmetry. From Falko et al. [46]

1.1.7.1 Bilayer graphene

Despite the name *graphene* having been coined for the monolayer, also the bilayer of graphite shows interesting properties. It consists of two graphene layers in Bernal-stacking, coupled vertically, which changes the energy dispersion (see Fig.1.13) and related properties. Its bandstructure can also be calculated by means of a tight-binding approach, introducing inter-layer hopping between the planes spaced $d \simeq 3.34\mathring{A}$. For a more detailed description see e.g. [29, 46]. The DOS e.g. is now similar to conventional two-dimensional electron gases (2DEGs), i.e., constant:

$$\rho(\epsilon) = \frac{2m^\star}{\pi\hbar^2} \tag{1.52}$$

Here, the effective mass obtained from bandstructure calculations is $m^\star \simeq 0.03$–$0.05\, m_0$ [29], where m_0 is the electron mass. The non-zero mass $m^\star$ comes alongside a small separation of the bands, which can be tuned electro-statically. [29, 46].

1.1.7.2 Carbon nanotubes

Carbon nanotubes (CNTs) are essentially rolled up graphene sheets. Their intrinsic properties mainly stem from the underlying honeycomb lattice arrangement of carbon atoms and the additional circular confinement. The exact way of rolling up the graphene sheet into a tube, the resulting diameter and the zigzag or armchair termination define the microscopic structure and therefore the transport behaviour CNTs. One defines a circumferential vector $\mathbf{C_h} = n\mathbf{a}_1 + m\mathbf{a}_2$ connecting two equal atoms (in terms of lattice) [47]. Due to the circumferential confinement only a discrete set of wave vectors $\mathbf{k}$ is allowed in the Brillouin zone, resulting in the point $\mathbf{K}$ being include or excluded. This

determines if a bandgap arises and the CNT becomes semiconducting or if it remains metallic. Semiconducting CNTs have recently been used to realise field-effect transistors (see also section 1.4.3).

1.1.7.3 Hexagonal Boron Nitride

Hexagonal boron nitride (hBN) is often also-called white graphene, due to its close match with the graphene lattice. Indeed, the mismatch between the two lattices is only of about 1.7% with boron and nitride atoms taking the place of the carbon in the sub-lattices. It is an ionic crystal with strong in-plane bonds. It is relatively inert and expected to have no dangling bonds or surface charge traps. On the contrary to graphene, hBN is an insulator with a bandgap of 5.97 eV [48]. Due to the close lattice match, low roughness of its surface and the reduction of dangling bonds, hBN is becoming increasingly interesting as a substrate for graphene devices [44].

1.1.8 Differences between MLG and 2D semiconductors

There exists a great number of quasi 2-dimensional systems, which have all been studied extensively over the last decades. Of special interest are here the semiconductor systems, i.e. for example inversion layers in Si or GaAs-AlGaAs heterostructures, which are quasi 2D, but exhibit several major differences compared to MLG as pointed out in [29]:

- Contrary to MLG, 2D semiconductor systems have rather large bandgaps, making it necessary to distinguish between electron and hole conduction devices. In graphene, both regimes are accessible within one device and conduction can be changed from electrons to holes by a gate potential. This gapless energy dispersion (see also Fig. 1.9) makes it however difficult to obtain an insulating state, in contrast to the 2D semiconductors, where the Fermi level can be placed in the bandgap.

- Additionally to being gapless, graphene's energy dispersion is also approximately linear in the vicinity of the Dirac points. 2D semiconductors in constrast exhibit a quadratic dispersion

$$\epsilon(k) = \epsilon_0 + \frac{\hbar^2 k^2}{2m^\star} \tag{1.53}$$

  The linearity in graphene has a strong impact on its transport behaviour. Energy is proportional to $\sqrt{n_s}$ in MLG, whereas one finds $\epsilon \propto n_s$ in 2D semiconductors.

- The carriers in graphene are chiral with a strong pseudo-spin orbit coupling, as we have seen in section 1.1.3.2. This leads to effects like the suppression of backscattering.
- Graphene is a true 2D system, with thickness of one atom. 2D semiconductor electron gases are quasi 2-dimensional as they are governed by 2D quantum physics, but their thickness is always of several nanometers. Their phonons are therefore 3-dimensional.
- 2D semiconductors have a constant DOS, as predicted by quantum mechanics, whereas MLG's DOS is linear in energy.
- Finally, graphene's carrier are massless in the vicinity of the Dirac points, as established theoretically and experimentally. Carriers in semiconductors are always of finite mass $m^\star$, its value depending on bandstructure. Typically e.g. $m^\star \simeq 0.07 m_e$ and $\simeq 0.38 m_e$ for electrons and holes in GaAs, respectively.

It is interesting to mention that BLG shows properties of MLG and 2D semiconductors alike [29]: For example the DOS is constant, but carriers are still chiral as the A/B sublattice symmetry remains.

1.2 Phonon modes in graphene

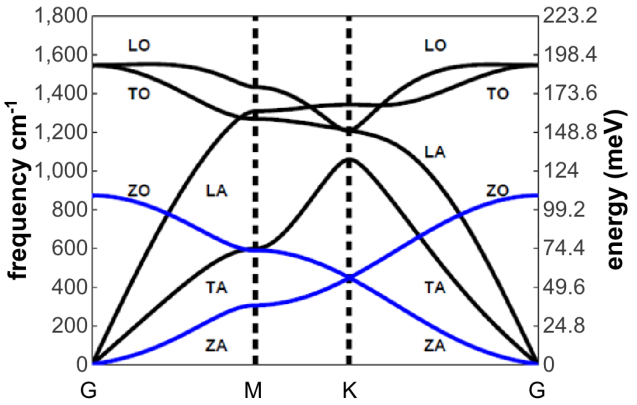

FIGURE 1.14: Phonon modes in graphene. Blue lines are flexuaral phonons and only of importance in suspended graphene layers. From Falkovsky et al. [49].

In a generic crystal, atoms are not fixed to their lattice position, but can vibrate around their center of mass. The stable equilibrium position of the mass centres in the lattice is a result of atomic interactions as e.g. Van-der-Waals forces, covalent bonds or others [30, 34]. Periodic, elastic displacements of crystal planes can be described by a set of

1-dimensional equations of motion. The dimensionality of the problem is given by the number of atoms in the unit cell. In the simplest case of a one-atomic unit cell, the equation of motion of a given lattice plane s is

$$M\frac{d^2u_s}{dt^2} = C(u_{s+1} + u_{s-1} - 2u_s) \tag{1.54}$$

with M the mass of the atom, C the force constant between planes s and $s \pm 1$ and u_i the displacement of plane i. The solving of the system of equations of motion leads in the case of a two-atomic unit cell to two sets of dispersion relations in reciprocal space, called *acoustic* and *optical* modes. These names are due to the in-phase (acoustic) or opposite-phase (optical) vibrations of neighbouring atoms and the possibility to excite the latter by means of electro-magnetic waves. The energy of these lattice vibrations is quantised and gives thus rise to a description in terms of harmonic oscillators. A quantum of of vibrational energy is called a *phonon* [30, 34].

Let us now turn to the phonon modes in graphene. These have been studied extensively even before the discovery of stable MLG flakes by Novoselov and Geim in the framework of e.g. carbon nanotubes. Similar to the electronic properties, lattice vibrational modes in CNTs can be understood from the ones of their precursor, monolayer graphene. We will base this brief description of graphene phonon modes on [10] and references therein. Due to the two-atomic unit cell of MLG, six degrees of freedom arise for lattice vibrations. It can be shown [10] that the motion of the carbon atoms within their lattice and couplings to neighbouring atoms can be described by a $3N \times 3N$ dynamical matrix, where N is the number of atoms in the unit cell. Calculations were performed up to the fourth-nearest neighbour, sufficiently describing the experimentally found phonon dispersion. A theoretical sketch of this dispersion can be found in Fig. 1.14. There is a total of six branches, which in order of increasing energy from the G point are: Out-of-plane acoustic (ZA), in-plane bond-bending (TA) and in-plane bond-stretching (LA) acoustic phonons, as well as the corresponding optical phonon modes ZO, TO and LO.

We will not consider out-of-plane modes in this work. They are mainly important in suspended graphene samples, whereas the samples we will present throughout this work are all supported by a substrate. As can be seen from Fig. 1.14, the optical phonon modes TO and LO have a considerable energy of $\sim$ 200 meV. Their effect will thus be accessible only at high electric fields, where carriers have acquired enough energy to interact with them. They are nevertheless of great importance as their electron-phonon coupling is strong enough to provide effects visible in DC transport measurements: Here, the drain-source current of a MLG device will show a current saturation at high field [50]. We will come back to this effect in chapter 3. Acoustic, in-plane phonons (AP) have low energies and could potentially show up in measurements even at low electric

field. However, their coupling to electrons is only weak [24] and special experiments have to be devised in order to see their effect (see chapter 5).

1.3 Electronics in mesoscopic systems

1.3.1 Length scales of mesoscopic systems

A macroscopic conductor or resistor is defined by the Ohmic relation $G = \sigma \frac{S}{L}$, where G is the conductance, S and L represent the conductor's cross-sectional area and length, and σ is a material dependent parameter. In a two-dimensional system like MLG, S can be replaced by the system's width W. Within the conductor the charge carriers can undergo elastic scattering processes for which we define the elastic mean free path $l_{mfp} = \tau_0 \nu_F$, giving the average distance an electron is travelling between two scattering processes. τ_0 is the time interval between two scattering events and ν_F the particle's velocity. If the conductor's length L is greater than l_{mfp}, the charge transport will be diffusive.
Another important length scale is the temperature T dependent phase coherence length $l_\phi = \nu_F \cdot \tau_\phi \leq \nu_F \cdot \frac{\hbar}{k_B T}$ (in the case of vanishing voltage bias V). If it exceeds L quantum effects can be expected, as the phase information of the electron is not randomised. In the case of graphene l_ϕ is on the nm scale at 300 K and on the μm scale at 4 K (liquid helium temperature). Typically, the channel length of our MLG devices is of the order of 1–2 μm. At low temperatures, we are thus approaching a quantum system and need to take into account its stochastic nature, i.e. the granularity of charge. The fact of having macroscopic sample dimensions on the one hand and quantum effects on the other hand is the reason to call these kind of systems *mesoscopic* (from greek *meso=between*).
Additionally, if one shrinks the system to scales comparable to l_{mfp} or smaller, a phenomena called ballistic transport occurs. The electrons are now no longer scattered but will always pass the conductor, meaning that the transmission probablity D reaches unity. We will however only deal with diffusive devices in this work.

1.3.2 Transport in mesoscopic graphene

1.3.2.1 Quantum description of the current and scattering approach

To arrive at a formula predicting the current through a mesoscopic system (which we take to be 1-dimensional for the sake of simplicity), one starts from a second quantisation approach with creation and annihilation operators acting on incoming and outgoing

states of the system [51]. The system is connected to large reservoirs at either side. Such a system can formally be described by the scattering matrix S formalism:

$$\begin{pmatrix} \hat{b}_L \\ \hat{b}_R \end{pmatrix} = \begin{pmatrix} S_{LL} & S_{LR} \\ S_{RL} & S_{RR} \end{pmatrix} \begin{pmatrix} \hat{a}_L \\ \hat{a}_R \end{pmatrix} \tag{1.55}$$

Here the operators $\hat{a}$ and $\hat{b}$ act on incoming and outgoing waves, respectively and L (R) denotes the left (right) contact. We will not go into details on the exact quantum mechanical calculus of the sample current, but refer the interested reader to the review by Blanter and Büttiker [51]. Let us simply state that the overall current through the system is in the end given by

$$I = \frac{e}{h} \int d\epsilon \, [f_L(\epsilon) - f_R(\epsilon)] \cdot \sum_n D_n \tag{1.56}$$

where f_i denotes the Fermi-Dirac distribution of contact i and D_n the transmission probability of the n-th electronic mode. This is closely related to the Landauer-Büttiker description of conductance, which is also readily extended to account for multiple electronic modes in a mesoscopic system [51]

$$G = \frac{e^2}{h} \sum_n D_n) \frac{\partial I}{\partial V} \tag{1.57}$$

where V is the voltage applied to the sample. The above formula is of great help e.g. in semiconductor 2DEGs.

1.3.2.2 Number of modes in graphene and impact on channel current

In the case of MLG however, there is a large number of modes to take into account; up to 10^4 depending on the width of the layer and the carrier concentration n_s. There is also a four-fold degeneracy arising from the electron spin and the two valleys K and K'. Near the Dirac point the energy dispersion is linear in wave vector k_F, as found earlier. Combining this fact with Eq. (1.47) we arrive at a relation between the Fermi wavelength and the density of charge carriers in the sheet:

$$\lambda_F = \frac{2\pi}{k_F} = \sqrt{\frac{4\pi}{n_s}} \tag{1.58}$$

ranging from $10^{-7}m$ to $10^{-8}m$ for $n_s = 10^{11}$ to $10^{13}\ cm^{-2}$. Assuming standard potential step boundary conditions, we now find the number of electronic modes in the graphene

layer

$$M = \frac{2W}{\lambda_F} = W\sqrt{\frac{n_s}{\pi}} \tag{1.59}$$

Since M depends on n_s, the number of modes nearly vanishes at the Dirac point. Several modes are always open, however, making it impossible to create a real OFF-state of the current. This is due to the minimum conductivity $\sigma_{min} = 4e^2/\pi h$ generally found in graphene, whose origin we will not discuss here, but refer the reader to [29] and references therein. For typical charge carrier densities ($n_s = 10^{11}$–10^{13} cm^{-2}) and sheet width of $W = 1$ μm, the number of modes is of the order of 20 to 200.
Besides tuning carrier concentration, the second option to control the number of transmission modes is to change the layer's aspect ratio W/L. In practical that usually means to use so-called nano ribbons of a width of several hundred nanometers to obtain only a few modes. Eq. (1.59) also highlights the possibility to modulate the current I flowing in the channel by changing the carrier density, i.e. by applying an external electric potential, the gate potential. In experiments we will thus in general deal with a drain-source current

$$I_{ds} = I(V_{ds}, V_g) \tag{1.60}$$

where V_{ds} is the voltage between the contacts and V_g the gate voltage modulating n_s.

1.3.3 Noise in mesoscopic systems

The stochastic nature of the charge transport aforementioned (see 1.3.1) leads us to another important topic in this work: charge fluctuations or electronic noise. They occur in every conductor as variations of the current around its average value.

1.3.3.1 Thermal noise

The first source of noise in an electric circuit is caused by finite temperature, due to which the occupation numbers n of the electronic states will fluctuate, even at equilibrium, where no driving potential difference is applied between the reservoirs. These occupation numbers are described by the Fermi-Dirac statistics, i.e. in equilibrium all states are occupied up to the Fermi level and the average number of occupied states is simply $< n(\epsilon) >= f(\epsilon)$, where f is the Fermi-function. The probability for a state being empty is thus $1 - f$ and f for being occupied. At finite temperature these probabilities deviate from the zero temperature values 0 or 1, as generally described by the Fermi function. The subsequent random changes in the occupation number of the electronic states, of variance $f(1 - f)$ and caused by the finite temperature of the conductor, then

give rise to equilibrium current fluctuations $\delta I(t)$: the charge carriers close to the Fermi level receive enough energy to contribute to the transport. Thermal noise is also-called Johnson-Nyquist noise with its spectral density given by [52, 53]

$$S_I = \frac{4k_B T}{R} \tag{1.61}$$

This noise source can be suppressed by decreasing the system's temperature, e.g. by the use of liquid helium (4.2 K).

1.3.3.2 Shot noise

A second source of noise in mesoscopic systems arises from the quantisation of charge and the stochastic character of quantum diffusive charge transport: The so-called *shot noise*. In order to observe it, the system needs to be in the non-equilibrium or transport state. The following description is adapted from [11], [54] and [12].

Poissonian noise In 1918 Walter Schottky was the first to investigate current fluctuations in conductors and coined the term *shot noise*. His result describes the noise due to uncorrelated variations around an average value, i.e. a random Poissonian process. Let us consider a flow of particles emitted independently during a time intervall τ. The average number of events is $\langle n \rangle = n_t \tau$, where n_t is the average number of particles emitted per unit time. The probability to find exactly n events occurring during the time $\tau = \langle n \rangle / n_t$ is given by the Poissonian distribution

$$P(n) = \frac{\langle n \rangle^n}{n!} e^{-\langle n \rangle} \tag{1.62}$$

Such uncorrelated events can e.g. be found in vacuum diodes or also tunnel junctions, where the average current $\langle I \rangle = e\langle n \rangle / t$ creates a *noise power spectral density* (PSD)

$$S = 2e\langle I \rangle \tag{1.63}$$

We will make use of this relation in chapter 5 when calibrating our noise thermometry setup.

Current correlations and noise In order to derive the above formula (1.63), we have to study the correlations of the electrical current in our simple 1D model conductor. For the sake of simplicity we shall only consider a single electronic mode in the following description. Similar to Eq. (1.56) this can easily be extended to multiple modes.

The quantity of interest is the correlation function of the current with respect to time

$$C(t) = \frac{1}{T}\int dt' \langle I(t')I(t+t')\rangle \tag{1.64}$$

where T represents a sufficiently long time interval. For a random quantity $x(t)$ fluctuating around its average $\langle x\rangle$ by $\delta x(t) = x(t) - \langle x\rangle$, $C(t)$ is a measure of how the fluctuations evolve in time *on average* [54].

In a more formal way this can be described in terms of time-dependent current operators $\hat{I}_m(x_m, t)$. To this effect one has to rewrite the corresponding current operators $\hat{I}$ in the Heisenberg picture [11, 51], and integrate over two different energies (ϵ and ϵ'). References [51] and [11] give the precise formulas of the above mentioned quantities. Our interest lies however on the noise spectral density of the conductor, which is given by twice the Fourier integral of the correlation function with respect to the two reservoirs. In terms of the current $I(t)$ and its average, it yields [11]

$$S_{mn}(\omega) = \lim_{T\to\infty}\frac{2}{T}\int_{-T/2}^{T/2} dt \int_{-\infty}^{\infty} dt' e^{i\omega t'} \left[\langle I_m(t)I_n(t+t')\rangle - \langle I_m\rangle\langle I_n\rangle\right] \tag{1.65}$$

The solution of the above formula requires the evaluation of expectation values of four annihilation or creation operators, which can be simplified by using Wick's theorem [55]. Again we refer the interested reader to the reviews [51] and [11] for more details.

It is generally sufficient to calculate the noise in the zero frequency limit [11]. For the case of a two-probe system only autocorrelation is of importance and we find:

$$\begin{aligned} S_{LL}(\omega = 0) = \frac{2e^2}{\pi\hbar}\int d\epsilon \{ & D(\epsilon)^2[f_L(1-f_L) + f_R(1-f_R)] + \\ & + D(\epsilon)[1-D(\epsilon)]\cdot[f_L(1-f_R) + f_R(1-f_L)]\} \end{aligned} \tag{1.66}$$

We can now evaluate (1.66) and obtain [11, 51]

$$S_I(0) = \frac{4e^2}{h}k_BTD^2 + \frac{2e^3V}{h}D(1-D)coth(\frac{eV}{2k_BT}) \tag{1.67}$$

To conclude this short introduction of electronic fluctuations let us have a closer look at the two limiting cases of the above expression. Taking $T = T_0$, where T_0 is the bath temperature and independent of bias, we will be in the limit of $0 \leq eV \ll k_BT$. Using the first order approximation $coth(x) \simeq x^{-1}$, Eq. (1.67) can then be transformed into

$$\begin{aligned} S_I(0) &\simeq \frac{4e^2}{h}k_BTD^2 + \frac{2e^2}{h}D(1-D)\cdot 2k_BT \\ &= 4e\cdot\frac{e^2D}{h}\cdot k_BT \end{aligned} \tag{1.68}$$

where we recover the Johnson-Nyquist formula (1.61) with $R = h/e^2D$.
One can consider another limit, the very hot electron limit, where the electron temperature $Te \sim eV/(2k_B)$. Then, we obtain

$$\begin{aligned} S_I(0) &\simeq \frac{2e^3V}{h}D^2 + \frac{2e^3V}{h}D\,(1-D) \\ &= 2e \cdot \frac{e^2VD}{h} \end{aligned} \tag{1.69}$$

where we recover the shot noise formula (1.63) with $I = e^2DV/h$.The usefulness of both limits will reveal in chapter 5.

1.4 Single charge detection

Mesoscopic physics lies, as mentioned in the beginning of the previous section, at the border of macroscopic and microscopic physics; Quantum effects of the microscopic world are made visible using macroscopic tools and devices. One of the most interesting and important challenges here is the emission, manipulation and detection of single carriers. Many experiments deal e.g. with quantum hall effect edge channels in two-dimensional electron gases in semiconductor heterostructures. Here, coherent transport can be achieved, with single electron injection into the channel, as shown recently at the LPA [56, 57]. It is however not the goal of this section to provide insight into this field, but merely point out the importance of single charge detectors and highlight the state-of-the-art.
Sensitive electrometers exist for DC, but difficulties start to arise once repetitive, single-shot detection is required. Then, one has to deal with the electronic noise proportional to the bandwidth of the frequency spectrum used in the detector. Nevertheless, such fast single charge detectors would make the ideal companion of the aforementioned single-charge emitters: Coupled capacitively to e.g. the edge channel it would be possible to read out single charge events at high precision. Ideally, the dimensions of the detector need to remain smaller than the coherence length of the carriers $l_\phi \leq \nu_F \cdot \frac{\hbar}{k_BT}$, which in turn translates into the requirement of sub-nanosecond time resolution for the typical Fermi velocity $\nu_F \lesssim 10^5$ ms^{-1} in 2DEGs. A second possibility is to trap the charge in a quantum confinement for a sufficiently long time in order to gain a good charge resolution. This second techniques is used throughout many detectors, as we will see in the following.
The most commonly used technique of detection today is the employing of the field-effect on a gate electrode of a transistor. Without going into details, which will be given in chapter 3, the working principle of a generic field-effect transistor (FETs) is the

following:
A conducting channel is connected to two reservoirs, allowing for a charge transfer between them. A third electrode, the gate, is coupled capacitively to the channel and generally modifies its conductance. Thus, in very broad strokes, the current I will depend on the amount of charge Δq_{gate} on the gate electrode. We find

$$I(q_{gate}) = I(0) + \frac{\partial I}{\partial q_{gate}} \Delta q_{gate} \tag{1.70}$$

and define our generic signal as the change of current with respect to the change of gate charge

$$S = \frac{\partial I}{\partial q_{gate}} = \frac{\partial I}{\partial V_{gate}} \frac{\partial V_{gate}}{\partial q_{gate}} = \frac{g_m}{C_{gate}} = \omega_T \tag{1.71}$$

In the last two right-hand side terms we have introduced three quantities crucial to the description of FETs: The transconductance $g_m = dI/dV_{gate}$, the gate capacitance C_{gate} and the transit frequency $\omega_T/(2\pi)$. Their exact purpose will reveal in chapter 3, where we will go into more detail. The last parameter, ω_T, identifies the frequency at which the current gain of a given transistor has decreased to unity. Since the device itself, as well as all components in the measuring setup exhibit electronic noise, one has to assure a strong signal S in order to achieve a high resolution. In a later chapter, we will introduce the *current noise spectral density* S_I of which the square root has to be compared to S to give an estimate of the charge resolution of a transistor. The maximum charge resolution is given when the ratio of signal-to-noise reaches 1 and therefore we find

$$\delta q_{rms} = \frac{\sqrt{S_I}}{S} = \frac{\sqrt{S_I}}{\omega_T} \tag{1.72}$$

δq_{rms} is in units of $e/\sqrt{Hz}$ and signifies the following: Charge fluctuations on the gate inferior to δq_{rms} will not be visible within the noise background in a single-shot experiment. Only fluctuations $\Delta q \gg q_{rms}$ can be detected without difficulty. There is of course the possibility of averaging over a sufficient number of events, however this defies the single-shot approach.
A sensitive single-charge detector is thus characterised by a large transconductance, small gate capacitance and small intrinsic electronic noise. The first two quantities can be probed by measuring the device's high frequency admittance (see chapters 3 and 4), the last one by means of noise thermometry (see chapters 5). Two kinds of transistors fitting the above mentioned requirements are mainly used today: Single-Electron-Transistors (SETs) and nano transistors based on quantum-point contacts (QPCs) or carbon nanotubes (CNTs).

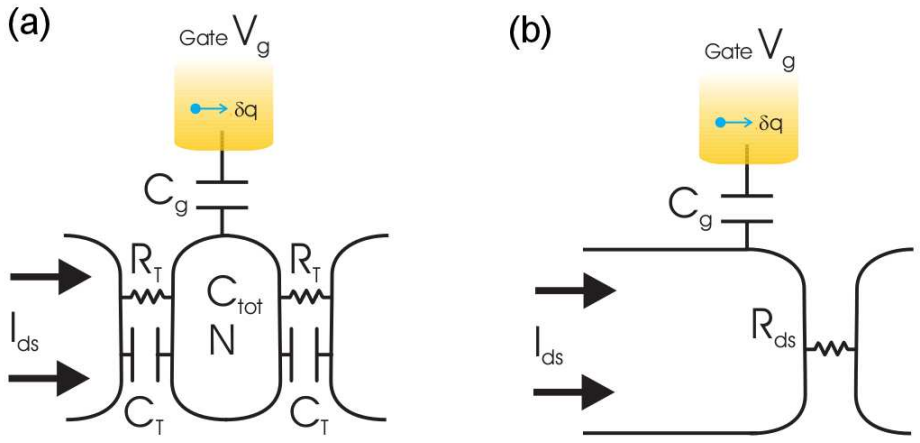

FIGURE 1.15: a) Working principle of an SET. b) Working principle of a QPC-FET or CNT-FET. From [58].

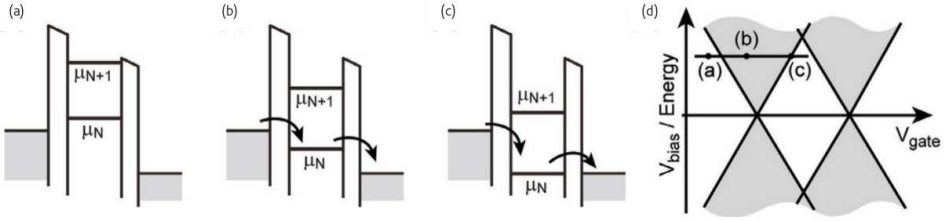

FIGURE 1.16: (a-c) Spaceenergy diagrams of a single-electron transistor in which electrons are confined between two tunnelling barriers. The gate voltage is increased from (a) to (c). (d) Current can flow only in the gray-shaded regions, where one of the energy levels is within the bias window. From Ihn et al. [59].

1.4.1 Single-electron transistors

A single-electron transistor (SET) consists of a conducting island, connected capacitively to two leads, as shown schematically in Fig. 1.15(a), allowing for tunnel events to happen. Islands can be made from metallisations, commonly Al, or defined electrostatically in the channel of a metal-oxide semiconductor FET (MOSFET). This spatial confinement of electrons creates a quantum well and a distribution of discrete energy levels within. The position of these energy levels can typically be changed by the variation of a gate potential. Charge transport between the two contacts is then possible through tunnelling of electrons from a contact into the island and further on into the second electrode, given a discrete level is within the window of contact potentials (see Fig. 1.16(a-c)). This results in the so-called *Coulomb blockade*, which is presented in Fig. 1.16(d): Diamond-shaped regions of suppressed conductance which repeat periodically. For a more detailed description please refer to e.g. [13]. SETs are typically limited to

the kHz frequency range, but RF-SETs operating in the MHz region are possible [60] as well by inserting the SET in a resonating cavity. Charge detection capabilities of such RF-SETs are of the order of $10^{-6}e/\sqrt{Hz}$ [60].

1.4.2 Quantum-point-contact transistors

In 2DEGs it is possible to control the carrier concentration in a given region by applying an electro-static potential. This is usually achieved with the help of a capacitively coupled gate electrode that can increase or reduce the number of carriers in the region and hence creates a channel of variable transparency. Such gating allows for the creation of a narrow channel with very low transparency, i.e. transport can be restricted to very few electronic modes, down to complete closure of the contact. This is called a *quantum-point contact* (QPC) (see Fig. 1.15(b)). Charge sensing in a QPC-FET is achieved by the variation of QPC transparency upon arrival of an additional charge on the gate electrode [61] and can be used e.g. to establish the so-called full counting statistic [62]. The change in gate potential will be visible in the current across the QPC. Similar to the SET detectors, an RF version of QPC-FETs exists with a charge resolution of $2 \cdot 10^{-4}e/\sqrt{Hz}$ in a bandwidth of 20 MHz at a temperature of 60 mK [63].

1.4.3 Carbon nanotube transistors

Another possibility for a fast an sensitive charge detector is the carbon-nanotube (CNT) FET. This kind of device, studied e.g. by Chaste et al. here at the LPA [14, 58, 64], constitutes the ultimate nano-transistor as it consists of a semiconducting CNT connected to two contacts and capacitively coupled to a gate electrode. The gate potential will essentially introduce a barrier of variable transparency in the ballistic CNT channel, whereas the gate charge controls the amount of carriers in the channel. The transit frequency ω_T, mentioned previously, is inversely proportional to the gate length L here and can reach values up to 50 GHz. This is due to the small gate capacitance and the high transconductance values g_m that can be achieved in CNT-FETs [58]. Chaste et al. were able to extract the aforementioned parameters from RF scattering-parameter characterisations (see also section 3.2.2.2) and low temperature noise thermometry experiments (see chapter 5) and estimate a charge sensitivity of $13 \cdot 10^{-6}e/\sqrt{Hz}$ in a bandwidth of 0.8 GHz at liquid helium temperature.

1.4.4 Sub-nanosecond charge detection in graphene transistors

Very good charge sensitivities and large bandwidths can already be obtained with different kinds of detectors, as we have seen previously. However, several drawbacks exist for each kind: SETs and QPC-FETs operate in the kHz to MHz range and thus limit the temporal resolution of the detector. CNT-FETs could possibly overcome this problem, as their bandwidth is in the GHz range. However, CNT-FETs, as well as SETs, exhibit a large impedance of the order of several kΩ, which makes it difficult to integrate these devices in a standard 50 Ω high frequency setup. Also, the carriers in CNTs are typically very hot, giving rise to an unsuppressed shot noise of the form (1.63) [64].
An option to overcome both restrictions, i.e. a device of large bandwidth and low impedance, could be the use of RF graphene-FETs (RF-GFETs). Typical graphene devices show impedances of the order of several hundreds of Ω [2, 16], much closer to the standard 50 Ω. Also very high transit frequencies can be achieved: A record 300 GHz was recently reported by Wu et al. [65]. This is related to the high transconductance and small gate capacitance achievable in RF-GFETs. As for the current fluctuations expectations are that current noise remains low, but still finite even in the ballistic regime. Tworzydlo et al. predicted [66] that due to evanescent wave transport shot noise is suppressed with a corresponding Fano factor of 1/3 at the charge neutral point of ballistic graphene. This was confirmed experimentally by Danneau et al. [25]. F then decreases further with increasing carrier density in the ballistic case. In diffusive graphene devices no n_s dependence is expected [67] but other effects like e.g. electron-phonon interactions may reduce the electronic noise. An additional option for noise reduction in RF-GFETs stems from the fact that the drain-source current I_{ds} of a RF-GFET is proportional to the channel width W, as we will discuss in chapter 3. Scaling the channel width will also decrease the noise level. Besides the RF-GFET design, other detectors based on graphene have been suggested, as e.g. bolometers taking advantage of the metal-insulator transition in superconductor-graphene hybrids [68, 69].
Overall, the low intrinsic impedance, good RF performance and a low noise level make graphene based microwave field-effect transistors suitable candidates for sensitive, sub-nanosecond charge detectors.

In order to study the fundamental problems involved in the sub nano-second charge detection we will concentrate in this work on the high frequency dynamics and noise in graphene field-effect devices. The next chapter will first of all give an overview of the typical fabrication process of the samples presented in this work. Device-specific details will be described in the corresponding chapters.
In chapter 3 we will then investigate the high frequency behaviour of RF graphene

field-effect transistors (RF-GFETs), in order to answer the question of maximum cut-off frequency in graphene nano-transistors mentioned in 1.4.4. It will be followed by a study of diffusion mechanisms in graphene devices involving a simplified structure, the graphene field-effect capacitor (GFEC, chapter 4). Last but not least we will approach the topic of charge noise in graphene in chapter 5.

Chapter 2

Fabrication of graphene devices

2.1 Obtaining graphene layers

Since the first experimental observation of graphene by Boehm et al. [6] several different ways have been explored to create stable graphene mono-layers and incorporate them in devices. Besides early methods of chemically separating or intercalating graphite layers [70], three main techniques of producing MLG are being used today: Micro-mechanical cleavage, growth on silicon carbide (SiC) [71, 72] substrates and more recently chemical vapour deposition (CVD). We will omit the SiC method in the following as only the other two techniques are used in this work. Other techniques of obtaining MLG exist and comprise e.g. anodic bonding [73, 74] and epoxy reversed exfoliation [75].

2.1.1 Exfoliation

The key to success for the fabrication of the first graphene devices in 2004 was the use of an unconventional tool: adhesive tape. In one of their *"Friday evening experiments [...] where you do just crazy things... "*[76] the Manchester group managed to produce very thin stacks of graphite layers with their so-called exfoliation technique [2].
Micro-mechanical cleavage, or *exfoliation*, of bulk graphite has not only been the first way to isolate stable graphene monolayers on a substrate at ambient conditions, but is still a widely used, fast and easy approach to obtaining quality MLG. Also, it is not limited to graphite but a wide selection of layered materials, e.g. hBN, can be treated this way. This way of producing thin flakes of graphite down to MLG relies on the rather large separation between graphite layers of more than twice the in plane nearest neighbour distance and the weak attractive force between them [30].

First, one sticks a piece of graphite (*NGS Dragon Seal*) to the adhesive tape, in our case *Blue Low Tack* tape (*Semiconductor Equipment Corp.*). Detaching it leaves behind a layer of carbon, which will then be separated into thinner layers by repeatedly folding the tape onto itself and peeling away again. This produces an increasing area dotted with thinner and thinner graphite flakes on the tape. Some of these flakes will have broken down to single atom thickness after a few times of folding. Finally, the graphite layers can be transferred to a substrate by simply sticking it to the tape. The carbon will partly adhere and after detaching the substrate one obtains a surface covered in graphite pieces and, amongst them, also few-layer graphene (FLG) and MLG. Isolated flakes can now be localised on the wafer by means of optical microscopy or other imaging techniques (see also p. 41). The surface area of exfoliated MLG is usually limited to a few tens of μm^2 but sizes up to $\sim 100\ \mu m^2$ have been reported [45]. Despite the need to actively search and localise MLG flakes, they remain unchallenged in terms of quality and electronic properties, such as mobility or low intrinsic doping.

2.1.2 Chemical Vapour Deposition

A second approch to producing MLG is the use of Chemical Vapour Deposition (CVD). This rather recent technique, first demonstrated in 2008 by Yu et al. [77] for growth on Ni substrates, consists of growing graphene from gaseous precursors on a metal surface that acts as catalyst to the reaction. Several methods are available, e.g. different catalyst substrates, that all result in large, more or less homogeneous films of MLG. Our CVD samples were produced by collaborators at the *Laboratoire de Photonique et de Nanostructures* (LPN) using the growth technique on Cu substrates introduced by Li et al. [78].

At the LPN, the Cu substrate, cut from a high quality Cu foil (in our case *Alfa Aesar* 5N quality), is placed in a furnace, where it is heated to 1040 ° C under a flow of 65 sccm H_2 at a pressure of 200 Torr. When the Cu reaches the desired temperature, an additional flow of C_3H_8 is introduced to the chamber. It pyrolises, decomposing into C and H_2 [79], and forms the mono-atomic carbon layer on the Cu surface. During this part of the cycle, the substrate is exposed to 65 sccm H_2 and 35 sccm C_3H_8 at 200 Torr for 25 min. After cooling down under He atmosphere, a thin layer of PMMA is spun on the graphene/Cu stack. Note that graphene will form on both sides of the Cu film, but using the PMMA transfer only one side can effectively be used. One then proceeds to etching away the Cu in an aqueous solution of iron nitrate, which leaves the PMMA/graphene stack floating at the solution's surface. The PMMA/graphene layer can now be "fished" from the solution by sliding the desired, final target substrate (e.g. Si/SiO_2) under it and lifting it off the solution. Finally, the iron nitrate residues are rinsed off in several

de-ionised water baths.

The advantage of CVD grown graphene over its exfoliated counterpart is its sheer size: while exfoliated flakes remain on the μm^2 scale, the size of a CVD grown MLG sheet is mainly limited by the size of the substrate: CDV graphene layers of sizes ≥ 1 mm^2 can usually be achieved [78]. It is thus easier applicable in large scale production and allows e.g for a statistical evaluation of the contact resistance (see also chapter 5). However, due to the transfer from the growth to the final substrate a disadvantage remains: the pollution of the sheet with polymer residues and an intrinsic doping coming along with it. An annealing step (see 2.3.3) can help to reduce this problem, though. Recently, Petrone et al. [80] reported on a new, dry transfer technique which overcomes the previously outlined problems and results in very high mobility devices.

Characterisation of graphene layers

In general, exfoliated MLG flakes have to be localised manually, e.g. via their optical contrast.

Optical contrast Despite being of mono-atomic thickness and thus transparent to the naked eye, one can make MLG visible nonetheless. In conjunction with a carefully selected oxide thickness of the underlying Si/SiO_2, interference effects create a slight contrast between the flake and the substrate [81]. This effect can also be used to characterise MLG flakes by comparing their contrast to that of a verified reference sample.

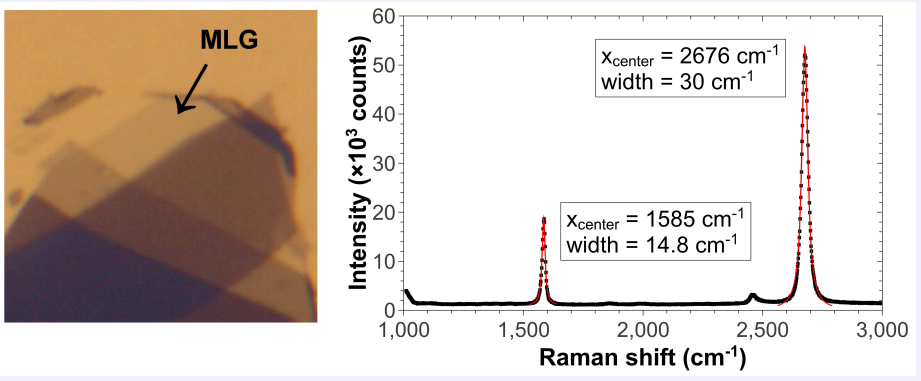

left: MLG and FLG in sample C16-L. right: Raman spectra of MLG part in C16-L

Raman spectroscopy A way to verify the mono-layer character of a flake is to analyse its Raman spectra. Without going into detail, one mainly studies here the intensity and shape of the so-called *2D* and G' peaks, at ~ 1580 and ~ 2700 cm^{-1} respectively. Raman spectroscopy is a useful tool since it allows to distinguish between mono-, bi- and few-layer grapehen. With increasing number of layers, the peaks broaden from a single Lorentzian to a superposition of Lorentzian curves. Also the difference in intensity drastically changes. For a more complete description of this MLG characterisation tool, please refer to e.g. [82, 83] and references therein.

2.2 Manual stacking of thin layers: Wedging transfer

As already mentioned in 1.1.7.3 the electrical properties of a graphene flake will benefit greatly if placed on top or encapsulated between hexagonal boron nitride (hBN). Therefore, different methods have thus been developed in the last years to fabricate stacked graphene-hBN devices (see e.g. [84]). In this work we will use a technique developed at Delft University [15].

2.2.0.1 Wedging transfer setup

The employed method to transfer arbitrary thin films, in our case MLG and hBN flakes, from a donor to a target substrate calls for the following material: an optical microscope, a syringe pump, a micro-positioner and a cellulose based polymer. The complete setup is shown in Fig.2.1. It is crucial to use large working distance objectives in the microscope (*MITUTOYO MF-U*), in our case *MITUTOYO M plan APO SL* $x20$ and $x80$. The polymer is cellulose acetate butyrate (CAB), dissolved in ethyl acetate. The setup is completed by a *Cascade* micro-positioner and a *Razel R-99* reversible syringe pump.

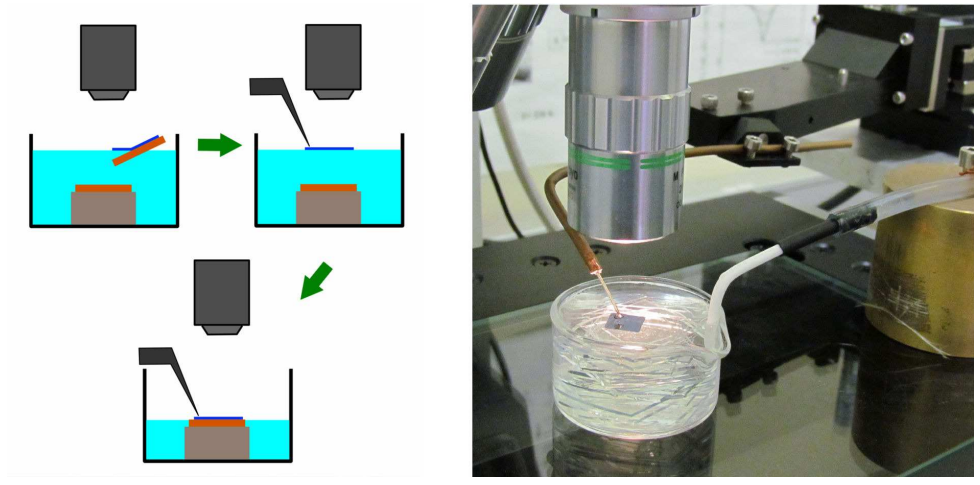

FIGURE 2.1: Transfer Setup

2.2.0.2 Wedging transfer technique

Preparation Before depositing graphene or hBN flakes on the donor substrate, both donor and, if possible, target wafer are cleaned chemically (acetone, IPA) and exposed to a strong O_2 plasma (RIE) for several minutes. Prior to the cleaning step a grid of Cr/Au localisation marks has been prepared on the donor, via UV-lithography and Joule evaporation (see p. 49). The plasma renders the SiO_2 surface hydrophilic and

removes any organic residue. The donor is then cleaned again in a second, lower power O_2 plasma oven. We have found that this second plasma exposure enhances the lift-off of the polymer, possibly due to a condensation of water on the surface.

Now, exfoliated hBN or graphite is deposited on the donor as described in 2.1.1 and suitable flakes are localised optically. Using a spin coater at very high speed (see table 2.2.0.2) the polymer solution is then spun over the substrate. In our opinion spin coating the CAB is favourable compared to the suggested dipping into the solution, as it results in a thinner CAB layer. It is thus more transparent and more easily removed from the target after the transfer. An additional useful feature are the imprints of the Cr/Au marks left in the thin CAB film, which greatly aid in finding and placing the flake to be transferred.

Transfer The target substrate is now placed in de-ionised water under the microscope. After removing the edges of the CAB film, which opens a path for the water to separate the polymer from the substrate, the donor is slowly dipped into the same beaker. This needs to be done very slowly and at a low angle in order to give the water ample time to lift the CAB layer off the donor. All thin layers, graphene or hBN, remain attached to the polymer and are now floating on the water. The desired flake is localised and moved above the target structure by means of the micro-positioner. Slowly lowering the water level and keeping its position steady, the flake is then precisely deposited on the target. The precision is of the order of a few μm. Once the transfer is completed, water residues are removed by baking the target substrate above 80 °C or simply leaving it to dry overnight. Finally the CAB layer is dissolved in ethyl acetate. An overview of the wedging transfer process and details for each step can be found in table 2.2.0.2.

step	*description*	*tool(s)*	*notes*
1	CAB preparation	magnetic mixer	dissolve CAB in ethyl acetate $\sim$ 30 mg/mL, mix well (1–2 h)
2	substrate(s) preparation	RIE *Corail 200R*	3–5 min O_2 plasma, 60 W, P $\lesssim$ 12 nbar
3	substrate(s) preparation	*Harrick* plasma oven	5–10 min O_2 plasma, 200 W, P $\lesssim$ 10 μbar
4	exfoliation & localisation	graphene/hBN & *Semiconductor Equipment Corp* "Blue Low Tack" & Olympus microscope	see 2.1.1
5	spin coating	spin coater & CAB	10 s, 8000 rpm, 5000 rpm/s
6	donor preparation		remove CAB around substrate edges
7	lift-off	de-ionised water	separate CAB from donor, low angle
8	positioning	microscope & micro-positioner	move flake over target
9	deposition	microscope & micro-positioner & syringe pump	lower water level & deposit flake on target
10	drying	heater plate	$\geq$ 10 min. at $\geq$ 80 ° C
11	CAB removal	ethyl acetate	$\geq$ 1 h

TABLE 2.1: Wedging transfer of graphene or hBN flakes.

2.3 Device fabrication

This section will describe the different procedures employed to realise the graphene based microwave devices studied during this theses. For the purpose of simplicity and completeness we will follow the production steps of a top-gated device based on exfoliated graphene and point out the differences to the fabrication of CVD and graphene-on-hBN samples where necessary. A short description of the main fabrication tools, such as electron-beam lithography, UV-lithography and metal evaporation, will also be given (see p. 49).

substrate	*size* (mm^2)	*oxide thickness*(nm)	$\rho(\Omega cm)/\sigma$
doped Si/SiO$_2$	8×8	1000	$\sim 10^{-3}$
high resistivity Si/SiO$_2$	8×8	90	≥ 20000
sapphire	circular $\varnothing = 9.5$ mm	$\emptyset$	$\emptyset$

TABLE 2.2: Different substrates and their characteristics.

2.3.1 Substrate preparation

2.3.1.1 Choice of substrate

Before carrying out the actual exfoliation and deposition of MLG, the backing substrate has to be chosen and prepared. Depending on the intended measurements we have used doped Si/SiO_2, highly resistive Si/SiO_2 and also sapphire substrates in this work. See 2.2 for a list of their individual characteristics. The pre-deposition steps are the same for all substrates: The substrates are cleaned and a grid of metallised crosses and numbers is produced on the surface. This grid will serve as orientation marks in the following steps, as e.g. during the localisation of graphene flakes.

2.3.1.2 Cleaning

As a first step, the substrates undergo a cleaning procedure of 10 minutes in acetone and isopropyl alcohol (IPA), respectively, in conjunction with ultrasound. After drying with nitrogen gas follows a 10–15 minute O_2 plasma treatment. UV-lithography (see p. 49) and Joule evaporation ($\sim$ 2 nm Cr, 50–100 nm Au) are then used to create a grid of crosses and numbers on the wafer. The spacing of 500 μm horizontally and 400 μm vertically between crosses was chosen with respect to the field of view of our microscope and the mounted *ALTRA 20* CCD camera.

2.3.2 Deposition and localisation

For a successful deposit of exfoliated MLG the underlying substrate has to be vigorously striped of all organic residues, as an insufficiently cleaned wafer will result in graphene flakes prone to detaching and crumbling during the following production steps. Therefore, we expose the substrates to a strong O_2 plasma at very low pressure ($\sim$ 12 nbar) for $\sim$ 5 minutes prior to depositing the exfoliated graphene as described in the end of 2.1.1. With the help of the localisation grid we can now search optically for suitable flakes. Please see 41 for more information about the optical discrimination of MLG. Due

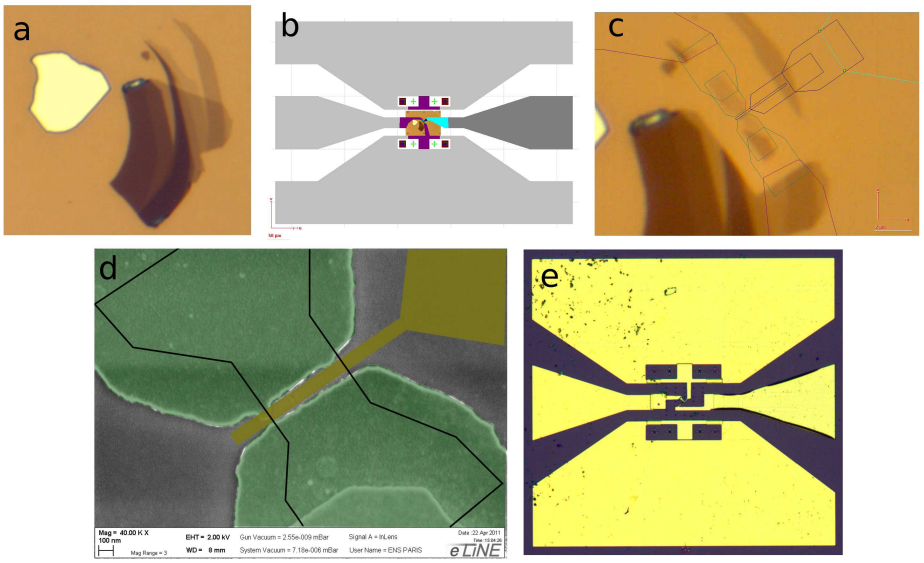

FIGURE 2.2: Fabrication steps of a top-gated graphene device. a) Exfoliated graphene flake C16-A on Si/SiO_2. b) GDSII mask with underlying micrograph of targeted graphene flake. c) GDSII FET structure design. The flake has been dry etched into a handle shape. Contacts (green) will be made from Pd, the gate electrode (blue) from Cr/Au. The separating AlOx layer is not shown. Ground plane dimensions: 550 μm $\times$ 400 μm. Note that this design was adapted for Janis microwave probe heads. d) SEM micrograph of graphene FET C16-A. The handle shape and gate electrode (here gold) were superposed manually to indicate their location. e) Micrograph of a complete graphene FET. Note the larger design adapted for the pitch of Cascade microwave probe heads.

to the well defined grid, we can calculate the coordinates of the graphene flakes with respect to a chosen origin (here, the first cross bottom left) at a precision of ± 10 μm.

2.3.3 GHz adapted coplanar waveguide

The final aim is to measure our graphene devices in a macroscopic GHz frequency setup. It is therefore necessary to provide a) an interconnect between the micrometer sized RF environment and the nanometer sized graphene and b) a good match to the standard 50 Ω impedance of our high frequency equipment. We achieve this by creating a coplanar waveguide around the MLG as shown in Fig. 2.2, which gradually decreases in size all the whilst keeping 50 Ω impedance.

Pre-contacts The first step in the production of the coplanar waveguide, is to define the so-called pre-contacts by means of e-beam lithography. The pre-contacs consist of the ground and preliminary drain electrodes (light grey structures in Fig. 2.2 (b)), as well as a set of localisation marks in a $100x100$ μm^2 window around the MLG flake.

step	*description*	*duration*	*temperature* ° C	*gas*	*flux* *sccm*
1	flush	2 min	∅	Ar	1500
2	heat up	20 min	300	Ar	1500
3	anneal	2–5 h	300	Ar & H	1500 & 800
4	cool down	60 min	∅	Ar	1500

TABLE 2.3: Thermal annealing under H_2/Ar atmosphere of graphene devices.

Joule evaporation of $\sim$ 2 nm chromium (Cr) and 100–150 nm gold (Au) is used to metallise the structures. After the lift-off process, optical imaging allows to determine the position of the MLG with respect to the localisation marks at a sub-micron precision. These images, imported into the GDSII lithography database, will then serve to design the desired etching masks, small contact electrodes and top-gates; in short the overall functional design of the device.

blank space

Etching In some cases, e.g. when the MLG is surrounded by thicker graphene layers or if a specific shape is desired, it is necessary to cut the MLG sheet. This can be done by exposing the areas to be eliminated to a strong O_2 plasma for 5–8 s. Prior to this, one needs create an etching mask by means of e-beam lithography and diluted PMMA, opening windows where etching is to occur. Also, it is advisable to reduce the exposure dose and developing time, as the plasma will also attack the edges of the windows. A slightly underexposed PMMA will minimise the risk of unwanted etching into the graphene channels. After removal of the remaining PMMA the samples can be checked for successful etching and then undergo the creation of the contact electrodes.

Note that in the case of CVD graphene devices a first etching step has to occur before the pre-contacts, in order to open windows for the metallisations. Due to the rather large scale production (30–40 devices on one sheet), the finer etching of the graphene channels is automated and wider contact electrodes will prevent a possible mismatch with the graphene sheets. Graphene-on-hBN samples require no different treatment.

Contacts After having isolated the MLG, or having brought it into the desired shape, the contact electrodes are formed. We use again e-beam lithography, diluted PMMA and a carefully calibrated exposure dose, in order to prevent proximity effects. The contacts are usually 1–1.5 μm wide, but are generally tailored and orientated to suit the MLG

flake. One of the electrodes connects the graphene channel to the drain, the second one establishes a connection to the ground (source). After developing the polymer, the groves in the PMMA are filled with 100–150 nm palladium (Pd) by means of e-gun evaporation and a lift-off in acetone is performed (see also 49).

Hydrogen/Argon annealing As reported in [85], a thermal treatment under H/Ar atmosphere enhances graphene device properties, as e.g. the graphene-metal interface or the sheet resistance. Especially the latter is important in our case, since several lithography steps are necessary and each one leaves behind PMMA residues. See table 2.3.3 for a description of the annealing process. It occurs in general after the contact electrode creation.

Dielectric and top-gate The final step of the fabrication process is to create a top gate, separated from the graphene channel by a thin dielectric: We use a very thin (≤ 2 nm) layer of Al, deposited on the sample via Joule evaporation. The Al film is then oxidised in the evaporator chamber for 15–30 min. at an oxygen pressure $P \simeq 10^{-4}$ mbar. Several steps of deposition and oxidation assure a thin but electrically tight dielectric. In general we achieve a thickness of 8–10 nm. The relative dielectric constant of such a AlOx layer is ~ 7. The top-gate electrode is finally formed by means of e-beam lithography and Joule Cr/Au evaporation. Top-gate sizes depend on the type of device and the length of the graphene channel, defined by the Pd contacts (see chapters 3 and 4).

E-beam Lithography

Micro- and nano-structures are generally created by means of a type of lithography and a subsequent metallisation. During this work, we have employed electron-beam (e-beam) and ultraviolet light (UV) lithography, as well as Joule and e-beam evaporation.
The principle of operation of e-beam lithography is the precise exposure of a polymer solution to a beam of electrons. The exposure degrades the poly methyl methacrylate (PMMA) chains, making it possible to remove only the exposed parts during the developing process. With our *Raith e-Line* e-beam lithography setup we can create structures at a resolution of ~ 15 nm. Table 2.4 and Fig.2.3 (steps 1–4) summarise a typical process.

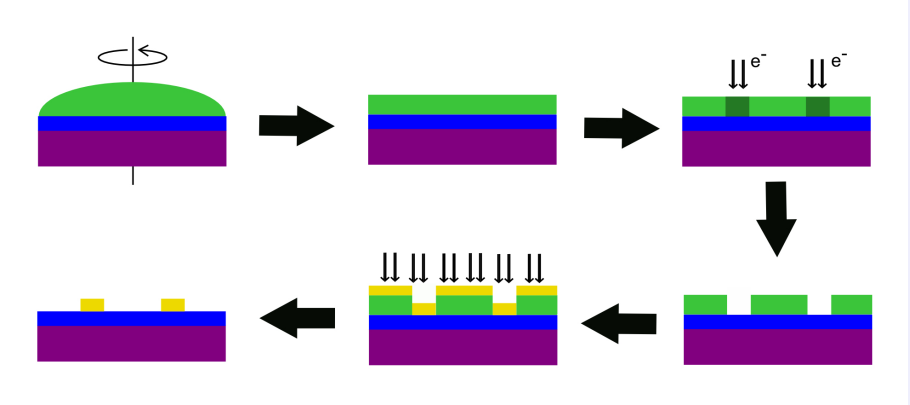

step	*description*	*tool(s)*	*notes*
1	substrate preparation	acetone & IPA	1–5 min, if possible
2	spin coating	spin coater & PMMA	30 s, 4000 rpm, 4000 rpm/s, PMMA *AZ6* $\rightarrow\sim$ 550 nm or $\sim$ 260 nm if diluted
3	baking	heater plate	10 min., 165 ° C
3(b)	Al coating	Joule evaporator	$\geq$ 15 nm, sapphire substrates
4	e-beam lithography	*Raith e-Line*	small structures: 7.5 μm aperture, 20 kV, 250 μC/cm^2
			large structures: 120 μm aperture, 20 kV, 260 μC/cm^2
5	developing	MIBK & IPA	small structures: 1.5 min.MIBK/30 sIPA
6			large structures: 2 min.MIBK/30 sIPA

The developing agent is methyl isobutyl ketone (MIBK) diluted with IPA at a ratio 1 : 3.

TABLE 2.4: Typical e-beam lithography process.

UV-lithography

E-beam lithography is a very precise, but rather time consuming technique. For repetitive structures with no need for nano-metric resolution optical lithography is a good choice to speed up the process. Here, the use of UV light and a shadow mask (created once beforehand by means of e-beam lithography) made from a quartz sheet and Al metalisations, allow for a fast production of e.g. the localisation marks at a resolution of ~ 2 μm. The basic working principle is the same as for e-beam lithography: UV light changes the properties of a polymer layer and the exposed or shadowed parts can be eliminated during the developing. We have used the so-called negative lithography process for our samples, where it is the shadowed parts that are removed in the end. Table 2.5 gives a summary of a typical localisation marks lithography.

step	*description*	*tool(s)*	*notes*
1	substrate preparation	acetone & IPA & ultrasound	5–10 min
2	substrate preparation	*Harrick* plasma oven	10–15 min O_2 plasma, 200 W, P $\lesssim 10$ μbar
3	spin coating	spin coater	30 s, 4000 rpm, 4000 rpm/s, resin AZ5214E $\rightarrow\sim 1.4$ μm
4	pre-bake	heater plate	1 min.50 s, 125 ° C
4	align & expose	*SüssMicroTec MJB4* mask aligner	12 s
5	reversal bake	heater plate	1 min.50 s, 125 ° C
6	flood exposure	*SüssMicroTec MJB4* mask aligner	30 s
7	developing	AZ726 & de-ionised H_2O	35 s & ≥ 30 s

Table 2.5: Typical UV-lithography process.

Metallisation

As indicated in Fig. 2.3 the last steps of a typical nano-fabrication are the metallisation of the created structures and the lift-off of the unwanted parts. Two of the most common ways are evaporation by Joule heating and by electron gun. To obtain a long mean free path of the metal atoms, evaporation systems need a high vacuum (P$\leq 10^{-5}$ mbar) and thus generally require two-stage pumping. Both consists of heating a small piece of metal (in our case Al, Cr, Au and Pd) to the point of sublimation by either sending a large current through a molybdenum or tungsten crucible (Joule) or irradiating it with a beam of high energy electrons (e-gun). The latter is especially needed for metals like Pd or Ti.

Joule evaporation

metal	*pressure (mbar)*	*velocity (nm/s)*	*current (A)*	*thickness (nm)*
Cr	10^{-5}	≤ 0.01	65	1–2
Au	2×10^{-6}	0.15	75	100–150
Al	5×10^{-6}	≤ 0.01	50	< 2

E-gun evaporation

metal	*pressure (mbar)*	*velocity (nm/s)*	*current (mA)*	*thickness (nm)*
Pd	8×10^{-7}	0.15	45	100–150
Al	8×10^{-7}	0.1	50	< 2

Lift-off After the successful evaporation, the unexposed, metal covered resin parts are removed by a lift-off in acetone. Preferably this is done at ambient temperature over night, or for at least several hours. If however necessary, the process can be sped up to about 15 min. by heating the acetone to 45 ° C.

TABLE 2.7: Typical e-gun evaporation parameters.

Chapter 3

Microwave graphene field-effect transistors

The discovery of semiconductors and the invention of the field-effect-transistor (FET) have greatly shaped today's way of life and technology. The first device based on semiconductors was a Germanium bipolar transistor developed at Bell Laboratories in 1947 [86], leading to a Nobel prize for Shockley, Bardeen and Brattain in 1956.
Metal-oxide-semiconductor field-effect transistors (MOSFETs) only played a minor role in the early days of semiconductors, but became more and more popular in the course of the years, taking the lead during the 1980's. This was in particular due to the scalability of MOSFET devices to smaller planar sizes. The probably most well known statement about the scalability issue is the so-called *Moore's law*: the number of components on an integrated circuit (IC) doubles every 12 months. With planar scales reaching predicted technological obstacles also vertical scalability becomes a new challenge. Suitable candidates for such new concepts could be layered materials like graphene or carbon nanotubes (CNTs).
An example is the carbon nanotube FET (CNT-FET) which followed the discovery of the carbon nanotube in 1991 by Ijima. As pointed out e.g. in J. Chaste's PhD thesis [58], expectations were high for CNTs playing a major role in micro-electronics due to their high current transport ability and gate sensibility, outshining standard metal-oxide-semiconductor field-effect transistors (MOSFETs) and high electron mobility transistors (HEMTs). CNT-FETs can operate at high frequencies, the GHz regime, again making them suitable for fast micro-electronics and moreover, as will be revealed in the following, ultra-fast, sensitive charge detectors. Additionally, due to the small tube diameter they are the ultimate nano-MOSFET.
Another example for new candidates in micro-electronics are graphene FETs (GFETs) and top-gated graphene-oxide FETs (RF-GFETs). As already pointed out in chapter 1

graphene shows, just as CNTs, a large mobility and is predicted to have low charge noise (this subject will be addressed in detail in chapter 5). Graphene FETs have much lower impedance than their CNT counterparts, making impedance matching a less sensitive issue than in CNT-FETs [58], and a much greater and tunable number of conduction channels (4 in CNTs). Furthermore, due to graphene's planar nature gate access is optimal as well as the control of device geometry.

Let us now briefly study the main characteristics and working principle of field-effect

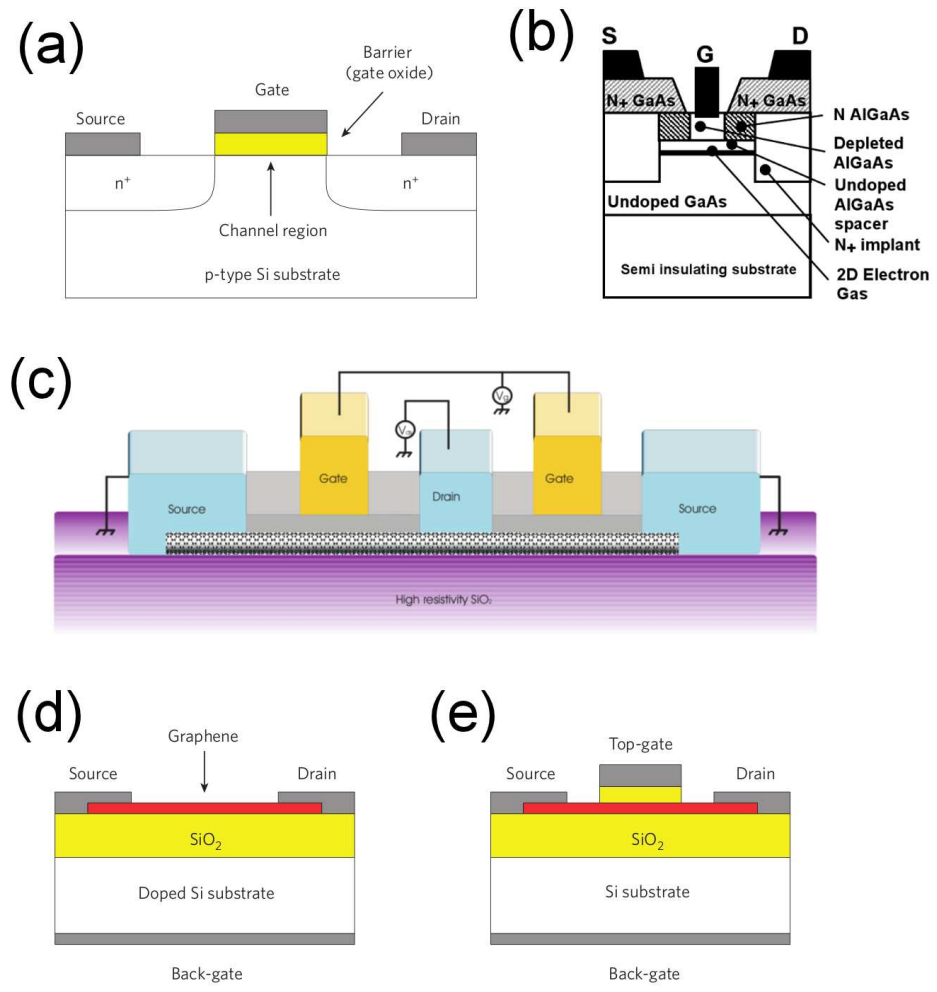

FIGURE 3.1: Schematic overview of a) Metal-oxide-semiconductor FET (MOSFET). From F. Schwierz [86] b) High-electron-mobility transistor (HEMT). From Ellinger et al. [87]. c) Carbon-nanotube FET (CNTFET). From Chaste et al. [58]. d) Back-gated graphene FET (GFET) e) Top-gated metal-oxide-graphene FET (RF-GFET). d) and e) from F. Schwierz [41].

transistors, taking as a first example a standard Si/SiO_2 n-type *metal-oxide-semiconductor FET* (MOSFET), schematically shown in Fig. 3.1(a). It is governed by the following principles [86]: Two n-doped regions of silicon are separated by a p-doped channel (or

vice versa in a p-type MOSFET). If a sufficiently large voltage is applied to the gate situated above the the channel, an inversion layer is created and the channel becomes conductive. Thus, a current can flow if a bias voltage is applied between source and drain. Through variation of the gate voltage V_g it is then possible to create an ON-state, where current flows and an OFF-state, where the channel is completely depleted of n-type carriers, thus blocking the current. Most commonly used are so-called enhancement MOSFETs, which are in the OFF-state at zero gate voltage. Semiconductors other than Si are used, such as Ge and GaAs for example as well as different gate dielectrics. The Si/SiO_2 combination remains however the industrially most important. Also, more complicated transistor designs are used, as e.g. double- and tri-gate structures, enhancing the transistors' properties and scalability. A similar type of transistor relies on the effect of a Schottky diode between gate and channel and is called *metal-semiconductor FET* (MESFET). It is not displayed among Figs. 3.1. The difference to MOSFET devices is the direct contact of the metal gate with the semiconductor channel. Fig. 3.1(b) is yet a third type of transistor, the *high electron mobility transistor* (HEMT) [87], often employed for high frequency applications. In a HEMT, a heterojunction of semiconductors with different bandgaps creates a two-dimensional electron gas (2DEG) in the channel region with considerably high carrier mobilities and velocities. Upon application of a bias voltage between drain and source a current is established, which can be controlled by the gate potential to create ON and OFF states. Previously, we have already briefly introduced the *carbon-nanotube FET* (CNTFET) (see Fig. 3.1(c)). Here, a semiconducting carbon-nanotube is used as channel, connected to two leads and separated from the gate by a thin oxide. It is thus a metal-oxide-CNT-FET and due to the semiconducting nature of the CNT total current suppression is possible. Switching speeds are in the GHz frequency range [58]. Fig. 3.1(e) depicts a top-gated metal-oxide-graphene FET (RF-GFET) which relies on the same principles as MOSFETs and CNTFETs but has a monolayer graphene (MLG) channel. Similarly, a non-RF graphene transistor will simply be called GFET throught this work. It is a back-gated devices as shown in Fig. 3.1(d), where a doped silicon substrate acts as gate electrode and is separated from the MLG by a layer of SiO_2. In both cases, the gate electrode controls the charge carrier concentration in the MLG channel, effectively varying the current between drain and source. Let us now point out a few differences between RF-GFETs and conventional MOSFETs. While MOSFETs are suitable for logical applications due to the possibility of distinct current-ON and current-OFF states, the drain-source current cannot be completely suppressed in a RF-GFET. Extensive research into the creation of a bandgap in graphene is thus under way: The use of bi-layer graphene or the reduction of the channel width into the nanometer region, i.e. the creation of so-called graphene nano-ribbons, are highly investigated routes [88–92]. If a sufficient ON/OFF ratio can be achieved, logical transistors with clock speeds higher than today's silicon technology

are possible (see table 3.2), since RF-GFETs are closing in on MOSFETs in terms of transit frequency f_T. A second possible application of RF-GFETs are high frequency low-noise amplifiers (LNAs). Here however, graphene transistors still suffer from their low power gain and maximum frequency f_{max} as compared to their silicon counterparts. This chapter follows however the spirit of [58], i.e. we will not be as much interested in the micro-electronic applicability of GFETs, but in their use as fast single charge detectors for mesoscopic science, where one most prominently is in need of high transit frequency and a low charge noise.

In this section, after a short description of charge detection in CNT nano-FETs, we will first introduce the concepts necessary to understand and model charge detection at high frequencies in GFETs, in particular the transconductance g_m and cut-off frequency f_T. The following part will then describe how we access these quantities in our experiments. Finally, we will discuss the results in the light of ultra fast charge detectors.

3.1 Single charge detection in CNT nano-FETs

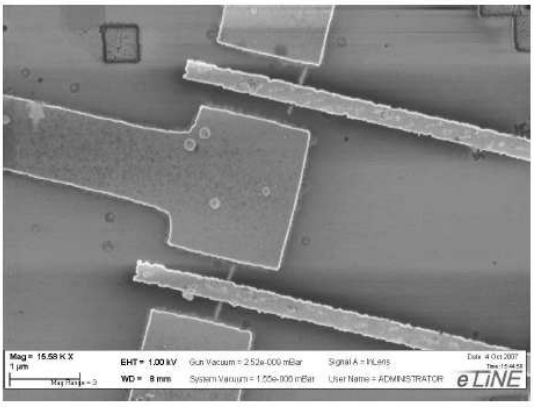

FIGURE 3.2: SEM micrograph of a double-gated CNT-FET with gate length L_g = 300 nm. Adapted from Chaste et al. [58].

Chaste et al. have studied in detail the DC and RF behaviour of CNT-FETs and in particular their use as fast single charge detectors[58]. From high frequency measurements at room and liquid helium temperature they were able to extract the cut-off frequency of CNT-FETs, their input charge noise and finally estimate the CNT-FETs charge sensitivity $\delta q_{rms} = \sqrt{S_I}/\omega_T = 13\ \mu e/\sqrt{\text{Hz}}$ [14]. These results have been obtained with a GHz setup of bandwidth 0.8 GHz. Chaste et al. found cut-off frequencies as high as 50 GHz (see also section 3.2.3.1) and concluded that CNT-FETs suitable for fast single charge detection [58].

However, despite being the ultimate nano-detector, their small size also carries disadvantages, like the high impedance and large contact resistance, which makes it difficult to measure and integrate into a standard RF setup.

3.2 Important concepts and formulas

Some important quantities describing FET behaviour, as e.g. the transit frequency f_T, have already been mentioned throughout this thesis. Let us now introduce more formally the concepts and formulas that will allow us to quantify our RF-FET properties and compare them to other transistors. First, the DC transport characteristics will be mentioned, followed by a brief description of radio frequency (RF) properties.

3.2.1 DC characteristics of graphene FETs

As pointed out in chapter 1 section 1.3.2.2, the current through the sample I_{ds} is governed by the electric field applied between the contacts (drain and source) and, as mentioned previously, the gate potential changing the charge carrier density.

3.2.1.1 Drain-source dependence

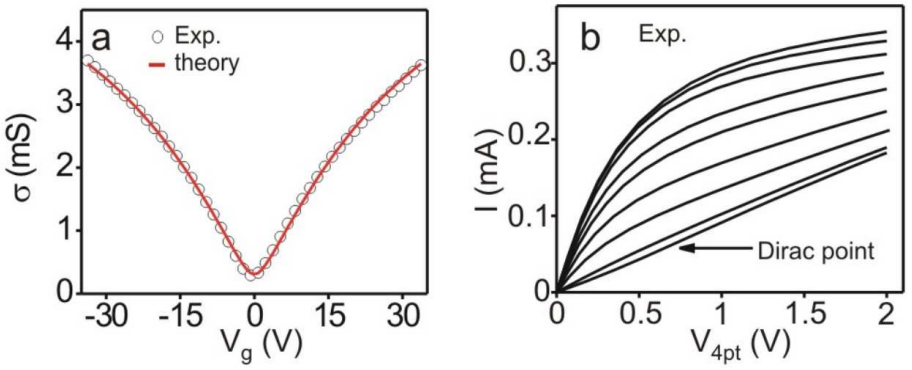

FIGURE 3.3: a) Conductivity as function of back-gate voltage at $V_{ds} = 0$. Note that here the notation differs from the rest of this work. b) $I - V$ characteristics for different gate voltages in a 4-point measurement. The mobility of this device is $\mu_c \simeq 14\,000\ \mathrm{cm^2V^{-1}s^{-1}}$. Both graphs from Barreiro et al. [50]

The dependence of drain-source current on drain-source voltage V_{ds} can be divided in two regimes: A bias voltage region of linear behaviour and a saturation region, where I_{ds} does not increased linearly with V_{ds} any more (see Fig. 3.3(b)).
In the linear regime, the sample's $I_{ds} - V_{ds}$ characteristic follows Ohm's law, i.e. increases

with a constant slope, for a fixed gate potential. Note that this assumes negligible interface resistance [50] between the metal contact and the graphene in a two-point device. Four-point measurements as performed by [50] circumvent this problem. The slope of the $I-V$ curve expresses the drain-source conductance

$$g_{ds}(V_{ds}, V_g^{\Delta}) = \left.\frac{\partial I_{ds}(V_{ds}, V_g^{\Delta})}{\partial V_{ds}}\right|_{V_g^{\Delta}=const.} \tag{3.1}$$

which nearly vanishes at the Dirac point due to the density of charge carriers dropping to its minimal value. V_g^{Δ} signifies now and in the following the change of gate voltage V_g with respect to the charge neutrality point (CNP): $V_g^{\Delta} = V_g - V_{CNP}$.
As can be seen in Fig. 3.3(b) [50], the graphene $I-V$ characteristic deviates from the linear Ohmic behaviour from a certain threshold voltage onwards. The current starts to saturate to a value I_{sat}, which can nevertheless be modulated by gate voltage. This (incomplete) saturation is attributed to the scattering of electrons with optical phonons: Once the accelerating electric field provides enough energy, electrons can activate an optical phonon and are subsequently backscattered. This effectively decreases the total current I_{ds}. The fact that the saturation remains incomplete in graphene devices is due to elastic scattering events in addition to the scattering of electrons with optical phonons [50]. In other words, considerable current saturation can only be achieved in high mobility samples. Otherwise, the electron elastic mean free path remains substantially shorter than the optical phonon activation length and only little inelastic electron-optical phonon scattering occurs. Thus, the charge carrier mobility $\mu_c(V_g^{\Delta})$, effectively a measure of sheet quality, also provides insight into the dominant scattering mechanism. A more detailed study of scattering mechanisms in graphene will follow in chapter 4. An interesting side note is the possibility to observe Zener-Klein tunnelling in the I–V curves close to the CNP. Vandecasteele et al. [93] showed that a power law $I \propto V^{\alpha}$ correctly models the characteristics and stems from defect related Zener-Klein tunnelling.

3.2.1.2 Gate dependence

The charge carriers in graphene form effectively a two dimensional electron gas with certain particularities due to graphene's planar nature and honeycomb arrangement (see chapter 1). One of these particular features is the possibility to tune the charge carrier density by field-effect [2]: The gate voltage V_g^{Δ} modulates the charge density and therefore the Fermi energy ϵ_F. This behaviour is displayed in Fig. 3.3(a).
In back-gated GFETs it is usually assumed that $n_s \propto V_g^{\Delta}$. This is not generally valid for top-gated RF-GFETs, however we will neglect the effect of electron compressibility

here and assume perfect coupling of n_s and V_g^{Δ}. The aforementioned correction due to electron compressibility will be discussed in more detail in chapter 4. Note also that as mentioned before $V_g^{\Delta} = V_g - V_{CNP}$.
The carrier concentration can be estimated from the empirical formula

$$n_s(V_g^{\Delta}) = \sqrt{n_0^2 + \left(C_g' V_g^{\Delta}/e\right)^2} \tag{3.2}$$

where n_0 is the minimum sheet carrier density, C_g' the gate capacitance per unit area and V_g the gate voltage with respect to the Dirac point [94]. Typically, $n_0 \simeq 2.2 \cdot 10^{11}$ cm^{-2} for graphene on SiO_2 [95, 96]. This is generally attributed to the presence of electron-hole puddles in the graphene sheet, making the exact value of n_0 dependent on graphene quality.

3.2.1.3 Drain-source current I_{ds}

Eq. (1.51) leads us now directly to the dependence of drain-source current on V_{ds} and V_g:

$$I_{ds}\left(V_{ds}, V_g^{\Delta}\right) = \frac{W}{L}\sqrt{n_0^2 + \left(C_g' V_g^{\Delta}/e\right)^2}\mu_c(V_g^{\Delta})eV_{ds} \tag{3.3}$$

W, L are sample width and length, respectively, μ_c the charge carrier mobility and e the electron charge. Note that this description remains valid only in the ohmic regime.

3.2.1.4 DC-transconductance

As pointed out above, the drain-source current depends on the applied gate voltage. The sensibility of current variation with respect to gate voltage is generally expressed by the transconductance at fixed drain-source voltage [86]

$$g_m(V_{ds}, V_g^{\Delta}) = \left.\frac{\partial I_{ds}}{\partial V_g^{\Delta}}\right|_{V_{ds}=const.} \tag{3.4}$$

The highest reported values of g_m per unit gate width for RF-GFETs are [17]: 0.15 mS μm^{-1} for SiC grown, 0.02 mS μm^{-1} for CVD grown and 1.27 mS μm^{-1} for exfoliated graphene. The highest obtained value for a III-V device is 1.62 mS μm^{-1} as of November 2011 [17]. CNT-FETs reach transconductance values of the order of 11.4 mS μm^{-1} (see also table 3.2).
Besides a few exceptions [17], the transconductance of RF-GFETs remains still lower than in MOSFETs. Note also the dependence of g_m on gate length and carrier mobility: $g_m \propto \mu_c L_g^{-1}$. This will be of importance in the assessment of the transit frequency f_T.

3.2.1.5 Voltage gain

Another important property of transistors is their voltage gain

$$G_V = \frac{\delta V_{out}}{\delta V_{in}} = \frac{\delta V_{ds}}{\delta V_g} = \frac{g_m}{g_{ds}} \propto \frac{V_{ds}}{V_g^{\Delta}} \tag{3.5}$$

where we have used Eq. (3.4) and Eq. (3.1). In RF-GFETs the voltage gain remains still below 1, in contrast to e.g. silicon MOSFETs or CNTFETs. Also GFETs based on bilayer graphene show substantial voltage gain, as shown e.g. by Szafranek et al. [92] who measured $G_V^{bilayer} \simeq 35$.

3.2.1.6 Gate capacitance

Contrary to CNTFETs, where the gate capacitance is between a cylinder (the CNT) and a plane (the gate), capacitance calculation in GFETs is fairly simple: That of two planes separated by a dielectric.

$$C_{geo} = \epsilon_0 \epsilon_r \frac{LW}{t} \tag{3.6}$$

where t is the distance between MLG and gate, ϵ_0 and ϵ_r are the vacuum and relative permittivity, respectively. In our devices we generally use the high-κ dielectric aluminium oxide with $\epsilon_r \simeq 7$ at a thickness of the order of 10 nm. The value $\epsilon_r \simeq 7$ is within the range outlined e.g. by Gloss et al. [97] of $\epsilon_r^{AlO_x} \leq \epsilon_r^{Al_2O_3} = 4.5$–$8.9$ for ultra-thin AlOx layers. For the devices presented in this chapter, the total gate capacitance is thus typically of the order of a few fF.

Note that here we assume the total gate capacitance C_g to be dominated by the geometrical capacitance, as we generally have $n_s \gg n_0$, and we neglect corrections due to electron compressibility, which may dominate close to the Dirac point. This particular issue will be addressed in more detail in chapter 4.

	SiO_2	hBN	Al_2O_3	HfO_2
ϵ_r	3.9 [98]	3–4 [44]	4.5–8.9 [97]	25 [98]

TABLE 3.1: Comparison of different gate dielectrics for RF-GFETs.

3.2.2 RF characteristics of graphene FETs

Let us now turn to the high frequency properties of GFETs. In the following we will always work in the linear response regime, i.e. the intrinsic properties of our transistor as e.g. g_m or C_g will remain unchanged when changing the excitation magnitude.

3.2.2.1 Small signal equivalent circuit

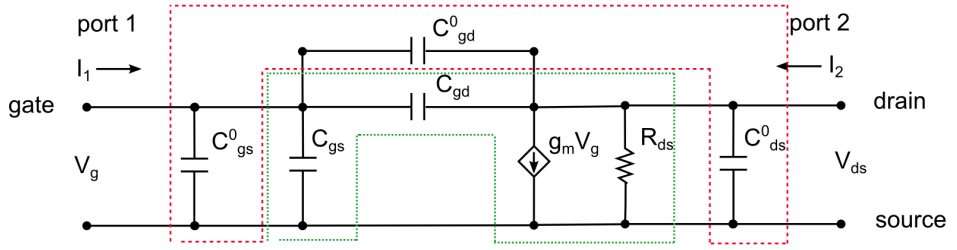

FIGURE 3.4: Small signal equivalent circuit for graphene FETs

Contrary to DC measurements, where the characteristics only depend on the geometries of channel and gate and the device's dependence on drain-source and gate voltage, the whole device layout is important in RF experiments, in particular at GHz frequencies. There, contributions due to coupling between gate and drain/source can occur, as well as parasitic contributions due to the environment. Fig. 3.4 shows the simplest small signal equivalent circuit of a graphene FET (see also [18]). Here, the label "gs" denotes gate-source, "gd" gate-drain and "ds" drain source couplings. The superscript ^{0} points out the parasitic contributions. g_m is the transconductance.
The currents I_1 and I_2 can be calculated by short circuit analysis, where one considers a shunt across one of the voltage sources and calculates the current flow in the circuit. This technique will be used in the following calculation of admittance parameters (see 3.2.2.3).

3.2.2.2 Scattering parameters

A versatile tool to study the high-frequency properties of a given object, without any prior specification, is the technique of the so-called *scattering parameters* (S-parameters). They have been very briefly introduced in chapter 1 Eq. (1.55). We will now adapt this formalism for an AC-voltage signal incident on a two-terminal electric device. In more general terms, the frequency dependent elements of the scattering matrix S describe the

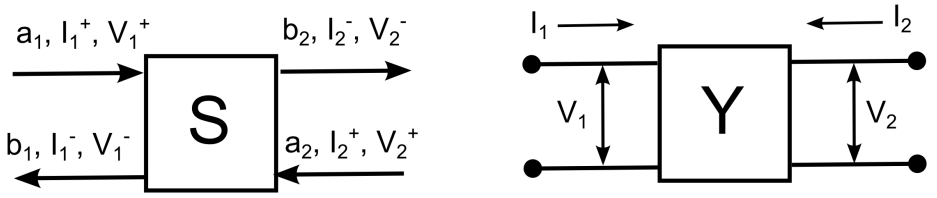

FIGURE 3.5: Left: Scattering matrix S and applied voltages and currents. Right: Admittance matrix Y and corresponding currents and voltages

transmission between ports and the reflection at each individual port:

$$\begin{pmatrix} b_1 \\ b_2 \end{pmatrix} = \begin{pmatrix} S_{11} & S_{12} \\ S_{21} & S_{22} \end{pmatrix} \begin{pmatrix} a_1 \\ a_2 \end{pmatrix} \tag{3.7}$$

The scattering parameter approach is in principle valid for any number of ports. However, in Eq. (3.7) we only consider two ports, for the sake of simplicity and applicability to our measurements.
Here, the elements of S are

$$S_{ij} = \left(\frac{b_i}{a_j} \right)_{a_i=0} \quad , \quad i,j = 1,2 \tag{3.8}$$

wherein a_i and b_i are defined by

$$a_1 = \frac{V_1^+}{\sqrt{Z_0}} = I_1^+ \sqrt{Z_0} \quad , \quad a_2 = \frac{V_2^-}{\sqrt{Z_0}} = I_2^- \sqrt{Z_0} \tag{3.9}$$

$$b_1 = \frac{V_1^-}{\sqrt{Z_0}} = I_1^- \sqrt{Z_0} \quad , \quad b_2 = \frac{V_2^+}{\sqrt{Z_0}} = I_2^+ \sqrt{Z_0} \tag{3.10}$$

I_i and V_i are the incoming/outgoing current and voltage at port i, $Z_0 = 50\ \Omega$ is the standard input and output impedance of our measuring system.

3.2.2.3 Y-parameters

Although S-parameters are widely used to characterise RF components, the use of *admittance parameters* is more beneficial for our devices [86]. They offer the possibility to easily subtract parallel elements, such as the parasitic contributions to the device capacitance. As can be seen from Fig. 3.4, the parasitic contributions (highlighted in red) are in parallel to the intrinsic circuit elements (green in the diagram). For our

considered two-port, 4-terminal system the admittance matrix is defined by

$$\begin{pmatrix} I_1 \\ I_2 \end{pmatrix} = \begin{pmatrix} Y_{11} & Y_{12} \\ Y_{21} & Y_{22} \end{pmatrix} \begin{pmatrix} V_1 \\ V_2 \end{pmatrix} \quad , \quad V_i = V_i^+ + V_i^- \quad , \; i = 1, 2 \tag{3.11}$$

where

$$Y_{ij} = \left(\frac{I_i}{V_j} \right)_{V_{k \neq j} = 0} \qquad i, j = 1, 2 \tag{3.12}$$

The Y-parameters can easily be derived from S-parameters via the following relations:

$$Y_{11} = \frac{1}{Z_0} \cdot \frac{(1 - S_{11})(1 + S_{22}) + S_{12}S_{21}}{(1 + S_{11})(1 + S_{22}) - S_{12}S_{21}} \quad , Y_{12} = \frac{1}{Z_0} \cdot \frac{-2S_{12}}{(1 + S_{11})(1 + S_{22}) - S_{12}S_{21}} \tag{3.13}$$

$$Y_{21} = \frac{1}{Z_0} \cdot \frac{-2S_{21}}{(1 + S_{11})(1 + S_{22}) - S_{12}S_{21}} \quad , Y_{22} = \frac{1}{Z_0} \cdot \frac{(1 + S_{11})(1 - S_{22}) + S_{12}S_{21}}{(1 + S_{11})(1 + S_{22}) - S_{12}S_{21}}$$

Performing the aforementioned short circuit analysis of the equivalent circuit model, the admittance parameters can be linked to the elements in the circuit: Placing a short at port 1 (port 2), i.e. $V_1 = 0$ ($V_2 = 0$), and calculating currents I_1 and I_2, we obtain (see 3.12)

$$\begin{aligned} Y_{11}(\omega) &= j\omega \left(C_{gs}^0 + C_{gs} + C_{gd}^0 + C_{gd} \right) & Y_{12}(\omega) &= -j\omega \left(C_{gd}^0 + C_{gd} \right) \\ Y_{21}(\omega) &= g_m - j\omega \left(C_{gd}^0 + C_{gd} \right) & Y_{22}(\omega) &= R_{ds}^{-1} + j\omega \left(C_{gd}^0 + C_{gd} + C_{ds}^0 \right) \end{aligned} \tag{3.14}$$

where j signifies the imaginary unit.

3.2.2.4 RF-transconductance

As discussed previously in the DC description, the drain-source current depends on both the drain-source and gate voltages. In order to quantify the change of I_{ds} with respect to V_g, we introduced the transconductance g_m^{DC} (see Eq. (3.4)).
At high frequencies the transconductance g_m^{RF} can be extracted from Eq. (3.14):

$$g_m^{RF} = \Re \left(Y_{21} \right) \tag{3.15}$$

It is often slightly inferior to its DC counterpart in RF-GFETs. Note that in CNTFETs $g_m^{RF} > g_m^{DC}$ due to capacitive shunting of the interface resistance between nanotube and metal electrode. For a comparison of typical transconductance values for different materials see table 3.2.

3.2.3 Current gain and characteristic frequencies

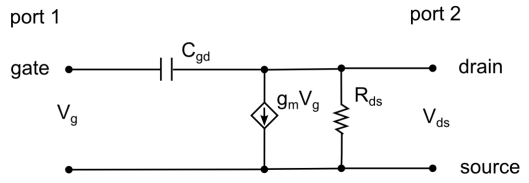

FIGURE 3.6: Simplified model of a transistor. The transfer function is given by $T = V_{ds}/V_g^{\Delta}$.

In order to understand another couple of figures of merit, the cut-off frequency f_T and maximum frequency f_{max}, it is helpful to study a simplified schematic of a transitor shown in Fig. 3.6. It contains only the drain-source resistance R_{ds}, the gate-drain capacitance C_{gd} and the current generator $g_m V_g$, which models the impact of gate potential on the channel conductance. The transfer function can then be derived by circuit analysis as described in 3.2.2.3 and yields

$$T = \frac{V_{ds}}{V_g^{\Delta}} = g_m R_{ds} \frac{1 - j\omega/\omega_T}{1 + j\omega/\omega_{RC}} \propto G_V \tag{3.16}$$

with the two cut-off frequencies $\omega_T = g_m/C_{gd}$ and $\omega_{RC} = (R_{ds}C_{gd})^{-1}$ and the voltage gain $g_m R_{ds}$.

In the case of high-impedance samples with rather small gate-drain capacitance, which typically describes back-gated samples, the response is mainly characterised by ω_{RC}. It is the frequency at which half of the original power is attenuated. Thus, these samples are rather dissipative and mainly governed by the channel resistance R_{ds}.

3.2.3.1 Transit frequency f_T

Of greater interest to us is the *transit frequency* $\omega_T = g_m/C_{gd}$. Its importance is best highlighted by considering the short circuit current gain of a given transistor [18]

$$|H_{21}| = \left|\frac{Y_{21}}{Y_{11}}\right| = 1 + j\frac{\omega_T}{\omega} \tag{3.17}$$

which describes the gain in drain-source current due to the effect of the gate potential. As one can immediately see from (3.17),

$$f_T = \frac{g_m}{2\pi C_{gd}} \tag{3.18}$$

characterises the frequency at which the device's gain becomes inferior to 1. It thus defines the limit of current amplification capability of the transistor. Eq. (3.18) is yet another reason to engineer large transconductance values and reduce the gate capacitance to a minimum. The transit frequency is of special relevance for logic devices. Here, the output current due to gate switching must be large enough to control the next gate in line, i.e. sufficient current gain is needed. We will see later that $2\pi f_T$ also has great impact on the charge resolution of a RF-GFET (see chapter 5).

3.2.3.2 Maximum oscillation frequency f_{max}

Another figure of interest in a transistor is its unilateral power gain U and the associated maximum oscillation frequency f_{max} [86], which describes up to which point the transmitted power ratio is greater than 1:

$$f_{max} \simeq \frac{f_T}{2\sqrt{2\pi f_T R_g C_{gd}}} \tag{3.19}$$

The above equation is an approximated evaluation. More detailed expressions can be found in [18, 86].

There is no general rule as to which values f_T and f_{max} should have, but as a rule of thumb it is generally accepted that for RF-FETs f_{max} should be comparable to f_T [86]. Also, these two maximum frequencies should be considerably higher than the desired operating frequency [86].
It is also clear from Eq. (3.19) that in order to obtain a large f_{max} the drain-source conductance must be minimised in addition to a large transconductance.

3.2.3.3 Recent achievements in terms of f_T in GFETs and other materials

As mentioned previously, one expects $f_T \simeq f_{max}$ for good RF FETs. However, for the development of a single charge detector the transit frequency f_T is most important. A sensitive charge detection on the sub nano-second time scale (see chapter 1) calls for a $f_T \gg 1$ GHz in addition to a low current noise (see chapter 5).
Different attempts using diverse materials such as CNTs, nano wires or semiconductor hetero-structures have been made, in particular here at the Laboratoire Pierre Aigrain, where J. Chaste et al. investigated ultra-fast CNT based single charge detectors [58]. As shown in [14, 58] transit frequencies up to 50 GHz could be estimated with single nanotube nano-FETs. Higher values are possible with more conventional micro-scale Si or III-V devices: f_Ts up to 485 GHz and 628 GHz have been demonstrated for Si and InAs FETs, respectively [17] (see also table 3.2).

	graphene	*CNT*	*Si*	*III-V*
mobility ($cm^2V^{-1}s^{-1}$)	$\geq 10^6$[45]		1400	$1.5 \cdot 10^5$
max. g_m^{RF}/W (mS μm^{-1})	1.27 [99]	11.4[100]	1.3	1.62
f_T (GHz)	300 [65] estimated: 1400	50 [58]	485	628
f_{max} (GHz)	44 [65]	-	-	1100

TABLE 3.2: Overview of important properties of different materials for RF transistors. Values are measured at room temperature and according to [17] if not stated otherwise.

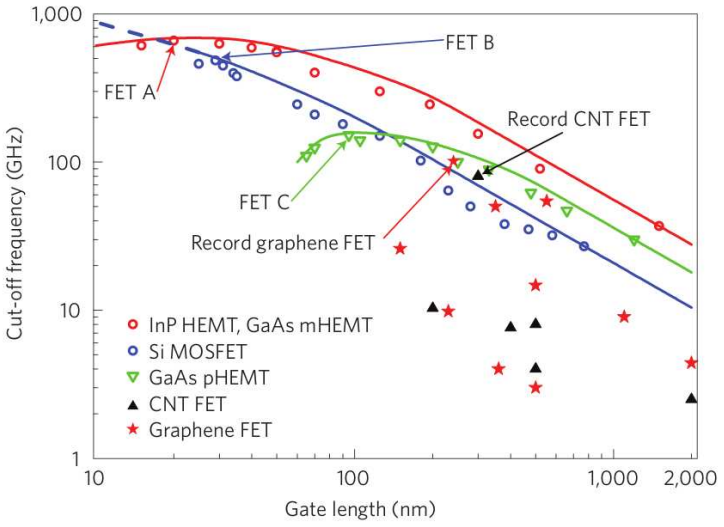

FIGURE 3.7: Cut-off frequencies for different FETs as a function of gate length. From F. Schwierz [41].

As for the case of graphene, transit frequencies of 210 GHz and 300 GHz have been reported by [101] and [102] (see Fig. 3.8). While [102] uses a self-aligned nano-wire as gate, very recently similar values of $f_T = 300$–350 GHz have been reported by researchers at IBM [65] for CVD based RF-GFETs with conventional 40 nm long gates [1]. However, the still modest values of f_{max} (see table 3.2), i.e. the low power gain, and the lack of a significant bandgap make the development of RF applications involving graphene a difficult, yet highly active subject. As we saw earlier f_{max} gives information about the power gain of a given RF-GFET. A large maximum oscillation frequency is thus necessary for the use of RF-GFETs as RF amplifiers. Great effort is invested here especially at IBM (US). On the other hand, graphene based logic applications are highly

[1] Note that these f_T values, while being most impressive, are obtained by extrapolation.

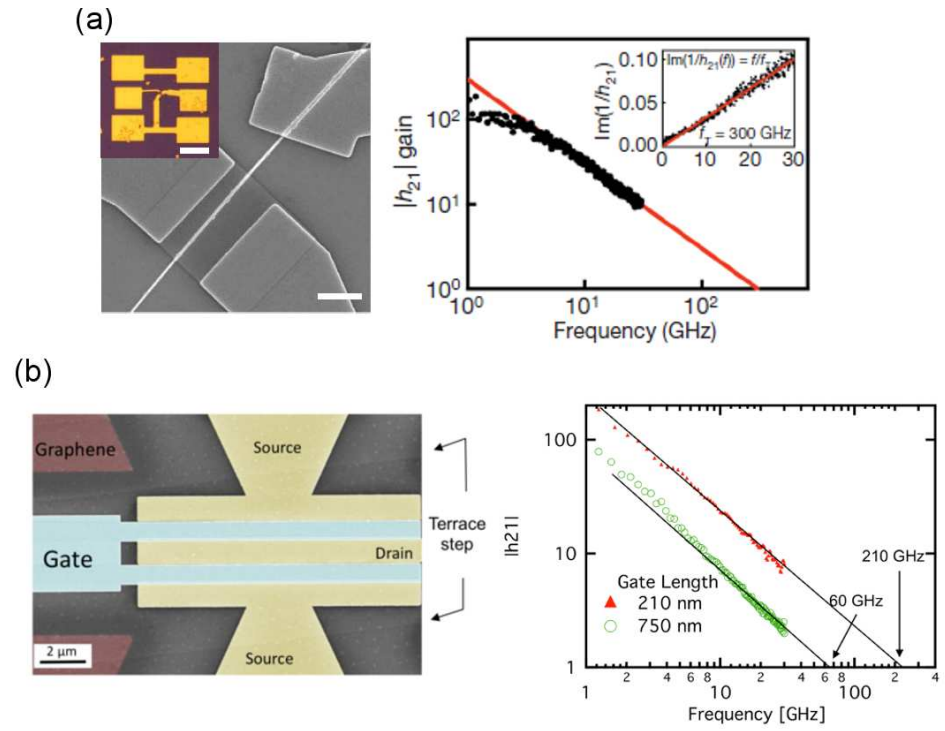

FIGURE 3.8: a) Micrograph and current gain measurement of an RF-GFET with a self-aligned nanowire as gate electrode. f_T reaches 300 GHz. From Liao et al. [102]. b) Micrograph and current gain of an RF-GFET with 40 nm long gate, entirely fabricated on a SiC terrace. The transit frequency reaches 210 GHz. From Lin et al. [101].

sought after as well. The creation of a bandgap in the otherwise linear band structure is thus another vibrant subject. Besides the creation of nano-ribbons, the use of bilayer graphene may lead to a break through in this area. An electrically tunable bandgap can be opened here and good current ON/OFF ratio can be obtained, as shown e.g. by Szafranek et al. [90–92].

In the light of the above mentioned efforts towards high-speed graphene electronics, it is not the aim of this work to improve the standard, but to investigate the possibilities of RF-GFETs as robust and sensitive charge detectors.

3.3 Experimental techniques

In the following section we will present experimental data of two RF-GFETs. They will be use exemplary, as we have studied several similar devices with similar DC and RF properties. A more systematic study of effect of scaling on the transconductance and transit frequency could not be carried out due to technical problems unresolvable at the

time. The collaboration with *Karlsruhe Institute of Technology* in Germany provides us therefore with the means to further compare the DC and high frequency behaviour of top-gated graphene FETs.

3.3.1 Device fabrication

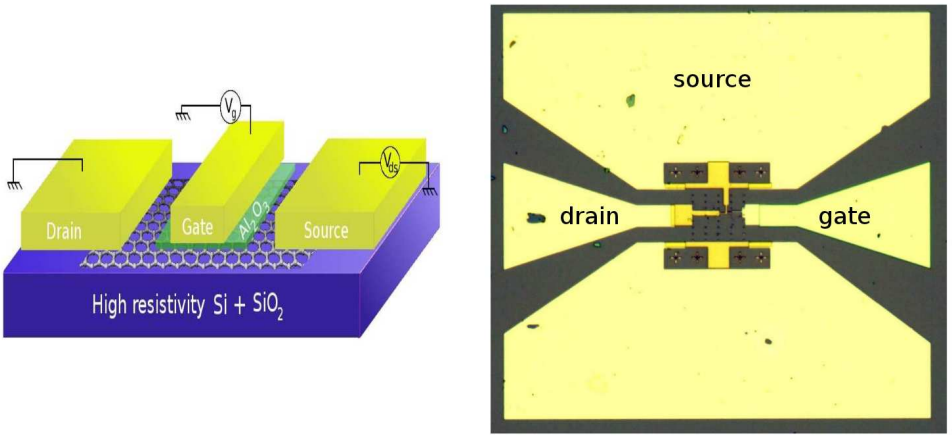

FIGURE 3.9: Left: Schematic overview of a top-gated GFET on a Si/SiO_2 substrate. Right: Micrograph of complete GFET

Our GFETs are fabricated from exfoliated graphene on two different highly resistive substrates. The main production steps follow the description in 2: After exfoliation and optical localisation of the graphene flakes the pre-contacts are patterned (see Fig. 2.2(b)). The flakes are then brought into a desirable shape by means of dry etching (see Fig. 2.2(c) and (d)). After the Pd contact electrodes are defined and metallised, a thin layer of AlOx is formed and lastly the top-gate electrode is created (golden structure in Fig. 2.2(d)). The Pd metallisation was carried out by means of e-gun evaporation in the Paris-Centre clean-rooms (Salle Blanche Paris Centre (SBPC) facility): First at the *Ecole Supérieure de Physique et de Chimie Industrielles* under the supervision of T. Kontos and later at Paris Diderot University in collaboration with the *Matériaux et Phénomènes Quantiques* group. A more detailed overview of the characteristics of the samples presented in this work can be found in table 3.3

3.3.1.1 Substrates

The substrates used for our RF-GFETs are either undoped silicon of high resistivity or sapphire wafers. This choice is due to the high-frequency measurements to be performed

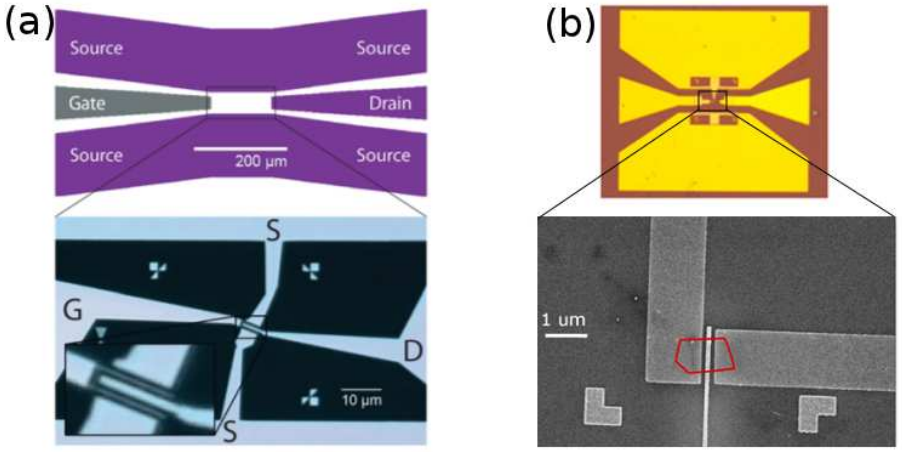

FIGURE 3.10: a) Schematic overview and micrograph of graphene-on-sapphire RF-GFET. b) Micrographs of graphene-on-SiO_2 RF-GFET. The graphene flake is indicated in red.

	sapphire RF-GFET	*Si/SiO_2 RF − GFET*	*units*
oxide/substrate thickness	330	190	μm
contacts	Ti/Al (10/120)	Pd (100)	nm
dielectric	AlO_x (25)	AlO_x (5)	nm
gate length L_g	200	110	nm
channel dimensions ($L \times W$)	1×3.7	0.3×0.9	μm × μm
gate capacitance C_g	~ 3.5	~ 2.6	fF
carrier mobility μ_c	200–500	≤ 300	$cm^2V^{-1}s^{-1}$
max. g_m^{DC}	0.22	2.3	mS μm^{-1} V^{-1}
max. g_m^{RF}	0.25	1	mS μm^{-1} V^{-1}
f_T	80	17	GHz
f_{max}	3		GHz

TABLE 3.3: Overview of RF-GFET characteristics

on the chips, which calls for an avoidance of electrical conduction via the substrate. Otherwise, charging effects in the silicon could open a pathway for the RF signal and make it more likely for the electromagnetic waves to travel through the substrate instead of the device. This was previously shown for RF carbon nanotube FETs at our lab [58]. The main properties of the two highly resistive types of substrate can be found in table 2.2. The oxide thickness of the silicon type wafer was chosen with respect to the enhanced contrast predicted for graphene [81].

Sapphire is another very good choice of substrate regarding RF applications, as it is completely insulating and devoid of trapped charges which are likely to induce extrinsic noise.. However, this property also complicates the fabrication process of sapphire based GFETs: It is necessary to provide a means of charge evacuation during e-beam lithography, due to which an Al evaporation step has to occur prior to each lithography (see also table 2.4). The Al layer is subsequently removed chemically (KOH solution).

3.3.1.2 Pd contacts

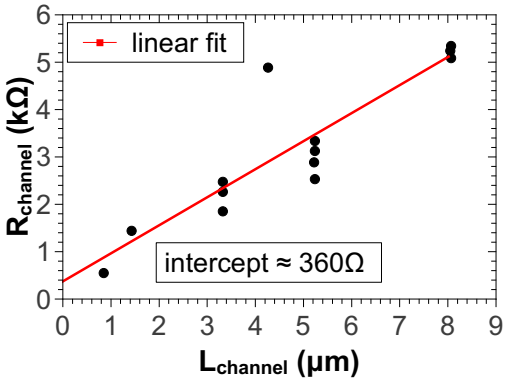

FIGURE 3.11: Estimation of contact resistance from $R_{channel}(L)$ measurements in back-gated CVD samples of channel width $W = 1$ μm [103]. The charge carrier density is of the order of $10^{13} cm^{-2}$.

As mentioned in chapter 2, we use palladium (Pd) as contact metallisation. This renders the production more intricate (Pd needing to be deposited by means of e-beam evaporation), but also has one advantage over standard Cr/Au or Ti/Au contacts: a lower interface resistance. Fig. 3.11 shows a statistical analysis of Pd contacted, back-gated GFETs of various channel lengths L made from CVD graphene (provided by A. Madouri, LPN). Extrapolating to zero channel length we find a contact resistance $R_c \simeq 360$ Ω. We conclude that compared to typical channel resistances of the order of kΩ, R_c remains negligible [103]. These measurements were carried out by Andreas Inhofer during his BSc internship at our laboratory. The charge carrier density is estimated at $n_s \simeq 10^{13}$ cm^{-2} from Hall bar measurements on similar CVD sheets performed at LPN.

3.3.1.3 Coplanar waveguide

All RF-GFETs are embedded in a coplanar waveguide, as described in subsection 2.3.3. It serves to avoid mismatch with the standard 50 Ω impedance of RF equipment and to allow a lossless propagation of electromagnetic waves. It also provides the possibility to

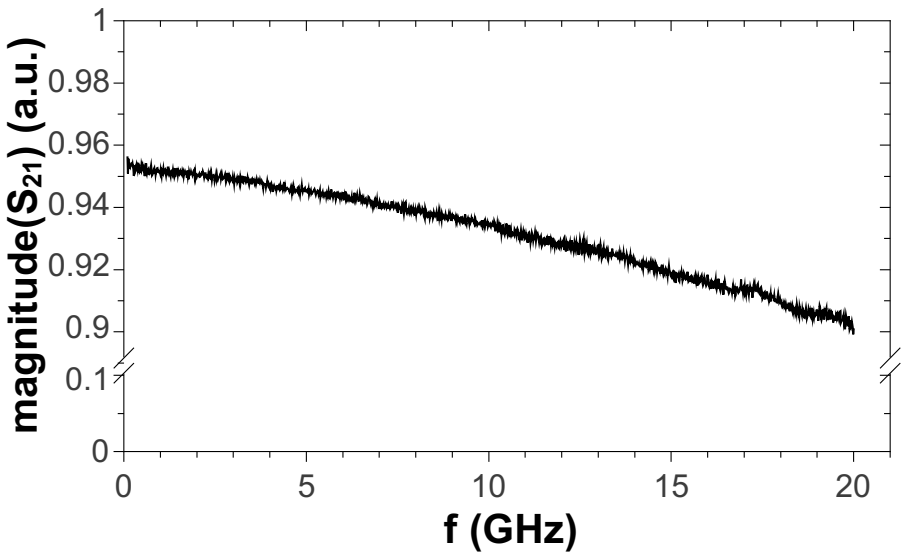

FIGURE 3.12: GHz verification of coplanar waveguide structure: Drain and gate are connected to create a through line.

establish a connection between the macroscopic probe heads and the microscopic sample contacts. Hence the progressive scaling from 400 μm appropriate for the probe heads to $\sim$ μm of the contact electrodes. We tested the quality of the structures in terms of GHz frequencies by establishing a connection between drain and gate electrode: a custom made through line. From Fig 3.12 it is clear that our waveguides are of good quality and allow a nearly lossless propagation: The magnitude of the transmitted signal (parameter S_{21}) decreases by only 6% over a frequency range of 20 GHz. This highlights again the importance of the high resistivity of our substrates for RF experiments: For a given material resistivity ρ the dielectric relaxation frequency is given by

$$f_{dr} = \frac{1}{2\pi\epsilon_0\epsilon_r\rho} \tag{3.20}$$

This is the frequency above which the free carriers in the substrate cannot follow the signal excitation any more. For a highly doped Si substrate of $\rho = 1$ mΩcm we obtain thus $f_{dr} \simeq 150THz$, whereas in the case of highly resistive ($\rho = 20$ kΩcm) substrates this frequency drops to $f_{dr} \simeq 8MHz$. Hence the advantage of high resistivity Si/SiO_2. For more details on the RF measurement techniques please refer to subsection 3.3.2 below.

3.3.1.4 Gate dielectric

The gate dielectric of our RF-GFETs is a thin layer of Al_2O_3, as mentioned previously in chapter 2. To ensure a pin-hole free dielectric we employ a multi-step process: less

than 2 nm of Al are deposited on the sample per step. This means that we can convert the Al layer to Al_2O_3 at the full layer depth by in-situ oxidation. The resulting 5–25 nm thin film is a high-κ dielectric with $\epsilon_r \simeq 7$.

3.3.2 Experimental setup

3.3.2.1 RF probe station setup

Sample characterisation at room temperature is performed on a *Cascade Summit 9000* probe station (Fig. 3.13(a) and (b)). The DC and AC voltages are supplied via a bias-T connected to each probe head. We use two *Yokogawa 7651* voltage sources to polarise the drain and gate, respectively. DC currents are measured with a *Keithley 2000* multimeter, via the voltage drop at a bias resistance (see Fig3.13(d)). The AC excitations and subsequent S-parameter measurements are performed using a *Anritsu 37369C* vector-network analyser (VNA).

DC measurements As displayed in Fig. 3.13(d), we supply a drain-source current I_{ds} to the sample by applying a bias voltage V_{bias} to the series combination of the sample and a bias resistance R_{bias}. I_{ds} and the sample resistance R_{ds} are then calculated from the voltage drop across R_{bias}, typically 4.9 kΩ. On the gate side the resistance R_{gate}, typically 3.2 MΩ, allows us to detect leak currents towards the drain and prevent dielectric break-down.

RF measurements High-frequency S-parameter characterisation is carried out in a frequency range of 0.1 GHz up to 20 GHz. The VNA's two ports are connected to the sample's source and gate electrode via the bias-Ts and probe heads. The excitation levels are kept inferior to the thermal energy of 25 meV (at $300K$) to ensure linear conditions. Typically, each data point is averaged 100 times at 1600 points per bandwidth.

3.3.2.2 Cryogenic probe station setup

We also have the possibility to carry out RF experiments at low temperatures using a *Janis* cryogenic, variable temperature probe station (see Fig. 3.13 (c)). Here, a flow of cooling agent (liquid nitrogen or helium) and a heatable chip holder allow to vary the temperature in the range $T \simeq 4.2$ K(liquid helium) to $T \simeq 400$ K in vacuum. The calibration and measuring procedures remain unchanged. Data presented in this chapter was obtained essentially on the Cascade room temperature setup, however. RF-GFET

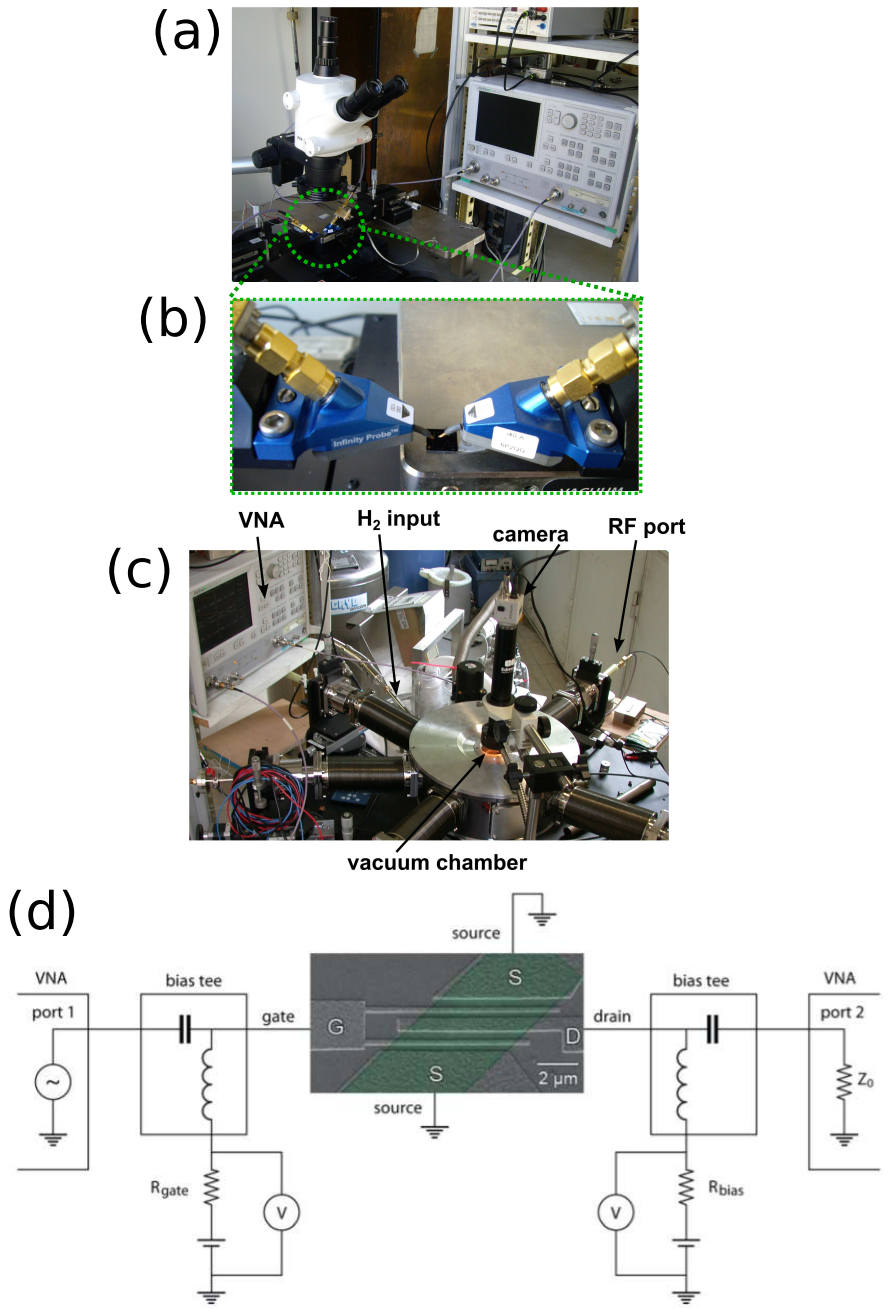

FIGURE 3.13: a) Cascade probe station. b) Cascade probe heads with a device under test. c) Janis cryogenic probe station. d) Schematic circuit diagram of the probe station setups.

measurements at low temperature are less stable and more difficult to perform and do not generate new physical insight, as could be shown in [16].

3.3.2.3 Calibration

Both probe systems have to be calibrated thoroughly in order to take into account any spurious contribution of cables, connectors and the electrical environment of the device under test (DUT) and finally subtract them from the measured signal. This is done in a first step by means of a calibration pad and secondly by means of a dummy structure.

Short-open-load-through calibration The first step of calibration consists of the subtraction of all spurious contributions up to the tips of the probe heads. To this purpose we use a standard *short-open-load-through* (SOLT) procedure for the required frequency range and at low input power (typically $-27\ \mathrm{dB_m}$).

Dummy structure In order to also eliminate any parasitic contributions on-chip, we use a dummy structure. This device is fabricated in the exact same way as the actual DUT, but leaving out the graphene layer, i.e. no graphene mediated transmission can occur. After conversion from S to Y-parameters, all parasitic on-chip contributions can be subtracted from the measured signal:

$$\begin{pmatrix} Y_{11}^{exp} & Y_{12}^{exp} \\ Y_{21}^{exp} & Y_{22}^{exp} \end{pmatrix} = \begin{pmatrix} Y_{11}^{DUT} & Y_{12}^{DUT} \\ Y_{21}^{DUT} & Y_{22}^{DUT} \end{pmatrix} + \begin{pmatrix} Y_{11}^{dummy} & Y_{12}^{dummy} \\ Y_{21}^{dummy} & Y_{22}^{dummy} \end{pmatrix} \tag{3.21}$$

The dummy subtraction is possible and easy in this case, since all parasitic contributions are in parallel to the intrinsic ones (see Fig. 3.4). This dummy-subtraction approach is especially important for the extraction of e.g. the cut-off frequency f_T or the device capacitance in chapter 4.

3.4 Results

We will now turn to the result obtained on two kinds of samples. For each type we will show data of one exemplary device: first a large, double gated graphene-on-sapphire (GoS) RF-GFET [16], then a small single gate graphene-on-SiO_2 (GoSiO) device. The graphene-on-sapphire results have been obtained in collaboration with the Karlsruhe Institute of Technology (KIT): Sample fabrication was carried out at KIT, measurements at LPA.
This section deals at first with the stationary electronic properties of the samples: I-V-characteristic, channel resistance and DC transconductance. In a second step, the RF characteristics will be presented, followed by a short conclusion of the obtained results and a description of the evolution of f_T in GFETs over the years.

3.4.1 Graphene-on-sapphire micro-transistor

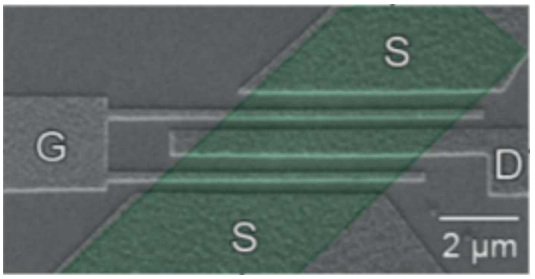

FIGURE 3.14: SEM picture of GoS sample. The graphene layer is highlighted in green.

3.4.1.1 DC characteristics

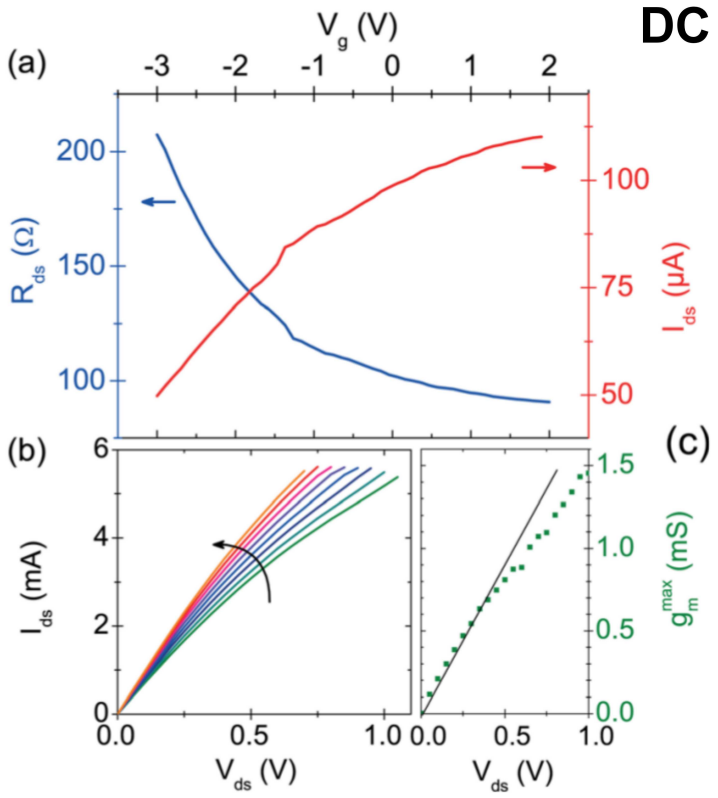

FIGURE 3.15: DC characteristics of sapphire RF-GFET. a) I_{ds} and R_{ds} as function of gate voltage, measured at $V_{ds} = 10$ mV. b) I-V characteristics for different gate voltages in the range $V_g = [-2, \ldots, -0.25]V$ in 0.25 V steps. c) Maximum DC transconductance versus drain-source voltage. The black line is a guide for the eye.

All samples are first of all characterised at continuous voltage, before being examined at high frequency. This provides information e.g. about the devices' conductance and

the position of the charge neutrality point with respect to gate voltage. Knowing the DC behaviour then helps in determining the AC experimental parameters.

I-V characteristic The $I-V$ characteristics can be found in Fig. 3.15(b) for the GoS device.

The sample exhibits a non-linear $I_{ds}(V_{ds})$ at high electric field as expected from section 3.2.1.1. Despite the high current of $\sim$ 5.5 mA through the sample, the saturation is however not complete. A lack of full saturation at high field is commonly observed in GFETs [50, 94].

In Fig. 3.15(a) we present the sample's drain-source resistance R_{ds} as a function of gate voltage V_g. Note that we use "raw" gate voltage V_g here and not V_g^{Δ}, i.e. it is not with respect to the Dirac point. As a matter of fact, the charge neutrality point was not in the range of applied gate voltage. We nevertheless can state that the sample's impedance remains low at $R_{ds} \simeq$ 100–200 Ω. We find sample GoS to be n-doped, in agreement with the expectations for Al as contact metal: The work function of aluminium is lower than carbon's with a difference of 720 meV between the two (see Fig. 3.16). Additional doping is present in GoS, which is generally a contribution of impurities at the substrate-channel interface. As a result of the strong doping, the charge neutral point could not be reached with this sample.

									$_{5}$B	$_{6}$C	$_{7}$N
									8.30	11.26	14.54
									4.45	5.0	
									0.227	1.2629	−0.07
									$_{13}$Al	$_{14}$Si	$_{15}$P
									5.98	8.15	10.55
									4.28	4.85	
									0.442	1.385	0.7464
$_{22}$Ti	$_{23}$V	$_{24}$Cr	$_{25}$Mn	$_{26}$Fe	$_{27}$Co	$_{28}$Ni	$_{29}$Cu	$_{30}$Zn	$_{31}$Ga	$_{32}$Ge	$_{33}$As
6.83	6.74	6.76	7.43	7.90	7.86	7.63	7.72	9.39	6.00	7.89	9.81
4.33	4.3	4.5	4.1	4.5	5.0	5.15	4.51	4.33	4.15	5.0	4.77
0.080	0.526	0.667	<0.005	0.164	0.662	1.157	1.228	0.093	0.31	1.23	0.81
$_{40}$Zr	$_{41}$Nb	$_{42}$Mo	$_{43}$Tc	$_{44}$Ru	$_{45}$Rh	$_{46}$Pd	$_{47}$Ag	$_{48}$Cd	$_{49}$In	$_{50}$Sn	$_{51}$Sb
6.95	6.88	7.18	7.28	7.36	7.46	8.343	7.57	8.99	5.78	7.34	8.64
4.05	4.3	4.6	4.9	4.71	4.98	5.12	4.26	4.22	4.12	4.42	4.55
0.427	0.894	0.747	0.55	1.05	1.138	0.558	1.303	0.260	0.30	1.15	1.07
$_{72}$Hf	$_{73}$Ta	$_{74}$W	$_{75}$Re	$_{76}$Os	$_{77}$Ir	$_{78}$Pt	$_{79}$Au	$_{80}$Hg	$_{81}$Tl	$_{82}$Pb	$_{83}$Bi
7.00	7.89	7.98	7.87	8.70	9.0	8.96	9.22	10.43	6.11	7.41	7.29
3.9	4.25	4.55	4.87	4.83	5.27	5.65	5.1	4.49	3.84	4.25	4.22
≥0.1	0.323	0.816	0.12	1.12	1.566	2.128	2.309	0.186	0.3	0.364	0.946

FIGURE 3.16: Extract of the periodic table of elements. First row: symbol of elements, second row: ionisation energy, third row: work functions, fourth row: electron affinities, all given in eV/atom. From [104]. Highlighted are carbon (cyan) and suitable contact metals with work functions smaller (yellow) and bigger (green) than carbon.

Charge carrier mobility We estimate charge carrier mobilities from Eq. (1.51) as $\mu_c = e^{-1}\sigma/n_s$, where the carrier density is obtained from Eq. (3.2). For the device under investigation we find $200 \leq \mu_c \leq 500$ cm^{2}V^{-1}s^{-1}.

Transconductance and voltage gain Although the Dirac point was out of reach and therefore saturation of the transconductance g_m^{DC} could not be obtained, the value reaches nevertheless a valuable maximum of $g_m^{max}/(2WV_{ds}) = 0.22$ mSμ^{-1}V^{-1}. A factor 2 intervenes here, due to the double gate design. The maximum transconductance is plotted in Fig. 3.15(c) versus drain-source voltage. It increases with bias as expected from Eq. (3.3) and 3.4. However, as pointed out before, this only remains valid in the limit of Ohmic behaviour. Beyond this regime, I_{ds} starts to saturate which in turn also means a saturation of g_m. An onset of this behaviour can be seen in Fig. 3.15(c), when data deviates from the solid line indicating the linear regime [16].
Using conductance values g_{ds} extracted from Fig. 3.15(b) (e.g. $g_{ds} \simeq 8.6$ mS and 5 mS) in conjunction with the corresponding maximum transconductance (Fig. 3.15(c), $g_m \simeq 0.9$ mS and 1.5 mS), the voltage gain (see (3.5)) reaches values $G_V = g_m/g_{ds} \simeq 0.1$–0.3. Compared to e.g. CNT-FETs, where G_V can reach values ≥ 1 [58], this remains to be improved. Conventional MOSFET amplifiers can exceed these values by orders of magnitude.

3.4.1.2 RF characteristics

In this section we will be interested in the high frequency behaviour of our graphene transistor. The focus will lie on the RF transconductance and the cut-off frequency f_T. The high frequency transconductance can be extracted from the complex admittance parameter Y_{21} as shown in section 3.2.2.4: $g_m^{RF} = \Re(Y_{21})$. The intrinsic values are obtained via the de-embedding procedure described earlier.
From the transconductance and the gate capacitance we can then estimate the cut-off frequency and compare to experimental results.

Transconductance and gain For our GoS sample, the maximum RF transconductance is displayed in Fig. 3.17(a) as a function of V_{ds}. It reaches values of the order of 1 mS at $V_g = -4.3$ V and $V_{ds} = \pm 1$ V, thus $g_m/(2WV_{ds}) \simeq 0.14$ mSμm^{-1}V^{-1}. Slightly off the presented data points we were able to reach even higher RF transconductance: $g_m^{RF,max}/W \simeq 0.25$ mS V$^{-1}\mu$m^{-1} at $V_g = -5.2$ V and $V_{ds} = -1.1$ V. Comparing to its DC counterpart,where $g_m^{DC} = 0.22$ mSμ^{-1}V^{-1}, we find g_m^{RF} to be superior to g_m^{DC}, a fact that is not commonly seen in RF-GFETs. This excellent agreement between the DC and RF behaviour could be due to the fully insulating sapphire substrate and the

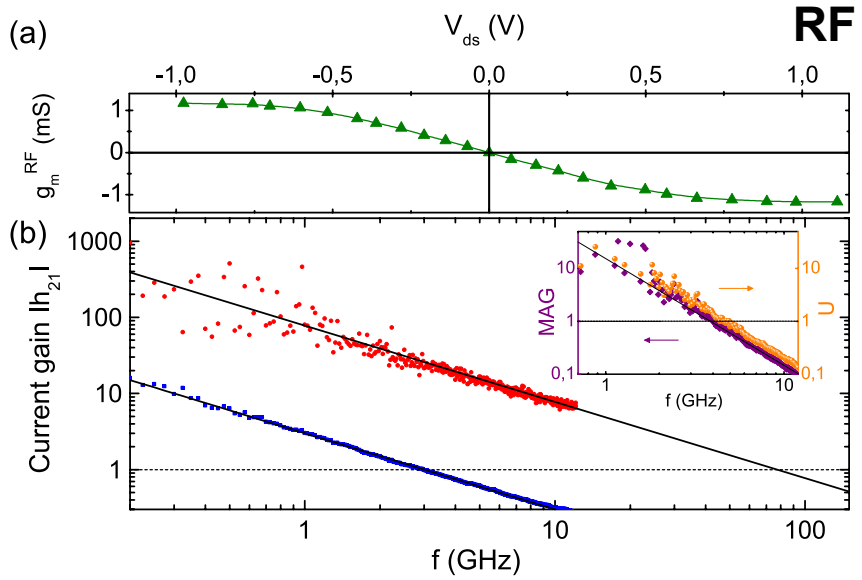

FIGURE 3.17: GHz characteristics of sapphire RF-GFET. a) RF transconductance as function of V_{ds} at $V_g = -4.3$ V. b) Current gain as function of frequency at $V_{ds} = -1.1$ V and $V_g = -5.2$ V, Blue squares show raw data with $f_T \sim 3$ GHz, red dots correspond to de-embedded data with $f_T \sim 80$ GHz. The inset displays the maximum available gain (MAG) and the unilateral power gain U as function of frequency. The solid line in (b) and the inset indicates a $1/f$ dependence.

resulting suppression of substrate losses.

The transconductance values also allow us to estimate the mobility. From Eq. (3.3) we find

$$\mu_c = g_m \frac{L_g L_{channel}}{C'_g V_{ds}} \simeq 500 \text{ cm}^2\text{V}^{-1}\text{s}^{-1} \tag{3.22}$$

at the maximum RF transconductance point and omitting minimum charge carrier density effects. C'_g is the gate capacitance per unit area (see table 3.3).

Transit frequency As mentioned previously, the cut-off frequency can be estimated from $f_T = g_m/(2\pi C_g)$. Using the above mentioned transconductance value and the geometrically estimated gate capacitance one expects $f_T \sim 70$ GHz for sample GoS at $[V_g = -5.2 \text{ V}, V_{ds} = -1.1 \text{ V}]$.

The cut-off frequency obtained experimentally is a close match to this value: $f_T^{exp} \simeq 80$ GHz. We extract it from the measured current gain $|H_{21}|$ shown in Fig. 3.17(b).

A clear $1/f$ behaviour of $|H_{21}|$ is observable and Fig. 3.17(b) additionally highlights the necessity of de-embedding for the extraction of intrinsic values: Raw data reveals a transit frequency of ~ 3 GHz, whereas we obtain the intrinsic f_T close to the estimate after de-embedding $Y^{DUT} = Y^{measured} - Y^{dummy}$.

As a short, preliminary conclusion we can state that RF-GFETs seem to make good candidates for charge detectors. It is possible to reach high transit frequencies, while keeping the device impedance low and close to the standard 50 Ω. However, for the issue of sensitive charge detection, we not only require a high f_T but also low current noise S_I. It will thus be necessary to further reduce the sample's width (for GoS $W = 3.7$ μm), since $S_I \propto I_{ds} \propto W$, in order to enhance the charge resolution δq_{rms} (see chapter 1 and beginning of this chapter) while keeping $f_T >> 1$ GHz.
Therefore, let us now turn to the smaller sample GoSiO ($W = 1$ μm), where we will study the effect of scaling on the important transistor properties and in particular on the RF-GFETs transit frequency. Actually, the graphene-on-SiO_2 RF-GFETs, for which GoSiO stands exemplary, have been fabricated measured earlier than the GoS sample. Data analysis is therefore less controlled than in the more advanced graphene-on-sapphire devices.

3.4.2 Graphene-on-SiO_2 nano-transistor

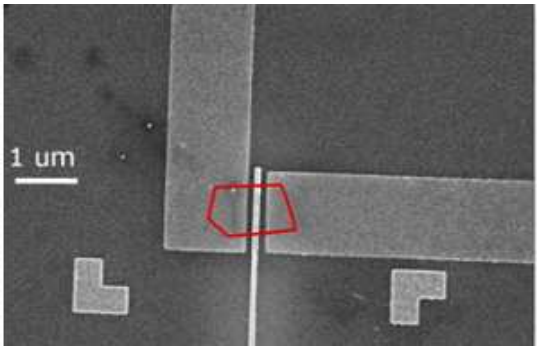

FIGURE 3.18: SEM picture of GoSiO sample. The graphene layer is highlighted in red.

As mentioned just above, this sample is of smaller lateral and channel size ($L \times W = 0.3$ μm $\times$ 0.9 μm), in addition to its smaller gate ($L_g = 110$ nm).

3.4.2.1 DC characteristics

I-V characteristic Sample GoSiO exhibits a non-linear $I_{ds}(V_{ds})$ at high bias just as previously sample GoS. In this smaller sample however, the saturation is more pronounced and we find $I_{ds} \simeq 0.8$ mA at highest applied V_{ds} (Fig. 3.19(a)). GoSiO's drain-source resistance is shown in Fig. 3.19(b) with the maximum R_{ds} about twice the value of the larger GoS sample. This is consistent with expectations from Eq. (3.3) ($I_{ds} \propto W$).

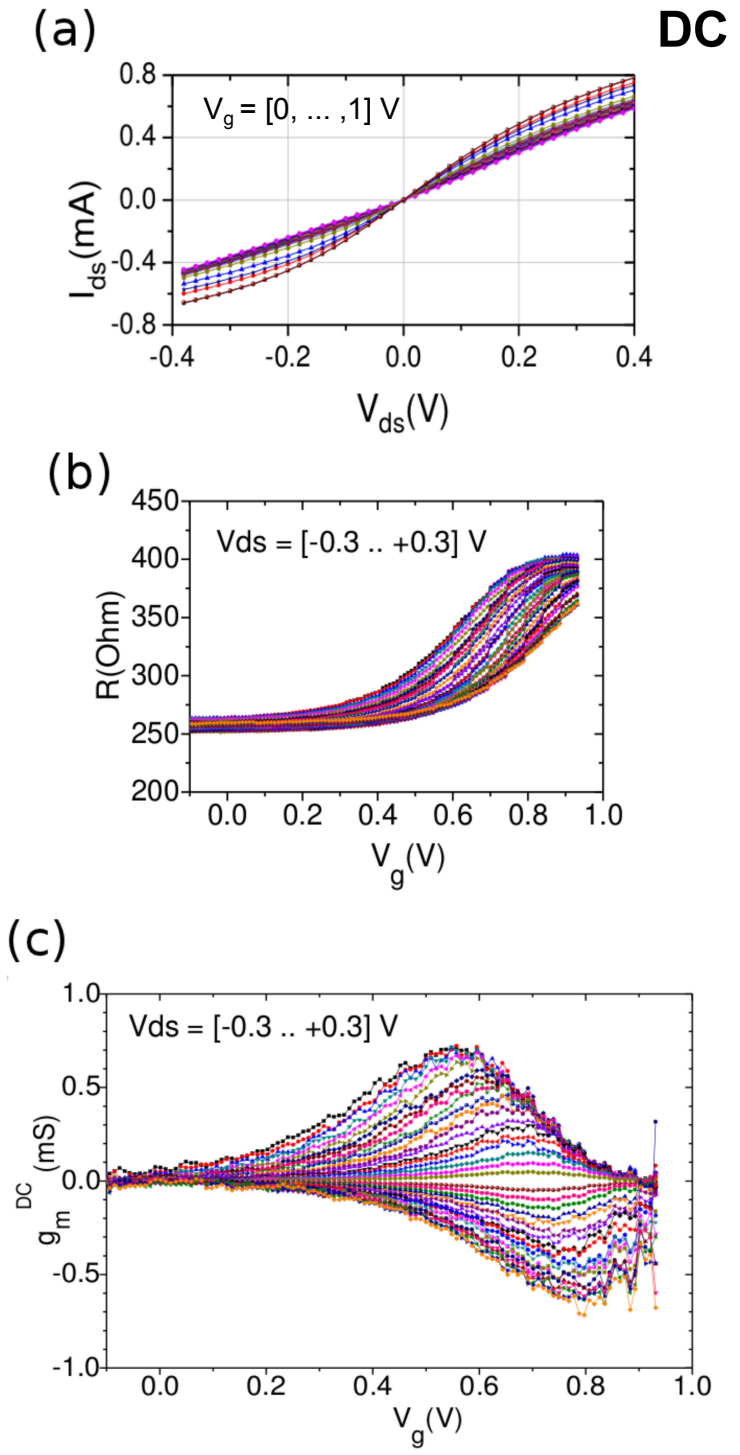

FIGURE 3.19: a) I-V characteristics of graphene-on-SiO_2-FET. Different colours correspond to different gate voltages. b) Channel resistance R_{ds} as function of gate voltage. Different colours correspond to different bias voltages. c) DC transconductance as function of gate voltage. Different colours correspond to different bias voltages.

With the Dirac point at positive gate voltage, sample GoSiO is p-doped, as expected from the Pd contacts (see Fig. 3.16). Doping remains lower than in the sapphire supported sample due to the smaller work function difference of 150 meV, hence bringing the charge neutrality point into gate reach.

Transconductance and gain Sample GoSiO exhibits a lower "raw" DC transconductance than GoS, as visible in Fig. 3.19(c), where g_m^{DC} is diplayed as a function of gate voltage for different V_{ds}. However, normalised to $g_m^{max}/(WV_{ds})$ we find that GoSiO's maximum values are one order of magnitude higher: $g_m^{max}/(WV_{ds}) = 2.3$ mSμ^{-1}V^{-1}. This high transconductance value exceeds even standard 45 nm node CMOS devices. Here maximum reported values are $g_m \simeq 0.95$ mSμm^{-1} at $V_{ds} = 1V$ in an n-channel MOSFET [105] and 0.69 mSμm^{-1} at $V_{ds} = 5V$ in an InAlN/GaN HEMT on SiC substrate [106]. Normalised with respect to applied drain-source voltage these values are considerably lower (0.95 mSμm^{-1}V^{-1} and $\simeq 0.14$ mSμm^{-1}V^{-1}) than the DC transconductance in our GoSiO sample. Again as in the sapphire supported device, g_m^{DC} increases with V_{ds} in the limit of Ohmic behaviour. Beyond we again observe a saturation of the transconductance (not shown).
Fig. 3.19(c) reveals another particular feature of GoSiO, which is the shift of g_m^{max} with respect to gate voltage for different V_{ds}. This is likely to be due to the unbalanced voltage bias across the channel length: We only apply a change in chemical potential to the drain, while keeping the source contact at ground. The working point has therefore to be chosen carefully depending on drain-source voltage.
The voltage gain is estimated as described earlier and we obtain $g_{ds} \simeq 2.8$ mS for the GoSiO sample.

Charge carrier mobility As in the previous sample we extract the carrier mobility from the DC measurements: $\mu_c \leq 300$ cm^{2}V^{-1}s^{-1} in GoSiO. This is however a quite optimistic estimate. Since we will later be interested in the RF properties, we can also approximate μ_c from the dependence of g_m on V_{ds}, revealing a much lower value:

$$\mu_c \simeq \frac{L}{WC_g'}\frac{dg_m}{dV_{ds}} \simeq 130 \text{ cm}^2\text{V}^{-1}\text{s}^{-1} \tag{3.23}$$

Here, we neglected the finite charge carrier population n_0 at the Dirac point for the sake of simplicity and used the maximum RF transconductance shown in Fig. 3.20.

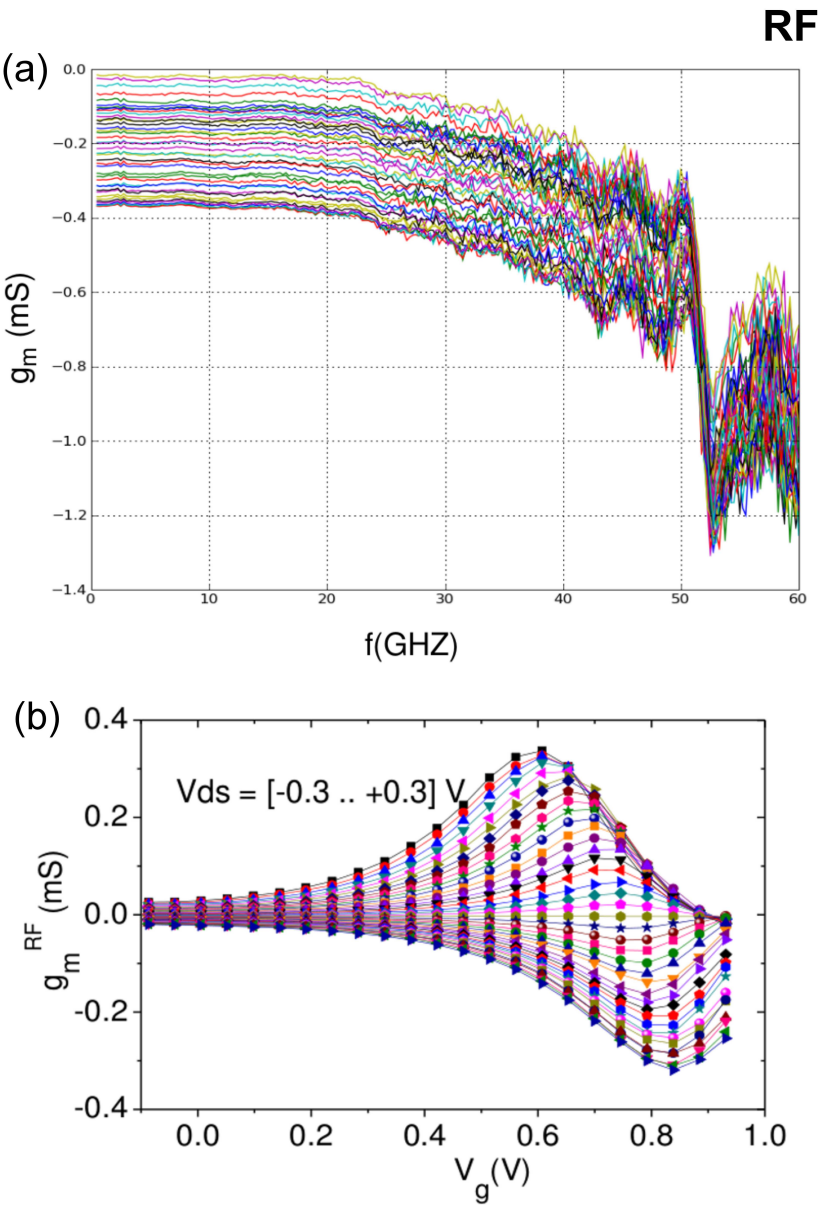

FIGURE 3.20: a) $g_m = \Re(Y_{21})$ as function of frequency. Different colours correspond to different gate voltages in the range $V_g = [0, \ldots, 1]V$ at a bias voltage $V_{ds} = -0.2V$. b) Maximum RF transconductance as function of gate voltage. Different colours correspond to different bias voltages in the range $V_{ds} = [-0.3, \ldots, 0.3]V$.

3.4.2.2 RF characteristics

Transconductance and gain Fig. 3.20(a) shows the real part of the forward admittance as a function of frequency from 0.1 to 60 GHz in sample GoSiO. These measurements were carried out at the *Institut d'Electronique de Microelectronique et de Nanotechnologie* (IEMN). The transconductance g_m^{RF} remains stable up to $f \simeq 20$ GHz

and starts to deteriorate at higher frequencies. Fig. 3.20(a) also shows the control of gate voltage over the gate sensitivity: different colours correspond to different gate voltages in the range $V_g = 0 - 1$ V at a bias voltage $V_{ds} = 0.2$ V. The constant value of g_m^{RF} at $f \leq 20$ GHz is displayed in Fig. 3.20(b) as a function of V_g for different $V_{ds} \in [-0.3, \ldots, 0.3]$V. The maximum RF transconductance is inferior to its DC counterpart, but shows the same shift of working point with respect to gate voltage. Normalised to voltage and unit area we obtain a maximum transconductance of $g_m^{RF,max} \simeq 1$ mSV$^{-1}\mu$m^{-1} for sample GoSiO, which is close to the maximum reported value for graphene at high frequencies (see table 3.2) and closing in on Si and II-V structures.

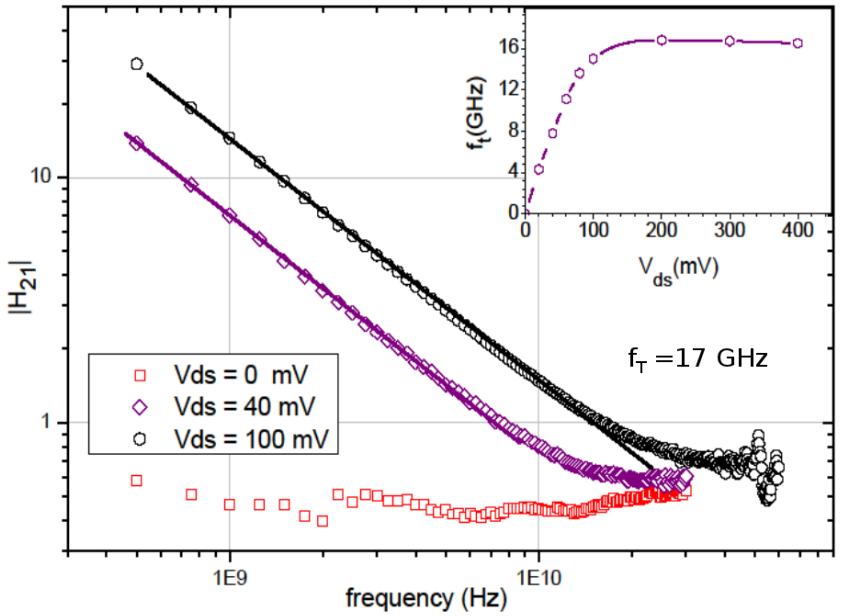

FIGURE 3.21: Current gain $|H_{21}|$ as a function of frequency in graphene-on-SiO_2-FET. Different colours correspond to different drain-source voltages. The inset shows the evolution of the transit frequency f_T with drain-source voltage.

Transit frequency The derived DC and RF properties allows us now again to give an estimate of the transit frequency of our SiO_2 supported RF-GFET. Transconductance and geometrical gate capacitance (table 3.3) suggest $f_T \sim 18.4$ GHz for sample GoSiO at the working point $[V_g = 0.6$ V$, V_{ds} = 0.3$ V$]$. The cut-off frequency we obtain experimentally from the current gain is again a close match at $f_T^{exp} \simeq 17$ GHz. Fig. 3.21 displays the evolution of $|H_{21}|$ with frequency for three drain-source voltages. As expected from Eq. (3.18) transit frequency increases with bias, ranging from virtually zero to 17 GHz. To emphasise the impact of current saturation on f_T we show the evolution of transit frequency with drain-source voltage in the inset of Fig. 3.21. The

maximum transit frequency is already reached at low bias $V_{ds} \simeq 200$ mV, i.e. a low power consumption favourable for detector applications. The maximum oscillation frequency f_{max} remained very low (not shown here), due to an unfavourable gate design entailing a significant gate access resistance. The GoSiO device was the first RF-GFET to be realised, contrary to the line of presentation in this thesis. The gates of the following devices, RF-GFETs as well as GFECs (chapter **??**), have been adapted accordingly.
Together with the inset of Fig. 3.17(b) the two plots in Fig. 3.21 point out the challenge graphene application research faces: The increase of transit and maximum oscillation frequency towards their theoretical limit. Current saturation hinders the further increase of f_T, whereas it is beneficial for f_{max} (see Eq. (3.19)). However, f_{max} remains still very low in RF-GFETs and a way has to be found to at least match both frequencies in order to build powerful graphene amplifiers. Requirements for a low noise graphene amplifier (LNGA) are a large f_{max} and low charge noise S_I, whereas logic applications would need a high f_T and well defined ON/OFF states. Band gap engineering is therefore a major concern in this section of graphene research.

3.5 Synopsis and conclusion

The statement above is of great concern for logic application and amplifier graphene research. In our case of a sub-nano second charge detector however, f_{max} and band gap are of very little importance. Our main concern is the increase of transit frequency f_T in conjunction with a low current noise S_I.
As we have found in the introductory part of this chapter, the transit frequency is proportional to transconductance g_m and inversely proportional to gate capacitance C_g. Thus, it is clear that $f_T \propto L_g^{-2}$. While this opens a clear path towards high transit frequencies by decreasing the gate length L_g, it omits the importance of graphene quality. The cut-off frequency also depends on charge carrier mobility, since $g_m \propto \mu_c$. This explains why GoSiO's transit frequency remains inferior to the one of sample GoS, although gate length differs by a factor 2. The improvement of sample quality, i.e. charge carrier mobility, remains therefore a main issue, even for charge detectors. As pointed out above, a sensitive charge detection requires not only a large transit frequency, but also a low electronic noise S_I. A route to minimising S_I is, as mentioned in the end of the GoS section, the reduction of channel width W.
Our experiments provide evidence that a good RF performance can be kept in scaled RF-GFETs. Transit frequency drops in the process but still remains in the GHz range and promising for sub-nano second charge detection. We are sure that engineering the RF-GFETs parameters and optimising the graphene sheet quality will provide fast and reliable graphene based single charge detectors. Necessary steps will include the

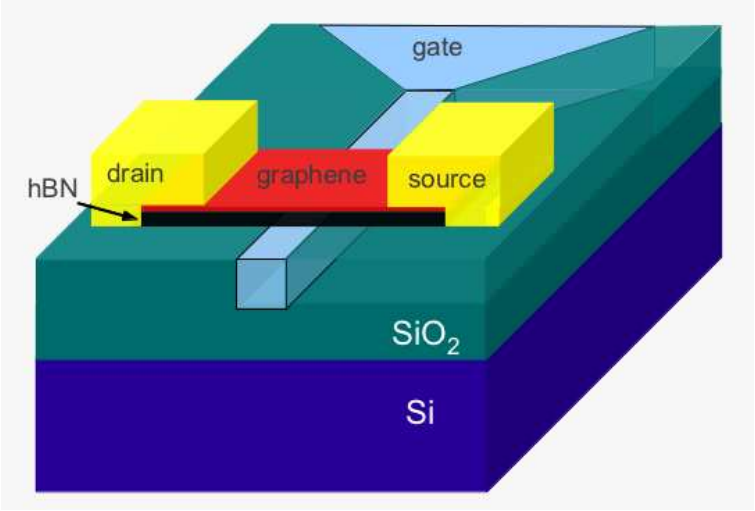

FIGURE 3.22: Design of a buried gate RF-GFET.

improvement of graphene quality, i.e. carrier mobility, for example by using hBN as a substrate. Furthermore, a buried gate design (see Fig. 3.22) where a thin hBN layer serves as dielectric and substrate at the same time, would additionally allow for thermal annealing further improving sample quality. Research into such graphene transitors is currently in progress in collaboration with the IEMN.

However, we have not pursued this avenue of direct optimisation of RF-GFETs, but we have instead investigated the physics of diffusive charge transport under the gate and the electronic noise of a graphene transistor. To this end, we will in the following chapters study two very simple structures, a graphene capacitor and a graphene resistor, that will provide direct access to diffusion and electronic noise in graphene, respectively.

Nevertheless, the results obtained in this chapter on GHz behaviour of graphene FETs will be important in the following to give a conclusive prediction of the charge sensitivity δq_{rms} of RF-GFETs.

Chapter 4

Probing elastic scattering in a graphene field-effect capacitor

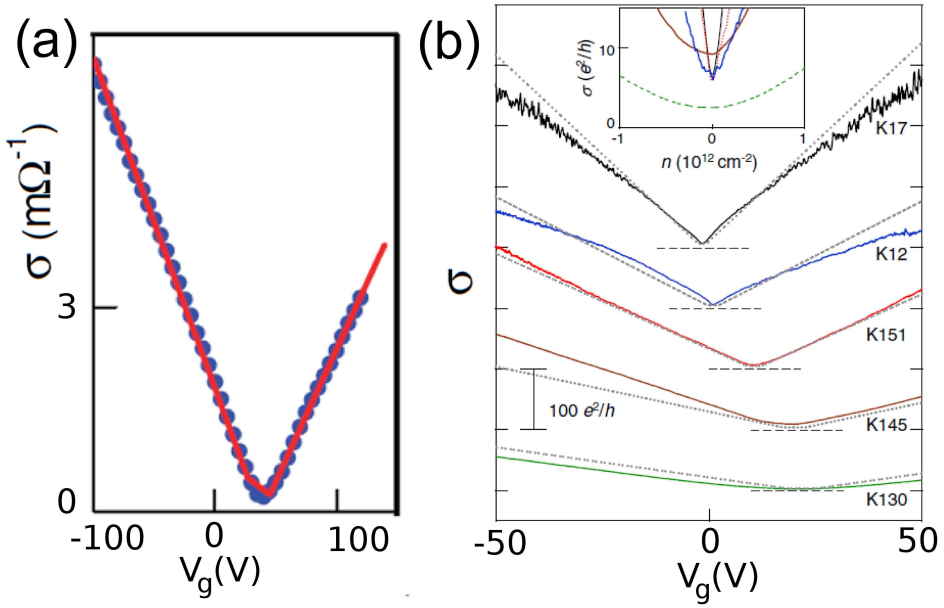

FIGURE 4.1: a) Conductivity as function of back-gate voltage V_g at $V_{ds} = 0$. From Novoselov et al. [2]. b) Conductivity as function of back-gate voltage V_g for different impurity densities. From Tan et al. [107].

Extensive attention has been given to the subject of diffusion in graphene devices in the past years. These efforts started nearly as early as 2004, when Novoselov et al. demonstrated the first graphene field-effect device. In their seminal paper [2] they presented amongst others a measurement of the conductivity σ with respect to back gate voltage V_g (see Fig. 4.1(a)) and found σ to be linearly dependent on V_g. The charge carrier density n_s is controlled capacitively in a back-gated GFET, i.e. $\sigma \propto n_s \propto V_g$. The linear

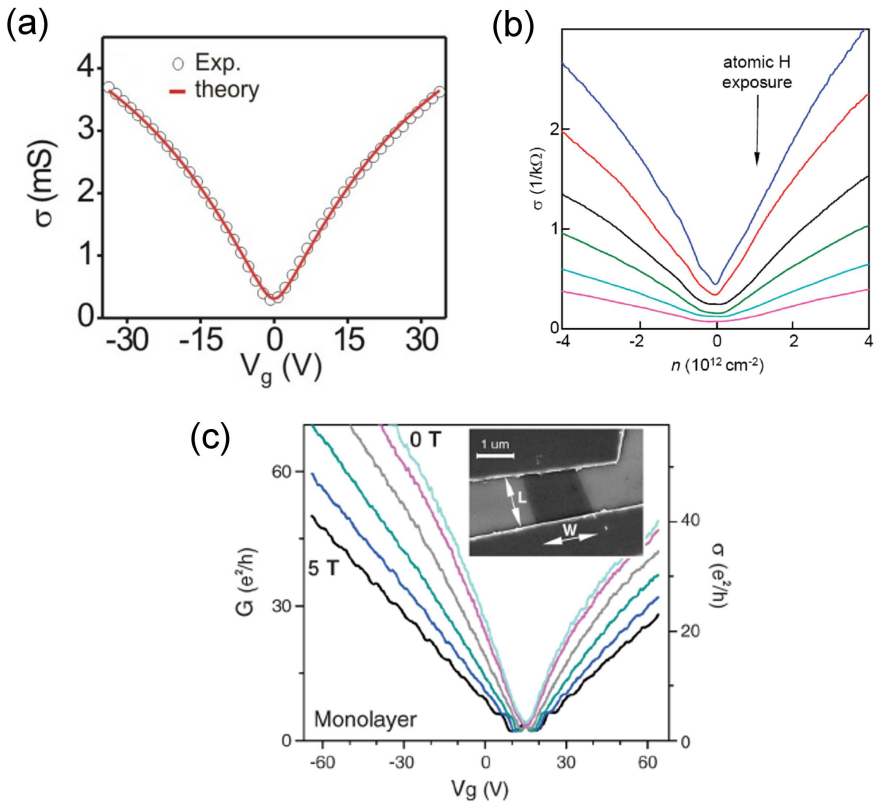

FIGURE 4.2: a) Conductivity as function of back-gate voltage V_g in a four-point measurement at zero bias and $T = 300$ K in MLG on SiO_2. The line is a theoretical calculation. From Barreiro et al. [50]. b) Conductivity as function of charge carrier density for different concentrations of hydrogen adsorbates in MLG on SiO_2. From Ni et al. [108]. c) Conductivity as function of V_g at several magnetic fields. From Monteverde et al. [109].

behaviour with respect to V_g therefore translates into a linear dependence as a function of n_s. These findings were later confirmed by different groups, as e.g. by Tan et al. [107] or Chen et al. [110]. In their experiments they varied the amount of charged impurities (substrate impurities or added potassium atoms, respectively) in a graphene flake and recorded $\sigma(n_s)$. As can be seen from Fig. 4.1(b), Tan et al.'s measurements suggest that these charged impurities are responsible for the linear dependence due to scattering of carriers on these charged centres. Chen et al. conclude from their experiments that charged impurities and their induced carrier density inhomogeneities contribute strongly to the observed $\sigma(n_s)$ behaviour. Their results also contradict early theories that favoured short range scatterers; such mechanism would give a constant conductivity. We will detail this more in 4.1.3.

More recent measurements [50, 108, 109] paint however a slightly different picture: In Figs. 4.2 the conductivity deviates from a linear dependence and enters a sub-linear regime at higher carrier concentration or gate voltage, respectively. This contradicts the

early experiments and puts the explanation of charged, long range impurities being the core diffusion mechanism in graphene into question. A short range mechanism seems more likely for MLG on SiO_2. Therefore, several different mechanism have been suggested to model diffusive electron transport in MLG, as e.g. impurities with a resonant mid-gap state (resonant scatterers) or out-of-plane corrugations of the graphene sheet, so-called ripples. Ni et al. and Monteverde et al.'s results point mainly towards the resonant scatterer scenario [108, 109]. Theoretical descriptions of said mechanisms produce a sub-linear dependence as observed in the experiments and will be presented in greater detail in section 4.1.3. As of today, no conclusive answer can however be given as to which of the mechanisms is the dominant one in MLG.
In this chapter, we will add another facet to this subject by directly measuring the diffusion coefficient D and the transport scattering time τ_{tr} in a GHz admittance study of a graphene field-effect capacitor (GFEC) [21]. Contrary to the GFET devices used in the experiments mentioned above, which have three terminals (source, drain and back-gate), our GFECs are 2-terminal objects with a close vicinity top-gate. Due to the very thin dielectric, our experiment will be particularly sensitive to changes in the density of states, which will intervene in the description of the sample capacitance. Back-gated GFETs with a typical oxide thickness of 300 nm cannot sense these changes in the DOS directly and need additional tools to determine them. The combination of two simple techniques – a graphene capacitor design on the one hand, and high frequency admittance probing on the other hand – will allow us in the end to directly access information about diffusive charge transport in graphene.

This chapter is arranged as follows: First, we will give a brief introduction to the different diffusion mechanisms discussed in literature, the quantum capacitance phenomena and other important formulas. GFEC specific fabrication details and a description of the experimental setup follow the introductory part. We will then present and discuss our experimental data and draw conclusions with respect to diffusion mechanisms.

4.1 Important concepts and formulas

In chapter 1 we have introduced a Dirac representation of the graphene Hamiltonian (Eq.(1.36)), which emphasised the importance of taking into account both sub-lattices and valleys: H is a $4x4$ matrix; the wavefunctions 4-dimensional spinors. In the limit of low energies, however, a description in terms of 2-dimensional spinors is sufficient and inter-valley coupling can be neglected.
Extending the present description of a *perfect crystal* by the introduction of disorder, one immediately recognises that several scenarios are possible. The disorder potential

can be scalar, i.e. act on the diagonals of the $4x4$, respectively $2x2$ matrix, or act as a gauge field. Another possibility is a behaviour $\propto \sigma^z$, in the case of a local non-zero carrier mass. A detailed overview can e.g. be found in [20].
Before we investigate these different sources of diffusion in more detail, let us first consider more general subjects, as for example the description of the quantum corrections to the charging of a capacitor at low DOS or the transport scattering time τ_{tr} in the Boltzmann approach.

4.1.1 Quantum capacitance - electron compressibility

An important quantity in our top-gated GFECs is the so-called *quantum capacitance* C_Q or *electron compressibility* $C_Q/e^2 \equiv dn_s/d\mu$. Both are a measure of the effect of quantum corrections to the overall capacitance, which can in turn generally be described by a series combination of geometrical capacitance C_{geo} and the afore mentioned correction C_Q. We will use both nomenclatures interchangeably, although the term *quantum capacitance* can strictly speaking only be applied in the limit of zero temperature. The *electron compressibility* describes the effect to be introduced below for finite temperatures.
Let us consider a capacitor formed by a metal gate electrode and a mesoscopic conductor, separated from the former by a thin dielectric layer. A potential difference ΔV shall be applied to the two plates. At $T = 0$ and $\Delta V = 0$ all states of both the metal plate and the quantum conductor will be filled up to the Fermi level (Fig. 4.3(a)). Due to its metal nature the gates DOS is very large, whereas the it is relatively small in the mesoscopic conductor. When applying a gate voltage $\Delta V \neq 0$ all states are shifted upwards by the amount of energy equal to the electrostatic work $e\Delta V$ (Fig. 4.3(b)), which is determined by C_{geo}. Additionally, charges are accumulated at both sides of the capacitor. In order to accommodate these charges the chemical potential μ has to change. This means additional work needs to be done on the system. Due to its large DOS the metal's chemical potential remains quasi unaffected, whereas the chemical potential changes drastically in the conductor (Fig. 4.3(c)).
Thus, we can split the applied voltage ΔV into to two contributions:

$$\Delta V = \Delta V_{el-stat} + \Delta V_{chem} \tag{4.1}$$

with

$$\Delta V_{el-stat} = \frac{\Delta q}{C_{geo}} \tag{4.2}$$

and [111]

$$\Delta V_{chem} = \frac{\Delta \mu}{e} = \frac{1}{e}\frac{d\mu}{dn_s}\Delta n_s = \frac{1}{e^2}\frac{d\mu}{dn_s}\Delta q = \frac{\Delta q}{e^2 \rho(E)} \tag{4.3}$$

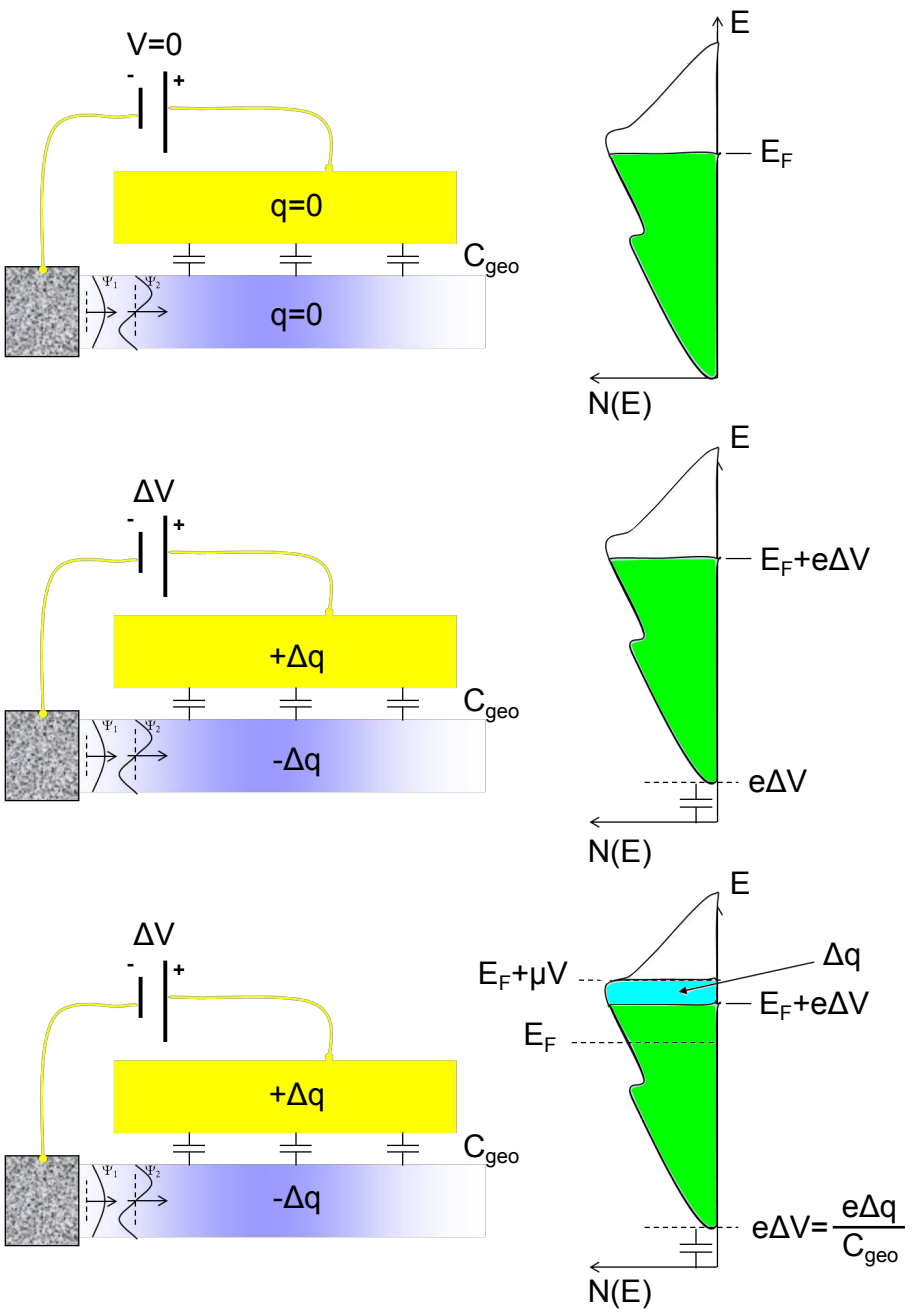

FIGURE 4.3: (a) Capacitor at $\Delta V = 0$. (b) Capacitor at $\Delta V \neq 0$: electro-static effect. (c) Capacitor at $\Delta V \neq 0$: effect on the chemical potential μ.

at zero temperature.

Combining the equations above we arrive at

$$\Delta V = \Delta q \left(\frac{1}{C_{geo}} + \frac{1}{e^2 \rho(\epsilon)} \right) \tag{4.4}$$

This looks like the series combination of two capacitances and we therefore define the so-called *quantum capacitance* depending on the density of states:

$$C_Q = e^2 \rho(\epsilon) \tag{4.5}$$

4.1.1.1 Geometrical versus quantum capacitance

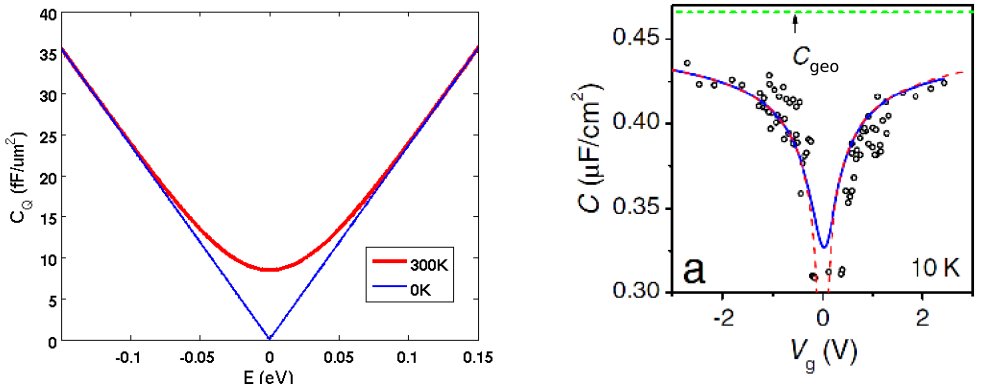

FIGURE 4.4: Left: Electron compressibility C_Q at 0 K (blue) and 300 K (red) in graphene. The finite temperature gives rise to a correction at low energy. Right: Total capacitance as a function of gate voltage. The energy dependent quantum capacitance gives rise to a dip in the vicinity of the Dirac point. Away from the CNP a plateau starts to form, due to the series combination $C_g^{-1} = C_{geo}^{-1} + C_Q^{-1}$. From Ponomarenko et al. [112].

The geometric part of the total capacitance of a graphene based device is particularly easy to calculate. It is simply a capacitor made of two plates:

$$C_{geo} = \epsilon_r \epsilon_0 \frac{L_g W_g}{d} \tag{4.6}$$

with L_g and W_g the gate length and width, respectively and d the oxide thickness. ϵ_r and ϵ_0 are the relative and absolute permittivity.

Following a model derived by D. Jena et al. [113], we will now focus on the quantum capacitance and it's behaviour for finite temperature in the graphene monolayer.

Then, one needs to take into account the Fermi-Dirac distributions for both left and right contact in the density of charge carriers (1.47). Doing so, one arrives at the charge density Q:

$$Q = e \cdot n_S = e \int_0^\infty \rho(E) \left[f(E+\mu) - f(E-\mu) \right] dE \tag{4.7}$$

$$= \int_0^\infty \frac{|E|}{(\nu_F \hbar)^2 \pi} \left[\left(e^{\frac{E+\mu}{k_B T}} + 1 \right)^{-1} - \left(e^{\frac{E-\mu}{k_B T}} + 1 \right)^{-1} \right] dE \tag{4.8}$$

Using this, one finds the electron compressibility per unit area of a graphene sheet at $T \neq 0$ (including spin and $K - K'$ degeneracy) [113]

$$C_Q = \frac{2e^2 k_B T}{\pi(\nu_F \hbar)^2} ln \left[2 + 2\cosh\left(\frac{\mu}{k_B T}\right)\right] \tag{4.9}$$

Under the condition $\mu \gg k_B T \simeq 25$ meV at $T = 300$ K this reduces to the expected DOS dependent formula of the quantum capacitance

$$C_Q \simeq \frac{2e^2}{\pi(\nu_F \hbar)^2} \mu = e^2 \rho(\epsilon_F) \tag{4.10}$$

A comparison of the zero temperature limit, i.e. the quantum capacitance, and the electron compressibility at finite temperature is shown on the left-hand side of Fig. 4.4: The blue line indicates the DOS dependent zero temperature approximation, which is linear in energy. In red we see the effect of finite temperature ($T = 300$ K) on the electron compressibility. Note the minimum of 10 fFμm^{-2} which is equivalent to an effective AlOx thickness of ~ 9 nm. This temperature effect was confirmed experimentally e.g. by [112].

4.1.2 Boltzmann equation and transport scattering time

The transport or Boltzmann equation is an approach to describing the effects of external fields, temperature gradients and scattering on the charge carriers in a conductor by looking at the local distribution of carriers $f_{\mathbf{k}}(\mathbf{r})$ and its temporal change. It states that for any given wave vector $\mathbf{k}$ and at any point in the phase space the overall change of $f_{\mathbf{k}}$ is zero [114]:

$$\left.\frac{\partial f_{\mathbf{k}}}{\partial t}\right|_{diff.} + \left.\frac{\partial f_{\mathbf{k}}}{\partial t}\right|_{field} + \left.\frac{\partial f_{\mathbf{k}}}{\partial t}\right|_{scatt.} = 0 \tag{4.11}$$

This is not the equilibrium state $f^0_{\mathbf{k}}$, where fields and temperature gradients would be absent, but the steady state. Since we are dealing with electrons, the equilibrium distribution is given by the Dirac statistic. At constant temperature, one can then calculate the conductivity of a given conductor with respect to the external electric field and intrinsic scattering contributions from its corresponding current density [114]. Within this approach it is useful to introduce the *transport scattering time* τ_{tr}, which is the average time to reverse a carriers motion. For the case of a degenerated two-dimensional gas of electrons, we then obtain [29]

$$\sigma(\epsilon) = \frac{e^2}{2} \int d\epsilon \rho(\epsilon) \nu_F^2 \tau_{tr}(\epsilon) \left(-\frac{df}{d\epsilon}\right) \tag{4.12}$$

Above, f signifies the Fermi distribution. Assuming elastic scattering processes, the *transport scattering time*[114] is given by

$$\frac{1}{\tau_{tr}} \propto \int (1 - cos\Theta)|F(\Theta)|^2 d\Omega' \tag{4.13}$$

which is the inverse average time it takes to reverse the direction of motion of a carrier. Θ is the angle between initial state $\mathbf{k}$ and final state $\mathbf{k}'$; $|F(\mathbf{k},\mathbf{k}')|^2 = |F(\Theta)|^2$ the scattering amplitude and $d\Omega'$ is a solid angle element after the scattering event in $\mathbf{k}'$ direction. For scattering on impurities in two dimensions one obtains in detail [115]

$$\frac{1}{\tau_{tr}} = \frac{2\pi}{\hbar} n_i \frac{\rho(\epsilon_F)}{4} \int \frac{d\Omega}{2\pi} (1 - cos\Theta) |\langle final|\hat{V}|initial\rangle|^2 \tag{4.14}$$

Here, n_i is the density of impurities, ρ the density of states and $\hat{V}$ the scattering potential. A special feature of graphene is the absence of backscattering already introduced in chapter 1. This is now taken into account in the transport scattering time by using

$$|\langle final|\hat{V}|initial\rangle|^2 = |\tilde{V}(\mathbf{q})|^2 cos^2\Theta = |\tilde{V}(\mathbf{q})|^2 \frac{1 + cos\Theta}{2} \tag{4.15}$$

where $\mathbf{q} = \mathbf{k}' - \mathbf{k}$ is the transferred momentum [115] between final and initial state. Since we are considering elastic scattering $k' = k = k_F$ and thus $q = 2k_F sin(\Theta/2)$. Finally, we arrive at

$$\frac{1}{\tau_{tr}} = \frac{2\pi}{\hbar} n_i \frac{\rho(\epsilon_F)}{4} \int \frac{d\Omega}{2\pi} (1 - cos\Theta) \frac{1 + cos\Theta}{2} |\tilde{V}(\mathbf{q})|^2 \tag{4.16}$$

for the transport scattering time in graphene, depending on the exact scattering potential $\tilde{V}(\mathbf{q})$ and at $k_B T \ll \epsilon_F$. It will be the aim of the following part to introduce the existing proposals for $\tilde{V}(\mathbf{q})$ in graphene.

4.1.3 Mechanisms of diffusion in graphene

We will now turn to the description of mechanisms of diffusion in a 2D monolayer graphene sheet. Several theories have been suggested to explain the linear or sub-linear dependence on charge carrier density of the conductivity $\sigma(n_s)$. They can mainly be classified into two groups, one where $\sigma \simeq$ const. and the second resulting in a linear dependence of σ on n_s. Intermediate situations are also considered in which sub-linear conductivity behaviour is obtained. Please see Fig. 4.6 for an overview of theory predictions of $\sigma(n_s)$. A more detailed discussion, including references below and further papers, can be found in the review by Abergel et al. [20].

FIGURE 4.5: a) Conductivity as function of back gate voltage in a MLG on SiO_2. From Novoselov et al. [116]. b) Conductivity as function of carrier density in a MLG on hexagonal boron nitride. From Dean et al. [44].

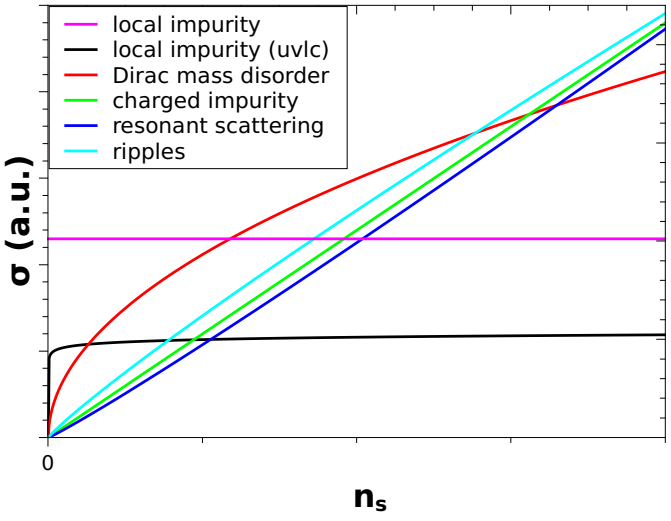

FIGURE 4.6: Conductivity as function of carrier density for different diffusion mechanisms.

Local impurity The local impurity scattering theory is the prime example for a description finally yielding $\sigma(n_s) =$ const.. Here [117], one considers uncharged impurities distributed at a density n_i in the graphene lattice. The scattering potential u can be either short or long range compared to the lattice constant. Both cases can be calculated in a self-consistent Born approximation (SCBA), which gives access to DOS or localised conductivity within a disordered system. Shon et al. find that in a 2D graphene sheet with local impurities the transport scattering time is given by

$$\frac{1}{\tau_{tr}} = \frac{\pi n_i u^2}{2\hbar}\rho(\epsilon) \tag{4.17}$$

where the graphene DOS $\rho \propto |\epsilon| \propto k_F$.
Thus, for local impurities one expects [117]

$$\tau_{tr} \propto \frac{1}{k_F} \qquad \text{and} \qquad \sigma \simeq const. \tag{4.18}$$

which is not seen experimentally.
Therefore, recent calculations [118] suggest a slightly modified behaviour. Aleiner et al. argue that due to graphene's Dirac like energy spectrum SCBA is not appropriate when calculating the effects of local impurities. Using their so-called *ultraviolet logarithmic corrections* method, they find

$$\tau_{tr} \propto \frac{ln(k_F)}{k_F} \qquad \text{and} \qquad \sigma \propto ln(n_s) \tag{4.19}$$

Charged impurity A second diffusion mechanism widely discussed in literature is the scattering of carriers on charged impurities. Nomura et al. [119] argue that a possible explanation for the enhancement of scattering at low carrier densities could be due to charged impurities in the substrate, close to the graphene sheet. The scattering potential entering in the Boltzmann integral (4.16) is then given by

$$\tilde{V}(q) = \frac{2\pi e^2}{q} \qquad \text{with} \quad q = 2k_F sin(\Theta/2) \tag{4.20}$$

Evaluation of the integral yields in the end

$$\tau_{tr}(k_F) = \frac{n_s}{n_i}\frac{4\hbar^2\nu_F}{\pi e^4} \cdot k_F^{-1} = \frac{4\hbar^2\nu_F}{n_i\pi^2 e^4} \cdot k_F \tag{4.21}$$

where we have used $n_s = \epsilon^2/(\pi\hbar^2\nu_F^2)$ and n_i is the density of impurities. Only charged defects within a Fermi wavelength from the graphene plane are of importance to the scattering, as the more remote scatterers' contribution is decreased by a factor $exp(-qd)$. Here, d is the distance to the MLG. Screened charged defects will generate the same kind of qualitative behaviour [119].
In the case of scattering on charged impurities we have thus $\tau_{tr} \propto k_F \propto \sqrt{n_s}$. Also, we found $\rho \propto \sqrt{n_s}$ in chapter 1. The Einstein relation (4.33) then gives us the conductivity signature for this kind of scattering:

$$\sigma(n_s) \propto \rho\tau_{tr} \propto n_s \tag{4.22}$$

This seems to agree with early results found in graphene on SiO_2 devices (Fig. 4.5(a)). However, a more recent study of the effect of substrate and dielectric on diffusion by Ponomarenko et al. [120] comes to the conclusion that charged impurities are not the primary scattering mechanism in graphene.

Resonant scattering Another way to recover a sub-linear behaviour of the conductivity for massless Dirac fermions is the use of a strong, resonant short-range scattering potential [121]. These so-called midgap states [122] are bound states due to vacancies, cracks or boundaries in the graphene layer whose energies can coincide with the energy of the Dirac fermions. They have to be treated by taking into account the phase shift they induce on the wave function. Doing so, one obtains

$$\tau_{tr} = \frac{k_F}{\pi \nu_F n_i} ln^2(k_F R_0) \tag{4.23}$$

for the transport scattering time. R_0 is the vacancy radius and n_i the density of impurities. The above formula is valid for a DOS $\rho \propto k_F$, i.e. at $T = 0$ or at high carrier density for samples at finite temperature. One finally recovers a sub-linear behaviour of the conductivity [123]

$$\sigma \simeq \frac{2e^2}{\pi n_i} n_s ln^2(n_s) \tag{4.24}$$

It coincides well with experimental data for graphene contaminated with H-atoms for example [121].

Ripples In theoretical descriptions exfoliated graphene is often assumed to be a perfectly smooth, planar film of carbon atoms. It is however also usually deposited on a substrate that does not necessarily exhibit the same smoothness. SiO_2 e.g. is known to have a rather rough surface owing to thermal oxidation of the silicon. Additionally, as argued in [123], the MLG will behave like a free-standing membrane during the exfoliation and deposition process. It is then subject to thermal fluctuations perpendicular to the graphene plane, which are then captured during the attachment to the substrate via Van-der-Waals forces. This can be described in the framework of a gauge-field modifying the nearest and next-nearest neighbour hopping. An estimate can be given by using a height-correlation function $g(x) = \langle\, (z(x_0+x) - z(x_0))^2 \,\rangle \propto x^{2H}$ [124, 125] of the ripples, yielding [123]

$$\sigma \propto ln^{-2}(n_s) \quad \text{for } 2H = 1 \tag{4.25}$$

and

$$\sigma \propto n_s^{2H-1} \quad \text{for } 2H > 1 \tag{4.26}$$

where H characterises the dimension of the ripples. In the case of SiO_2 substrate the height correlation function is mainly due to the surface roughness and then $2H \simeq 1$ [123, 124]. The resulting conductivity estimate does not explain the experimental data, however.

Random Dirac mass disorder Lastly there is the possibility of explaining the diffusive electronic transport in MLG by a random potential [22]. A difference in potential between the two sub-lattice sites leads to the opening of a gap and makes the carriers massive (see chapter 1, 1.1.4.1). A random distribution of impurities, e.g. adsorbants like H-atoms, can then create random gap fluctuations throughout the sample. This means the Dirac fermions locally acquire a fluctuating, non-zero mass while *on average* $m^\star = 0$ [22]. Recent theoretical and experimental work by Cheianov et al. and Haberer et al. suggests that the necessary sub-lattice symmetry-breaking can occur due to long-range ordering of adatom adsorption on graphene [126, 127].
In Ziegler's paper [22], the introduced random Dirac mass fluctuations have a Gaussian distribution with variance g around the average value 0. Intervalley scattering is ignored, i.e. only one Dirac cone is taken into account. Treating the random mass self-energy η in the framework of perturbation theory of Green's function, Ziegler finds that conductivity scales linearly with energy (see Fig. 4.7)

$$\sigma \propto \epsilon_F \propto \sqrt{n_s} \tag{4.27}$$

From the given formulas we gather that g is a dimensionless parameter in the calcula-

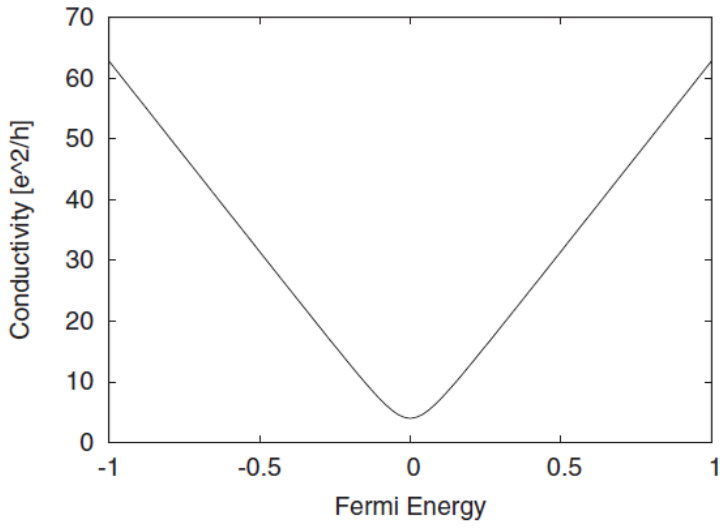

FIGURE 4.7: Conductivity as a function of chemical potential ϵ_F as result of random Dirac mass. From K. Ziegler [22]

tions, whereas the energy ϵ and the self-energy η are reduced variables in units m^{-1}. The diffusion coefficient is finally given as

$$D = \frac{g}{4\pi(\eta + \epsilon)} \simeq \frac{ge^{\pi/g}}{4\pi} \tag{4.28}$$

The last term is an approximation for small energies ϵ, where the self-consistent Green's function can be expressed as $\eta \simeq e^{-\pi/g}$, thus as dimensionless parameter. Qualitatively, we may expect the diffusion coefficient to be independent of energy and only a function of the variance of mass disorder g.
Unfortunately we are not able to resolve the apparent unit mismatches and can only speculate on the exact value of D. In order to obtain the right dimensionality $[D] = \mathrm{m^2 s^{-1}}$, we suggest that in the above limit, $\epsilon \ll \eta$, the diffusion coefficient is

$$D = 4\pi g \cdot \frac{\hbar \nu_F^2}{U} \tag{4.29}$$

with U being the magnitude of the random potential creating the Dirac mass fluctuations and $g \simeq 1$–2. Quantitatively, we predict therefore diffusion coefficients of the order of $D \simeq 300$–$600\ \mathrm{m^2 s^{-1}}$. Again we would like to stress the suggestive nature of the above formula.

Mechanism	*Scattering time*	*Conductivity*	*Reference*
Local impurity	$\tau \propto k_F^{-1}$	$\sigma \propto$ const.	[117]
Local impurity	$\tau \propto ln(k_F) k_F^{-1}$	$\sigma \propto ln(n_s)$	[118]
Dirac mass disorder	$\tau \propto$ const.	$\sigma \propto \sqrt{n_s}$	[118]
Charged impurity	$\tau \propto k_F$	$\sigma \propto n_s$	[118]
Resonant scattering	$\tau \propto k_F ln^2(k_F)$	$\sigma \propto n_s ln^2(n_s)$	[118]
Ripples	$\tau \propto k_F^{2H-1}$	$\sigma \propto n_s^{2H-1}$	[118]

TABLE 4.1: Main scattering mechanism suggested for graphene, in order of increasing carrier density dependence: Fermi wave vector dependence of transport scattering time $\tau_{tr}(k_F)$ and carrier density dependence of conductivity $\sigma(n_s)$.

Table 4.1 summarises the different suggested scattering mechanisms and their predictions for $\tau_{tr}(k_F)$ and $\sigma(n_s)$. The transport scattering time is closely related to the diffusion coefficient D, as will reveal in the following section.

4.1.3.1 Einstein relation

At thermal equilibrium two contributions enter the description of the current through a sample under bias: On the one hand electrons move due to the external electric field.

On the other hand, their movement is hindered by scattering processes. The overall current density can thus be expressed as

$$j = \sigma E - eD\frac{dn_s}{dx} \tag{4.30}$$

Here, we have introduced the diffusion coefficient D and assume only one-dimensional transport for the sake of simplicity. In the equilibrium state, the electric field and the diffusion term will cancel to give $j = 0$. Therefore, also the chemical potential $\mu = \mu_0(n_s) + eV(x)$ will be static, i.e.

$$\frac{d\mu(x)}{dx} = 0 = \frac{d\mu_0}{dn_s}\frac{dn_s}{dx} + e\frac{dV}{dx} \tag{4.31}$$

Hence we find, in conjunction with (4.30),

$$\sigma(\epsilon) = e^2 D(\epsilon)\frac{dn_s}{d\mu_0} \tag{4.32}$$

where $dn_s/d\mu_0$ is the *electron compressibility* introduced in section 4.1.1. For the zero temperature limit we can thus write down the following *Einstein relation*:

$$\sigma(\epsilon) = C_Q(\epsilon)D(\epsilon) = e^2\rho(\epsilon)\frac{\nu_F^2}{2}\tau_{tr}(\epsilon) \tag{4.33}$$

where $\rho(\epsilon)$ is the DOS, ν_F the Fermi velocity and τ_{tr} the transport scattering time introduced above. It is therefore possible to directly extract information about the diffusion if the conductivity and DOS are well known. The relation given above is in the zero temperature limit. At finite temperature C_Q has of course to be replaced by the electron compressibility and $\nu_F^2\tau_{tr}(\epsilon)/2$ by its thermal average. As mentioned at the end of the last section on scattering mechanisms, τ_{tr} is directly proportional to D due to the constant Fermi velocity in graphene.

Following this rather theoretical description of concepts, mechanisms and important formulas concerning elastic scattering in a graphene field-effect capacitor, we will now turn to the more experimentally motivated modelling of the GFEC in terms of a 1-dimensional distributed line model.

4.2 Working principle of a graphene field-effect capacitor

As mentioned in the beginning of this chapter, we will investigate the effects and mechanism of diffusion in MLG in a simple, but slightly out-of-the-ordinary device: A graphene field-effect capacitor (GFEC). Contrary to the more common back-gated GFETs, a GFEC device is a purely AC-coupled system, best suited for the studying of elastic

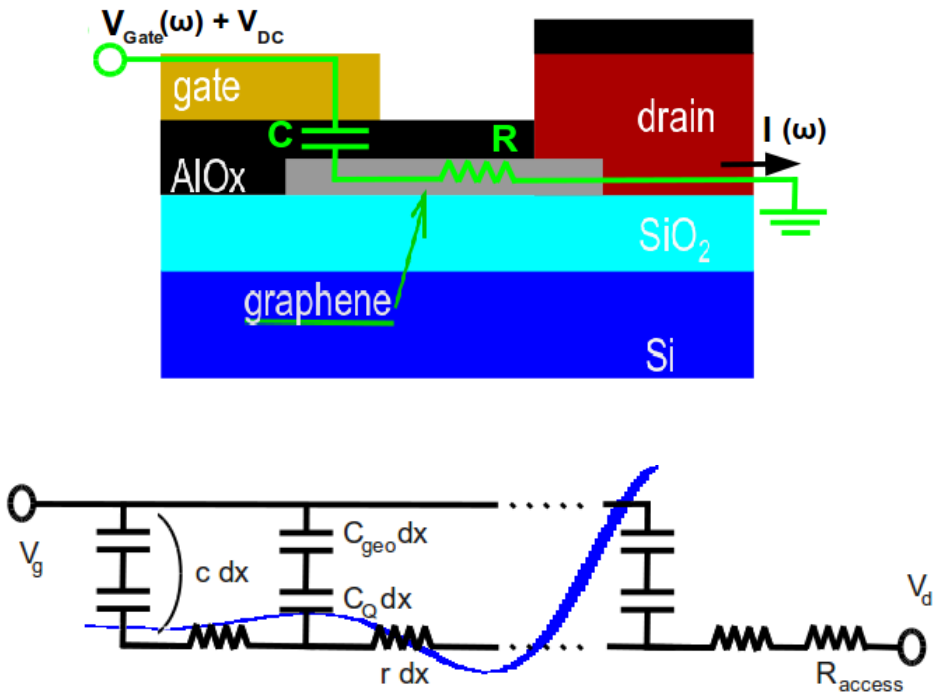

FIGURE 4.8: Top: Vertical sketch of the GFEC layout. The MLG layer is indicated in grey, gate and drain electrode in yellow and red, respectively. In green we highlight the simple RC circuit one could expect in such a system. Bottom: 1 dimensional distributed line model.

scattering as there is no dissipation from DC currents. The general device structure is displayed in Fig. 4.8: A capacitor is formed between a MLG sheet and a metal top-gate electrode, allowing only AC currents to pass. The plates are separated by a thin dielectric, whose thickness is chosen small enough for the electron compressibility C_Q to dominate the device capacitance.

It is the purpose of this section to describe the implications of the aforementioned two-terminal design and to model its high-frequency behaviour.

4.2.1 2-terminal design

The devices under test are plane-plane capacitors, the bottom plane being the graphene sheet and the upper one the top-gate. It is thus a two-terminal design where the top-gate electrode will serve two purposes at a time: It will impose the gate potential, thus change Fermi energy in the MLG and hence the name GFEC, but also probe the capacitor's RF properties via an AC signal. Such a Y-parameter experiment is thus essentially the RF equivalent of a 4-point DC measurement. In more conventional 3-terminal devices (drain, source and back-gate) used to characterise diffusion one assumes $n_s \propto V_{backgate}$.

Since there the backgate electrode (the doped silicon substrate) is usually at a distance of several hundred nano-meters from the MLG channel, quantum corrections to the density of states can be neglected in these devices. In the case of a top-gate in close vicinity to the channel, as it is the case in our samples, the electron compressibility will however play an important role (see 4.1.1). This has to be taken into account in the calculation of the charge carrier concentration and chemical potential. Here, V_g will not be directly proportional to the carrier density but rather to the chemical potential $\epsilon \propto \sqrt{n_s}$. Due to the finite oxide thickness this is actually hard to achieve in experiments, especially at high n_s. We will rather deal with a mixed chemical potential and carrier density bias scenario. However, we can deduce ϵ from the measured compressibility $C_Q(V_g)$ and express all measured quantities directly as a function of chemical potential ϵ_F using the relation

$$\epsilon_F(V_g) = e(V_g - V_{CNP}) - \int_{V_{CNP}}^{V_g} \frac{eC_Q}{C_{geo} - C_Q} dV \tag{4.34}$$

where $V_g - V_{CNP} = V_g^{\Delta}$ is the gate voltage with respect to the charge neutrality point (CNP). In general one can of course calculate the compressibility C_Q. We will however gain access to it by measuring the GFEC's admittance, as will reveal below.

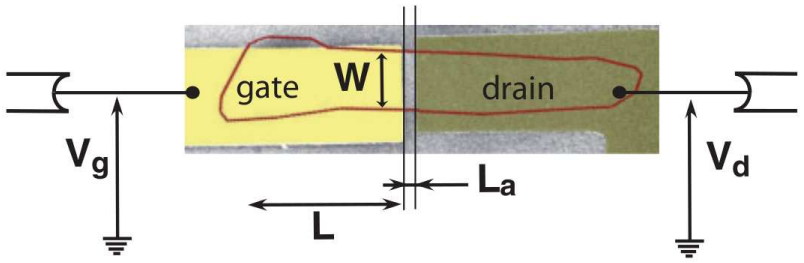

FIGURE 4.9: SEM micrograph of sample E9-Zc showing the Pd drain, the gold top-gate and the outline of the MLG flake as well as electrical environment.

4.2.2 Evanescent waves in a capacitor

An important question regarding data analysis will be how to model the GFEC correctly. Here, we will be especially interested in the RF admittance, described in the previous chapter.

From the device structure (see Fig. 4.8) one expects it to act like an RC circuit of sorts. Two possibilities of modelling the sample exist however: Either one treats resistance and capacitance as lumped, separate entities, or one assumes them to be distributed along the channel underneath the gate. The simpler view of lumped components is indicated in green in the top panel of Fig. 4.8, the 1-dimensional distributed elements model in

the lower panel.
For the RC circuit model, one calculates the admittance

$$Y(\omega) = \frac{I(\omega)}{V(\omega)} = 0 + j\omega C_g + R_{ds} C_g^2 \omega^2 + ... \tag{4.35}$$

where j signifies the imaginary unit.
The 1D line model exhibits an admittance of

$$\begin{aligned} Y(\omega) &= \frac{c\omega}{k} tanh\,(jkL) & r &= (\sigma W)^{-1} \\ k &= \sqrt{-jrc\omega} & c &= C_g W \end{aligned} \tag{4.36}$$

that can be derived as detailed in appendix B. There are three features of Eq.(4.36) worth special attention:

- At very high frequencies, $\omega \to \infty$, the complex impedance can be written as

$$Z(\omega) = Y^{-1}(\omega) \simeq (1-j)\sqrt{\frac{r}{2c\omega}} \tag{4.37}$$

  signifying an equal real and imaginary part. This behaviour with respect to frequency is reminiscent of the evanescent wave regime, where an RF wave can only penetrate a part of the transmitting conductor. In the case of our 1 dimensional model a similar effect occurs: The probing AC wave will decay rapidly with increasing frequency (highlighted in blue in Fig. 4.8(right)). Analogue to the skin effect we define a penetration depth $\delta = \sqrt{2/(rc\omega)}$. In the current limit of $\Re(Y) = \Im(Y)$, it is thus $\delta \ll L$, where L is the total length of the line.

- At low frequencies we can approximate the impedance to leading contributions by

$$Z \simeq \frac{k}{c\omega}\left(\frac{1}{jkL} + \frac{jkL}{3}\right) = \frac{L}{3}r + (j\omega Lc)^{-1} \tag{4.38}$$

  Here, $coth(x) = 1/x + x/3 - x^3/45 + ...$ was used and we find that this limit is characterised by $\delta \gg L$.

- Finally, there is the crossover of real and imaginary part of the admittance spectrum. It occurs at the crossover frequency

$$\omega_c \simeq \frac{\pi^2\sigma}{2C_g' L^2} = \frac{\pi^2\sigma}{2C_{geo}' L^2} + \frac{\pi^2 D}{2L^2} \tag{4.39}$$

which can thus also give insight into diffusion via the diffusion coefficient D (see 4.1.3.1). C'_g is the total gate capacitance and C'_{geo} the geometric capacitance per unit area, respectively. The first term is the normal cut-off of a capacitor, whereas the second term on the right-hand side is a mesoscopic correction due to the finite DOS. Note that the last term on the right-hand side $D/L^2 \simeq \omega_{Thouless}$ is also a measure of the Thouless energy often encountered in mesoscopic physics. Using typical chemical potential values of the order of $\epsilon \sim 100$ meV, we can estimate D from (4.33) and (1.46) to $D = \mu_c|\epsilon|/(2e) \sim 150$ cm^{2}s^{-1} for standard mobilities of a few thousand $cm^2V^{-1}s^{-1}$. The Thouless frequency would thus be in the vicinity of $f_{Thouless} \simeq 10$ GHz for a sample of length $L = 10$ μm.

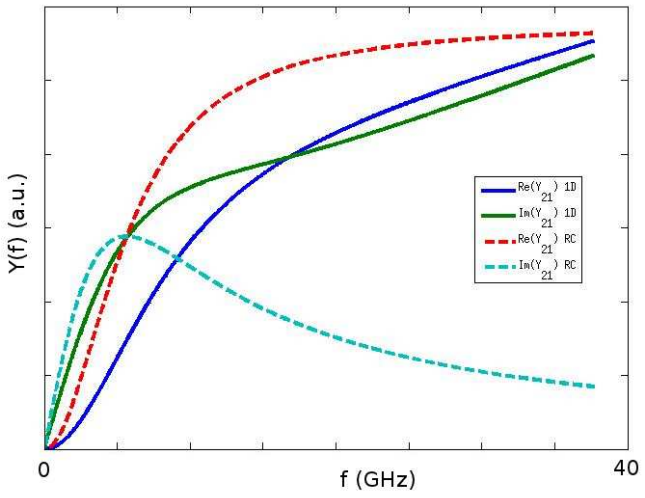

FIGURE 4.10: Real and imaginary part of the forward admittance of an RC circuit and a 1-dimensional distributed line model. Note that the plots are not necessarily to scale. The plot shows the qualitative behaviour.

Comparing the admittance of the RC circuit and 1D distributed line model (see Fig. 4.10), we note a distinct difference at high frequency: The 1D line model shows the afore mentioned decaying wave effect, whereas the lumped RC components view would result in a large gap between real and imaginary parts of Y. In the lumped components view, the imaginary part vanishes in the high frequency limit, whereas the real part will ultimately be limited by the series resistance.
Note that both models assume homogeneous transport circumstances along the width of the sample, in contrast to finite frequency effects in RF resistors, where the AC current distribution is generally two-dimensional.

To differentiate between the two possible models introduced above, it is necessary to investigate the devices at GHz frequencies: No clear discrimination is possible below the

crossing over of $\Re(Y)$ and $\Im(Y)$. Even assuming negligible conductivity at the CNP, frequencies $2\pi f \gg 0.5\pi^2 \cdot \omega_{Thouless} = 0.5\pi^2 D/L^2$ are needed. As we have estimated above this requires us to choose $f = 0.1$–10 GHz as our typical, experimental frequency range.

During data analysis we will make use of the fact that at frequencies below the crossover, conductivity σ and electron compressibility C_Q (as energy dependent part of the total gate capacitance) are readily separated into real and imaginary part of the admittance signal. We will therefore have direct access to both quantities at the same energy, imposed by the gate potential, and can deduce the desired diffusion coefficient $D(\epsilon)$ or transport scattering time τ_{tr}, respectively

4.3 Experimental techniques

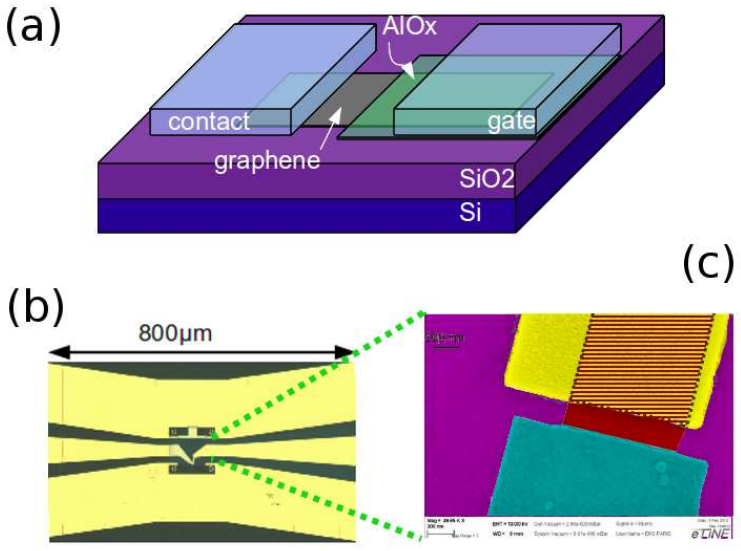

FIGURE 4.11: a) Schematic overview of graphene field-effect capacitor. b) Micrograph of complete GFEC. c) SEM micrograph of GFEC. The contact electrode is highlighted in cyan, the gate in yellow. The graphene sheet is marked in red and extends under the gate electrode, as indicated by the red diagonal stripes.

4.3.1 Device fabrication

The devices presented in this chapter were fabricated from exfoliated graphene deposited on highly resistive Si/SiO_2 substrates. Deposition, localisation and characterisation of

the graphene sheets were performed as described earlier in chapter 2. Equally, chapter 2 points out the main lines alongside which the GFEC devices were fabricated: The coplanar waveguide surrounding the MLG flakes, the annealing steps as well as contact and gate patterning. As in the FET devices, it is equally important to minimise losses due to substrate conduction. Parasitic substrate contributions can be strong at microwave frequencies and effectively shunt the capacitor signal. We therefore use Si/SiO_2 substrates with resistivity $\rho \geq 20k\Omega cm$. Also, we again use Pd for the contact metallisation in order to reduce the interface resistance and induce only small doping: Pd hole-dopes the interface region and remaining in hole-doped gate range ($V_g \leq V_{CNP}$) we can neglect the arising interface resistance [128]. Our devices will therefore be operated at hole doping. The chosen MLG flakes are tailored into a rectangular shape prior to contact patterning by means of reactive ion etching (RIE). Please refer to chapter 2 for more details. The rectangular shape greatly simplifies the calculation of the geometric capacitance between graphene and top-gate.

AlOx dielectric We use aluminium oxide (AlOx) as dielectric layer separating the capacitor plates. As detailed in chapter 3 we obtain a typical layer thickness of 8–10 nm by multiple step Al evaporation and oxidation. The relative dielectric constant of such a thin AlOx film was estimated at 7 by [58].

4.3.2 Experimental setup

4.3.2.1 Probe station setup

The characterisation of our GFECs was mainly performed at room temperature using the probe station setup previously described in chapter 3, with the difference that no DC current can flow in this device configuration. Therefore there is only need for one voltage source controlling the gate potential V_g. The small AC signal is fed into the line via bias-Ts on each side, i.e. source-drain and source-gate. The VNA can then probe the S-parameters as a function of frequency for different V_g imposed by the voltage source. Finally, the conversion to admittance parameters (see chapter 3) allows again for a precise de-embedding via a short-open-load-through calibration and a dummy structure. The parasitic contribution due to a parallel gate-drain coupling is $C^0 \simeq 1.8$ fF. The used frequency range is 0.1–16 GHz and linear response conditions are secured by probing the devices well below the thermal noise floor with an AC excitation $V_{AC} \sim 1$–10 mV. The gate range was $V_g = 0$–1 V corresponding to a chemical potential range 0–230 meV or an average electron and hole concentrations of $n_s = 2.5 \cdot 10^{11}$–$4 \cdot 10^{12}$ cm^{-2}. The non-zero starting concentration is estimated from the omnipresent charge puddles in graphene.

We will however later on assume $n_s \simeq 0$ at the CNP for simplicity. Besides the room temperature experiments we could also carry out one low temperature measurement using the Janis cryogenic probe station.

4.4 Results and discussion

We have fabricated and measured several samples of different sizes and chemical dopings. In this section, we will however concentrate on results [21] obtained on two exemplary samples: E9-Zc and C7-F. Their sizes were $L \times W \simeq 3 \times 1$ μm^2 (E9-Zc, see Fig. 4.9) and $L \times W \simeq 2 \times 0.6$ μm^2 (C7-F) with a dielectric layer of ~ 8 nm AlOx.

4.4.1 Admittance spectra

Let us first of all have a look at one of the admittance spectra recorded at an arbitrary carrier density: Fig. 4.12 shows real and imaginary part of $Y(\omega)$. At low frequency we find a linear increase of $\Im(Y)$ and nearly zero real part (highlighted in green). This corresponds to the purely capacitive response expected at low frequencies. At high frequencies, however, the spectrum shows signs of a decaying wave effect. This points to a description by the one-dimensional distributed line model introduced earlier, instead of a lumped components model. We would like to stress that the one-dimensional character of the probing AC field penetrating the capacitor should not be confused with the two-dimensional electronic diffusion probed by this AC field. The possibility to use a 1D probing field greatly simplifies the analysis of the GFEC response. In the case of a three-terminal device with source, drain and gate, the current distribution is two-dimensional making the analysis of high frequency experiments much more complicated. Last but not least we find the crossover frequency ω_c as pointed out earlier. For sample E9-Zc it is plotted in Fig. 4.14. The correction $0.5\pi^2 D/L^2$ to the cut-off frequency $0.5\pi^2\sigma/(C'_{geo}L^2)$ of a capacitor dominates at the CNP and at low temperature. There, the conductivity is at its lowest value σ_{min} and close to zero for experimental considerations. It can hence be neglected in terms of ω_c. Under these conditions ω_c becomes another direct measure of the diffusion coefficient D, which is an example of a mesoscopic effect (the Thouless energy $\hbar D/L^2$) showing up in a macroscopic measurement (the cut-off frequency of a capacitor). For sample E9-Zc we find $\omega_c/2\pi \simeq 3.1$ GHz and therefore have a first estimate of the diffusion constant: $D \simeq 350$ cm^{2}s^{-1}. This is of course only a rough estimate as the conductivity never completely vanishes in graphene. However it shows that even at charge neutrality the cut-off frequency stays finite and above the value expected for σ_{min}; the inclusion of the Thouless frequency D/L^2 in ω_c protects it from vanishing at the CNP.

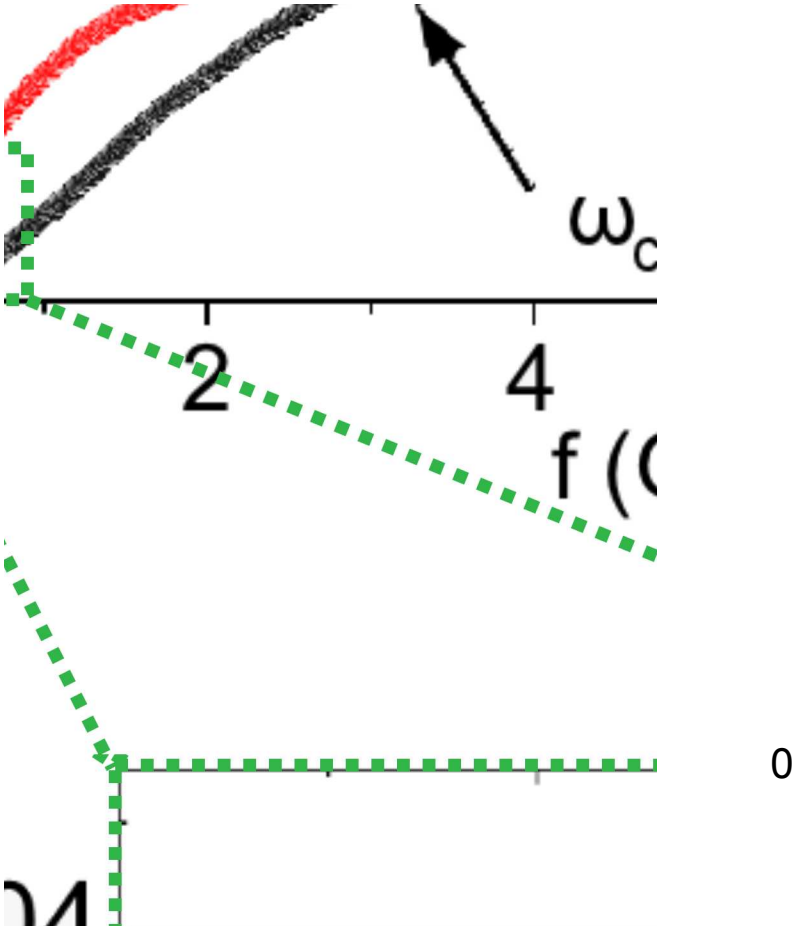

FIGURE 4.12: Admittance of graphene GFEC as function of frequency at arbitrary carrier concentration. The highlighted regions show the low and high frequency behaviour and the crossover of real and imaginary part at ω_c. These observations justify the use of the 1D distributed line model.

Fig. 4.13 displays three admittance spectra for different carrier densities in sample E9-Zc: At the CNP (panel a), at medium (panel b) and at higher carrier concentration (panel c). The low frequency development (4.38) of the forward admittance of the 1D line model

$$Y(V_g) \simeq \left(\frac{L}{3} r(V_g) - \frac{j}{\omega L c(V_g)} \right)^{-1} \tag{4.40}$$

allows us to extract conductivity and capacitance values separately at each imposed gate voltage (see Figs. 4.16 and 4.17): real and imaginary part of $Y(\omega)$ are recorded separately and contain only σ and C_g, respectively. The requirements to access information about the diffusion via the *Einstein relation* (4.33) are therefore fulfilled.

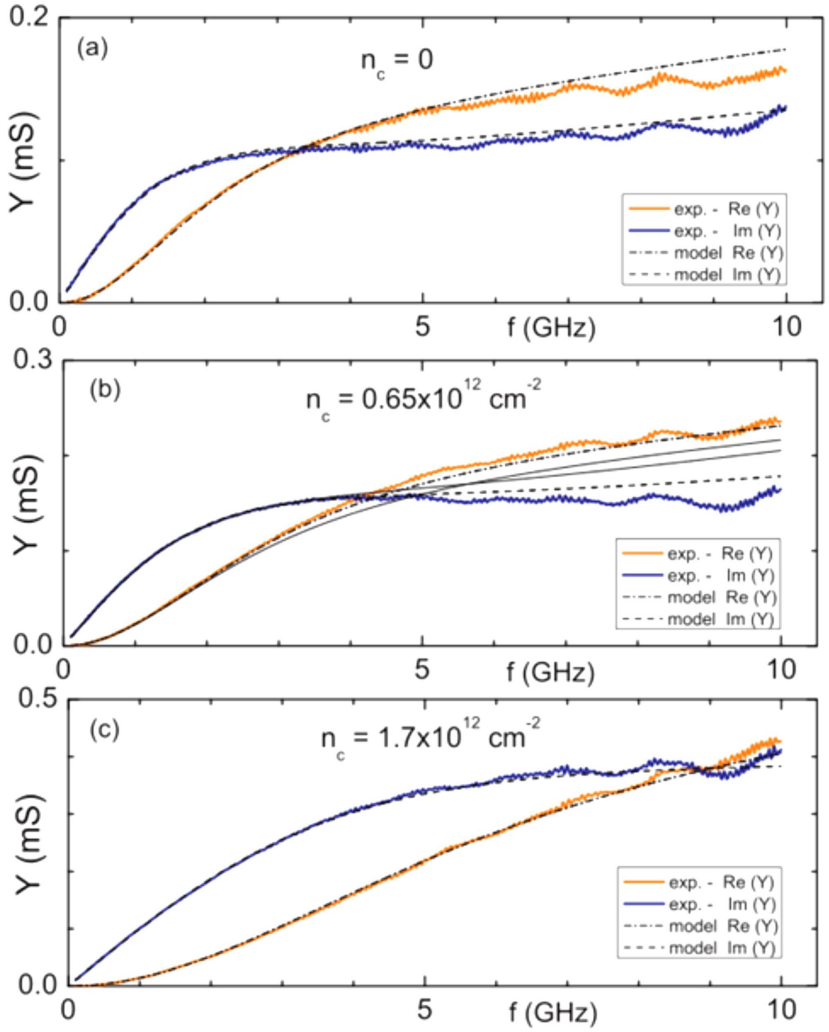

FIGURE 4.13: Admittance spectra of sample E9-Zc as function of frequency for three different carrier densities. The spectra are accurately fitted using the 1D distributed line model (dashed black lines) and an access resistance $R_a = 0.15R_g$. Omitting R_a, one obtains a slight mismatch of the fit at high frequencies as indicated by the solid lines in panel (b).

Although found at low frequencies, the full Y-spectra can be reproduced in good agreement by plugging the extracted values $\sigma(V_g)$ and $C_g(V_g) = \left(C_{geo}^{-1} + C_Q^{-1}(V_g)\right)^{-1}$ into the complete formula (4.36). A minor disagreement still occurs (solid lines in Fig. 4.13(b)) especially at high frequencies, which can be explained by taking into account an access resistance R_a comprising both interface resistance and the sheet resistance of the ungated graphene. We estimate $R_a \simeq 0.15R_g$. Sample C7-F exhibits similar behaviour with a higher cut-off partly due to the smaller gate length (Figs. 4.15). Also, the diffusive correction to ω_c is much higher, shifting the crossover point beyond the investigated frequency range of 0.1–15 GHz.

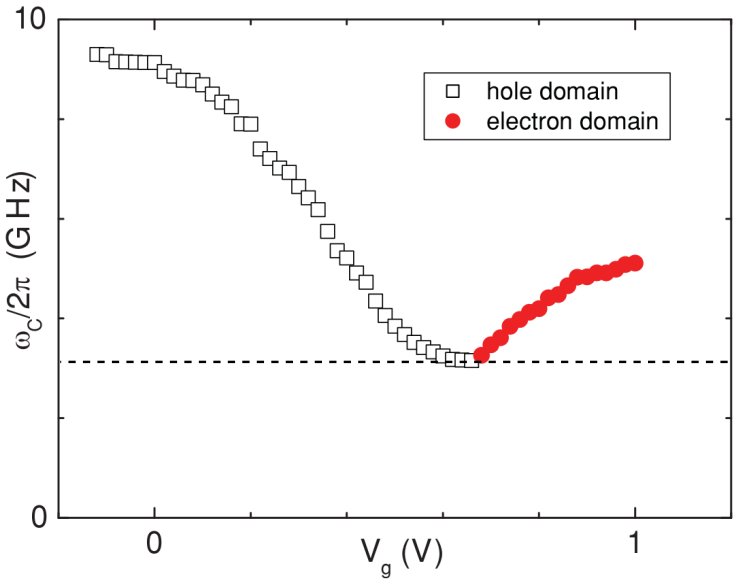

FIGURE 4.14: Gate voltage dependence of the crossover frequency $\omega_c/2\pi$ of sample E9-Zc estimated from the crossing of real and imaginary part of the admittance spectra Y.

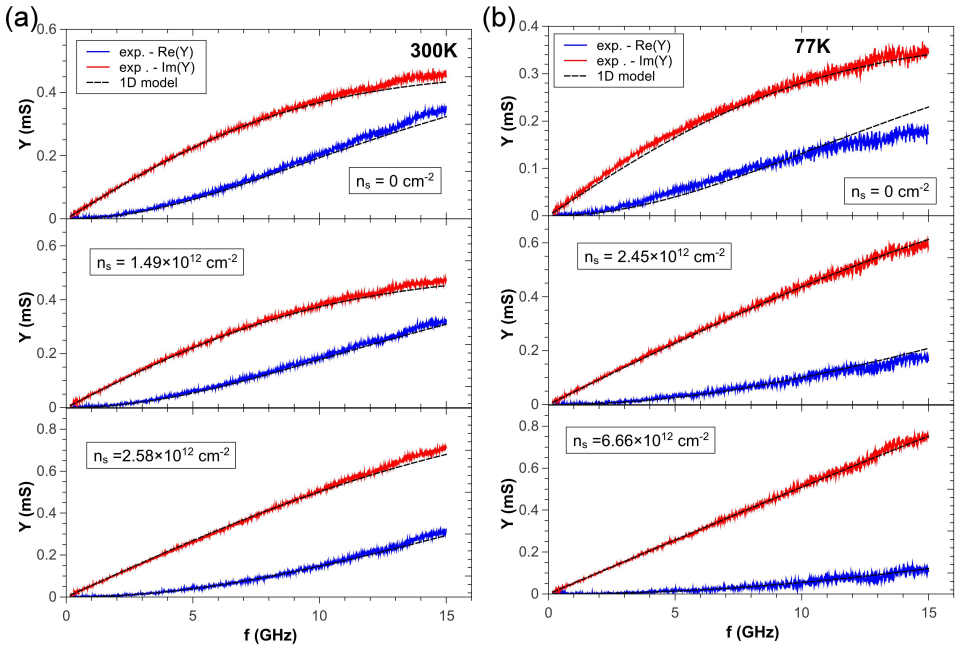

FIGURE 4.15: Admittance spectra of sample C7-F as function of frequency for different carrier densities. a) At room temperature (300 K). b) At low temperature (77 K).

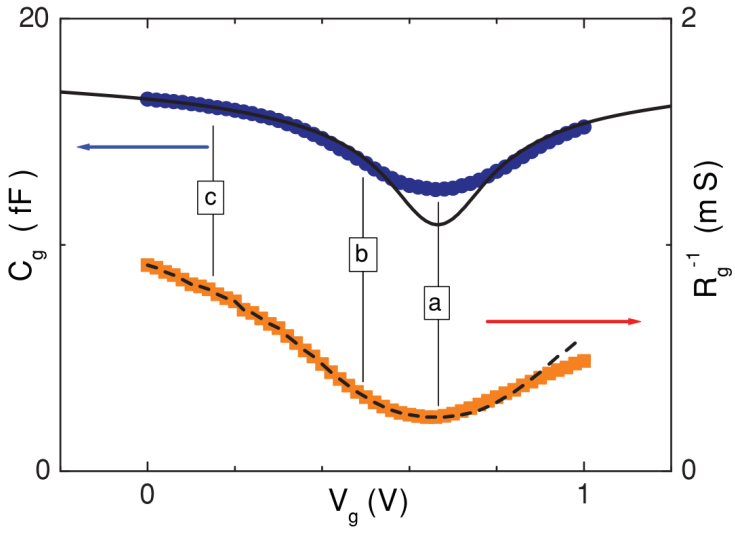

FIGURE 4.16: Gate capacitance C_g and charge relaxation conductance R_g^{-1} of sample E9-Zc as function of top-gate voltage V_g. The values are extracted from the low frequency fits to the corresponding admittance spectra. Labels (a), (b) and (c) refer to the panels in Fig. 4.13, i.e. to the charge carrier densities 0, 0.65, and 1.7×10^{12} cm^{-2}. The solid line is a fit to the capacitance using Eq.(4.9) and $C_{geo} = 19.2$ fF. The dashed line is a guide for the eye representing an electron-hole symmetric resistance fitted to the hole values.

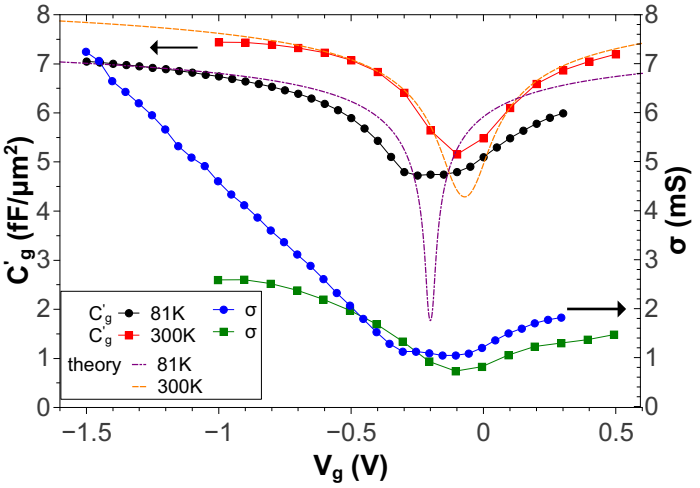

FIGURE 4.17: Gate capacitance C_g per unit area and charge relaxation conductivity σ of sample C7-F as function of top-gate voltage V_g for $T = 300$ K and 81 K. The values are extracted from the low frequency fits to the corresponding admittance spectra. The dashed lines are fits to the capacitance using the series combination of C_{geo} and C_Q.

4.4.2 Conductivity and gate capacitance

From the fits to the full sets of Y-spectra we obtain the total gate capacitance C_g and sample conductance R_g^{-1} as a function of gate voltage. Both are shown in Fig. 4.16 for sample E9-Zc which was measured at room temperature. We identify $V_g = 0.67$ V as

the charge neutrality point from the broad minimum both C_g and R_g^{-1} exhibit there. In rough agreement with the work function difference for graphene and Pd (see table 3.16) E9-Zc is p-doped; there seems to be additional chemical doping present, since the shift of 600 meV cannot be completely accounted for by the Pd contact. The dashed line in Fig. 4.16 indicates the expected resistance in an electron-hole symmetric scenario. The measured R_g^{-1} deviates from the expectation at high electron concentration, which we assign to the formation of a p-n junction in the access region (the contact and ungated graphene). It is therefore favourable to work in the p-doped region of gate voltages and we shall focus on this part of the admittance set in the following. At large hole density the fit to the capacitance data using the series combination $C_g^{-1} = C_{geo}^{-1} + C_Q^{-1}$ allows an accurate determination of the geometrical capacitance: $C'_{geo} = 6.4 \pm 0.5$ fFμm^{-2} in sample E9-Zc and $C'_{geo} = 8.3 \pm 0.5$ fFμm^{-2} in C7-F (see Fig. 4.17). This is in agreement with the rough estimate from geometry $C'_{geo} = \epsilon_0 \epsilon_r t_{ox}^{-1} \simeq 7$ fFμm^{-2} for an oxide thickness $t_{ox} \simeq 8$ nm. The small mismatch in geometrical capacitance between room and low temperature experiment of C7-F displayed in Fig. 4.17, is attributed to a small variation in the de-embedding.

Sample C7-F was measured at room and liquid nitrogen temperature using both the

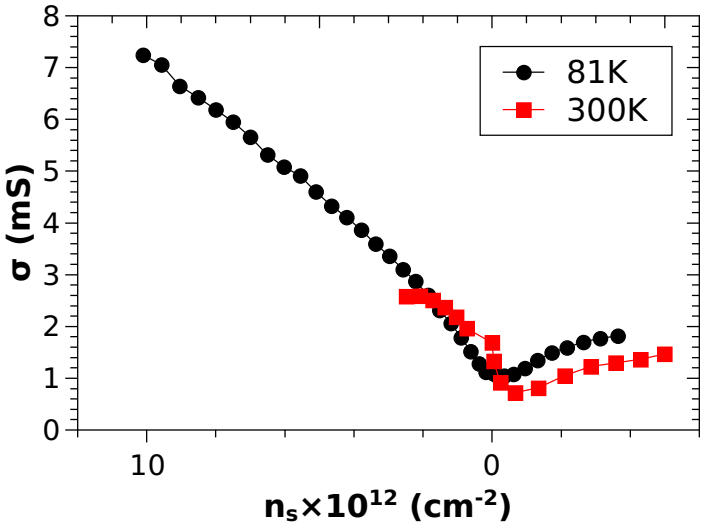

FIGURE 4.18: Conductivity as a function of carrier density in sample C7-F at $T = 300$ K and 81 K.

Cascade (300 K) and Janis (300 K and 81 K) probe station. The spectra shown in Fig. 4.15 were obtained on the latter. Spectra for the Cascade measurements are very similar and not shown here. Despite the Pd contact, sample C7-F is slightly n-doped as can be seen from Fig. 4.17: the CNP is estimated at $V_g = -0.25$ V and -0.4 V at 300 K and 81 K, respectively. The measurements were performed successively without changes to the environment other than temperature. Decreasing the temperature has thus changed

the doping further away from undoped, pristine graphene. Additionally, there is no improvement in terms of electron compressibility, which would be expected to create a much sharper dip of the total capacitance in the vicinity of the CNP, due to the stronger effect of the small graphene DOS. While the room temperature capacitance is reproduced with good accuracy up to a small window around the CNP, the low temperature data deviates from theoretical expectations not only close to the CNP but also in the electron doped regime. At low carrier densities, the difference between data and theory is likely be due to inhomogeneities in the chemical doping in the MLG sheet. Unfortunately, this problem could not be resolved by cooling the device to liquid nitrogen temperature.

Carrier mobility A slight improvement can nevertheless be found in the hole mobility of C7-F when cooling the sample. It then yields $\mu_c \simeq 5600$ cm^{2}V$^{-1}s^{-1}$ at 81 K as compared to $\simeq 4600$ cm^{2}V$^{-1}s^{-1}$ at 300 K at a typical carrier density $n_s \simeq 10^{12}$ cm^{-2}. We will thus expect to find also an improvement in terms of diffusion in sample C7-F. Sample E9-Zc was of similar quality with $\simeq 3100$ cm^{2}V$^{-1}s^{-1}$ at 300 K and $n_s \simeq 10^{12}$ cm^{-2}. One has to keep in mind that the usual assumption of a linear proportionality $n_s \propto V_{backgate}$ is not valid here, due to the close vicinity top-gate geometry of our GFECs. To obtain the charge carrier concentration we must now rather use Eq.(4.34) to calculate the energy $\epsilon(V_g)$ and then find $n_s \propto \epsilon(V_g)^2$ (see Eq.(1.47)):

$$n_s = \frac{1}{\pi(\hbar\nu_F)^2}\left(eV_g^{\Delta} - \int_{V_{CNP}}^{V_g} \frac{eC_Q}{C_{geo} - C_Q} dV\right)^2 \tag{4.41}$$

Electron compressibility In the same way as for the carrier density, we can now also express the experimental $C_g(V_g)$ as a function of the chemical potential ϵ_F. Of special interest here is the electron compressibility $C_Q(\epsilon_F)$ extracted from the total capacitance, plotted in Figs. 4.19 (Janis setup) and 4.20 (Cascade setup). The room temperature results are well explained by the theoretical estimate from Eq.(4.9). Particularly reassuring is the fact that all three 300 K measurements closely match, as C_Q only depends on ϵ and T and not on sample geometry or other device characteristics. Deviations from theory are observed in both samples and setups. They are a result of experimental uncertainties and disorder contributions. A quantitative estimate of the latter was not possible due to the uncertainties in the experimental data.

In principle, the precision of the electron compressibility measurements should enhance with increasing sample size (more accurate de-embedding), thinner gate oxide (reduced electrostatic gate impedance) and lower temperatures (larger contrast in C_Q). We have tested the latter, as pointed out beforehand, on sample C7-F. Further reduction of the dielectric thickness was not a suitable option, due to the possibility of pin-hole formation in the AlOx; sample sizes are depending on successful exfoliation of MLG only. As

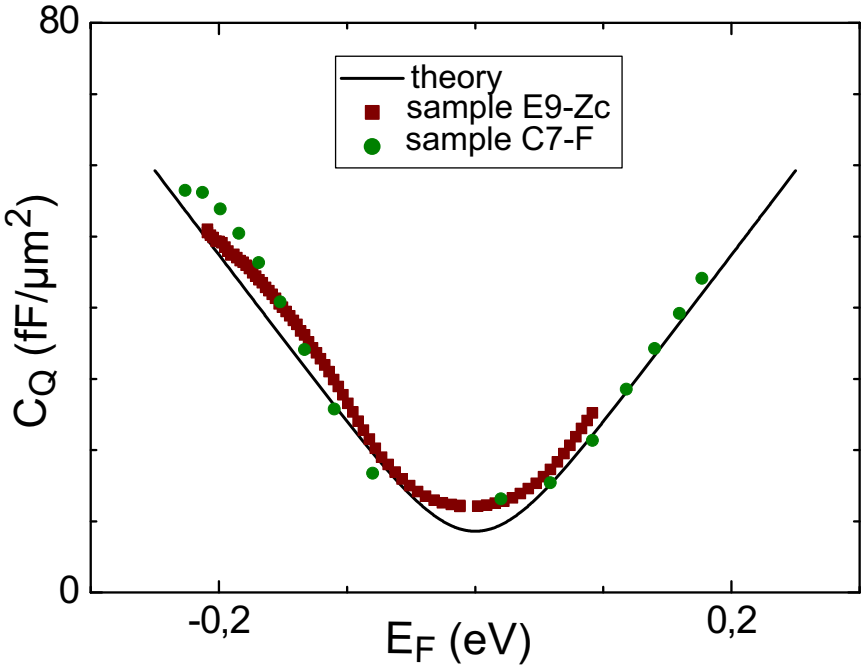

FIGURE 4.19: Electron compressibility as a function of energy at $T = 300$ K (Cascade setup). The solid line is the theoretical expectation for $C_Q(\epsilon, 300\text{K})$ (Eq.(4.9)).

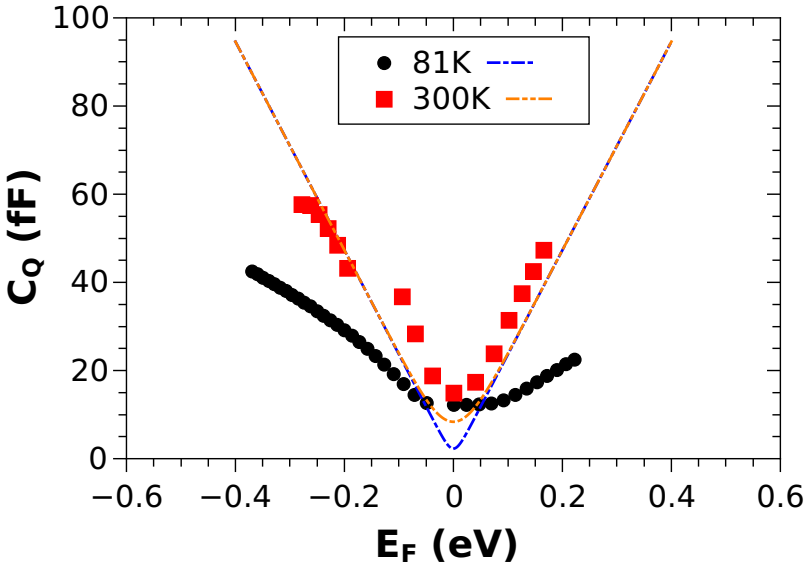

FIGURE 4.20: Electron compressibility as a function of energy at $T = 300$ K and 81 K in sample C7-F (Janis setup). The dashed lines represent the electron compressibilities $C_Q(\epsilon, T)$ expected from Eq.(4.9).

discussed previously, low temperatures did not have the expected effect on the electron compressibility in sample C7-F. In fact, the extracted $C_Q(\epsilon, 81\text{ K})$ largely deviates from the theoretical expectation (dashed blue line in Fig. 4.20). Owing to the liquid nitrogen temperatures, measurements at 81 K are more difficult to perform, including the calibration and de-embedding of the system. We have therefore focussed on the room

temperature setup, where the aforementioned processes are more reliable.

4.4.3 Diffusion coefficient $D(\epsilon)$

A direct way of accessing information about diffusion in our graphene field-effect capacitor is the use of the *Einstein relation* (4.33)

$$\sigma(\epsilon) = C_Q(\epsilon)D(\epsilon) = C_Q(\epsilon, T)\frac{\nu_F^2}{2}\langle\tau_{tr}(\epsilon)\rangle_T \tag{4.42}$$

The conductivity σ and electron compressibility C_Q are measured simultaneously but separately for different chemical potentials ϵ_F. We can thus directly deduce the diffusion coefficient $D(\epsilon)$ and transport scattering time τ_{tr} from the ratio of σ and C_Q. For this purpose we plot the inverse electron compressibility $(C_Q LW)^{-1} = C_g^{-1} - C_{geo}^{-1}$ versus the charging resistance R_g for the measurements on the Cascade and Janis setup (Figs. 4.21 and 4.22). The ratio

$$\alpha(\epsilon) = \frac{(C_Q(\epsilon)LW)^{-1}}{R_g(\epsilon)} \propto \omega_c \tag{4.43}$$

is then directly proportional to the diffusion coefficient, since

$$D(\epsilon) = \frac{\sigma}{C_Q} = \frac{L}{3W}R^{-1}C_Q^{-1} = \frac{L^2}{3}\frac{(C_Q LW)^{-1}}{R_g} = \frac{L^2}{3}\alpha(\epsilon) \tag{4.44}$$

The factor 3 intervenes due to low frequency development (4.38) which allowed us to extract σ and C_Q. In both samples E9-Zc and C7-F and at room and liquid nitrogen temperature we find a linear dependence of $C_Q(R_g)$ (see Figs. 4.21 and 4.22), which corresponds to an energy-independent diffusion coefficient D: the ratio $\alpha(\epsilon)$ remains the same throughout the investigated energy range. For sample E9-Zc we obtain $D \simeq 180\ \mathrm{cm^2 s^{-1}}$, which corresponds to a scattering length

$$l = \nu_F\tau_{tr} = \frac{2D}{\nu_F} \simeq 40\ \mathrm{nm} \tag{4.45}$$

Sample C7-F exhibits a diffusion coefficient of $D \simeq 540\ \mathrm{cm^2 s^{-1}}$ (Cascade setup) and $\simeq 600\ \mathrm{cm^2 s^{-1}}$ (Janis setup), thus $l \simeq 100$ nm and 120 nm at room temperature. At liquid nitrogen temperature mobility enhances, which in turn also improves the diffusion coefficient: At 81 K we obtain $D \simeq 840\ \mathrm{cm^2 s^{-1}}$ and $l \simeq 170$ nm. The above values are within the range of values extracted by other methods (see e.g. [109]). Since the Fermi velocity ν_F is independent of energy in graphene, the thermal average of the transport scattering time $\langle\tau_{tr}\rangle_T$ is directly proportional to D. Therefore we find [21]

$$\langle\tau_{tr}\rangle_T = const. \tag{4.46}$$

This result coincides with the sub-linear dependence of conductivity on carrier density, most notably in our room temperature experiments (see Figs. 4.16 and 4.18). The $T = 81$ K measurement shows a less pronounced, but still visible sub-linearity (see Fig. 4.18). The finite temperature does not alter the linear behaviour of C_Q at high n_s but merely prevents the carrier density from attaining its minimum value, as displayed in Fig. 4.4. The constant transport scattering time therefore leads us to an equivalent

$$\sigma \propto \sqrt{n_s} \tag{4.47}$$

dependence.

In section 4.2.2 we also found that the the Thouless frequency $\omega_{Thouless} \simeq D/L^2$ intervenes in the crossover of real and imaginary part of the admittance. From the extracted values of the diffusion coefficient we can therefore estimate $f_{Thouless} \simeq 0.7$ GHz in sample E9-Zc as well as $f_{Thouless} \simeq 2.4$ GHz and 3.2 GHz in sample C7-F at room and liquid nitrogen temperature, respectively. A measurement of the correlation energy E_c of the conductance fluctuations in graphene providing also the Thouless energy from $E_c \simeq E_{Thouless} = \hbar D/L^2$ [129] comes to the conclusion that in MLG $D \propto \sqrt{n_s}$. In our opinion however, the presented data points are not conclusive and a $D \simeq const$ estimate could be equally valid.

As presented in the beginning of this chapter, most of the scattering mechanisms discussed in literature predict a linear or slightly sub-linear dependence of the conductivity on charge carrier concentration (see table 4.1). Our $\tau_{tr} = const.$ findings can thus not be explained by charged impurities, resonant scatterers or standard ripples. Choosing a peculiar value $H = 3/4$ in the ripple scenario would account for our $\sigma \propto \sqrt{n_s}$ results but differs from the experimentally established height correlations $H \simeq 1/2$ for rough SiO_2 substrates and $H \simeq 1$ for free standing membranes [130]. Nevertheless the effect of ripples cannot be dismissed in graphene devices on SiO_2, as shown by Xu et al. [131], who found large ripples to be omnipresent. Furthermore, these ripples exhibit a lower conductance than flat parts of MLG.

In the overview over scattering mechanisms, we encountered one particular mechanism resulting in $\tau_{tr} = const.$ and $\sigma \propto \sqrt{n_s}$, the *random Dirac mass disorder*. According to Ziegler [22] the randomly distributed impurities create gap fluctuations and thus carriers acquire locally a finite mass. In this context D can be approximated from theory by

$$D \simeq \frac{g e^{\pi/g}}{4\pi} \tag{4.48}$$

in the vicinity of the CNP, i.e. for small energies ϵ, where g is the variance of the Dirac mass. Our samples therefore exhibit variances $g \simeq 1$ (E9-Zc), $g \simeq 0.66$ (C7-F, 300 K) and $g \simeq 0.61$ (C7-F, 81 K). As pointed out in the presentation of this mechanism, we

were unable to solve the matter of dimensionality. The precise meaning of the above Dirac mass disorder values remains therefore elusive.

Yet a third possibility is an admixture of different mechanisms with various strengths. Following Matthisen's rule one can construct an effective conductivity

$$\sigma^{-1} = \sum \sigma_i^{-1} \tag{4.49}$$

for example adding local, charged and resonant scatterers:

$$\sigma^{-1}(n_s) = \sigma_{local}^{-1} + \sigma_{charged}^{-1} + \sigma_{resonant}^{-1} = \frac{1}{\alpha\, ln(n_s)} + \frac{1}{\beta\, n_s} + \frac{1}{\gamma\, n_s ln^2(n_s)} \tag{4.50}$$

Depending on the precise mixture, i.e. values of α, β, γ, and given minor experimental uncertainties, this could be another valid option to explain $\tau_{tr} = const.$

Overall, diffusion remains a highly debated subject in graphene research as discrepancies between theory and data have yet to be resolved. We have added a new facet to the picture of diffusion in graphene by directly probing the transport scattering time in a simple capacitor geometry. More data and experiments are needed in order to clarify scattering mechanisms in graphene.

One possibility is to change the underlying substrate and/or dielectric. During his MSc internship at the LPA, Q. Wilmart could make a first step in this direction: He fabricated graphene-hBN field-effect capacitors, where the usual AlOx dielectric is replaced by a thin hexagonal boron nitride sheet [132]. The graphene flake was priorly exfoliated on highly resistive Si/SiO_2 substrate and after the manual stacking of hBN on the MLG (see chapter 2), the capacitor was established following the procedure outlined earlier in this chapter. However admittance measurements did not reveal major improvements, as there are technical challenges yet to be overcome: The drain electrode is metallised before the hBN deposition, leading to a large height step ($\sim$ 100 nm) at its boundary. The subsequently placed hBN sheet does not fold along this edge, leaving a void space between dielectric / gate electrode and graphene flake. Precise de-embedding and measurements, especially of the capacitive signal, are therefore not possible. A way of overcoming this drawback could be yet again the inversion of the structure, as suggested once before for RF-GFETs: The gate electrode is buried in the SiO_2 substrate and a thin hBN film place on top of it. Then the subsequently transferred MLG sheet can be contacted without disturbing the plane-plane capacitor configuration and remains additionally accessible for thermal annealing and/or purposeful contamination.

n_s

1

FIGURE 4.21: Inverse electron compressibility as a function of resistance in Cascade setup measurements. Each data point corresponds to a different gate voltage, thus different energy. The slope to each point gives information about the diffusion coefficient $D(\epsilon)$.

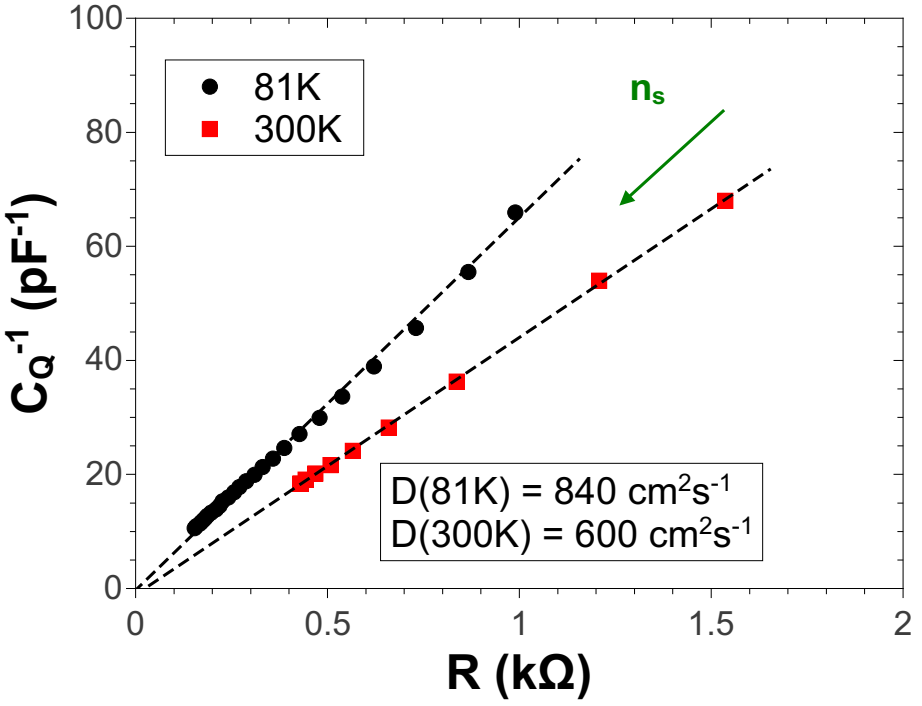

FIGURE 4.22: Inverse electron compressibility as a function of resistance in sample C7-F at room and liquid nitrogen temperature.

Chapter 5

Electronic noise and phonon cooling in graphene

In general today's standard semiconductor MOSFETs work at biases high enough to provoke electron-phonon interactions in their channel. It is thus of great importance to study these interactions and understand their role in the electronic transport.
In this context noise measurements can yield information about the physics involved in electronic transport that is not readily available from standard DC transport measurements. It can reveal the role of disorder, scattering or carrier statistics in a given structure. Contrary to e.g. GaAs heterostructures, where optical phonons arise at comparatively low energies, their threshold is quite high in MLG. They intervene therefore only at high electrical fields in clean materials and will therefore be neglected throughout this chapter. Their acoustic counterparts however, remain elusive due to their weak coupling to the carriers. Using noise thermometry, we can nevertheless investigate the effect of acoustic phonons on the cooling of carriers in graphene.
In this chapter we will first introduce the background of electron-acoustic phonon scattering and its signature in different temperature regimes. A short description of electronic noise in MLG will be given, as well as an overview of hot electron and noise experiments in different materials. This introductory part is followed by the presentation of experimental techniques, where we detail the device fabrication, the cryogenic noise thermometry setup and the device characterisation process. We will end the chapter with a presentation of the results and their discussion with respect to electron-acoustic phonon cooling [26].

5.1 Important concepts and formulas

5.1.1 Phonons in graphene

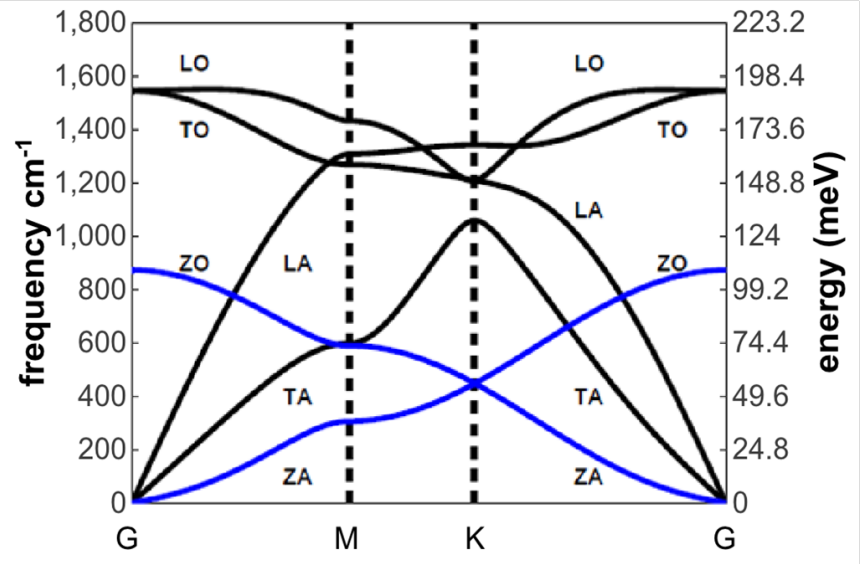

FIGURE 5.1: Phonon dispersion in MLG. Lines highlighted in blue are out-of-plane (ZO and ZA) phonons which are of little importance in supported graphene. Adapted from [49].

We have already briefly introduced the phonon dispersion of graphene in chapter 1. A sketch of it is shown in Fig. 5.1 for different directions in the Brillouin zone. The accuracy of this theoretical prediction, which had been established long before Novoselov and Geim's discovery, has been proven for the optical branches experimentally e.g. via Raman spectroscopy [82, 83]. Associated with the large sound velocity of $\nu_s \simeq 2 \cdot 10^4$ ms^{-1} (for the case of the longitudinal branch) optical phonons (OPs) have a rather high energy of $\sim$ 160–200 meV, as compared to e.g. GaAs where OPs start as low as $\sim$ 35 meV [18]. The sound velocity in GaAs is $\nu_s \simeq 5110$ ms^{-1}. The carriers in MLG couple strongly to OPs at high electric fields as already presented in chapter 3.

Acoustic phonons Acoustic phonons (APs) are nearly omnipresent in MLG, as can be seen from the corresponding branches in Fig. 5.1; their energy is arbitrarily small in the middle of the zone (point G). Nevertheless little influence of APs on charge carrier mobility can be observed in electric DC transport measurements, as pointed out previously in Fig. 1.12(b). We thus expect a low coupling of APs to carriers in graphene, as compared to their optical counterparts. A more detailed estimation of the electron-AP coupling constant Σ is given below.

5.1.2 Electron-acoustic phonon coupling in graphene

5.1.2.1 Temperature dependence of electron-phonon scattering in 2D

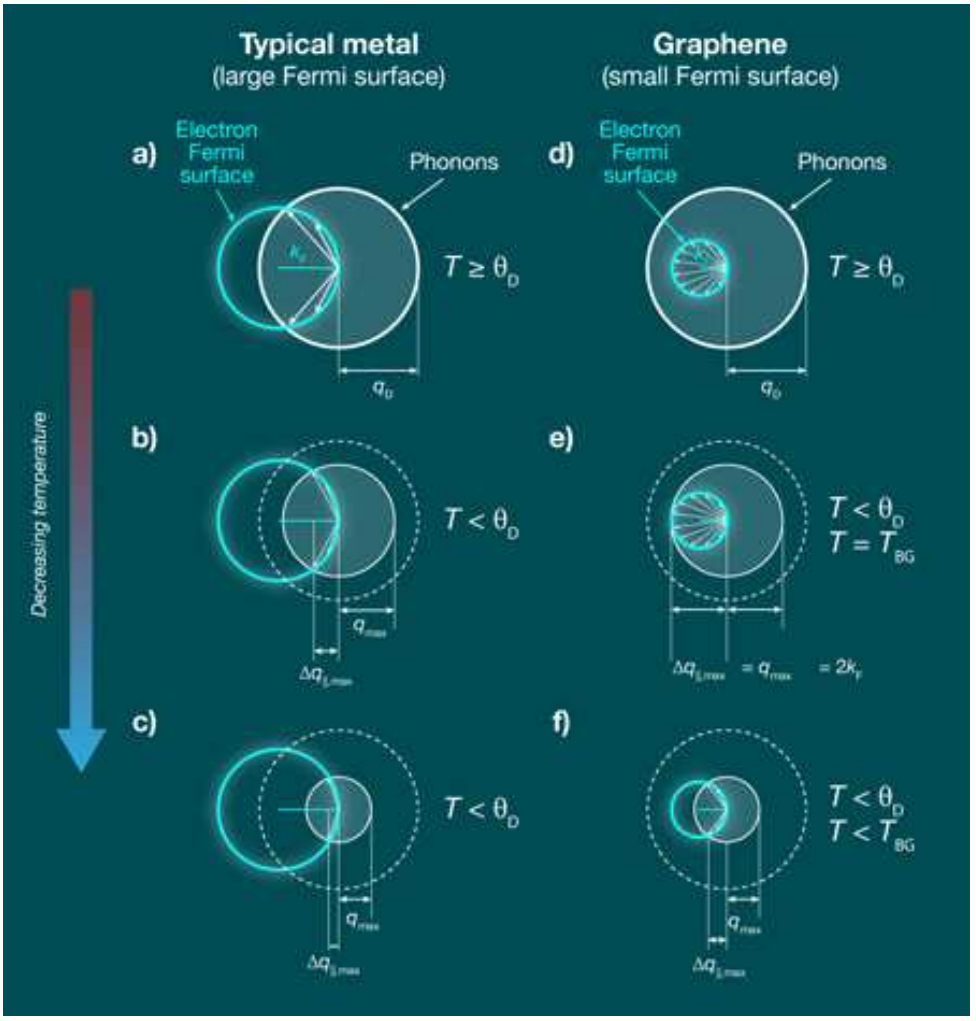

FIGURE 5.2: Illustration of high-temperature and low-temperature electron-phonon scattering behaviour in typical metals (a-c) and graphene (d-f). From M. Fuhrer [23].

We will now consider the very basic, but important issue of electron-phonon coupling in 2 dimensions, for which MLG is the prime example.

Normal metals First of all, however, let us turn to the description of electron-phonon scattering and its temperature dependence in normal metals, by which we mean metallic systems with large Fermi surface. Here, the typical scale is the so-called *Debye temperature* Θ_D given by the maximum phonon wavevector q_D. It sets the crossover between the high temperature resistivity $\rho(T) \propto T$ for $T \geq \Theta_D$ and the low temperature limit

$\rho(T) \propto T^{\alpha}$ for $T < \Theta_D$. The coefficient α is 5 for 3D metals and 4 for 2D metallic systems, i.e. 2D systems with high carrier concentration and large Fermi surface [23]. For $T \geq \Theta_D$ all phonon modes are thermally populated and the maximum phonon vector is

$$q_D = \frac{k_B \Theta_D}{\hbar \nu_s} \tag{5.1}$$

where ν_s is the phonon velocity in the metal. Scattering of electrons by phonons is the main source of resistivity at $T \geq \Theta_D$ in normal metals, as these interactions redirect the electron wave vector k_F from one point on the Fermi surface to another within reach of the phonon space (see Fig. 5.2(a)). Due to their bosonic nature the number of excited phonons in each mode is proportional to T, hence the $\rho(T) \propto T$ result [34]. For T below Θ_D the phonon surface shrinks (Fig. 5.2(b) and (c)), leaving a maximum phonon vector $q_D = k_B T/(\hbar \nu_s)$. Therefore, only a smaller part of the Fermi surface remains available to the scattering processes, reducing the allowed scattering angles. This "freezing out" of phonon modes and the reduction of available scattering angles is responsible for the observed $\rho \propto T^5$ dependence in 3D metals [23]. Typical Debye temperatures, below which the resistivity increases rapidly with temperature, are e.g. 170 K for Au or 428 K for Al [34].

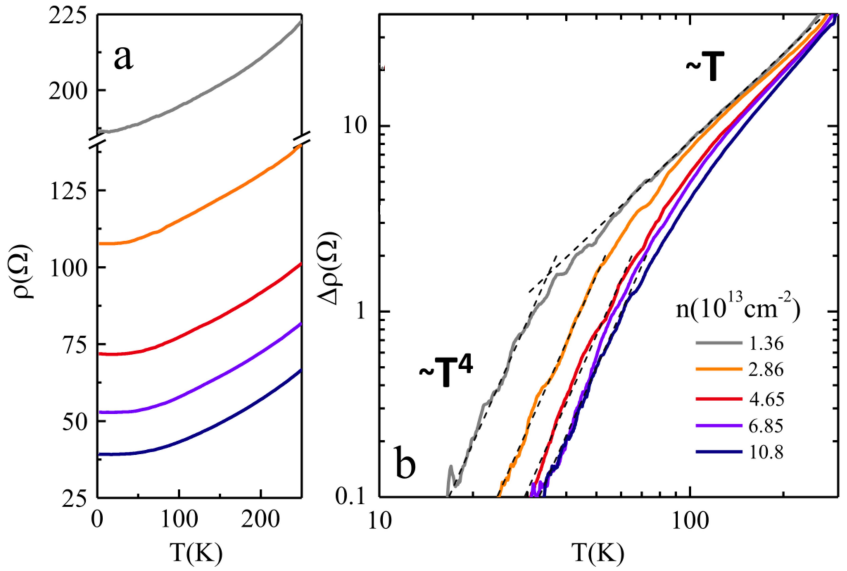

FIGURE 5.3: (a) Temperature dependence of the resistivity for different charge carrier densities. (b) The temperature dependent part of the resistivity $\Delta\rho(T)$ scales as T^4 in the low T range and smoothly crosses over into a linear T dependence at higher T. The dashed lines represent fits to the linear T and T^4 dependencies, respectively. From Efetov et al. [133]

Graphene In a 2D metal with small Fermi surface, thus e.g. graphene, one expects in turn $\rho \propto T^4$ at $T < \Theta_D$, in particular in MLG below $\Theta_D \simeq 2300$ K, i.e. up to room

temperature and beyond [133]. This is however not observed in experiments. Recent measurements by Efetov and Kim [133] rather find the transition in resistivity to take place around 10–30 K $\ll \Theta_D$. How can this be explained?
The key element, as pointed out in [133] and [23], is the small Fermi surface of MLG. Fig. 5.2(d-f) illustrates the transition: At $T \geq \Theta_D$ all redirections of the electron wave vector are possible, since the Fermi surface is much smaller than the available phonon space ($k_F \ll q$). Even below Θ_D, this remains valid in graphene, thus explaining the $\rho(T) \propto T$ behaviour at room temperature. It is only after decreasing below the so-called *Bloch-Grüneisen* temperature

$$T_{BG} = \frac{2\nu_s}{\nu_F}\frac{\epsilon_F}{k_B} \simeq 54\sqrt{\tilde{n_s}}\ \mathrm{K} < \Theta_D \tag{5.2}$$

that the previous situation is restored: The Fermi surface available to scattering events reduces (see Fig. 5.2(e-f)) and one finds $\rho(T) \propto T^4$ [23, 133]. This means that for $T \leq T_{BG}$ the maximum phonon wave vector is $q_{max} \leq 2k_F$, due to the restriction of available Fermi surface. We can hence define our low temperature limit as the situation where $k_F \gg q$, i.e. the electron energy is much bigger than the phonon energy:

$$\hbar\nu_F \cdot k_F \gg \hbar\nu_s \cdot q \tag{5.3}$$

Here, the electron energy is either given by the chemical potential μ or the temperature, $\hbar k_F \nu_F \propto max\{k_B T_e, \mu\}$. Note also that in contrast to Θ_D the Bloch-Grüneisen temperature can be tuned through the variation of the carrier density. The afore mentioned change of temperature dependence of the resistivity, $\rho \propto T^4$ to $\rho \propto T$, was confirmed experimentally by Efetov and Kim [133]. Subtracting a constant contribution ρ_0 stemming from scattering on static impurities and point defects in the lattice, the resulting $\Delta\rho(T) = \rho(T) - \rho_0$ is reproduced well by a resistivity calculated from Boltzmann theory:

$$\Delta\rho(T) = \frac{8D^2\epsilon_F}{e^2\hbar\rho_{gr}\nu_s\nu_F^3} f_s\left(T_{BG}/T\right) \tag{5.4}$$

where $\rho_{gr} \simeq 7.6\text{–}9.6 \cdot 10^{-7}$ kgm^{-2} (theoretical and experimental value, respectively) [134] represents the graphene mass density, $\nu_F = 10^6$ ms^{-1} and $\nu_s = 2 \cdot 10^4$ ms^{-1} are the Fermi and sound velocity in graphene, respectively and D is the acoustic deformation potential coupling electrons and APs. Typical theoretical values of D are in the range ~ 4 eV [135, 136] and 10–30 eV [29, 137, 138], whereas experimentally $D = 7.5$ eV [139] and $D \sim 17$ – 29 eV [133, 140, 141] are found for few-layer and monolayer graphene, respectively. A recent theoretical paper suggests an effective $D = 6.8$ eV [142] due to the different acoustic phonon modes. The generalised Bloch-Grüneisen function $f_s\left(T_{BG}/T\right)$

is given by the integral

$$f_s(\psi) = \int_0^1 \frac{\psi x^4 \sqrt{1-x^2} e^{\psi x}}{(e^{\psi x}-1)^2} dx \tag{5.5}$$

Eq. (5.4) differs from the standard 3D metal case as it involves T_{BG} instead of Θ_D and also contains x^4 rather than x^5, which is a manifest of the 2D nature of carriers and phonons in MLG. Furthermore, the absence of backscattering discussed earlier in chapter 1 is introduced by the factor $\sqrt{1-x^2}$. Using $D = 25$ eV, as found by Efetov and Kim, Eq. (5.4) can be approximated by $\Delta\rho \simeq 0.58\ \Omega \cdot f_s\,(T_{BG}/T)\sqrt{\tilde{n_s}}$. The limits for $T \ll T_{BG}$ and $T \geq T_{BG}$ are highlighted in table 5.1. They are obtained using $\psi = T_{BG}/T = 2\hbar\nu_s k_F/(k_B T)$ in Eq. (5.5), yielding $f_s(\psi \to 0) \simeq 0.196/\psi$ and $f_s(\psi \to \infty) \simeq 24\zeta(4)/\psi^4$, where ζ is the Riemann-Zeta function ($\zeta(4) = \pi^2/90$). The crossover between regimes occurs for $T_{BG}/T \simeq 4$.

Efetov and Kim use an electrolytic gate to obtain large carrier densities, which enables them to increases T_{BG} up to very high temperatures and map the crossover between regimes. Their method excludes however explicitly the effects of disorder by removal of ρ_0 and requires carrier concentrations of the order of $n_s \sim 10^{14}$ cm^{-2}. It will be shown in the following that disorder can in general not be subtracted and an unexpected temperature dependence is found at low n_s. In order to access these effects, we are in need of a different way of investigating the electron-AP coupling: Instead of probing the temperature dependence of resistivity, we will study the energy relaxation of charge carriers, i.e. their energy transfer to acoustic phonons.

5.1.2.2 Electron-acoustic phonon energy relaxation in graphene

Several theoretical papers have dealt with the aforementioned energy transfer from electrons to acoustic phonons in graphene in the low ($T \leq T_{BG}$) [137] and high ($T \geq T_{BG}$) temperature limits [138]. A recent numerical calculation of the heat conductance due to the electron - 2D acoustic phonon interaction shows the whole range, including the crossover region around T_{BG} [24] (see Fig. 5.4). It maps the heat conductance

$$G_{e-AP}(\mu, T) = \left.\frac{\partial Q}{\partial \Delta T}\right|_{\Delta T=0} \tag{5.6}$$

as a function of the ratio of thermal energy to chemical potential. G_{e-AP} is therefore directly related to the cooling power Q, that is the amount of energy transferred from electrons to APs per unit area. At low temperatures is generally of the form

$$Q = V_{dim}\Sigma\left(T_e^{\delta} - T_{phonon}^{\delta}\right) \tag{5.7}$$

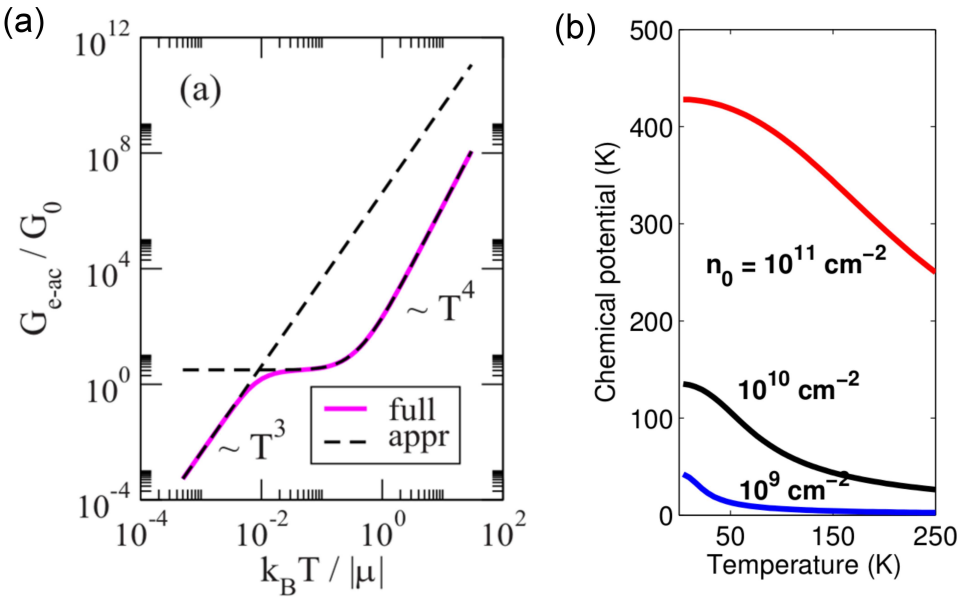

FIGURE 5.4: a) Thermal conductance as function of chemical potential μ and temperature T in units of $G_0 = LW \cdot \frac{D^2 k_B}{2\pi^2 \rho_{gr} \hbar^5 \nu_F^6} |\mu|^4$. The dashed lines indicate the analytical approximations [137] and [138], the solid line the full numerical estimate. From Viljas et al. [24]. b) Chemical potential μ in K as function of temperature for carrier densities as noted in the plot. From Falkovsky et al. [143].

where V_{dim} stands for the volume of the sample and Σ characterises the electron-phonon coupling strength. As mentioned in the section above, the exponent δ depends on the dimensionality of the system; $\delta = 5$ is generally accepted for 3D metals and $\delta = 3$ for 1D systems like e.g CNTs. The latter dependence has been investigated e.g. by Wu et al. [144] who confirm $\delta = 3$ in CNTs by noise thermometry. In 2D, thus in graphene, one expects $\delta = 4$ [24, 138]. In the high temperature regime in MLG the cooling power takes the form [24, 138]

$$Q \propto g(\mu, T_e)(T_e - T_{phonon}) \tag{5.8}$$

where $g(\mu, T_e)$ is an asymmetric function specifying the coupling[24]

$$g(\mu, T_e) = \frac{D^2 k_B}{30\pi\rho\hbar^5 \nu_F^6} \left(15\mu^4 + 30(\pi\mu k_B T_e)^2 + 7(\pi k_B T_e)^4\right) \quad , \; T \geq T_{BG} \tag{5.9}$$

From the point of view of the cooling power Q, one expects then the following temperature dependences:

- In the low temperature limit, where $k_B T_e \ll \mu$, $G_{e-AP} \propto T^3$. Hence $Q \propto T^4$.
- In the intermediate range $T_{BG} \leq T_e \ll \mu/k_B$, where we have $\frac{k_B T_{BG}}{|\mu|} = \frac{2\nu_F \nu_s}{\hbar k_F \nu_F} \simeq 0.04$, the cooling power should be linear in temperature: $Q \propto T$, as can be seen from the lowest order approximation of Eq. (5.9).

- In the high temperature limit $k_B T_e \gg \mu$, $G_{e-AP} \propto T^4$ and therefore $Q \propto T^5$. Note however that this regime will not be approached in this work and is mentioned only for completeness.

Falkovsky et al. [143] numerically calculated the chemical potential μ for a set of carrier densities as a function of temperature, as displayed in Fig. 5.4(b). At low sample temperatures one finds e.g. $\mu \simeq 430$ K at $n_s = 10^{11}$ cm^{-2}. Our samples are generally in the metallic regime, i.e. degenerated and at high carrier densities $n_s \sim 10^{12}$ cm^{-2} Following the $\mu \propto \sqrt{n_s}$ law, we therefore estimate $\mu \sim 1300$ K for our samples. Typical experimental average electron temperatures T_e will be $\lesssim 400$ K. Therefore, data analysis will generally deal with the low temperature limit, $k_B T_e \ll \mu$, and the cooling power is then expected to follow the aforementioned

$$Q = LW\Sigma \left(T_e^4 - T_{phonon}^4\right) \tag{5.10}$$

dependence. For this limit, an analytical expression for the coupling constant of electrons with longitudinal-acoustic (LA) phonons can be obtained [24]:

$$\Sigma_{LA} = \frac{\pi^2 D^2 |\mu| k_B^4}{15 \rho_{gr} \hbar^5 \nu_F^3 \nu_s^3} \tag{5.11}$$

with ρ_{gr}, ν_F, ν_s and D as introduced below Eq. (5.4).
Using a rather low value $D = 10$ eV in (5.11), one estimates a LA phonon coupling constant of

$$\Sigma_{LA} \simeq 10\sqrt{\tilde{n_s}}\ \mathrm{mW \cdot m^{-2} K^{-4}} \tag{5.12}$$

The carrier density n_s is to be given in units of cm^{-2}.
Table 5.1 summarises the expressions in the high and low temperature regime of both methods allowing to access electron-AP interactions: The energy relaxation of carriers Q and its counterpart in resistivity $\Delta\rho$. For the sake of easy comparison, we transform $\Delta\rho$ to a power per unit area by multiplying with the squared current density $J^2 = (n_s e \nu_F)^2 = (k_F^2 e \nu_F / \pi)^2$. Additionally, we used the evaluation of the Riemann-Zeta function $\zeta(4) = \pi^4/90$.

	$T_e \ll T_{BG}$	$T_{BG} \leq T_e \ll k_B \epsilon_F$
$J^2 \cdot \Delta\rho(T_e)$	$= \frac{12\pi^2}{90} \cdot \frac{D^2}{\rho_{gr}\nu_s} \cdot k_F \cdot \left(\frac{k_B T_e}{\hbar \nu_s}\right)^4$	$= \frac{1}{4\pi} \cdot \frac{D^2}{\rho_{gr}\nu_s} \cdot k_F^4 \cdot \frac{k_B T_e}{\hbar \nu_s}$
$\frac{Q}{LW}$	$= \frac{\pi^2 \nu_s^2}{15 \nu_F^2} \cdot \frac{D^2}{\rho_{gr}\nu_s} \cdot k_F \cdot \left(\frac{k_B T_e}{\hbar \nu_s}\right)^4$	$= \frac{\nu_s^2}{2\pi \nu_F^2} \cdot \frac{D^2}{\rho_{gr}\nu_s} \cdot k_F^4 \cdot \frac{k_B T_e}{\hbar \nu_s}$

TABLE 5.1: Comparison of limiting cases of the temperature dependence of resistivity [133] and the energy transfer from carriers to APs [24]. For the transformation of $\Delta\rho$ to units of power per unit area we use $J^2 = (k_F^2 e \nu_F/\pi)^2$.

5.1.3 Heat equation in presence of acoustic phonon cooling

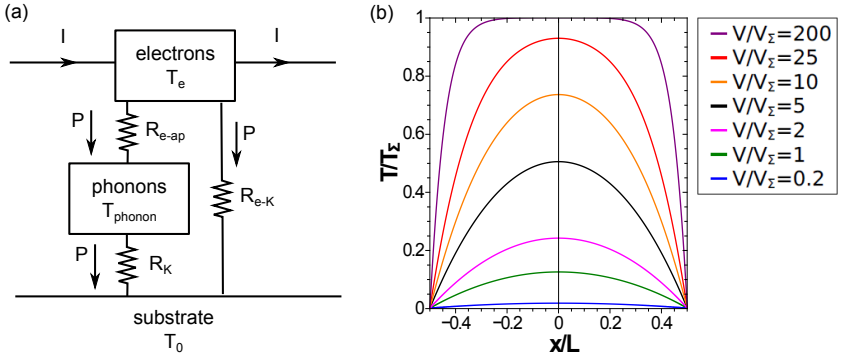

FIGURE 5.5: a) Competing routes for the energy relaxation in graphene: Electron-AP coupling followed by AP-substrate interaction and in parallel direct coupling of electrons to the substrate. R_K and $R)e-K$ are the Kapitza resistances for AP-substrate and electron-substrate coupling. b) Temperature profiles $T_e(x)$ for different bias voltages obtained from the solution of Eq. (5.13) under the assumption of cold contacts and cold phonons, $T(x/L = \pm 0.5) = 0$ and $T_{phonon} = 0$.

Besides the already discussed cooling by APs, carriers can relax their energy via other, competing routes. Of main interest here is the electron heat diffusion to the leads, described by the Wiedemann-Franz law. An overview of the cooling processes is shown in Fig. 5.5. The effectiveness of the different cooling mechanisms is described in terms of the Kapitza interface resistance R_K in Fig. 5.5(a), whereas we will rather express this via the coupling constant Σ in the following description. In more general terms, we are interested in the effect of bias voltage V in combination with the two cooling mechanisms. We therefore have to solve the heat equation

$$\frac{L_o}{2R} L^2 \frac{d^2 T_e^2(x)}{dx^2} = -\frac{V^2}{R} + LW\Sigma \left(T_e^4 - T_{phonon}^4\right) \tag{5.13}$$

where the left-hand side describes the heat conduction of carriers to the contacts via the Wiedemann-Franz law, the first term on the right-hand side the incoming Joule power and the second right-hand side term the effect of AP cooling. This is again a

1-dimensional description, as we assume homogeneity along the width of the sample, similar to the GFECs 1D line model. $L_o = \frac{\pi^2 k_B^2}{3e^2}$ is the Lorenz number and x denotes the coordinate along the graphene channel. Thanks to the T_e^2 and T_e^4 dependences, we obtain an analytical solution in the case of cold contacts ($T_e(\pm 0.5L) = 0$) and cold phonon bath ($T_{phonon} = 0$). The solution only depends on a single parameter Σ, the electron-acoustic phonon coupling constant, which sets the two characteristic scales of the system: the temperature $T_\Sigma^2 = \frac{V}{\sqrt{LW\Sigma R}}$ and the voltage $V_\Sigma = L_o/(\sqrt{4LW\Sigma R})$. $T_\Sigma^2 = \sqrt[4]{P/\Sigma}$ is the maximum temperature reached in the absence of electron heat conduction, whereas V_Σ defines the crossover between the electron cooling at low bias and the phonon mediated cooling at high bias. The temperature profile calculated from (5.13) is pseudo-parabolic at low bias and evolves towards a uniform temperature $T_e(x) = T_\Sigma$ at high bias. The spatial average $\langle T_e \rangle$, intervening in the noise description further below, is then calculated numerically. It is the *average* electron temperature that is probed by our noise thermometry experiments. For a more detailed description of the solution of (5.13), please see Appendix D.

5.1.4 Noise in diffusive graphene devices

In the introduction of this work (section 1.3.3) it was pointed out that there are two main intrinsic sources of noise in a mesoscopic system: thermal and shot noise. Additional contributions to the noise can arise from e.g. flicker or random telegraph noise. We will introduce the first of these additional source but omit the second due to lack of relevance in this work.

In chapter 1, we derived the noise power spectral density $S(\omega)$ in terms of current operators for finite frequencies. We found that the $S(\omega)$ can be calculated as the *Fourier transformation* of the current correlation function (Eq.(1.65)). Using Wicks theorem [55], one may in the end obtain a general result for the autocorrelated electronic noise in a two-terminal system evaluated for a chemical potential step $\Delta\mu = eV$, at finite temperature T and frequency ω. We will not go into more detail on this subject here but refer the interested reader to the reviews by Blanter and Büttiker [51] or Martin [11].
Let us simply state the final zero frequency limit of the electronic noise, describing the crossover between thermal and shot noise:

$$S_I(0) = \frac{4e^2}{h} k_B T D^2 + \frac{2e^3 V}{h} D(1-D) coth(\frac{eV}{2k_B T}) \tag{5.14}$$

The above equation is valid for a mono-mode conductor, but can be extended to multiple modes by summing over all modes n and their corresponding D_n (see also chapter 1, 1.3.3).

Thermal noise In the equilibrium state, where there is no potential difference between the contacts, we obtain the pure thermal limit. As pointed out in chapter 1 agitations of carriers in a two-terminal conductor of resistance R give rise to a current noise $\delta I(t)$, the so-called Johnson-Nyquist noise of spectral density

$$S_I = \frac{4k_BT}{R} = 4G_{noise}k_BT \tag{5.15}$$

Here, the last representation is probably the most common, showing the origin of thermal noise in conductance fluctuations due to dissipative processes in the sample. Generally in a two-terminal system one uses $G_{noise}(\omega) = G_{ds}(\omega)$. It has however recently been shown [64] that a more general relation has to be employed in three-terminal, mono-mode nano-transistors: There, corrections from the small DOS to the drain-source conductance have to be taken into account $G_{noise}(\omega) = G_{ds}(\omega) + O(C_Q^{-1})$ due to the close vicinity of the top-gate electrode. It reveals that $O(C_Q^{-1}) = 2g_mC_g/C_Q$, where g_m is the device's transconductance and C_g and C_Q the gate and quantum capacitance, respectively. In our experiments however, these corrections can be neglected as we will use back-gated devices with a dielectric thickness on the μm scale. Also, frequencies remain small enough to use the static conductance $G_{ds} = R_{ds}^{-1}$ in calculations.

5.1.4.1 Shot noise

The second source of electronic noise, shot noise, results from the stochastic nature of electron transport and the granularity of charge. It is a quantum effect stemming from fluctuations in the number of transmitted carriers. It reveals from the general zero frequency limit (5.14) in the limit $T \to 0$. We then find

$$S_I = \frac{2e^3V}{h}D(1-D) = 2eI(1-D) \tag{5.16}$$

In the case of low transmission ($D \ll 1$) this is equal to the result found by Schottky [145] in 1918

$$S_I = 2e\langle I\rangle \tag{5.17}$$

who derived this formula classically, assuming the intervals between particle arrivals to be Poissonian. It is therefore also referred to as the Poisson limit.

5.1.4.2 Fano factor

It has proven useful, especially in mesoscopic physics, to express noise information in terms of the so-called *Fano factor* F. It is defined as the ratio between zero frequency shot noise and Poisson noise [11]:

$$F \equiv \frac{S_I(\omega = 0)}{2e\langle I \rangle} \tag{5.18}$$

which, in a one-mode conductor, is proportional to $1 - D$. A ballistic system, i.e. unit transmission, does not exhibit noise and therefore then $F = 0$.
The Fano factor will thus taken on values between zero (transparent channels) and unity (poor transmission) and can be expressed in a more generalised form [51]

$$F \equiv \frac{\sum_n D_n(1 - D_n)}{\sum_n D_n} \tag{5.19}$$

taking into account all available channels and their transmission probability D_n. It is generally referred to as *real* Fano factor as compared to the *pseudo* Fano factor $\tilde{F}$ which we will introduce below. In the case of low transmission $D \ll 1$, which can e.g be achieved easily in tunnel junctions, we recover the full shot noise and $F = 1$. We will take advantage of this fact during the calibration of our setup.
As pointed out by Blanter and Büttiker [51] (see also references therein), the Fano factor can be $\ll 1$ in certain systems, i.e. the shot noise is partly suppressed. Depending on the length L of the sample with respect to the characteristic lengths for elastic and inelastic scattering of the carriers, several typical values and dependences will arise: For $L \ll l_{e-e}$, where l_{e-e} is the electron-electron scattering length, only elastic scattering among the carriers occurs and the system behaves like a non-interacting population of electrons, which in turn reduces the shot noise and leads to $F = 1/3$ (see [51] or also [146]). Once $L \geq l_{e-e}$, a homogeneous population of hot electrons establishes due to inelastic scattering among the electrons. This creates additional electronic noise and the Fano factor rises to $F = \sqrt{3}/4$ [51, 146]. Beyond this regime, when the characteristic length of electron-phonon interaction l_{e-ph} is reached, the noise decreases with system length and $F \to 0$ (see e.g. graph in [146]).
The aforementioned case $F = 1/3$, is a quantum interference effect first explained by [147]: In a diffusive, phase coherent conductor conductance is given by the amount and transparency of its open channels. As it is diffusive only few channels are open with transmission 1, all others are assumed to be closed. Evaluation of quantum transport

calculus then results in

$$S_I = \frac{2}{3} eV \langle G_{noise} \rangle = 2e\langle I \rangle \cdot \frac{1}{3} \tag{5.20}$$

The second case of $F = \sqrt{3}/4$ was studied theoretically by Nagaev [148] and Nazarov et al. [149] and verified experimentally by Steinbach et al. [146]. Here, $L \geq l_{e-e}$ in the diffusive conductor, i.e. inelastic electron-electron scattering causes a redistribution of energy: Carriers thermalise and the only energy loss is provided by heat conduction to the contacts, described by the Wiedemann-Franz law [34] and introduced earlier in 5.1.3. A spatial temperature profile $T_e(x)$ establishes. This does however not cause a change in conductance as the average momentum of the electron gas remains unaltered. Nevertheless a positive contribution to the electronic noise arises, since the energy relaxation participates in the distribution of states f (see (1.66)). The noise spectral density can then be described similar to the thermal noise, exchanging T for the spatial average of the electron temperature $< T_e >$, $S_I = 4G_{ds}k_B < T_e(x) >$ or also $S_I = 2eI\tilde{F}$ with a pseudo Fano factor $\tilde{F} = \sqrt{3}/4 \simeq 0.43$ [148]. It is this *pseudo Fano factor* $\tilde{F}$ that intervenes in the analysis of our experiments; for the sake of simplicity will however refer to it simply as Fano factor F.

In the last regime, all carrier energy is removed by electron-phonon interactions and the only remaining source of noise is of the Johnson-Nyquist type. Hence S_I becomes independent of I and therefore $F \to 0$.

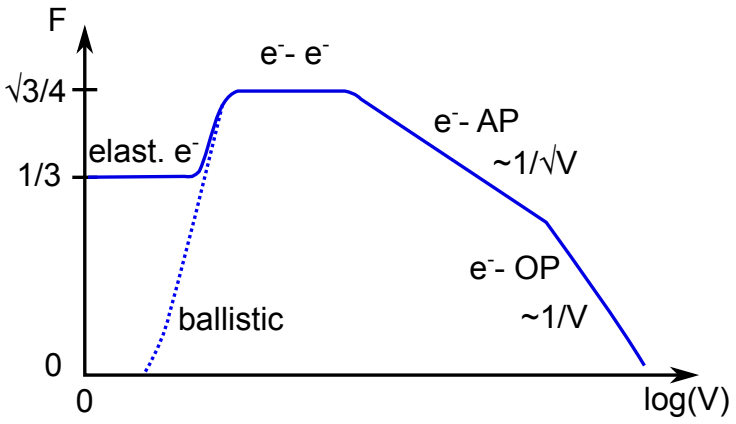

FIGURE 5.6: Schematic presentation of the Fano factor in graphene as a function of bias voltage. The solid line indicates the diffusive and the dashed line the ballistic case, respectively. Both are for the limit of high carrier concentration.

Fano factor in graphene As pointed out in the paragraphs above, the system size L determines the amount of noise suppression and thus the value of F. With respect to our experiments, we are however more interested in the scaling of F with bias voltage V. In graphene, the characteristic length scales are functions of the Fermi energy, hence

tunable, allowing us to keep a constant system length L. In particular the electron mean free path l_{mfp} can be estimated from the Drude conductivity [150]:

$$\sigma = n_s e \mu_c = \frac{2e^2}{h} k_F l_{mfp}$$
$$l_{mfp} = \frac{\mu_c \hbar}{e} \sqrt{\pi n_s} = \frac{\mu_c}{e \nu_F} \epsilon_F \tag{5.21}$$

A schematic overview of the expected $F(V)$ behaviour can be found in Fig. 5.6: The solid line indicates the diffusive and the dashed line the ballistic case, respectively, both in the limit of high carrier concentration. Close to zero bias we find $F \simeq 1/3$ in the diffusive case, as carriers are essentially non-interacting and one retrieves the result mentioned earlier. This has been predicted numerically [67] and experimentally values close to 1/3 are obtained from noise measurements [25]. In general, as pointed out by [25], $F \lesssim 1/3$ at low bias in diffusive graphene with little n_s dependence, whereas $F = 0$ in ballistic samples at high carrier concentration. Approaching the CNP in ballistic graphene Danneau et al. [151] confirm the predicted $F = 1/3$ value [66]. Above a certain threshold voltage, carriers interact inelastically and we obtain the universal $F \simeq \sqrt{3}/4$. Note that currently there is no full theory of electron-electron interactions describing both the doped regime and the region close to the CNP in graphene. In the diffusive, doped regime, we can however assume that results will be similar to other metallic disordered systems (see e.g. [146]).

Beyond this regime, electron-phonon interactions will intervene in the Fano factor. In a first stage cooling of carriers by APs dominates over the heat conduction. This effect is later replaced by the electron-OP interaction, when carriers acquire sufficient energy to overcome the optical phonon threshold energy. Both processes effectively cool the carriers and reduce thus the Fano factor. The latter OP cooling will introduce a very efficient noise reduction, as OPs are interacting strong enough to be visible even in DC transport measurements [50]. To our knowledge, no precise voltage dependence has been presented yet and the sketched "cosmology" in Fig. 5.6 is of rather predictive nature at medium to high bias:

- At medium to high bias, where electron-AP cooling dominates over the heat conduction to the contacts but no OPs are present yet, the average electron temperature is given by $T_e \propto \sqrt{V}$. We therefore predict a Fano factor $F(V) \propto 1/\sqrt{V}$.
- At high bias and high electric field the cooling of carriers is dominated by OPs. Their strong interaction will cause current saturation, i.e. no further increase of $S_I \propto I$ and hence one expects the Fano factor to reach the macroscopic limit $F = 0$ at very high voltage. For the transition we predict a $F \propto 1/V$ dependence. The samples we present in the following are however highly diffusive and we will

therefore not have access to this regime; it requires electron temperatures in excess of $\hbar\Omega_{OP}/k_B \simeq 160$ meV$/k_B \simeq 1900$ K.

The two sources of electronic fluctuations, thermal agitations and granularity of charge, outlined in the paragraphs above are however not the only ones present in an electronic system. Another source of noise is the so-called $1/f$ noise, which we will introduce briefly in the following.

5.1.4.3 1/f noise and Hooge parameter

$1/f$ or flicker noise is a type of random fluctuations found in a broad variety of systems, ranging from the rotation of the earth to fluctuations of current in microelectronic devices [152]. Such noise in current or voltage is always related to a direct current because its source are resistance fluctuations in the conductor. They translate into current or voltage fluctuations via Ohm's law. Electronic $1/f$ noise has first been observed by J.B. Johnson in 1925 [153], when he studied the fluctuations of emission of electrons of a thermionic tube. Within the spectral density he found a contribution decreasing with frequency, which was later coined *flicker noise*. The origins of flicker noise is not always fully understood, but e.g. for metals it has been shown that $1/f$ noise is closely related to the motion of defects and impurities [54]. We shall not go into detail on this particular and very rich subject, but merely introduce the so-called *Hooge relationship* [154]

$$\frac{S_{VV}(f)}{V^2} = \frac{\alpha_H}{N \cdot f} \tag{5.22}$$

with $\alpha_H \simeq 2 \cdot 10^{-3}$ the empirical Hooge constant and N the number of charge carriers contributing to the resistance. In our case of biased graphene samples, we will thus expect a $1/f$ contribution to S_I proportional to I_{ds}^2. This contribution will be all the more significant for higher bias and small sample sizes, where there are less carriers present in the channel.

The Hooge parameter has recently been characterised in graphene devices by measuring the $1/f$ noise up to the kHz region: Liu et al. [155] find $\alpha_H \sim 10^{-4}$ in backgated MLG devices on Si/SiO_2 substrate. In a second study [156] the same group could establish that $\alpha_H \sim 2 \cdot 10^{-3}$ in top-gated MLG devices with HfO_2 dielectric on Si/SiO_2 substrate. Additionally, Zhang et al. [157] show that in graphene $\alpha_H \propto n_s$ and suggest that α_H also depends on electron mobility and the exact scattering mechanism. They also present a model describing a variety of noise measurements by different groups based on the above suggestions. The scope of this chapter is however the frequency independent shot noise of GFETs and we will restrict the discussion of flicker noise to the above

mentioned. Flicker noise is nevertheless one of the motivations for measurements in the GHz frequency range; there its contribution is only minor.

5.2 Hot electrons and electronic noise experiments

The electronic noise, i.e. essentially fluctuations of electron occupation numbers around the average value, can be derived rather simply from the impedance of a conductor, if the former is in equilibrium. Then, one can use the Johnson-Nyquist relation (see chapter 1) where noise is directly related to the average current. The situation becomes more complicated for non-equilibrium systems, where a so-called *hot electron* population can arise if carriers (in principle electrons or holes, though we will use the term "hot electrons" only for simplicity) do not thermalise well with the phonons of the conductor or surrounding bath; that is, when the electron-electron scattering time τ_{e-e} is much shorter than the average energy loss time [158]. Then, one has to use different methods than the average current to probe the electron temperature or the noise itself, in order to gain information about the system's noise behaviour [54].

5.2.1 Measurement techniques

The different methods that can be employed to investigate a material's hot electrons and their energy relaxation towards equilibrium can be roughly divided into two groups: Transport and optical techniques. An overview is given e.g. in [158] and references therein.

Transport techniques generally aim at generating a hot electron population by supplying electrical power greater than the power loss via electron-phonon relaxation, establishing an average electron temperature $T_e \gg T_L$. T_L is here the lattice temperature which is usually close to the bath temperature T_0. Typical transport measurements supply power via a DC field or short electrical pulses and investigate the energy loss via acoustic phonons. The energy relaxation of carriers can then be probed by different means. Initial ideas involved the determination of the power loss from carrier mobility μ_c. However, μ_c not only depends on T_e but to some extend also on T_L, making this method less reliable [158]. Instead, Shubnikov-de-Haas oscillations in weak magnetic fields can be used to determine T_e very accurately, as their amplitude depends strongly on it. A third, commonly employed technique is the use of superconducting bolometers. Here, a short electro-magnetic pulse creates a hot electron population in the sample, which has the bolometer attached to the opposite side of its substrate. Energy loss is provided by interaction with phonons, which travel nearly ballistically to the detector. The bolometer

consists usually of a thin metal layer (commonly Al) evaporated on the substrate, with a certain superconducting transition temperature T_c. Close to T_c the small temperature increase due to the arriving phonons will create a detectable change in resistivity. This technique requires the use of cryogenics in order to achieve $T \simeq T_c \sim 1$–4 K. Last but not least, one can investigate T_e and the energy relaxation by means of noise thermometry. It consists in the measurement of current or voltage fluctuations of the hot electron sample, which has been suggested first by Arai [159] and then exploited experimentally in many studies. A more in depth description of this technique in connection with graphene samples will be given below (5.3.6).

The second group of methods involves optical measurements, which are generally used to probe the energy relaxation of hot electrons via optical phonons. Widely used are photoluminescence spectroscopy as well as "pump-probe" techniques like e.g. Raman spectroscopy. These techniques give access to the hot carrier relaxation time which is the product of the thermal resistance and the electronic specific heat. The electric measurements have the advantage to give direct access to the thermal relaxation resistance. Since the focus of this work lies on electrical measurements, we will not dwell on the non-electric group of methods but refer the interested reader to [158] and references therein.

5.2.2 Metals

Hot electron populations in metals are generally difficult to probe at room temperature. Supposing a thin metallic film on an insulating substrate, one can assume the system to be composed of three parts: the hot electrons population, a phonon system in the film and a second phonon system in the substrate. These three systems are then coupled, allowing for the energy relaxation of hot electrons towards the metal phonons and of the latter to the substrate phonons. If the coupling between the first two systems is weak a temperature difference between electrons and phonons will arise. At room temperature this difference is however very small and detectable signals would require power levels so high they would vaporise the film [160]. At low temperatures, typically below a few hundred mK, the thermal resistance increases and one can establish a hot electron population in the metal. It can subsequently be investigated e.g. by means of noise thermometry [146, 160]. Due to its small thickness the boundary resistance between metal and substrate phonons can be neglected, establishing $T_{phonon} \simeq T_0$. Subsequently, by probing the current or voltage noise in the sample, the average electron temperature can be extracted from the balance between incoming power and energy loss (see also 5.3.6). Wellstood et al. [160] and Steinbach et al. [146], as well as other

groups not mentioned here for shortness, showed that the cooling power in a metallic film follows a $Q \propto \Sigma(T_e^5 - T_{phonon}^5)$ law, with an electron-phonon coupling constant $\Sigma \simeq 5{\cdot}10^8$ $\mathrm{Wm^{-3}K^{-5}}$. For the 1-dimensional case of a metallic wire [161] found similarly $Q \propto \Sigma T^3$ with $\Sigma \simeq 5 \cdot 10^9$ $\mathrm{Wm^{-1}K^{-3}}$.

5.2.3 Two-dimensional electron gases

In 2DEGs formed at the interface of semiconductor hetereostructures hot electron populations can arise e.g. from electrical heating, similar to the way described priorly for metallic films. Electrical power dissipated in the 2DEG heats up the carriers above T_{phonon}, especially if the sample is cooled to low temperatures. Electron heat diffusion to the cold contacts also provides a cooling pathway but can be suppressed by the choice of sample geometry. A theoretical description of the expected cooling power and its temperature dependence was brought forward by Price [162]: For a piezo-electric coupling of carriers to acoustic phonons he found $Q \propto T_e^5 - T_{phonon}^5$ and $Q \propto T^7$ for deformation potential coupling. This could be confirmed by several groups, e.g. [163], [164] or [165], using Shubnikov-de-Hass oscillations, weak localisation or the thermopower of a 1D constriction.
Besides the above mentioned techniques noise thermometry is often employed to study the electron temperature in 2DEGs. Of particular interest is here the Fano factor $F = S_I/(2eI)$. F depends on the number of transmission channels as well as their transparency (see 5.1.4.2). Hence, QPC are often used here, as they allows for a precise variation of the number of channels [166, 167]. More information on this subject can be found in review [51].

5.2.4 Carbon nanotubes

In CNTs, the physics of carrier excitations and fluctuations can e.g. be studied by probing its resistivity or conductance. Park et al. [168] and Zhou et al. [169] found that the electronic properties of CNTs (metallic or semiconducting) are strongly related to the interaction of carriers with acoustic and optical phonons of the CNT lattice. At low bias APs dominate, while they are replaced by OPs at high bias, both limiting e.g. mobility and resistivity in their respective regime. At low bias the electron-AP scattering represents the lower limit of the carriers' mean-free path, while at high bias the electron-OP interaction results in a current saturation.
Using noise thermometry techniques, a deeper understanding of the phonon and other effects can be gained. Herrmann et al. [170] as well as Wu et al. [171] could effectively employ current noise measurements to investigate the Fano factor in CNT-FETs with

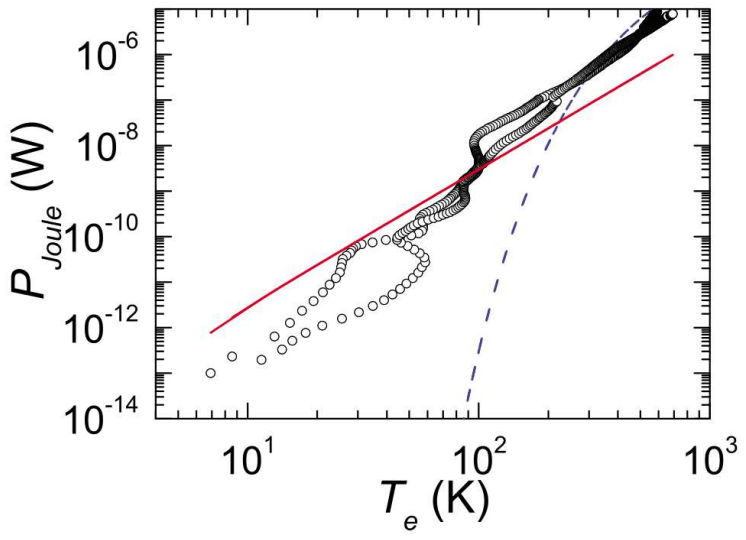

FIGURE 5.7: Joule power $P_{Joule} = I * V_{ds}$ as function of electron temperature $T_e = (FeV_{ds})/(2k_B)$ in carbon nanotubes. Solid and dashed lines are theoretical estimates for acoustic and optical phonon interactions, respectively. From Wu et al. [144].

metallic contacts and confirm the variation of shot noise from the ballistic (no shot noise, $F = 0$) to the diffusive (full shot noise, $F = 1/3$) regime. Also, the cooling of electrons by acoustic and optical phonons has been studied by Wu et al. by means of noise thermometry. They find in particular a $Q = L\Sigma(T_e^3 - T_{phonon}^3)$ cooling power (see Fig. 5.7), where L is the tube's length and Σ the electron-AP coupling constant. Contrary to the T_{phonon} assumption we made earlier for the heat equation in graphene, Wu et al. find $T_e \simeq T_{phonon}$ in CNTs and extract a coupling constant $\Sigma \simeq 3$ nWm^{-1}K^{-3}.

To estimate the final charge detection capabilities of a CNT-nano-FET, Chaste et al. [64] measured the dynamic properties and current noise spectra in the same fashion to the one described in 5.3.6. They found a hot electron population to arise at low bias voltages which manifests as a quasi unitary Fano factor. At higher bias the noise saturates and F drops to values ≤ 1. The current noise cannot be described by the standard Johnson-Nyquist formula, but by an extension of it which also takes into account the transistor's sensitivity to gate potential, the transconductance g_m. From the obtained noise values and the CNT-FET's transconductance and gate capacitance, Chaste et al. finally estimate a charge resolution $\leq 13{\cdot}10^{-6}$ e/$\sqrt{\text{Hz}}$. Even smaller values were achieved by Andresen et al. [172]; here $\delta q_{rms} \simeq 2.3 \cdot 10^{-6}$ e/$\sqrt{\text{Hz}}$.

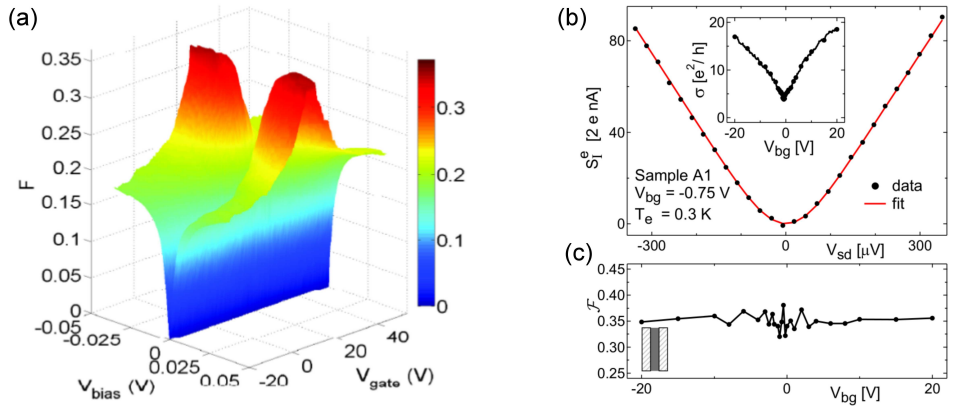

FIGURE 5.8: a) Mapping of average Fano factor as function of bias and gate voltage in a ballistic sample of ratio $W/L = 24$. From [151]. b) Shot noise as function of bias voltage close to CNP in a diffusive sample. c) Average Fano factor as function of gate voltage. Both b) and c) from [173]

5.2.5 Graphene

First shot noise experiments in graphene devices were performed by DiCarlo et al. [173] for diffusive and by Danneau et al. [151] for ballistic graphene samples. The latter use a 600–850 MHz bandwidth dedicated noise measurement setup, calibrated in-situ against the white noise of a tunnel junction. As can be seen from Fig. 5.8(a) the Fano factor rises to $F \simeq 1/3$ at the Dirac point at slightly elevated bias and descends towards 0 with increasing carrier density. Danneau et al. take this as a confirmation of the ballistic nature of the electronic transport and the presence of evanescent waves in the vicinity of the CNP. They find no temperature dependence of the shot noise, which rules out inelastic electron-phonon effects. In the case of diffusive MLG samples DiCarlo et al. confirm the predicted n_s independence of F of diffusive MLG devices [67]. They use the cross-correlation of two current channels at $f = 1.5$ MHz to extract S_I (Fig. 5.8(b)) and subsequently F (Fig. 5.8(c)). Further studies include shot noise characterisation of graphene nano-ribbons [174], where the Fano factor drops to very low values, and high bias measurements of the shot noise in bilayer graphene devices [175]. Both experiments were performed on setups similar to the one in [151].

The topic of hot electrons in graphene has also seen a boost of interest recently due to the realisation of hot electron based detectors [176–180]. Taking advantage of the weak coupling of carriers to APs in MLG very sensitive hot-electron bolometers and calorimeters can be built: For example, Yan et al. present in their work an optical bolometer based on a graphene bilayer that already surpasses conventional Bi/Nb devices [179]. Fong et al. present experiments on MLG bolometers that could lead to a sensitive microwave photodetector [180].

The presence of a hot electron population in graphene devices under bias as a consequence of weak electron-AP coupling leads to two questions: What is the signature of a 2D acoustic phonon interaction? Furthermore, as mentioned above, the electron-AP is supposedly small, but can one find an experimental value for it and how will it compare to theory? We have already answered the first question from a theoretical point of view in section 5.1.2.2: In 2 dimensions one expects the cooling power to have a T^4 dependence. Also the second question could be answered theoretically for the case of LA-phonon interaction, in which case Viljas et al. estimate the coupling constant at $\Sigma_{LA} \simeq 10\sqrt{n_s/10^{12}}$ mW $\cdot$ m^{-2}K^{-4} with n_s in units of cm^{-2}. It will be the subject of the following parts of this chapter to verify said predictions experimentally.

5.3 Experimental techniques

We present in the following measurements of two types of samples: On the one hand a sample obtained from CVD graphene and on the other hand two samples incorporating a stack of exfoliated hBN and graphene. We will label them CVD1, BN1 and BN2 respectively in the following. In this section we will present first of all specific fabrication details and then turn to a description of the noise thermometry setup, comprising the sample holder, the amplification line as well as the calibration and measurement procedure.

5.3.1 Device fabrication

All three samples sit atop a doped Si/SiO_2 substrate which is used as backgate in the experiments. The oxide thickness is 1 μm which results in a gate capacitance per unit area of ~ 35 aFμm^{-2}.

CVD graphene samples The CVD sample presented here is one of several devices fabricated from a CVD graphene sheet grown at the *Laboratoire de Photonique et Nanostructures*. The graphene layer was produced and transferred to the substrate as outlined in chapter 2. Its size of ~ 0.8 cm^2 allowed us to create a large number of devices from the same sheet with variation of channel length and width. After being transferred from the Cu to the Si/SiO_2 and an initial H/Ar annealing, the sheet is etched into rectangles of 100×100 μm^2 size, freeing the substrate around them for metallisation. After forming the first elements of the waveguide (ground planes and drain accesses) by means of e-beam lithography and Cr/Au evaporation (see chapter 2), the remaining graphene rectangles are patterned into the required handle shape, defining channel length, width

and creating large contact pads for the next step. Here, the drain and source contacts are created, using e-beam lithography and Pd evaporation. A final H/Ar annealing allows for a low contact resistance (see below).

sample	$L \times W$ (μm^2)	R(kΩ)	$n_s(10^{12}\,cm^{-2})$	$\mu_c(cm^2V^{-1}s^{-1})$
BN1	2.2×5.7	2.8–3.8	1–2	350
BN2	2.2×2.7	1.3–2.3	0–2	3000
CVD1	1×1	1.67	$\gtrsim 10$	–

TABLE 5.2: Characteristics of the graphene samples. L is the sample length, W the sample width and R the drain-source resistance.

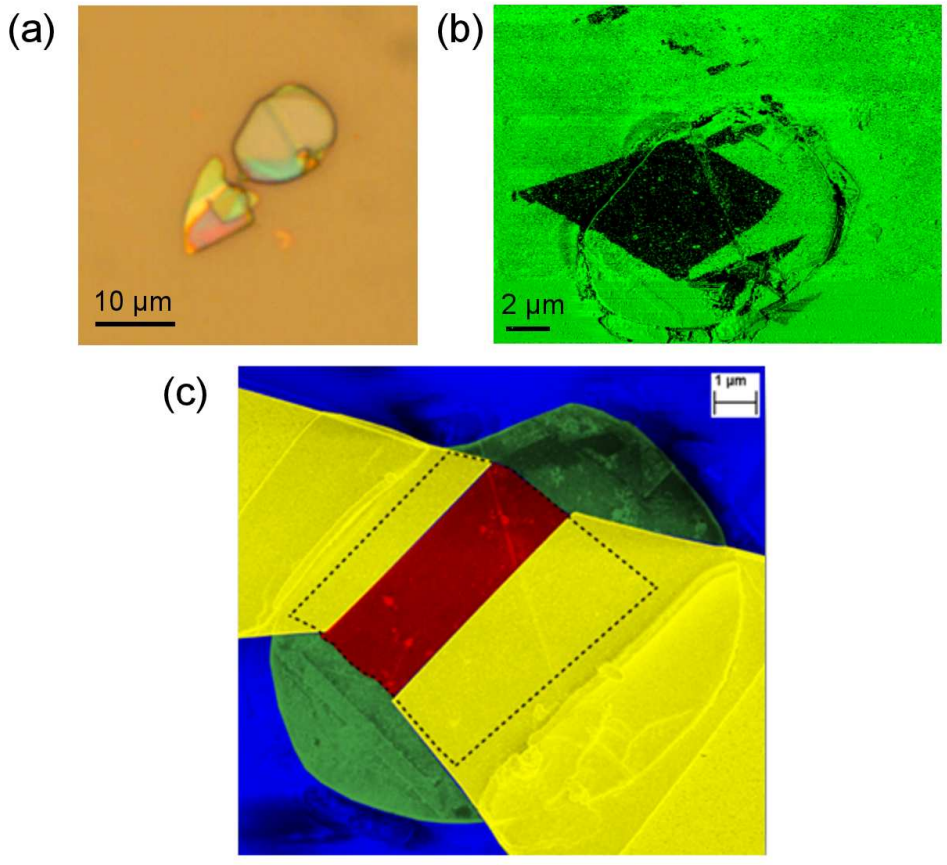

FIGURE 5.9: a) Micrograph of hexagonal boron nitride platelets after exfoliation for sample BN1. b) AFM phase profile showing the outline of the chosen hBN with the MLG on top (black shape). c) Coloured SEM micrograph of BN1. The MLG flake is highlighted in red, the underlying hBN in green itself supported by the Si/SiO_2 substrate (blue). Pd contacts are coloured yellow.

Graphene-on-hBN samples The graphene-on-hBN samples are fabricated in a similar way as their CVD counterparts, with a few differences: Prior to transfer of the graphene flake, hBN platelets are deposited on the substrate by exfoliation from a high quality powder (*St. Gobain* "Très BN", see Fig. 5.9(a)). Among these platelets we optically choose suitable ones of typically 10 μm diameter and $\sim$ 30 nm thickness. We then form the first waveguide elements by e-beam and evaporation and manually place an exfoliated MLG flake on top of the hBN (Fig. 5.9(b)). Here, we employ the wet transfer technique introduced in chapter 2. The MLG is then tailored into the desired shape and the drain-source Pd contacts are patterned (Fig. 5.9(c)). The fabrication is finalised by an H/Ar annealing step.

5.3.2 Sample holder

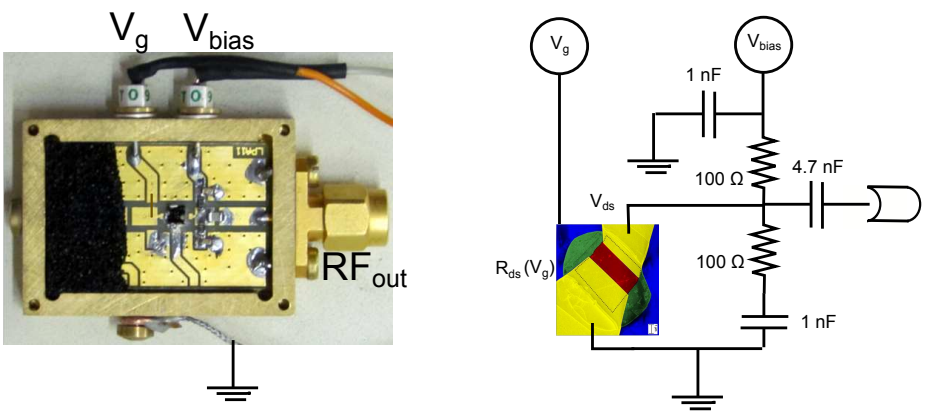

FIGURE 5.10: Picture and circuit diagram of sample holder A3mod. The substrate wire-bonded in the sample holder holds tunnel junctions for setup calibration. The circuit diagram contains a coloured SEM micrograph of sample BN1.

We use a custom made sample holder, calculated and fabricated by A. Denis at the laboratory's electronics workshop, shown in Fig. 5.10. It comprises DC polarisations of gate and drain electrode with integrated capacitive shunts to ground to avoid external high frequency contributions from the DC lines. The RF output is decoupled from the DC by a 4.7 nF capacitance; an effective 50 Ω to ground provide a match to the RF equipment. The samples, their underlying substrate cut to $\sim 2 \times 2$ mm pieces, are fixed on the gate access using Ag paste and wire-bonded to the corresponding metallisations of the sample holder.

5.3.3 Cryogenic setup

The sample, embedded in the sample holder, is then mounted into the cryogenic noise setup. The total setup, shown in Fig. 5.11, consists of the sample holder, a first cryogenic low noise amplifier (LNA), two room temperature amplifiers, an oscilloscope as well as two voltage sources and two voltage meters. It follows the principles established by Chaste et al. [58] and mostly incorporates the same equipment. The voltage fluctuations in the sample's channel are amplified by a nominal 33 dB by the first *Miteq AMFK-2F-001-020* LNA, which is at liquid helium temperature (4.2 K) together with the sample holder. The signal then passes through a second *Miteq* LNA at room temperature and finally a *Agilent Sonoma-310* amplifier before being recorded by the *Agilent Infinium 54854A* oscilloscope. A 3 dB attenuator between each amplifier stage reduces standing wave interferences in the cables. In total we achieve an amplification of $\sim$ 82 dB over a bandwidth of $\sim$ 1 GHz as displayed in Fig5.13(a). See table 5.3 for more details on the amplifiers. The two *Yokogawa 7651* control the drain-source and gate voltage, respectively; the *Keithley 2000* voltmeters are used to record the bias and gate voltage.

stage	*model*	*T (K)*	*gain (dB)*	Δf (GHz)
1	Miteq *AMFK-2F-001-020*	4	30	0.04–2 GHz
2	Miteq *AMFK-2F-001-020*	300	32	0.04–2 GHz
3	Agilent *Sonoma-310*	300	32	0.04–1 GHz

TABLE 5.3: List of amplifiers in the cryogenic setup. The gains were established experimentally by [58].

The amplified electronic noise of the sample is registered as time dependent voltage signal $V(t)$ by the oscilloscope. We use sets of 25 000 samples at a rate of 5 Giga samples/second, which after transformation results in a resolution of 153 kHz in the chosen bandwidth f = 0–2.5 GHz. As described earlier, we can obtain S_{VV} by Fourier transforming the time dependent signal. Here, we use the fast Fourier transformation (FFT) function of the oscilloscope with a Hanning-window correction to account for the finite sampling. It is this FFT spectrum, at given V_{ds} and V_g, that is averaged 2000 times before being analysed.

A particular issue is the effective 50 Ω RF-shunt in front of the amplification line. In

combination with the internal 50 Ω impedance of the first amplifier, noise power is equally divided over both elements. The maximum attainable resolution of our setup is therefore also greatly reduced. However, we avoid impedance mismatch and subsequent reflection problems, as can be seen from the reflection coefficient $\Gamma = (R_{in} - Z_0)/(R_{in} + Z_0)$ [181], where $Z_0 = 50\ \Omega$ and R_{in} is the parallel combination of R_{ds} and 50 Ω. It is this match of impedances that allows us to operate at a very large bandwidth in our experiments, a feature that will be of great advantage in the following.

5.3.3.1 Noise calibration

The setup is calibrated with the white noise of a custom-made Al-AlOx-Al tunnel junction (TJ). Their fabrication process is outlined in Appendix C. The noise of a tunnel junction is Poissonian, i.e. the stochastic tunnelling events are uncorrelated and the Fano factor is 1. The measured voltage power spectral density S_{VV} is thus directly proportional to the drain-source current:

$$S_{VV}^{TJ} \propto 2eI_{ds} \tag{5.23}$$

Taking advantage of this dependence, we proceed with the calibration as follows: The S_{VV} spectra are recorded for different I_{ds} and are obtained by averaging the fast Fourier transformed $V(t)$ signal 2000 times, using a frequency range of 0–2.5 GHz, as detailed above. At each recorded frequency, we perform a linear fit of the S_{VV} data as a function of I_{ds}, as shown in Fig. 5.12. The total noise power is given by the white noise of the tunnel junction and the additional noise of the subsequent amplification line, $S_{VV}^{meas.} = S_{VV}^{TJ} + S_{VV}^{amp.\,line}$. The intersection of the linear fit to $S_{VV}(I_{ds})$ with $S_{VV} = 0$ represents thus the current $-I_{noise}$ producing the equivalent voltage noise as the total cryogenic setup. We will use this quantity, I_{noise}, in the analysis of our noise spectra; for sample holder A3mod it is plotted in Fig5.13(c). From this we can also calculate the equivalent total noise temperature T_{noise} of our setup (Fig. 5.13(b)), by equating shot and Johnson-Nyquist noise and assuming a Fano factor of 1:

$$T_{noise}(\omega) = 4.2\ \mathrm{K} + T_{noise}^{amp.\,line} = \frac{2eI_{noise}(\omega)R_{in}}{4k_B} \tag{5.24}$$

Here, k_B is the Boltzmann constant and the intervening $R_{in} \simeq 50\ \Omega$ is the input impedance of the amplification line. In the usable bandwidth 0.04–1 GHz of our amplification line we therefore estimate an equivalent noise temperature of $T_{noise}^{amp.line} \simeq 8.3$ K. Finally, we also obtain the total amplification G of the line, shown as a function of frequency in Fig. 5.13(a). G is calculated from the slope of the $S_{VV}(I_{DS})$ linear fits,

since the voltage power spectral density arriving at the oscilloscope is given by

$$S_{VV}^{out} = G \cdot \left(2eI_{ds} \left(\frac{50\ \Omega}{2} \right)^2 + S_{VV}^{amp.\,line} \right) \tag{5.25}$$

The total gain is $G \sim 82$ dB in the frequency range 0.04–1 GHz.

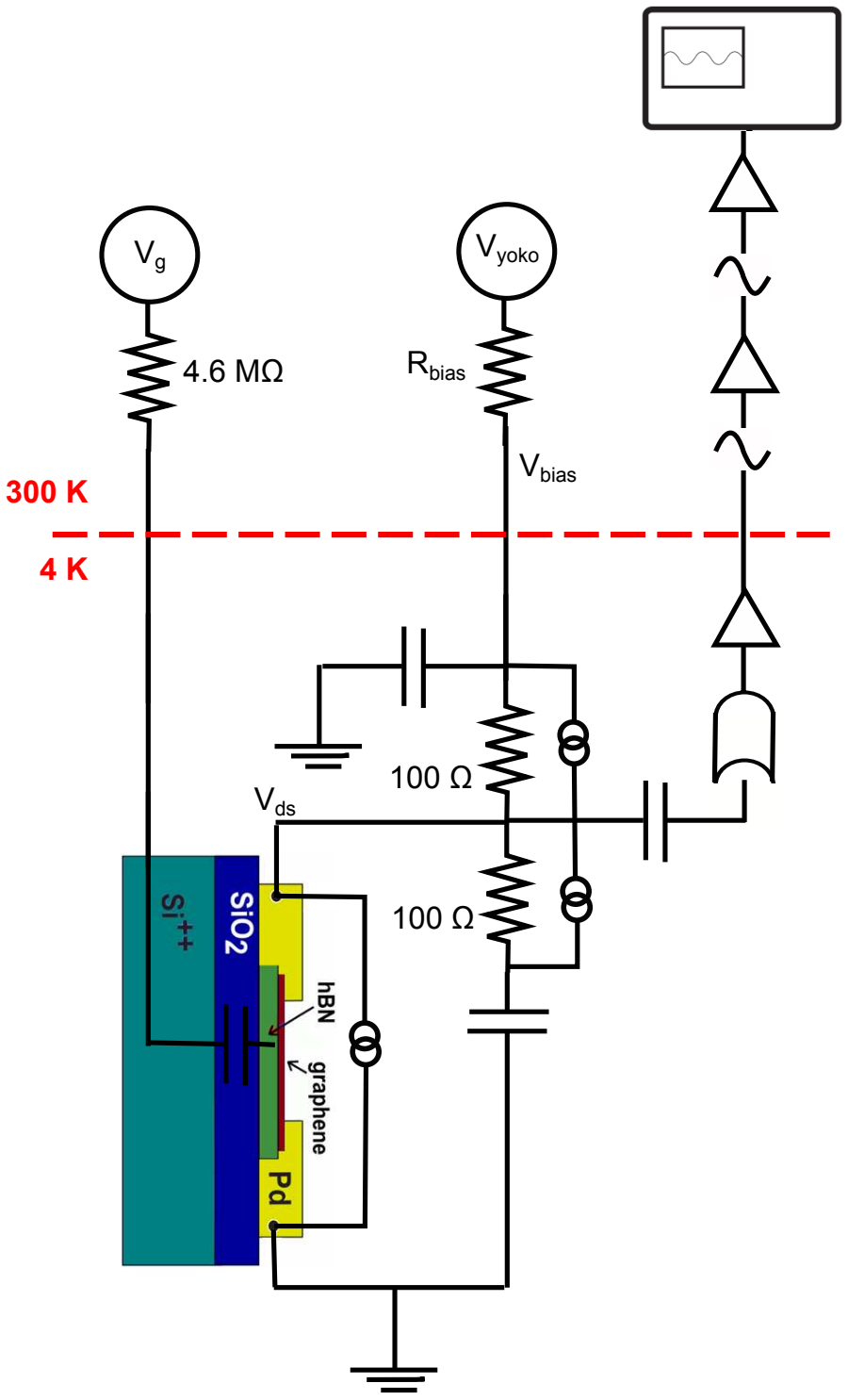

FIGURE 5.11: Schematics of the cryogenic setup.

Noise calibration using Al/AlOx/Al tunnel junction

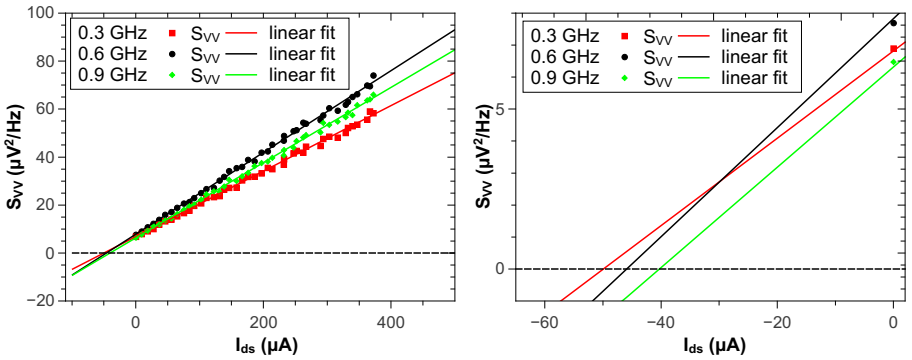

FIGURE 5.12: Calibration procedure: Voltage power spectral density as function of drain source current at three different frequencies in the calibration tunnel junction and corresponding linear fits. Left: Full I_{ds} range. Right: Zoom of region where the linear fits attain $S_{VV} = 0$. The corresponding value of $I_{ds} = I_{Noise}$ (see Fig. 5.13(c)).

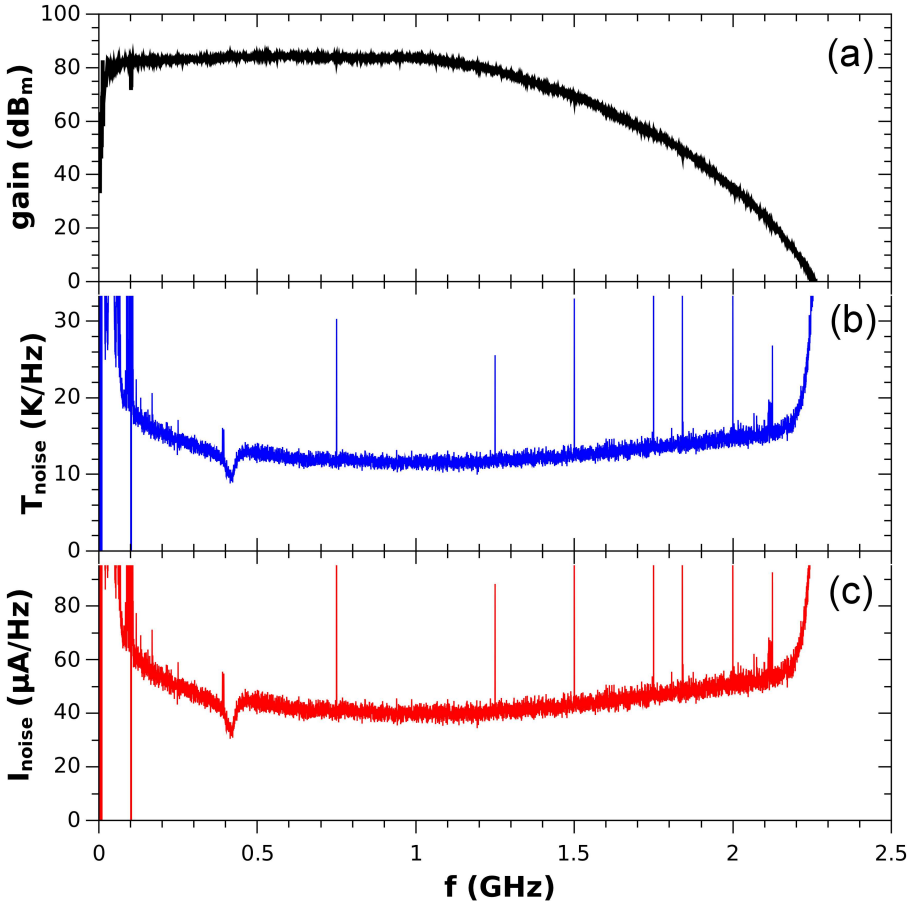

FIGURE 5.13: Calibtration: a) Overall setup gain as function of frequency. b) Equivalent noise temperature of cryogenic setup. c) Equivalent noise current.

5.3.4 Conversion from voltage to current noise spectral density

In order to extract information and draw conclusions regarding e.g. the Fano factor, we need to convert the measured voltage noise spectral density S_{VV} to current noise spectral density S_I. It is here that the calibration intervenes:

$$S_I(\omega) = \left(\frac{S_{VV}(\omega\,,\, I_{ds})}{S_{VV}(\omega\,,\, I_{ds}=0)} - 1 \right) \cdot 2eI_{noise}(\omega) \tag{5.26}$$

in units of A^2Hz^{-1}. It can be derived from the fact that the total output voltage noise arriving at the oscilloscope is $S_{VV}^{out} = S_{VV}^{sample} + S_{VV}^{amp.line}$ and the relation $S_{VV} = S_I R_{input}^{-2}$ connecting voltage and current noise. R_{input} is given by the parallel combination of the sample resistance R_{ds}, the effective 50 Ω to ground in the sample holder and the internal 50 Ω of the first amplifier. In general $R_{ds} \gg 50\ \Omega$, so that typically $R_{input} \simeq 25\ \Omega$. Using the two equations, we then arrive at

$$\begin{aligned} S_I^{sample} &= \left(S_{VV}^{out} - S_{VV}^{amp.line} \right) R_{input}^2 = \left(\frac{S_{VV}^{out}}{S_{VV}^{amp.line}} - 1 \right) S_I^{amp.line} = \\ &= \left(\frac{S_{VV}^{out}}{S_{VV}^{amp.line}} - 1 \right) 2eI_{noise} \end{aligned} \tag{5.27}$$

For convenience of analysis and to account for changes in the spectrum due to the substitution of the TJ with the sample, we replace $S_{VV}^{amp.line}(\omega)$ by $S_{VV}^{sample}(\omega\,,\, I_{ds}=0)$. A difference between the two is an indicator of problems within the setup, as e.g. badly connected cables. The TJs sit atop a highly resistive Si/SiO_2 substrate in contrast to the samples, where we use doped silicon substrates. An effective screening due to currents in the doped silicon in the area beneath the sample could therefore arise and not be taken into account by the calibration. A direct comparison of through line experiments (i.e. S-parameter measurements of coplanar waveguides with connected drain and gate pads, Fig. 5.14) on doped and resistive substrates shows that such an effect is of minor importance: the doped silicon layer induces a capacitive decrease of the transmitted signal of $\lesssim 10\%$ in the frequency range of interest $f = 0$–1 GHz. Note that here both electrodes contribute to the screening, in contrast to our samples, where one electrode is connected to ground. Therefore, we only have to take half of the effect into account, i.e. the calibration process and the change of substrate induces an uncertainty of $\lesssim 5\%$.

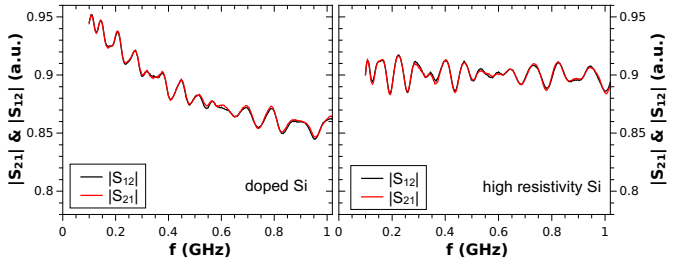

FIGURE 5.14: Comparison of through line tests on doped and resistive substrate in the frequency range of interest for our noise measurements

5.3.5 DC characterisation

In our noise thermometry measurements we record the DC characteristics of the samples in much the same way as described in the previous chapters on RF-GFETs and GFECs: We applied a voltage V_{yoko} to the ensemble of bias resistance R_{bias}, sample holder resistance $R_{sh} = 100\ \Omega$ and the sample (R_{ds}). The voltage at the sample holder drain-source input is labelled V_{bias} and is measured with a *Keithley 2000* voltmeter. Knowing the exact value of $R_{bias} = 4735\ \Omega$, we extract the drain-source current and resistance from this measurement:

$$R_{ds} = \frac{V_{bias}}{V_{yoko} - V_{bias}} R_{bias} - R_{sh} \qquad I_{ds} = \frac{V_{yoko} - V_{bias}}{R_{bias}} \tag{5.28}$$

These DC measurements will allow is in the following to extract the samples' I-V curves and draw first conclusions on the presence of optical phonons.

The backgate is controlled by the second *Yokogawa* source which applies V_g on the ensemble of gate resistance 4.6 MΩ and the sample's gate. The voltage usually entirely drops across the gate resistance; it is verified with the second voltmeter to prevent oxide breakdown. This procedure is especially important when using thin oxides. In our case of $t_{ox.} = 1\ \mu$m no real danger of breakdown prevails in the accessible gate range of $V_g = \pm 32$ V. As detailed in the previous chapters, the sweeping of gate voltage allows us also to deduce the carrier density $n_s \simeq e^{-1} C_g V_g$, where C_g is the gate capacitance. Finally, we can extract mobility values from the dependence of conductivity on gate voltage

$$\mu_c = \frac{1}{C_g} \frac{\partial \sigma}{\partial V_g} \tag{5.29}$$

This remains valid as long as there is no important contact resistance contribution. To ensure this being the case for our samples, A. Inhofer [103] performed a statistical analysis of the resistance of CVD-grown samples with various channel lengths. The results, presented earlier in chapter 3 and also in Fig. 5.15, show that interface resistance can be neglected compared to typical sample resistance (see table 5.2).

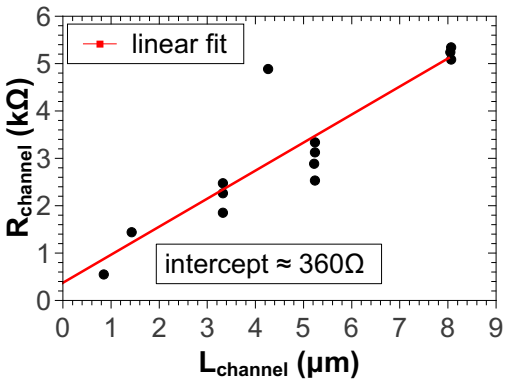

FIGURE 5.15: Estimation of contact resistance from $R_{channel}(L)$ measurements in back-gated CVD samples of channel width $W = 1$ μm [103].

5.3.6 Experimental investigation of electron-acoustic phonon cooling

After this introduction to formulas, mechanisms and the cryogenic setup, let us briefly summarise how we intend to extract information from our noise thermometry experiments and what signatures we are looking for in terms of electron-acoustic phonon coupling in graphene. As depicted schematically in Fig. 5.16, the applied bias $V \equiv V_{ds}$ supplies a power $P = V^2/R$ to the electrons in the MLG channel (grey). The electrons will therefore acquire a temperature T_e corresponding to their energy, which will in turn be responsible for the current noise S_I. It is thus from the noise spectral density that we can extract the electron temperature and try to confirm the $P \propto \Sigma T^4$ dependence of the cooling power due to electron-acoustic phonon interaction. For a direct coupling of electrons in the channel with substrate phonons, we rather expect the cooling power to have a T^5 dependence. The scenario we envision is sketched in Fig. 5.17: Electrons will interact with the 2D acoustic phonons of the MLG at a certain strength. The phonons in turn are coupled to the substrate, which is at liquid helium temperature $T_0 = 4.2$ K. The theoretical prediction by Viljas et al. [24] for the e-AP interaction and [182] for the coupling of APs to the substrate tell us that $\Sigma_{e-AP} \ll \Sigma_K$. The index K denotes the coupling at the graphene-SiO_2 thermal boundary, also-called *Kapitza* boundary. We will therefore expect hot electrons ($T_e \gg T_0$) and a cold phonon population ($T_{phonon} = T_0$) in addition to the T^4 law. According to calculations by Persson et al. [183] contributions that arise due coupling of the MLG to the surrounding gas or to the underlying (R_{e-K} in Fig. 5.17) substrate can be neglected.

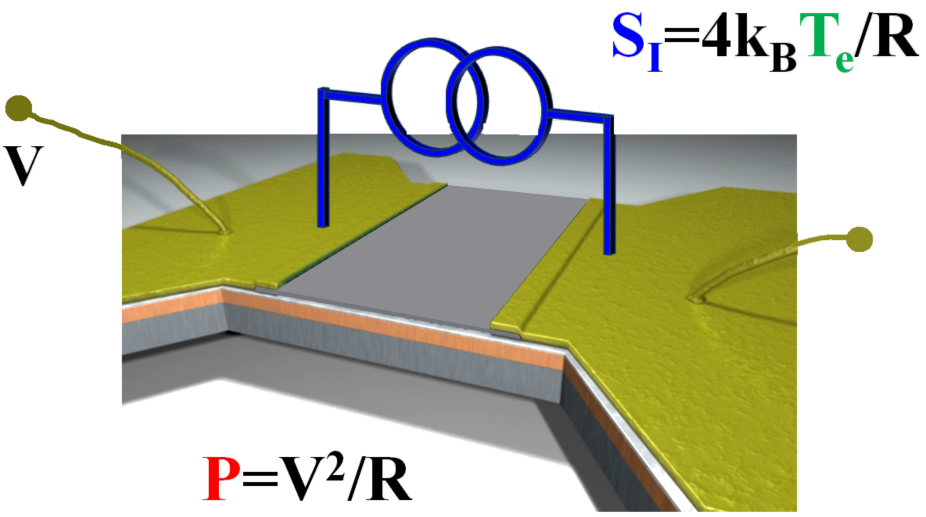

FIGURE 5.16: Principle of electron-acoustic phonon cooling experiment.

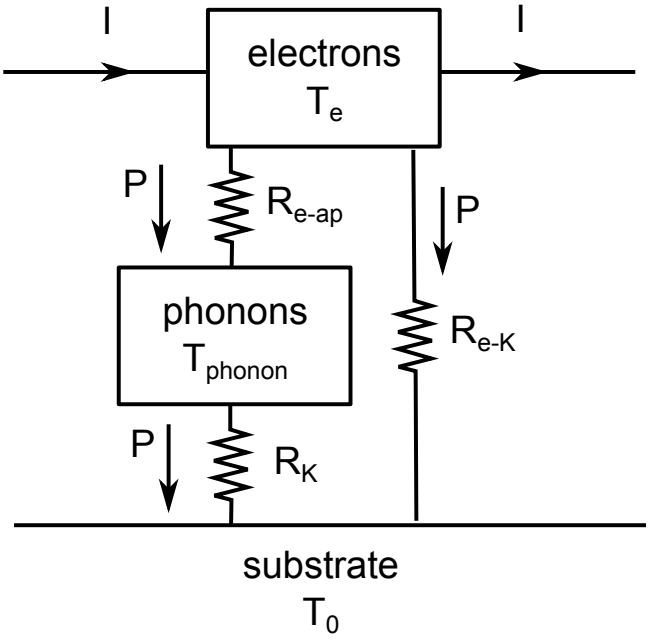

FIGURE 5.17: Simple model of heat transfer from electrons to phonons to substrate. Analog [160].

5.4 Results and discussion

Let us now turn to the results obtained for three different samples using the cryogenic setup and techniques described above. We will first of all present and analyse the DC characteristics and current noise spectra of the samples BN1, BN2 and CVD1. Then, we will show how the signatures of the 2D electron-acoustic phonon cooling emerge from the

electron temperature curves and analyse our findings with respect to the electron-AP cooling constant Σ [26]. As a final part to this section on experimental results, we will discuss additionally the Fano factor in our samples, as well as new effects close to the charge neutrality point.

5.4.1 DC characteristics

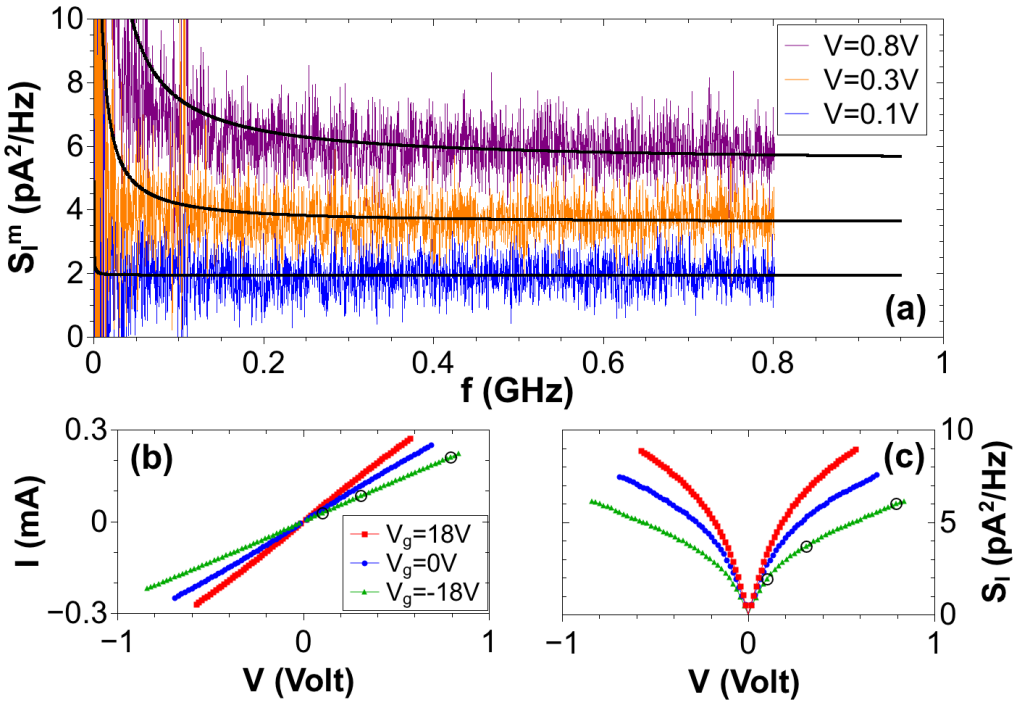

FIGURE 5.18: (a) Typical excess noise $S_I^m(V)$ spectra in sample BN1; it is a white noise with a superimposed $1/f$ contribution and fitted by $S_I^m = S_I + C/f$ laws (solid lines). (b) and (c) show the $I(V)$ and $S_I(V)$ data for different gate voltages in sample BN1 from which we deduce T_e. The circles point out the $I(V)$ and $S_I(V)$ values of the spectra shown in (a).

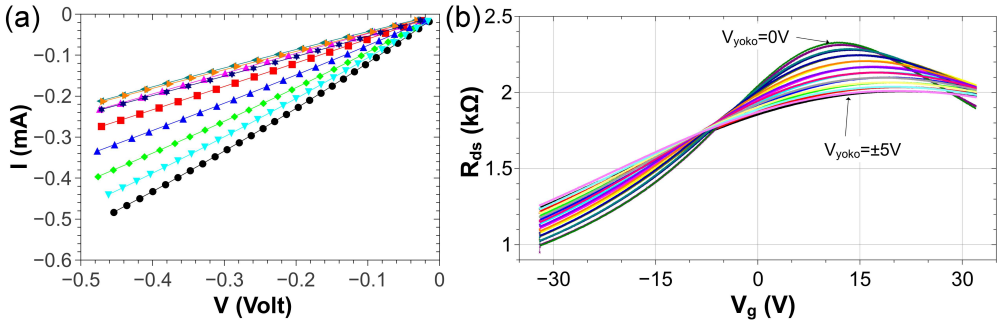

FIGURE 5.19: a) I–V characteristics of sample BN2 for several gate voltages. b) DC drain-source resistance as function of gate voltage in sample BN2 for a range of bias voltages.

As pointed out in the beginning of this chapter, optical phonons (OPs) cause a saturation of the drain-source current in MLG devices. However, this effect starts from a certain threshold voltage as the OP energy is $\sim$ 200 meV (see also Fig. 1.14). In order to study the acoustic phonon effect only, we deliberately restrict our measurements to a bias range where OPs can be neglected. The linear I–V characteristics of our samples are indicators of the required absence of OP scattering. In Fig. 5.18(c) we display the I–V curves of sample BN1 for three gate voltages, in Fig. 5.19(a) for sample BN2. Their linearity is a first sign for a cooling mechanism other than by OPs. In Fig. 5.19(b) we plot the drain-source resistance of sample BN2 as a function of gate voltage V_g. The charge neutrality point is at $V_g \simeq 12$ V

5.4.2 Current noise spectra

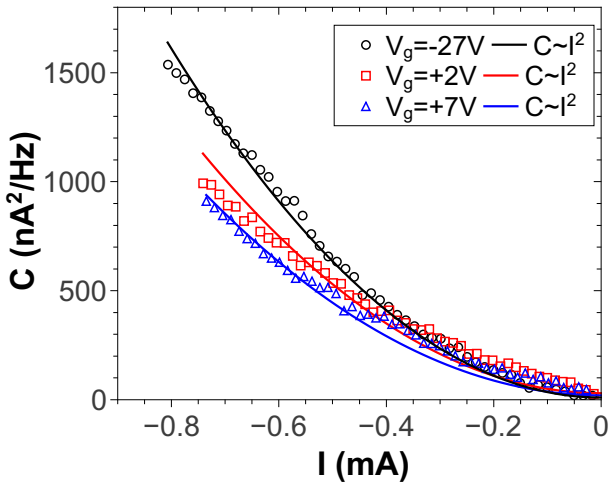

FIGURE 5.20: Hooge parameter $C = \alpha_H I^2/N$ in sample BN2 from $C/f + S_I$ fits as function of drain-source current. Solid lines are quadratic fits to the data.

Employing the noise measurement techniques described previously and after conversion from voltage to current noise spectral density, we obtain typical current noise spectra as shown in Fig. 5.18(a). Here, S_I is displayed for three different bias voltages as a function of frequency. At low bias (blue spectrum) the spectrum remains flat without prominent variation, as e.g. $1/f$ noise. As introduced earlier, flicker noise is proportional to I^2 and in addition to the frequency independent shot noise. Therefore, a clear $1/f$ contribution to the spectra arises at higher bias (orange and purple spectra). It is here that the large bandwidth of our setup comes in handy: Despite a low resolution, especially at low bias, we are now able to precisely and quantitatively separate the white shot noise from the

flicker noise contribution by fitting the spectra with

$$S_I^m = \frac{C}{f} + S_I \tag{5.30}$$

where additionally $C = \alpha I^2/N$ in accordance with Hooge's relationship (see Fig. 5.20). Here, N is the number of carriers. The fits appear as solid lines in Fig. 5.18(a). It is especially important to perform these fits for small samples size, since $C \propto 1/N$ and therefore in particular for sample CVD1, and at high bias, since $C \propto I^2$.

From the $1/f$ component of the current noise spectra, we extract a Hooge constant α_H of the order of $2 \cdot 10^{-4}$ at $n_s \simeq 1 \cdot 10^{12}$ and $8 \cdot 10^{-6}$ at $n_s \simeq 8 \cdot 10^{10}$, close to the CNP [1]. This is in accordance with the reported $\alpha_H \propto n_s$ dependence, mentioned earlier [157].

The frequency independent shot noise part S_I of the spectra is displayed as a function of drain-source voltage in Fig. 5.18(c) for three gate voltages. It is again a typical example for all measured samples and gate voltages. Schottky's formula $S_I = 2eI\tilde{F}$, where $\tilde{F}$ denotes a pseudo Fano factor, predicts a linear increase of S_I in an undisturbed system. However $S_I(V)$ in Fig. 5.18(c) is clearly sub-linear, i.e. a noise reduction mechanism is present. The noise level also depends on gate voltage, thus carrier concentration, with larger noise at higher n_s. As pointed out above, optical phonons are out of reach in the investigated bias range and acoustic phonon cooling remains a valid candidate for the present effect.

5.4.3 Electron temperature T_e

From the measured shot noise (Fig. 5.18(c)) we can now extract the average electron temperature as a function of bias

$$T_e(V) = \frac{S_I(V)R(V)}{4k_B} \tag{5.31}$$

which we display in Fig. 5.21 for BN1 and in 5.22 for BN2 for several gate voltages. In both cases T_e reaches values of several hundred K within the investigated bias range of linear I–V [2]. This is well above bath temperature (4.2 K) and indicates a hot electron population; a signature of acoustic-phonon cooling we were looking for. Fig. 5.21 also indicates the corresponding energy, which remains well below the OP activation energy of ~ 200 meV and suggests again the absence of OP cooling.

The main signature we are expecting for a 2D AP-cooling mechanism is, as described earlier, a T_e^4 dependence of the cooling power. In the absence of heat conduction to the

[1] Note that the estimate is less accurate at neutrality due to underestimation of n_s and therefore also of $\alpha \propto Cn_s$.

[2] Here R signifies strictly speaking the differential resistance which may differ from the standard Ohmic resistance in sample BN2 where I-V curves become slightly non-linear (see Fig. 5.19).

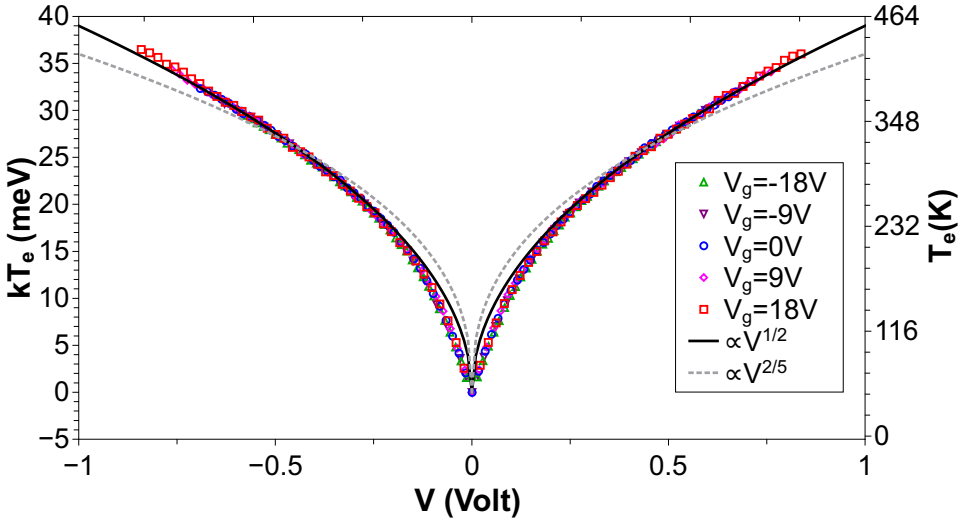

FIGURE 5.21: Electronic temperature in sample BN1 as function of voltage bias for a set of gate voltages. $T_e = S_I V/(4k_B I)$ is deduced from the $S_I(V)$ and $I(V)$ data shown in Fig. 5.18(c) and (b). Unlike $S_I(V)$, $T_e(V)$ is nearly independent of gate voltage and closely follows the $T_e \propto \sqrt{V}$ law (black solid line) expected for 2D phonons. A $T_e \propto V^{2/5}$ law (grey dashed line) is also plotted to highlight the difference with a standard 3D-phonons mechanism. Deviations are observed at low bias where a $T_e \propto V$ behavior is found.

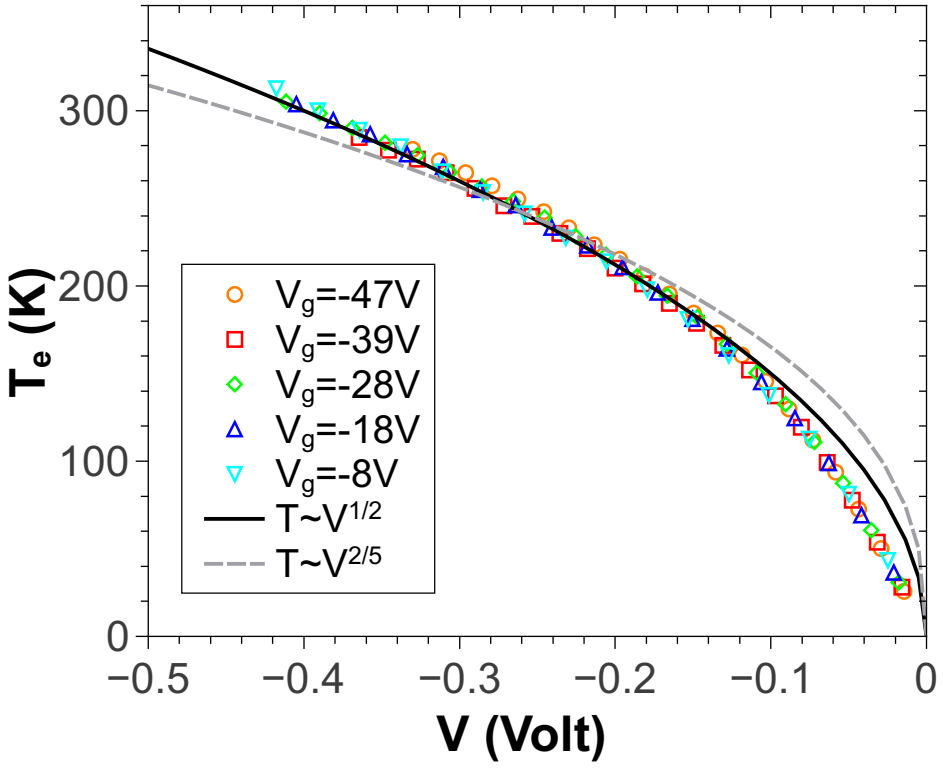

FIGURE 5.22: $T_e(V)$ in sample BN2. The solid line indicates the $T_e \propto \sqrt{V}$ expectation, the grey dashed line the $T_e \propto V^{2/5}$ law in case of 3D-phonons.

leads, i.e. neglecting the left-hand side in Eq. (5.13), one expects a $T \propto \sqrt{V}$ dependence of right-hand side temperature term of (5.13). If the cooling were to involve 3D-phonons, the same reasoning leads to a $T \propto V^{2/5}$ dependence. As can be seen from Figs. 5.21 and 5.22, we obtain a very good agreement of data with the $T \propto \sqrt{V}$ expectation for a 2D acoustic-phonon effect, up to a small region around zero bias, where heat conduction to the contacts is of greater importance and we rather find $T \propto V$. A more detailed discussion of this effect will be given later on. 3D-phonons can be disregarded in the cooling of electrons in our graphene samples, as is visible from the $T \propto V^{2/5}$ lines in Figs. 5.21 and 5.22.

We have thus found two of the signatures mentioned previously for 2D acoustic-phonon cooling of electrons in graphene: The hot electrons and the T_e^4 dependence of cooling power [26].

5.4.4 Raman verification of cold phonon hypothesis

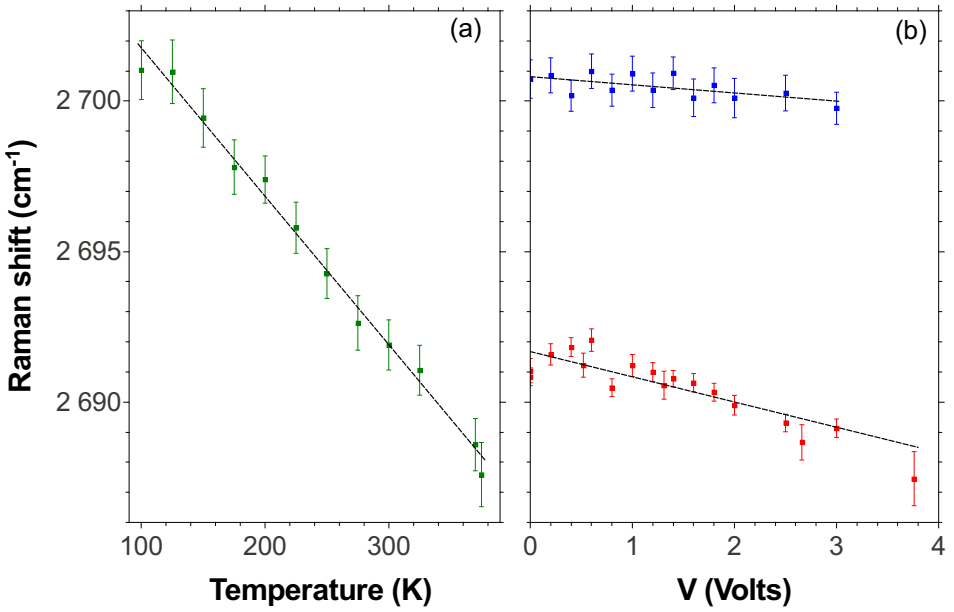

FIGURE 5.23: (a): Raman shift of the 2D-band of a graphene sample similar to CVD1, as function of the cryostat temperature T_0. The slope is (-0.051 ± 0.008) cm^{-1}K^{-1}. Excitation laser at 532 nm , $P = 25$ kWcm^{-2}. No laser power dependence was observed in this range. (b): Raman shift of the 2D band as function of the bias voltage for $T_0 = 100$ K (blue symbols) and $T_0 = 300$ K (red symbols). The slopes are (-0.3 ± 0.3) cm^{-1}V^{-1} and (-0.9 ± 0.3) cm^{-1}V^{-1} respectively. The bias-induced phonon heating is therefore below 30 K/V. Similar results and conclusions were drawn from measurements on the G band (not shown).

Another signature we pointed out in section 5.3.6 was a cold phonon population. We have already used this assumption in the solution of the heat equation and we will now

present quantitative reasoning as well as experimental data to support it.
The sought after ΣT_e^4 law for the electron-AP cooling is similar to the black body radiation of phonons to the helium bath or Si/SiO_2 substrate (both at $T_0 = 4.2$ K). In the black body radiation case one also expects a $\Sigma_K T_{phonon}^4$ law, where Σ_K is the coupling constant related to the thermal boundary resistance. Such a mechanism would occur in a hot phonon regime, i.e. $T_{phonon} \simeq T_e \gg T_0$. The corresponding coupling constant is however several orders of magnitude larger than Σ for AP cooling [182, 184]. Further, as both mechanisms appear in series and with the same power law in the electronic cooling, one obtains an effective coupling constant

$$\tilde{\Sigma} = \left(\Sigma_K^{-1} + \Sigma^{-1}\right)^{-1} \simeq \Sigma \tag{5.32}$$

This justifies the cold phonon assumption made earlier from a order of magnitude point of view.
In order to confirm the cold phonon hypothesis also experimentally, we have performed Raman spectroscopy experiments on sample BN1 in collaboration with F. Vialla, D. Brunel and C. Voisin from the LPA "Optique cohérente et non-linéaire" group. The down-shift of the Raman G and 2D peak positions is recorded as a function of sample temperature or bias voltage, respectively, using an excitation laser of wavelength 532 nm and power 25 $kWcm^{-2}$, as well as a nitrogen cooled CCD camera *Princeton Instruments Spec-10:100BR*. The bias is supplied in the same way as in the noise measurements. The experimental procedure follows the description by Calizo et al. [185]: First a calibration of the signal is performed at $V = 0$ by measuring the Raman shift for different sample temperatures. Then, we repeat the experiment but keep the substrate temperature at a constant level T_0. Instead of creating a thermal phonon population, we now apply a bias to the sample, which in turn creates hot electrons interacting with the graphene phonons. We can thus extract the phonon temperature that is equivalent to the same change in Raman signal as the one created by the bias voltage by comparing both experiments. Indeed, one can extract information about acoustic phonons from this kind of optical measurement as optical phonons decay into acoustic phonons with anharmonic decay rates [50].
In our calibration experiment the position of the Raman 2D-peak shifts 0.051 ± 0.008 $cm^{-1}K^{-1}$ downwards upon increasing the sample temperature from 100 to 380 K (Fig. 5.23(a)). This is in good agreement with previous measurements by e.g. [185]. Secondly, we have kept the sample at a fixed temperature of $T_0 = 100$ (blue symbols) and 300 K (red symbols) and varied the bias voltage. As one can see from Fig. 5.23(b), a similar decrease of Raman shift occurs, which is attributed to an increase of AP bath temperature. We find thus slopes of -0.3 ± 0.3 $cm^{-1}K^{-1}$ at $T_0 = 100$ K and -0.9 ± 0.3 $cm^{-1}K^{-1}$ at $T_0 = 300$ K, from which we deduce that the bias induced phonon heating remains below

30 K/V. Measurements of the Raman G-peak are similar and not shown here.
To put it in a nutshell, we have found yet a third key element signalling the presence of 2D AP cooling: the cold phonon population. It also validates leaving out T_{phonon} in the solution of the heat equation and strengthens the T_e^4 evidence we found in the previous paragraph.

5.4.5 Acoustic phonon coupling constant Σ

Besides the acoustic-phonon cooling discussed above, electron heat conduction to the contacts is the second cooling mechanism in our devices, mainly contributing at low bias. The balance between these two mechanisms and the incoming Joule power per unit area $P = V^2/(LWR)$ determines the average electron temperature T_e in our samples. Above, we have neglected the heat conduction contribution, i.e. the left-hand side term of Eq. (5.13). We will now present data analysis using the complete heat equation. To this end we plot in Figs. 5.24 and 5.25 temperature data in the form T_e^4/P, in order to enhance the carrier density dependence of the electron-AP coupling constant Σ. In this particular representation the high bias plateaus are a first estimate of Σ, since there $T_e^4/P \simeq 1/\Sigma$. They directly reflect the $T_e \propto \sqrt{V}$ dependence found earlier. A T^5/P representation of the data does not produce a saturation behaviour (see appendix F). The dips towards lower bias are caused by the here dominating electron heat diffusion to the contacts, reflecting the low bias $T_e \propto V$ dependence in Figs. 5.21 and 5.22. As one can see from Figs. 5.21(a) and (b), the electron heat conduction is more prominent in sample CVD1. This can easily understood from Eq. (5.13): The phonon cooling will be of greater importance the larger the sample area. Due CVD1's small size, phonon cooling remains comparatively weaker than in BN1 and BN2, but also exhibits a smoother crossover between the two regimes.
Using the solution of (5.13), we can now fit the temperature data under consideration of both AP cooling and heat conduction (solid lines in Figs. 5.21(a), (b) and 5.22). The only free parameter is the phonon coupling constant Σ and data is well fitted over the whole bias range. The fact that theory, with one single free parameter, accounts for both the plateau region and the dip is a strong confirmation of the model and the underlying 2D acoustic phonon mechanism. At high bias we do however also observe small negative deviations of data from the theoretical prediction; they may be caused by the onset of an additional cooling mechanism. It is possible that electrons couple here to optical phonons or phonons from the Si/SiO_2 substrate despite their still low average energy. Unfortunately, our experimental resolution at high bias is not good enough to give an conclusive answer to this question and further studies will be necessary to shed light on this particular subject.

Error bars in Figs. 5.21(a) and (b) are calculated from the deviation of the $C/f + S_I$ fits with respect to the S_I-spectra presented earlier. We calculate the deviations according to

$$\sigma_{S_I} = \sqrt{\frac{1}{N_f}\sum_{i=0}^{N_f}\left(S_I^m(V,f_i) - \left[\frac{C(V)}{f_i} + S_I(V)\right]\right)^2} \tag{5.33}$$

where i runs along the number of frequencies N_f recorded in the measurements and f_i denotes the precise frequency at each step. We then transfer this error in spectral density to an error in temperature by equating

$$\frac{\sigma_{S_I}(f)}{C(V)/f + S_I(f)} \equiv \frac{\delta T_e}{T_e} \tag{5.34}$$

Due to the T^4/P representation, a factor 4 intervenes additionally. Finally, we decrease the total error by a factor $\sqrt{2}$, as there are two erroneous quantities at play here. It is important to note that high bias and small sample size introduce a more pronounced $1/f$ contribution. This is why we see errorbars growing stronger in the CVD1 sample. Samples BN1 and BN2 are much larger and $1/f$ subtraction is less important here.

From the fits to the temperature data and the simultaneously recorded DC characteristics, we can now extract quantitative values of the acoustic-phonon coupling constant Σ as a function of carrier density. For all three samples this is plotted in Fig. 5.26. Note that we were not able to sweep CVD1's carrier density; the value of $\Sigma(CVD1)$ is thus merely an indicator in the plot. Hall-bar measurements on similar CVD sheets by Madouri et al. at the LPN allows us to estimate CVD1's carrier density to a few 10^{13} cm^{-2}. For samples BN1 and BN2 we use (3.2) to obtain n_s.

According to theory (see 5.1.2), longitudinal acoustic phonons (LA) are coupled to electrons via the deformation potential D. D ranges typically from 10 to 30 eV in experimental studies, but a recent theoretical work by Kaasbjerg et al. [142] suggests an even lower value of 6.8 eV. The cooling power of the 2D electron-LA interaction is predicted to follow a $P \propto \Sigma_{LA} T^4$ law, with $\Sigma_{LA} \propto D^2\sqrt{n_s}$ in the non-degenerate metallic regime. In the high temperature regime and close to the CNP deviations from the T^4 dependence are expected, which we will discuss in greater detail in the following. The $\Sigma_{LA} \propto \sqrt{n_s}$ expectation is fulfilled for carrier densities not too close to the Dirac point, as can be seen from Fig. 5.27. Here, we plot the extracted AP coupling constant as a function of $\sqrt{n_s}$ and find reasonable qualitative agreement with the theoretical prediction down to carrier concentrations $n_s \simeq 2.5 \cdot 10^{11}$ cm^{-2}.

As calculated earlier, we quantitatively estimate $\Sigma_{LA} \simeq 10\sqrt{\tilde{n_s}}$ mW $\cdot$ m^{-2}K^{-4} for a deformation potential $D = 10$ eV. Despite the qualitative confirmation of the T^4 law and the $\Sigma \propto \sqrt{n_s}$ dependence, we find a smaller coupling constant in our samples than predicted by theory: At a carrier density of 10^{12} cm^{-2}, sample BN1 exhibits

$\Sigma = 0.5$ mW $\cdot$ m^{-2}K^{-4} and BN2 $\Sigma = 2$ mW $\cdot$ m^{-2}K^{-4}. Simple experimental uncertainties are not large enough to explain this discrepancy. Our experimental data rather suggests an effect of lattice disorder on the electron-phonon coupling: The carrier mobility can generally be used as a measure of crystal quality, since disorder, i.e. defects of any kind in the crystalline structure, introduces scattering centres and leads to a decrease of μ_c. Generally, electronic and phononic disorder are not necessarily the same, however due to the 2D nature of graphene, we can use the electronic disorder as a measure of lattice disorder. Following this reasoning, it is clear from Fig. 5.26 that the lattice disorder, expressed by μ_c, plays an important role in the electron-AP coupling: Increasing crystal quality, i.e. improving carrier mobility, goes along with an increase of Σ in direction of the theoretical value. This disorder effect, not taken into account in theory [24] yet, could be a manifestation of e.g. reduced phonon lifetime. Indeed, lattice disorder is known to affect phonon heat conduction due to phonon-impurity scattering [182]. A second possibility is a change in phonon DOS: In graphene the phonon DOS is similar to the electron DOS, i.e. linear and vanishing at zero energy. Localised phonon states introduced by disorder in the lattice can lead to the opening of a gap at low energy, as e.g. discussed in [186] for the case of graphene ripples. According to [158] the phonon cooling is proportional to the phonon DOS at the electronic temperature T_e. A reduces coupling constant Σ could thus be related to a depletion or the opening of a gap in the phonon DOS due to disorder in the lattice. A more thorough theoretical investigation is needed to explain the found mismatch between experiments and theory.

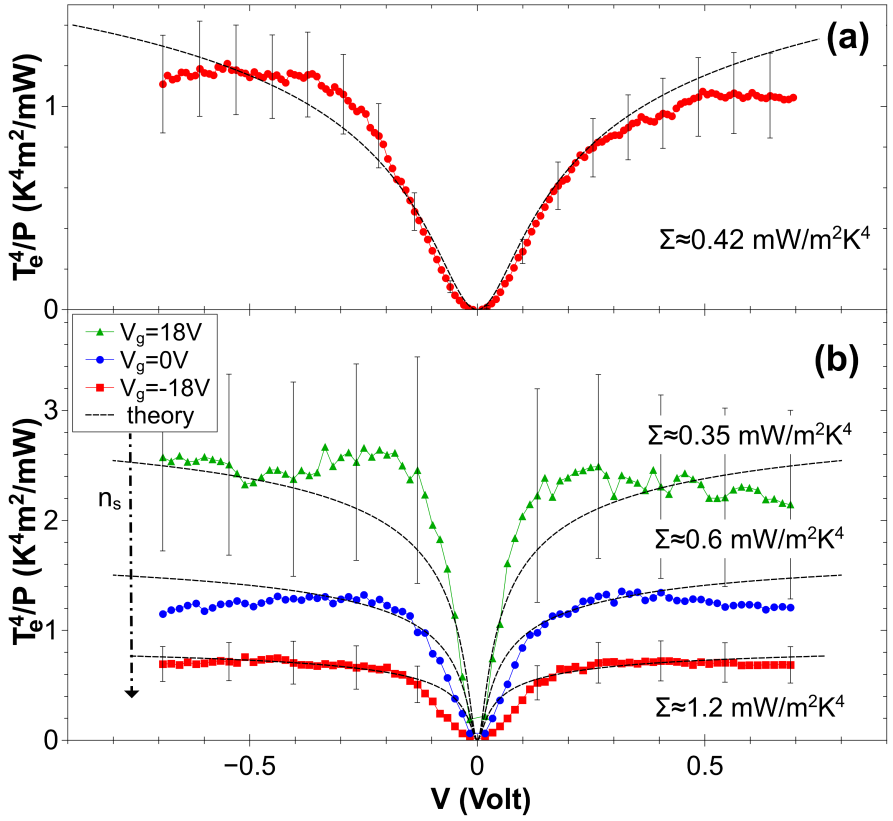

FIGURE 5.24: (a) and (b): Electron temperature of sample CVD1 (a) and BN1 (b) plotted as $T_e^4(V)/P$, where P is the Joule heating per unit area, $P = V^2/RLW$. The plateau at high bias is at a value $T_e^4/P \simeq 1/\Sigma$. The dip at low V is due to electron heat diffusion to the leads. Dashed lines are one-parameter fits with Σ as free parameter.

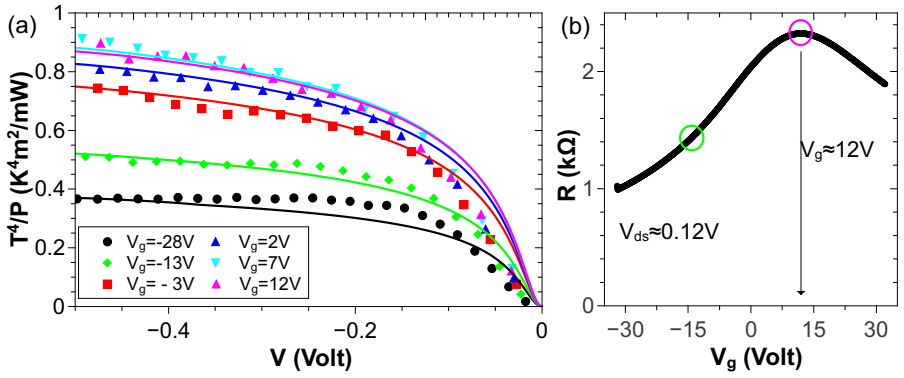

FIGURE 5.25: a) Electron temperature of sample BN2 plotted as $T_e^4(V)/P$ and their one-parameter fits. b) Sample BN2's drain-source resistance as function of V_g to indicate metallic regime (green circle) and CNP (pink circle).

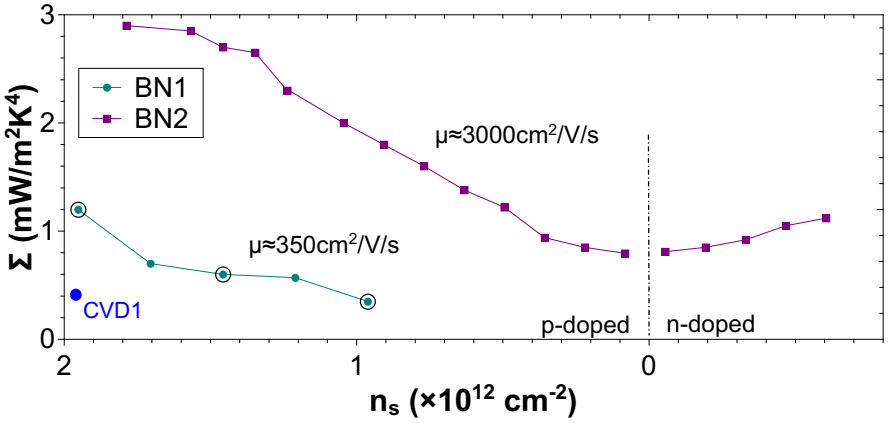

FIGURE 5.26: Σ as function of carrier density n_s for samples BN1 and BN2. The value of CVD1 is displayed as an indicator as its carrier concentration was $n_s \simeq 10^{13}$ cm^{-2}.

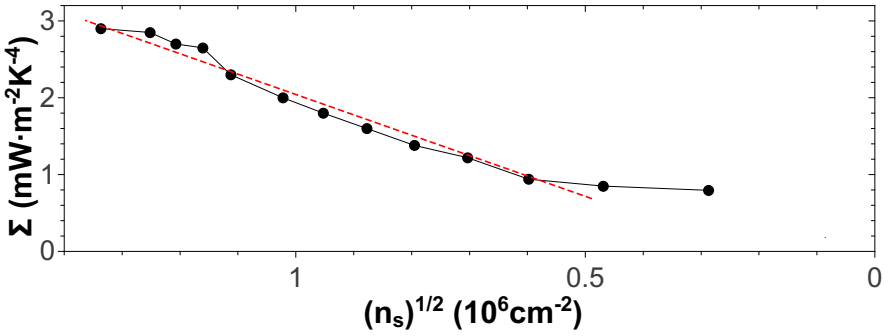

FIGURE 5.27: Σ as function of carrier density $\sqrt{n_s}$ for sample BN2. The red line indicates the predicted $\Sigma_{LA} \propto D^2\sqrt{n_s}$ behaviour.

5.4.6 Fano factor analysis

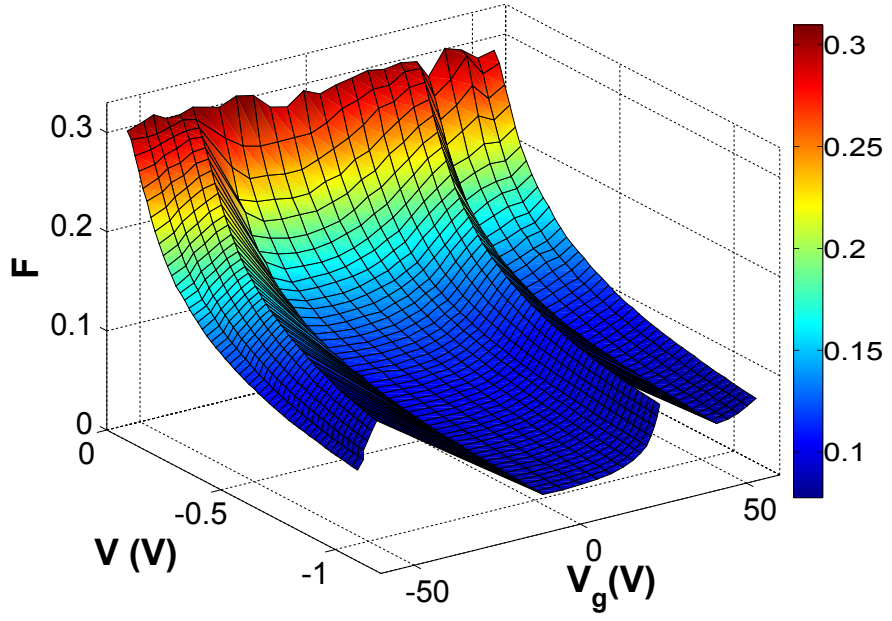

FIGURE 5.28: Fano factor as a function of gate voltage V_g and drain-source voltage V_{ds} (previously called V) in sample BN2 at $T = 4.2$ K. The plot consists of three measurements, hence the fringes at $V_g = \pm 35$ V.

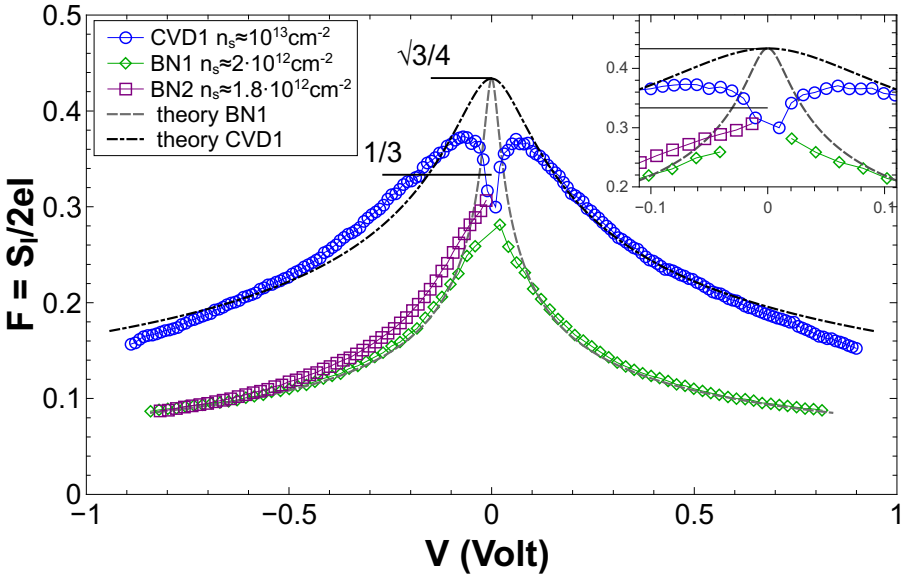

FIGURE 5.29: Fano factor as function of bias voltage of samples CVD1, BN1 and BN2 at high carrier concentrations. The inset shows a zoom of data around zero bias. The dashed lines are obtained from the solution of the heat equation and indicate the theoretical expectation from the electron-electron interaction regime onwards.

Let us now turn to the analysis of noise data in a mesoscopic physics spirit. The quantity of interest is here the Fano factor, giving the ratio between shot noise S_I and the Poissonian limit $2eI$. As pointed out before, one expects F to be independent of n_s in diffusive graphene samples with values $F \lesssim 1/3$ at low bias [25]. In Fig. 5.28 we present a measurement of the Fano factor in sample BN2 as a function of gate and drain-source voltage. Despite the carrier density dependence of the previously analysed quantities like e.g. the coupling constant Σ, the Fano factor F stays constant over the whole gate range. This is in agreement with theoretical predictions by Lewenkopf et al. [67] for the case of strong disorder. We observe $F \simeq 0.3$ in BN2 close to $V = 0$ and a power law decrease of F with increasing bias. Note that Fig. 5.28 is composed of three successive experiments, hence the slight mismatches at $V_g \pm 35$ V. We do not observe the dip $F \to 0$ towards zero bias as reported by [25], which is in part due to the insufficient resolution of our setup at low bias. A second reason is the sample's size: As can be seen from Fig. 5.29, both hBN based samples display no dip, whereas CVD1 transits from the power law to a decreasing F towards $V = 0$. In the analysis of the average electron temperature with respect to the heat equation we already pointed out that electron heat conduction to the leads is of greater importance in CVD1, due to its small size. In the same way, we explain the presence of the dip and maximum in CVD1's Fano factor by the stronger influence of electron-electron interactions as compared to BN1 and BN2, where electron-phonon cooling dominates the noise behaviour. Nevertheless phonon contributions are strong enough even in CVD1 to prevent F from reaching $\sqrt{3}/4$ expected for a gas of interacting electrons. Both hBN curves follow the theoretical line with good agreement. It is obtained from the solution of the heat equation and the Johnson-Nyquist relation, thus only predicting inelastic behaviour. $F = 1/3$ for the case of elastic scattering cannot be treated in the framework of the heat equation. For all three samples, we find $F \propto 1/\sqrt{V}$ for voltages above a few tens of mV, below which the aforementioned elastic regime begins. We attribute this $F \propto 1/\sqrt{V}$ dependence to the inelastic scattering of carriers with acoustic phonons, as this effect is dominating the noise behaviour in our samples. To our knowledge, this has not been studied yet. In samples of sufficient quality and above the threshold of optical phonon activation energy, we predict a further reduction of the Fano factor due to electron-OP interaction in addition to the near-omnipresent electron-AP scattering. Note in particular that we display unscaled data in Fig. 5.29. A direct comparison requires a voltage scaling by V_Σ (see Eq. (5.13)). V_Σ differs only slightly for the curves of BN1 and BN2 shown in Fig. 5.29 ($V_\Sigma^{BN1} \simeq 3.5$ mV and $V_\Sigma^{BN2} \simeq 2.3$ mV), but is about a factor 5 larger in sample CVD1 ($V_\Sigma^{CVD1} \simeq 15$ mV). Hence the possibility to observe the regime below the phonon cooling with greater precision in CVD1. As visible from the inset of Fig. 5.29, F tends to its limit value 1/3 at vanishing bias in all three samples.

5.4.7 Deviations from the T^4 law at low carrier densities

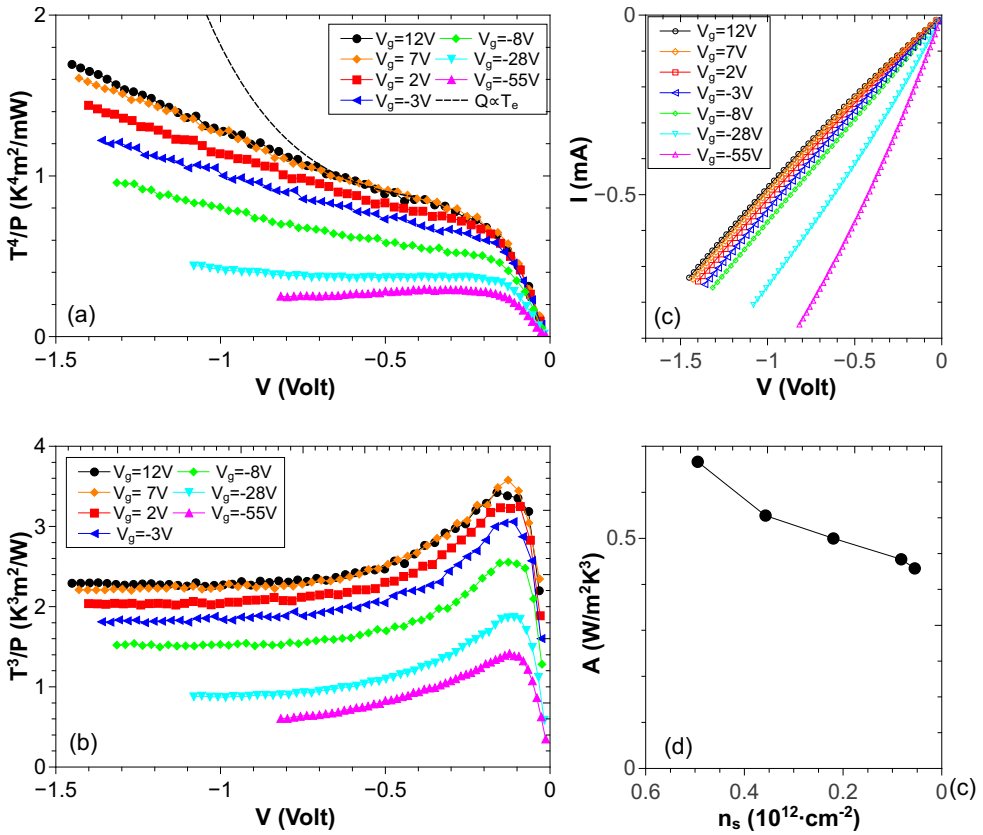

FIGURE 5.30: a) Average electron temperature in the representation T_e^4/P for several gate voltages in sample BN2. The dashed black line is a guide for the eye, indicating the expected behaviour for a $Q \propto T_e$ cooling at low carrier density, as predicted by [24]. b) Average electron temperature plotted as T_e^3/P as function of drain-source voltage V for several gate voltages in sample BN2. c) Corresponding I–V characteristics. d) Coupling constant A as function of carrier density extracted from the plateau values of (b).

As a last part of this chapter, we would like to present the currently ongoing investigation into the electron-AP coupling at low carrier densities. Previously, we have found that in the metallic regime, where n_s is very large, the cooling power has a T^4 dependence. At low carrier densities, i.e. towards the CNP and therefore $k_B T_e \ll |\mu|$, theory predicts a transition to $Q \propto T$ [24, 138] for the electron cooling by APs in graphene without lattice disorder. We do however not observe such a cooling dependence in our disordered samples.

Electron-acoustic phonon coupling beyond T_{BG} A recently presented theory [27] by Song et al. discusses exactly the effects of disorder on the electron-AP cooling. They study disorder assisted and two-phonon scattering of carriers in graphene. We will not go into detail on this particular subject, but shall merely introduce the key points of

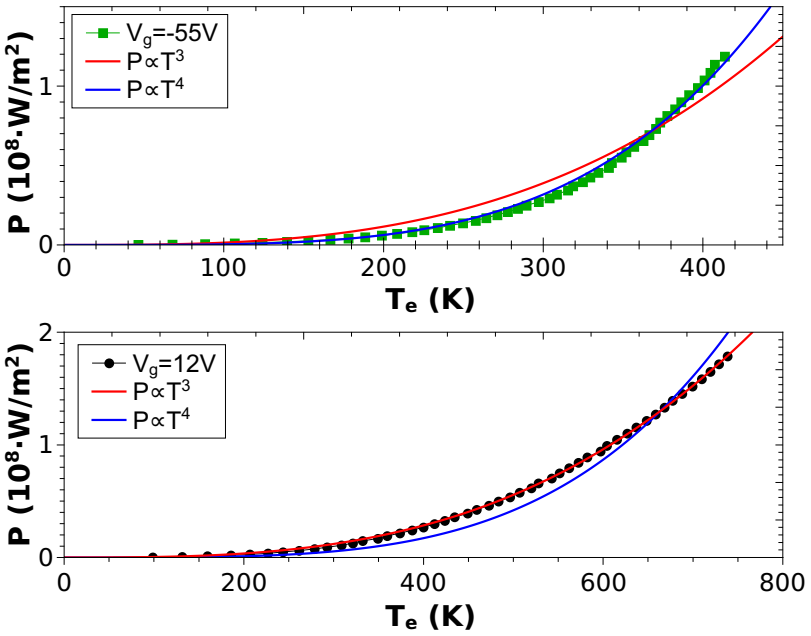

FIGURE 5.31: Joule power $P = V^2/(RLW)$ versus electron temperature for two different gate voltages in sample BN2. Upper panel: High carrier density; data consistent with a T_e^4 law. Lower panel: In the vicinity of the CNP; data consistent with a T_e^3 law stemming from supercollision mechanism [27]. Solid lines are best fits to the T_e^3 and T_e^4 dependence, respectively.

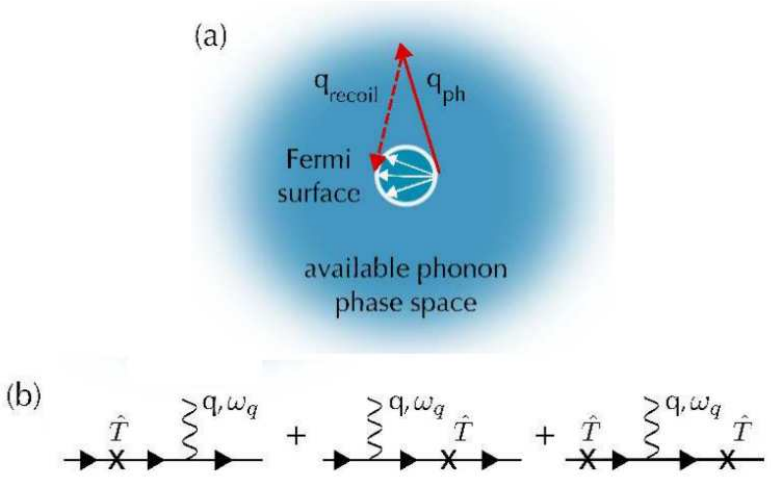

FIGURE 5.32: a) Kinematics of supercollisions and normal collisions at $T > T_{BG}$. Phonon momenta are constrained by the Fermi surface for normal collisions (white arrows), and totally unconstrained for supercollisions (q_{ph}), with the recoil momentum (q_{recoil}) transferred to the lattice via disorder scattering or carried away by a second phonon. b) Feynman diagrams for disorder assisted electron-phonon scattering processes. Adapted from [27].

their description: Disorder assisted and two-phonon effects do not require the same momentum conservation as the standard electron-phonon interactions and therefore do not limit the amount of energy carried away by the interaction. Fig. 5.32(a) visualises the disorder-assisted effect opening the full Fermi-surface to the cooling. Such collisions are estimated to occur less frequently than the electron-one-phonon kind, but drastically change the cooling power to a $Q \propto T_e^3 - T_{phonon}^3$ dependence. The supercollision scattering is not restricted to graphene, but a general effect also known e.g. in semiconductor physics. There however the low threshold of OPs obscures its trace. The presence of supercollisions along with the T^3 behaviour in MLG can either be explained by a short range potential accounting for mass disorder or by ripples in the graphene sheet. Both ways present accessible, but competing routes for the cooling. All aforementioned dependencies are under the assumption of $T_{phonon} \ll T_e$.

Deviations from the $Q \propto T_e^4$ law at low carrier concentration should be visible at higher bias, where phonon cooling dominates, similar to the electron-AP cooling in the metallic regime. Effectively, no plateaus are observed any more in the T_e^4/P representation when V_g approaches the CNP ($V_g = 12V$). Temperature data rises further above, but stays still below the aforementioned $Q \propto T_e$ prediction. In order to verify the $Q \propto T_e^3$ hypothesis, we plot the average electron temperature of sample BN2 in the representation T_e^3/P, presented in Fig. 5.30(b). The accompanying I–V characteristics (Fig. 5.30(c)) give a rough estimate of the bias region dominated by electron-AP interactions: Depending on gate voltage, an onset of saturation behaviour can be seen, especially towards high carrier concentrations. We remind that the CNP is in the vicinity of $V_g = 12$ V in this sample. For each carrier density we restrict the analysis to the linear region of Fig. 5.30(b).

The plateaus towards higher bias in the representation T_e^3/P suggest a cooling power dependence $Q \propto T_e^3$ at low carrier densities. A comparison, how the cooling power evolves from T_e^4 in the metallic regime to T_e^3 at low n_s is shown in Fig. 5.31 for sample BN2. The T_e^3 dependence could be a signature of disorder-assisted or two-phonon processes, as predicted by [27]. In general the cooling due to supercollisions takes the form $Q \propto LWAT_e^3$, where the prefactor A contains the coupling constant $\lambda \propto D^2$. A's exact make-up depends however on the type of disorder present in the sample. For a simple impurity scattering scenario Song et al. find

$$A = \frac{32\zeta(3)}{\pi^2} \frac{1}{k_F l} \frac{\nu_s^2}{\nu_f^2} \frac{D^2}{\rho_{gr}\nu_s} \frac{\epsilon_F^2}{\hbar^2 \nu_F^2} \frac{k_B^3}{\hbar^3 \nu_F^3} \tag{5.35}$$

where l is the mean free path and all other parameters as introduced earlier. Evaluating (5.35) we obtain $A \simeq 2.3\ \mathrm{WK^{-3}m^{-2}} \cdot n_s/(k_F l)$. From Fig. 5.30(b) we estimate $A \simeq 0.45\ \mathrm{W\,K^{-3}m^{-2}}$, which is of the right order of magnitude depending on the ratio $n_s/(k_F l)$ (see Fig. 5.30(d)). In general $k_F l \sim 10$ [187]. Besides the precise value of λ,

the plateaus in Fig. 5.30(b) suggests that supercollisions are becoming the dominant cooling pathway with decreasing n_s, effectively replacing the electron-one-AP interaction studied previously in this chapter. More evidence for the supercollision theory has recently been presented by Graham et al. [187], posted to arXiv towards the end of the manuscript preparation, who study the energy relaxation rate by means of photocurrent measurements. At the LPA further investigation into this subject is currently undertaken by S.-H. Jhang.

5.5 Synopsis and conclusion

In this chapter we have investigated the energy relaxation of hot carriers in a MLG sheet sitting on different substrates by means of noise thermometry. It effectively allowed us to study the elusive effect of electron-acoustic phonon cooling even in low mobility samples in the metallic regime. In the samples the carriers are heated by supplying electrical power to the device. Three pathways to loosing the acquired energy exist: First, carriers can conduct heat, i.e. their energy, to the contacts. This regime is well described by the Wiedemann-Franz law and goes approximately along with the standard diffusive noise suppression of 1/3. With increasing bias, thus supplied power, electron-acoustic phonon scattering becomes the dominant source of cooling and noise levels drop further. The AP interaction has a ΣT_e^4 signature, where Σ is the carrier density dependent AP coupling constant. The third cooling mechanism only arises at high electrical fields: Carriers interact strongly with optical phonons once they have reached the necessary energy. This third mechanism was absent in the experiments presented in this chapter, either due to low sample mobility or by restriction of the applied bias voltage. Our experiments confirm the T_e^4 signature, as well as the presence of a hot electron population, which points to a weak electron-AP coupling. The latter is estimated theoretically at $\Sigma_{LA} \simeq 10\ \mathrm{mW \cdot m^{-2}K^{-4}}$ at a typical carrier concentration of $n_s = 10^{12}\ \mathrm{cm^{-2}}$ and for a deformation potential of $D = 10$ ev. Our experimental values differ by nearly one order of magnitude, but also suggest an effect of lattice disorder on said coupling: Taking the carrier mobility as indicator of the 2D crystals quality, i.e. reference of the intrinsic disorder, Σ increases towards the theoretical value with increasing mobility, thus decreasing disorder. Further theoretical and experimental investigation into this particular topic are needed to clarify the role of lattice disorder on electron cooling in graphene.

The aforementioned temperature signature of the electron cooling changes when the system approaches the charge neutrality point. Here, at low n_s, we find $Q \propto T_e^3$. Several theoretical predictions exist for this regime; only one coinciding with our findings

however: so-called supercollision effects allow for a greater energy transfer by disorder-assisted or two-phonon scattering processes. Said collisions occur less frequently but dominate the cooling. We see strong evidence for the supercollision theory in our noise measurements: In the representation T_e^3/P plateaus arise at high bias in the vicinity of the CNP.

More data is still needed to pinpoint the value of the deformation potential D in our devices. We have found evidence of a $\sqrt{n_s}$ dependence of the coupling constant Σ, yet data remains insufficient to extract a precise value of D. Furthermore, an analytical expression of Σ only exists for LA phonons, but TA phonons may contribute to cooling as well. We hope that our work is a motivation for further theoretical investigation of electron-phonon interactions in graphene and the role of disorder.

Chapter 6

Outlook: An RF-GFET based sub-nanosecond single charge detector

The major topic when talking about future graphene applications is of course its use in field-effect transistors and the building of logical integrated circuits. As pointed out in the course of this work however, this requires a sufficient bandgap in order to create distinct ON and OFF states, which is still missing in graphene devices. Ways to overcome this obstacle have recently been presented, as e.g. the realisation of a vertical graphene heterostructure by Britnell et al. [188], where a thin hBN or MoS_2 layer creates a tunnel barrier between two MLG sheets. Furthermore, Yang et al. proposed a combination of graphene and Si to exploit properties of both materials and create a Schottky-barrier triode [189]. Further efforts are made in the field of RF low-noise amplification, where recent results are promising for future applications [65].

In this work, we have pursued a different goal: Characterising the properties of graphene field-effect transistors with respect to their use as ultra-fast single charge detectors. This was motivated by the work of Chaste et al. on carbon nanotube charge detectors, here at the Laboratoire Pierre Aigrain. Using CNT-FETs ultimate charge resolutions of $\delta q_{rms} = 13\ \mu e/\sqrt{\text{Hz}}$ at $0.8GHz$ bandwidth [64] or, in an even narrower window of $0.85MHz$, of $\delta q_{rms} = 2.3\ \mu e/\sqrt{\text{Hz}}$ [172] can be achieved. Similar sensitivities are found in e.g. InAs/InP nanowires [190], where $\delta q_{rms} = 2.5\ \mu e/\sqrt{\text{Hz}}$ in the MHz range. Furthermore sensitivities of $\delta q_{rms} \leq 10\ \mu e/\sqrt{\text{Hz}}$ can be achieved in electro-statically defined Si quantum dots [191] and $\delta q_{rms} \leq 1\ \mu e/\sqrt{\text{Hz}}$ in Al-SETs [60].

Such charge detectors can then be used e.g. to detect the time-resolved charging events of a quantum dot (QD). Gustavsson et al. [62, 192] used a GaAs heterostructure quantum point contact (QPC) coupled to a QD to count the electrons passing through the

QD. This allowed them to investigate the so-called *full counting statistic*, which gives insight into third and higher order moments of the charge distribution. The first moment of the distribution is the current, the second one is the shot noise. The third moment will reveal information about the time-reversal symmetry breaking. Typical times of the single charge events are on the ms scale. In a double QD experiment single electron interferences were also accessible [192] and similar experiments are carried out in graphene QD-QPC structures (see e.g. [193]). The above measurements rely on the sensitive charge detection capabilities in a relatively narrow bandwidth, keeping the noise level well below the single-event signal to be detected, but also limiting the temporal resolution to the above mentioned ms time-scale.

Detection of e.g. single charge wavepackets in a GaAs heterostructure quantum Hall edge channel in a coherent fashion require much faster detection. Here, one has to resolve events below the spacing given by Heisenberg's uncertainty principle $\Delta E \Delta t \sim h$, which results in a temporal resolution of $\tau \lesssim 0.15$ ns or bandwidth of $f \gtrsim 1$ GHz at typical dilution fridge temperatures of $T = 50$ mK.

From the results obtained throughout this work, in particular in chapters 3 and 5, we can now try to estimate the charge resolution δq_{rms} achievable with a RF-GFET. It involves the transit frequency f_T and the current noise S_I as presented in Eq. (1.72)

$$\delta q_{rms} = \frac{\sqrt{S_I}}{\omega_T} \tag{6.1}$$

As pointed out in Eq. (3.3), the current I_{ds} is proportional to the samples width W, therefore also the current noise $S_I \propto I \propto W$. Hence, in order to be able to estimate with a certain accuracy, we need to use values of similarly sized devices. In chapter 3 we found a maximum cut-off frequency of $f_T = 80$ GHz in our GoS sample sized $L \times W = 1 \times 3.7\ \mu\text{m}^2$. For the current noise, presented in chapter 5, we will base our estimate on the noise spectral density measurements of sample BN2, sized $L \times W = 2.2 \times 2.7\ \mu\text{m}^2$. Here, we find values of the order of $S_I \simeq 5\ \text{pA}^2\text{Hz}^{-1/2}$ at medium bias and carrier density. Inserting both in the above equation (as both samples are of comparable width) we expect a μm wide RF-GFET to have a charge resolution of

$$\delta q_{rms} \simeq 28\ \mu\text{e}/\sqrt{\text{Hz}} \tag{6.2}$$

in a multi-GHz bandwidth. This is already within reach of the capabilities of some of the above mentioned detectors. Contrary to the even more powerful SET devices, RF-GFETs have a much larger bandwidth and low impedance, though. Implementation into standard RF environments is thus easier. Furthermore, a reduction of channel width alongside with an increase of f_T would push the boundary towards the desired sensitivity. Already transit frequencies as high as 300 GHz are reported [65] in devices of

widths $W \sim 20\ \mu$m. The scaling of channel width may degrade this figure, as we could see in chapter 3. Nevertheless we believe that the constant progress in graphene research will soon allow to build graphene based devices capable of sub-nanosecond single charge detection. Engineering the RF-GFETs parameters to produce e.g. $S_I \simeq 10\ \mathrm{pA}^2/\sqrt{\mathrm{Hz}}$ (high mobility $\rightarrow$ stronger noise) in a bandwidth of 1 GHz and simultaneously a transit frequency $f_T \simeq 250$–300 GHz, the detectors resolution would already attain $\delta q^\star \simeq 0.33$ e at $\Delta f = 1$ GHz.

With these numbers in mind, one can readily imagine an integrated all-graphene coherent

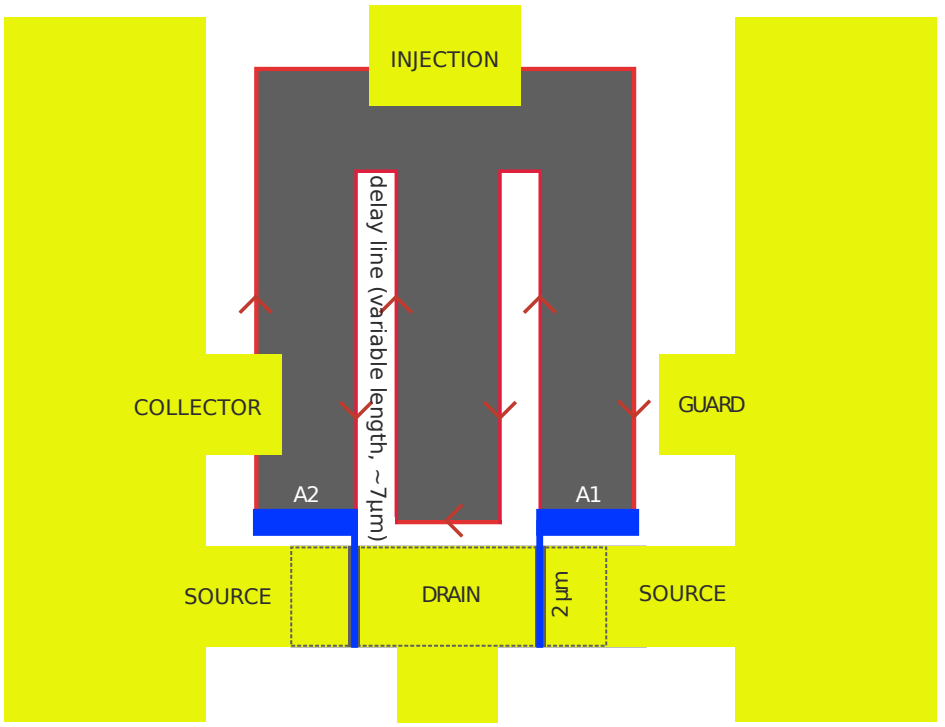

FIGURE 6.1: Proposal for an all-graphene coherent single-charge detector. A magnetic field induces edge states in the upper device part. Travelling carriers will be detected at two separate moments in time by the double gate RF-GFET. The gate electrodes are floating and couple the QHE device capacitively to the RF-GFET.

single-charge detector probing charges in a quantum Hall edge channel. Fig. 6.1 shows a proposal for such a device: A perpendicular magnetic field induces chiral edge channels in the upper graphene sheet. Injected carriers will thus travel in only one direction and provoke a response in the RF-GFET by capacitively coupling. The trace of one carrier will be picked up twice, at moments t and t', allowing for a precise signal-echo detection. The capacitance values C_g^{FET} and C_g^{QHE} of the RF-GFET and QHE part, respectively, have to be kept in balance in order to be able to precisely account for a single charge. Using an estimated edge channel carrier velocity $\nu_{QHE} \sim 10^5\ \mathrm{ms}^{-1}$ and a gate, respectively detector length of $L_g = L_{QHE} = 2\ \mu$m, we find a detection time $\tau \sim$

$2 \cdot 10^{-11}$ s. Precise detection will thus require a sufficient charge resolution at $f \simeq 8$ GHz. Carrier velocities are only estimated, as there is no precise measurement of ν_{QHE} for graphene edge channels yet. From 2DEG experiments however, it is known that $\nu_{QHE} \propto B^{-1}$ [194, 195] and $\nu \simeq 10^4$–10^5 ms^{-1}. We therefore suppose this to hold in graphene as well. Evidently $\delta q^\star$ worsens when increasing the bandwidth as suggested above. However, with the proposed signal-echo technique a much smaller frequency interval centred around 8 GHz could be chosen, restoring the previous, favourable state. A powerful oscilloscope of bandwidth $\Delta f = 16$ GHz and suitable ultra-low noise amplifiers of $\Delta f = 12$ GHz were recently bought; it is thus the author's hope that the graphene coherent single charge detection can be put into action soon at the Laboratoire Pierre Aigrain.

Appendix A

Appendix - Hexagonal Boron Nitride "Très BN"

A.1 Characterisation of hexagonal boron nitride

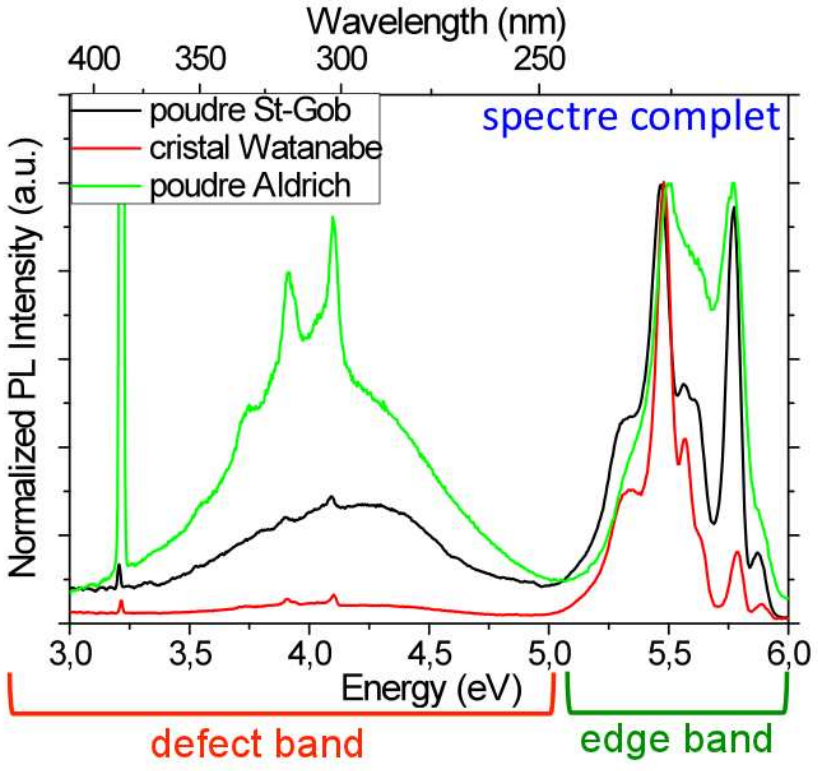

FIGURE A.1: Photo-luminescence spectra of three different hBN sources excited with a laser emitting at 6.4 eV (193 nm) at low temperature (5 K): single-crystal hBN (red), hBN powder "Très BN" by St. Gobain (black) and reference hBN powder by Aldrich (green)

In our sample fabrication we use, if required, an hBN layer as supporting substrate for the MLG. As pointed out in chapter 1 this enhances graphene's electrical properties. Best results are generally obtained when using layers exfoliated from hBN single-crystals. However, such crystals are hard to come by. Instead, we have pursued the approach of using a high-quality hBN powder as source for our samples. It can be treated much the same way as graphite or hBN single-crystals.
In Fig. A.1 we present a comparative photo-luminescence (PL) study of an hBN single-crystal (red), hBN powder "Très BN" by St. Gobain (black) and a reference hBN powder by Aldrich (green). The experiment was carried out by A. Pierret et al. at the *Office national d'études et recherches aérospatiales* (ONERA). The plot shows the PL spectra of the three hBN sources excited with a laser emitting at 6.4 eV (193 nm) at low temperature (5 K). Without going into details on the particularities of these measurements or the theory behind it, the following conclusions can be drawn [196]:

- The energy interval up to 5 eV, the so called defect band, gives insight into the amount of defects in the sample. Here, the single-crystal shows only minimal intensity, pointing to a minimal amount of defects in the lattice. As for the powders, the Très BN sample has a slightly higher PL intensity than the crystal, whereas the Aldrich powder displays a strong response in this region.

- In the energy range 5–6 eV, the so called edge band, excitons are excited and responsible for the observed PL peaks: At 5.5 eV bound state excitons arise, whereas the peak at higher energy is due to free excitons. A small linewidth of these peaks points to a higher crystal quality [196]. The single crystal, displays nearly only bound state excitons (due its high quality nearly all quasi-particle excitations are captured by defects). The peaks of the Très BN powder are almost equally fine with a balanced population of free and bound states. The exciton peaks of the Aldrich powder are much wider.

We can therefore summarise that the amount of defects in our Très BN powder is small compared to similar commercially available powders. Its quality is closer to the single-crystal than to the Aldrich powder.

Appendix B

Appendix - Admittance of a 1-dimensional distributed line

For one of the infinitesimal elements, including a resistance part rdx and an element of the series combination of capacitances cdx, we find two equations describing its behaviour:

$$-\frac{\partial V}{\partial x} = RI \tag{B.1}$$

$$\frac{\partial I}{\partial x} = \frac{\partial}{\partial x}\frac{\partial q(t)}{\partial t} = \frac{\partial}{\partial x}\frac{\partial}{\partial t}(CdxV) = C\frac{\partial V}{\partial t} \tag{B.2}$$

Together they form the differential equation

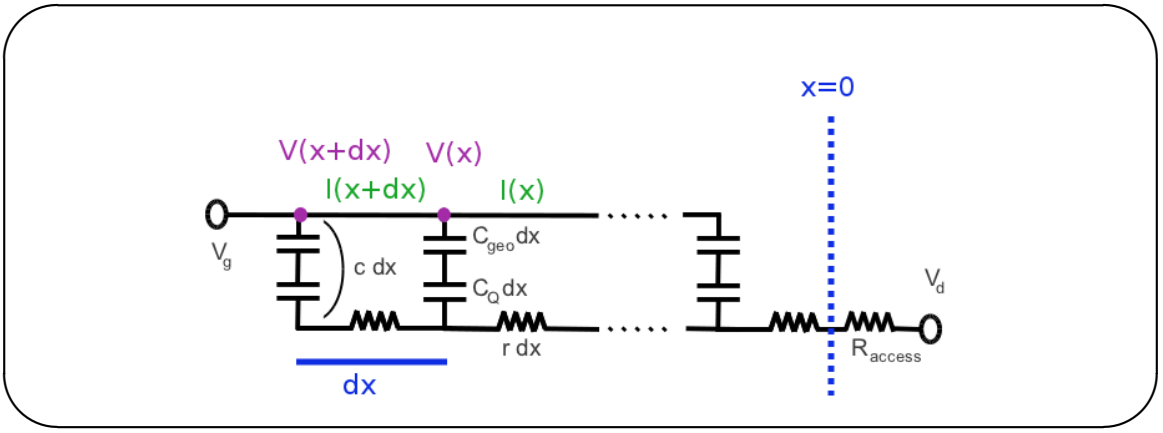

$$\frac{\partial^2 I}{\partial x^2} + RC\frac{\partial I}{\partial t} = 0 \tag{B.3}$$

modelling the element. Eq. B.3 is of course solved by the time and length coordinate dependent current

$$I(x,t) = I_0 e^{j(kx-\omega t)} \tag{B.4}$$

with the parameter $k^2 = -jRC\omega$.

We are however interested in the admittance of our device, i.e. we need knowledge of $I(0,t)$ and $V(0,t)$, the time-dependent current and voltage at $x = 0$, respectively. The measurements will effectively be taken at the border of the gate electrode, thus only the behaviour at $x = 0$ is of interest.

For a sample of gate length L we thus find

$$I(0,t) = I_0 \left(e^{jkL} - e^{-jkL}\right) e^{-j\omega t} \tag{B.5}$$

$$V(0,t) = \frac{I_0 k}{c\omega} \left(e^{jkL} + e^{-jkL}\right) e^{-j\omega t} \tag{B.6}$$

and finally the admittance

$$Y = \frac{I(0,t)}{V(0,t)} = \frac{c\omega}{k} tanh\,(jkL) \tag{B.7}$$

Appendix C

Appendix - Tunnel junction fabrication

Our cryogenic setup is calibrated against the white noise of custom-made Al-AlOx-Al tunnel junctions. The following table details the fabrication process. Note that the MMA+PMMA layer allows for the formation of a void underneath the PMMA bridge, which is then utilised to create two overlapping electrodes via the angled evaporation. We would like to thank the group of B. Huard, and in particular E. Flurin, for providing their expertise.

step	*description*	*tool(s)*	*notes*
1	cleaning	acetone, IPA and *Harrick* plasma oven	5–10 min
2	substrate preparation	heater plate	2 min 180° C
3	spin coating	spin coater & MMA	60 s, 8000 rpm, 4000 rpm/s
4	MMA bake	heater plate	2 min 180° C
5	spin coating	spin coater & MMA	60 s, 8000 rpm, 4000 rpm/s
6	MMA bake	heater plate	2 min 180° C
7	spin coating	spin coater & PMMA	60 s, 8000 rpm, 4000 rpm/s
8	PMMA bake	heater plate	2 min 180° C
9	lithography	*Raith* e-line	small structures: 7.5 μm aperture, 20 kV, 280 μCcm^{-2}
10	lithography	*Raith* e-line	large structures: 120 μm aperture, 20 kV, 280 μCcm^{-2}
11	developing	MIBK & IPA	35 s MIBK & 20 sIPA
12	angled Al evaporation	evaporator *Plassy*	130 nm at $-35°5$
13	oxidation	evaporator *Plassy*	in situ
14	angled Al evaporation	evaporator *Plassy*	130 nm at $+35°5$
15	lift-off	acetone & IPA	several hours & 30 s

Table C.1: Fabrication of Al-AlOx-Al tunnel junctions.

Appendix D

Appendix - Solution of the heat equation in presence of acoustic phonon cooling

In order to fit the electron temperature curves obtained experimentally and draw conclusions on the electron-phonon coupling constant, we have to solve the heat equation

$$\frac{L_o}{2R}L^2\frac{d^2T^2(x)}{dx^2} = -\frac{V^2}{R} + LW\Sigma\left(T^4 - T^4_{phonon}\right) \tag{D.1}$$

Here, the left-hand side describes the Wiedemann-Franz law of electron heat diffusion to the leads, V^2/R is the incoming Joule power and the second term on the right-hand side gives the cooling due to electron-acoustic phonon (AP) interaction. $L_o = \frac{\pi^2 k_b^2}{3e^2}$ is the Lorenz number, L and W the samples length and width, respectively and R its resistance. The electron-acoustic phonon coupling constant is Σ.
Let us now assume that the acoustic phonons are perfectly coupled to the substrate and therefore $T_{phonon} = 0$.
Without dissipation to the leads, i.e. vanishing left-hand side of (D.1), and $T_{phonon} = 0$ the electrons would reach a temperature given by

$$T^4(x) = \frac{V^2}{LW\Sigma R} \tag{D.2}$$

and we define therefore

$$T^2_\Sigma = \frac{V}{\sqrt{LW\Sigma R}} \tag{D.3}$$

Defining a second temperature

$$T^2_L = \frac{L_o}{2LW\Sigma R} \tag{D.4}$$

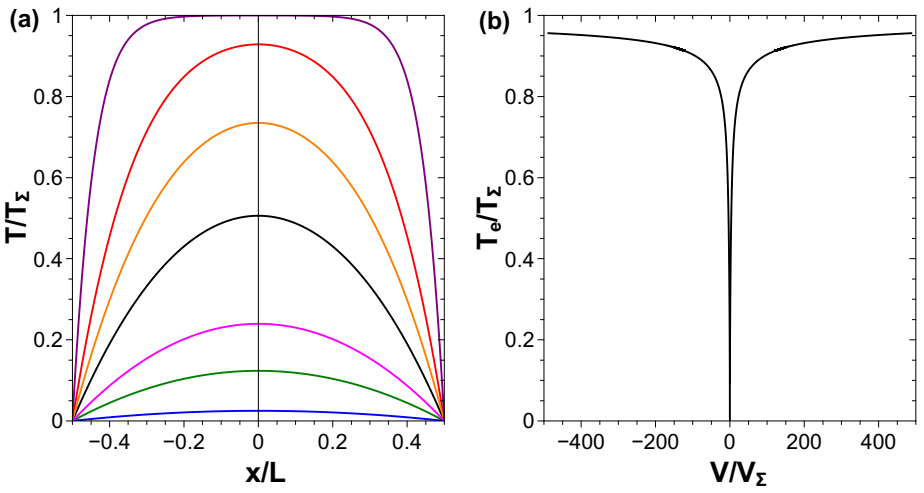

FIGURE D.1: a) Temperature profiles $T_e(x)$ for different bias voltages obtained from the solution of Eq. (D.1). b) Average electron temperature $\langle T_e(x/L)/T_\Sigma\rangle$ as function of reduced bias voltage V/V_Σ.

we can now introduce the dimensionless variables

$$U(x) = \frac{T^2(x)}{T_\Sigma^2} \qquad \text{and} \qquad U_L(V) = \frac{T_L^2}{T_\Sigma^2} = \frac{L_o}{2V\sqrt{LW\Sigma R}} \tag{D.5}$$

that, upon using them in (5.13), reduce the heat equation to

$$L^2 U_L \frac{d^2U(x)}{dx^2} = U^2(x) - 1 \tag{D.6}$$

Taking advantage of

$$U''(x) = \frac{dx}{dU}\left(\frac{(U')^2}{2}\right) \tag{D.7}$$

and simple integration rules for differential equations, as well as shuffling all terms depending on U on one side, we arrive at

$$\frac{x}{L} = \sqrt{\frac{3U_L}{2}} \int_U (x)_0^U \frac{dU}{\sqrt{(U_0 - U)(3 - U^2 - UU_0 - U_0^2)}} \tag{D.8}$$

where x runs from $-0.5L$ to $0.5L$ and $U_0 = U(0)$. The integral can be solved analytically

$$G\left(U(x), U_0\right) = 2\sqrt{\frac{2}{3U_0 + \sqrt{3}\sqrt{4 - U_0^2}}} \cdot \mathbf{\Gamma}\left(ArcSin\left[\frac{\sqrt{\frac{2U+U_0}{\sqrt{4-U_0^2}} + \sqrt{3}}}{\sqrt{2}\sqrt[4]{3}} \right], \frac{2\sqrt{3}\sqrt{4 - U_0^2}}{3U_0 + \sqrt{3}\sqrt{4 - U_0^2}} \right) \tag{D.9}$$

where $\mathbf{\Gamma}(\phi, k)$ signifies the elliptic integral of the first kind.

The value of $U_L(V)$ is fixed by the boundary condition that $T = 0$ at the samples

contacts, i.e. $U(\pm 0.5L) = 0$. This condition defines the upper limit U_0 and therefore we can find $U_L(U_0)$ by solving (D.6) under the condition $U(x) = 0$ and $x = 0.5L$. Thus

$$U_L(U_0) = \frac{1}{6} G\left(0, U_0\right)^2 \tag{D.10}$$

For each bias voltage V we can now solve (D.6) for $T(x)$ and plot the temperature profiles as shown in Fig.D.1(a). The crossover between electron heat dissipation and phonon mediated cooling is marked by the voltage scale $V_\Sigma = L_o/(\sqrt{4LW\Sigma R})$.
Finally we obtain the average electron temperature for a given bias voltage by computing the integral

$$\langle T_e \rangle = T_\Sigma \int_{-L/2}^{L/2} \sqrt{U(x)} dx \tag{D.11}$$

Appendix E

Appendix - Full current noise spectra

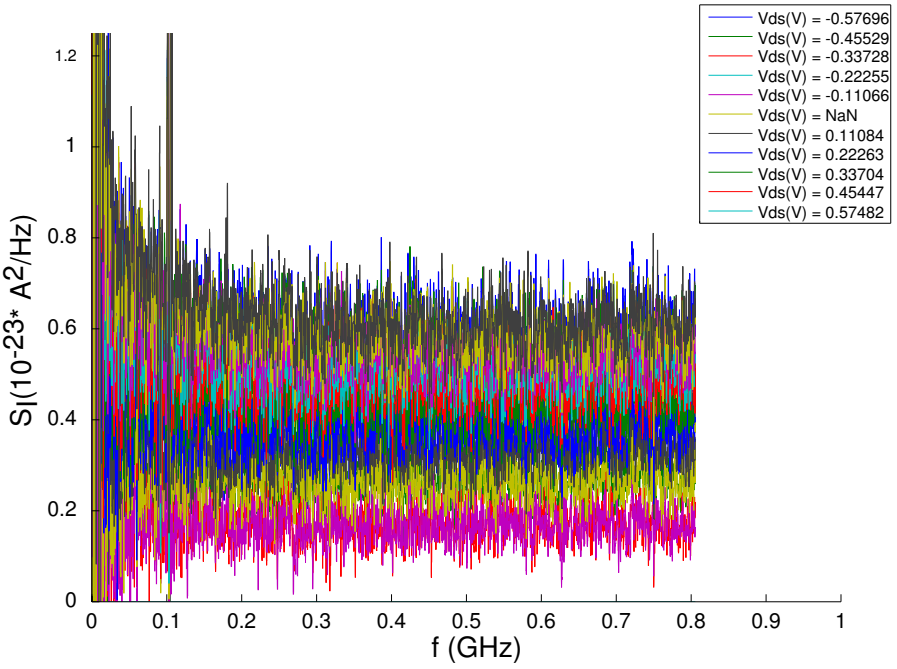

FIGURE E.1: Current noise spectra as function of frequency for different bias voltages in sample BN1 at $V_g = 18$ V.

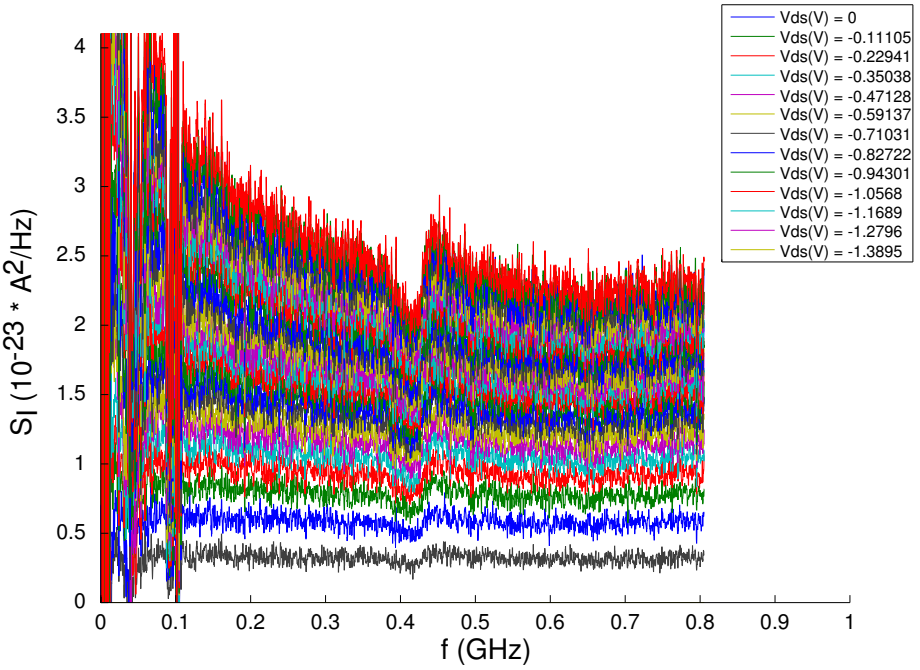

FIGURE E.2: Current noise spectra as function of frequency for different bias voltages in sample BN2 at $V_g = -28$ V.

Appendix F

Appendix - Electron temperature in representation T^5/P

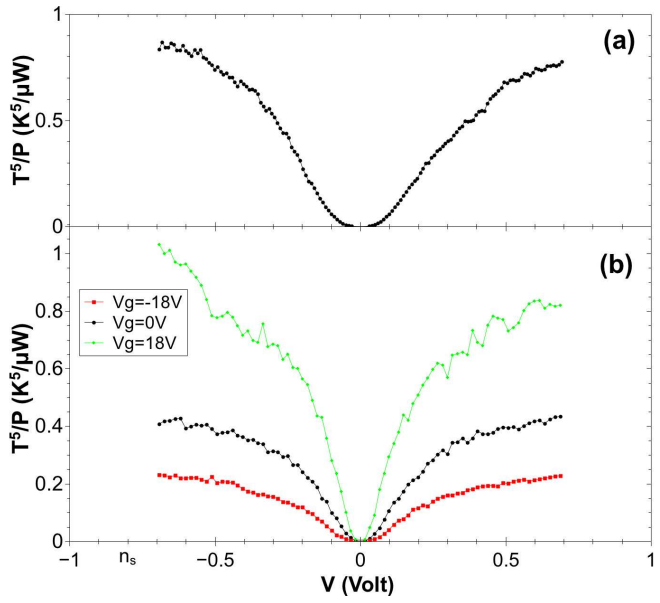

FIGURE F.1: (a) and (b): Electron temperature of sample CVD1 (a) and BN1 (b) plotted as $T_e^5(V)/P$. Contrary to the $T_e^4(V)/P$ representation, no plateaus at high bias can be observed.

Even though we find a small negative slope in the high bias data of the T_e^4/P representation, one can can easily convince oneself that the observed mechanism is truly 2D and hence the cooling power $\propto T_e^4$: Plotting the average electron temperature in the representation T^5/P (Fig.s F.1(a) and (b)), there is no saturation behaviour at high bias. T_e^4 is thus better fit to the data, which points strongly to the aforementioned 2D acoustic phonon effect.

Bibliography

[1] T. R. S. A. of Science, "Press release "The Nobel prize in physics 2010"", (2010).

[2] K. S. Novoselov, A. K. Geim, S. V. Morozov, D. Jiang, Y. Zhang, S. V. Dubonos, I. V. Grigorieva and A. A. Firsov, "Electric Field Effect in Atomically Thin Carbon Films", *Science* **306**, n° 5696, 666–669 (2004).

[3] K. S. Novoselov, A. K. Geim, S. V. Morozov, D. Jiang, M. I. Katsnelson, Grigorieva, S. V. Dubonos and A. A. Firsov, "Two-dimensional gas of massless Dirac fermions in graphene", *Nature* **438**, n° 7065, 197–200 (2005).

[4] D. R. Dreyer, R. S. Ruoff and C. W. Bielawski, "From Conception to Realization: An Historial Account of Graphene and Some Perspectives for Its Future", *Angewandte Chemie International Edition* **49**, n° 49, 9336–9344 (2010).

[5] A. K. Geim and K. S. Novoselov, "The rise of graphene", *Nature Materials* **6**, n° 3, 183–191 (2007).

[6] H. P. Boehm, A. Clauss, G. O. Fischer and U. Hofmann, "Das Adsorptionsverhalten sehr dünner Kohlenstoffolien", *Zeitschrift für anorganische und allgemeine Chemie* **316**, n° 3-4, 119–127 (1962).

[7] C. Berger, Z. Song, T. Li, X. Li, A. Y. Ogbazghi, R. Feng, Z. Dai, A. N. Marchenkov, E. H. Conrad, P. N. First and W. A. de Heer, "Ultrathin Epitaxial Graphite: 2D Electron Gas Properties and a Route toward Graphene-based Nanoelectronics", *The Journal of Physical Chemistry B* **108**, n° 52, 19912–19916 (2004).

[8] C. Bena and G. Montambaux, "Remarks on the tight-binding model of graphene", *New Journal of Physics* **11**, n° 9, 095003 (2009).

[9] M. O. Goerbig, "La matiére topologique - une introduction", Lecture in the framework of the Ecole Doctorale de Physique de la Region Parisien (ED107).

[10] *Physical Properties of Carbon Nanotubes*, Imperial College Press (1998).

[11] T. Martin, "Course 5 - Noise in mesoscopic physics", in H. Bouchiat, Y. Gefen, S. Guron, G. Montambaux and J. Dalibard, editors, "Nanophysics: Coherence and Transport - Ecole d'été de Physique des Houches Session LXXXI", vol. 81 of *Les Houches*, pages 283 – 359, Elsevier (2005).

[12] C. Glattli and P. Lafarge, "Physique mésoscopique", Lectures at Ecole Normale Supérieure.

[13] K. K. Likharev, *Proceedings of the IEEE* **87**, n° 4, 606–632 (1999).

[14] J. Chaste, L. Lechner, P. Morfin, G. Fève, T. Kontos, J.-M. Berroir, C. Glattli, H. Happy, P. Hakonen and B. Plaçais, "Single carbon nanotube transistor at GHz frequency.", *Nano Letters* **8**, n° 2, 525–528 (2008).

[15] G. F. Schneider, V. E. Calado, H. Zandbergen, L. M. K. Vandersypen and C. Dekker, "Wedging transfer of nanostructures.", *Nano letters* **10**, n° 5, 1912–6 (Mai 2010), ISSN 1530-6992.

[16] E. Pallecchi, C. Benz, A. C. Betz, H. V. Lhneysen, B. Plaçais and R. Danneau, "Graphene microwave transistors on sapphire substrates", *Applied Physics Letters* **99**, n° 11, 113502 (2011).

[17] K. Kim, J.-Y. Choi, T. Kim, S.-H. Cho and H.-J. Chung, "A role for graphene in silicon-based semiconductor devices", *Nature* **479**, n° 7373, 338–344 (November 2011).

[18] *Physics of Semiconductor Devices*, John Wiley & Sons (1981).

[19] Y. Wu, Y.-m. Lin, A. A. Bol, K. A. Jenkins, F. Xia, D. B. Farmer, Y. Zhu and P. Avouris, "High-frequency, scaled graphene transistors on diamond-like carbon", *Nature* **472**, n° 7341, 74–78 (2011).

[20] D. S. L. Abergel, V. Apalkov, J. Berashevich, K. Ziegler and T. Chakraborty, "Properties of graphene: a theoretical perspective", *Advances in Physics* **59**, n° 4, 261–482 (2010).

[21] E. Pallecchi, A. C. Betz, J. Chaste, G. Fève, B. Huard, T. Kontos, J.-M. Berroir and B. Plaçais, "Transport scattering time probed through rf admittance of a graphene capacitor", *Phys. Rev. B* **83**, 125408 (Mar 2011).

[22] K. Ziegler, "Robust Transport Properties in Graphene", *Phys. Rev. Lett.* **97**, 266802 (Dec 2006).

[23] M. S. Fuhrer, "Textbook physics from a cutting-edge material", *Physics* **3**, 106 (Dec 2010).

[24] J. K. Viljas and T. T. Heikkilä, "Electron-phonon heat transfer in monolayer and bilayer graphene", *Phys. Rev. B* **81**, 245404 (Jun 2010).

[25] R. Danneau, F. Wu, M. F. Craciun, S. Russo, M. Y. Tomi, J. Salmilehto, A. F. Morpurgo and P. J. Hakonen, "Evanescent wave transport and shot noise in graphene: ballistic regime and effect of disorder", *Journal of Low Temperature Physics* **153**, n° 5-6, 19 (2008).

[26] A. C. Betz, F. Vialla, D. Brunel, C. Voisin, M. Picher, A. Cavanna, A. Madouri, G. Fève, J.-M. Berroir, B. Plaçais and E. Pallecchi, "Hot Electron Cooling by Acoustic Phonons in Graphene", *Phys. Rev. Lett.* **109**, 056805 (Aug 2012).

[27] J. C. W. Song, M. Y. Reizer and L. S. Levitov, "Supercollisions and the Bottleneck for Electron-Lattice Cooling in Graphene", *Engineering* , n° 1, 1–6 (2011).

[28] A. H. Castro Neto, F. Guinea, N. M. R. Peres, K. S. Novoselov and A. K. Geim, "The electronic properties of graphene", *Rev. Mod. Phys.* **81**, 109–162 (Jan 2009).

[29] S. Das Sarma, S. Adam, E. H. Hwang and E. Rossi, "Electronic transport in two-dimensional graphene", *Rev. Mod. Phys.* **83**, 407–470 (May 2011).

[30] N. Ashcroft and N. Mermin, *Solid State Physics*, Saunders College, Philadelphia (1976).

[31] R. S. Deacon, K.-C. Chuang, R. J. Nicholas, K. S. Novoselov and A. K. Geim, "Cyclotron resonance study of the electron and hole velocity in graphene monolayers", *Phys. Rev. B* **76**, 081406 (Aug 2007).

[32] A. K. Geim and A. H. MacDonald, "Graphene: Exploring Carbon Flatland", *Physics Today* **60**, n° 8, 35–41 (2007).

[33] F. Schwabl, L. Hilton(Translator) and A. Lahee(Tranlator), *Advanced Quantum Mechanics*, Springer, Berlin (2008).

[34] *Introduction to solid state physics*, John Wiley and sons Inc. (1996).

[35] D. Torrin, *Nano transistor de graphène*, master thesis, Ecole Normale Supèrieure (2010).

[36] O. Klein, "Die Reflexion von Elektronen an einem Potentialsprung nach der relativistischen Dynamik von Dirac", *Zeitschrift für Physik, Volume 53, Issue 3-4, pp. 157-165* **53**, 157–165 (March 1929).

[37] M. I. Katsnelson, K. S. Novoselov and A. K. Geim, "Chiral tunneling and the Klein paradox in graphene", *Nature Physics* **2**, n° 9, 15 (2006).

[38] V. V. Cheianov and V. I. Fal'ko, "Selective transmission of Dirac electrons and ballistic magnetoresistance of *n-p* junctions in graphene", *Phys. Rev. B* **74**, 041403 (Jul 2006).

[39] B. Huard, J. A. Sulpizio, N. Stander, K. Todd, B. Yang and D. Goldhaber-Gordon, "Transport Measurements Across a Tunable Potential Barrier in Graphene", *Phys. Rev. Lett.* **98**, 236803 (Jun 2007).

[40] J. P. Hobson and W. A. Nierenberg, "The Statistics of a Two-Dimensional, Hexagonal Net", *Phys. Rev.* **89**, 662–662 (Feb 1953).

[41] F. Schwierz, "Graphene transistors.", *Nature Nanotechnology* **5**, n° 7, 487–496 (2010).

[42] D. G. Schlom and L. N. Pfeiffer, "Oxide electronics: Upward mobility rocks!", *Nature Materials* **9**, n° 11, 881–883 (2010).

[43] W. Gannett, W. Regan, K. Watanabe, T. Taniguchi, M. F. Crommie and A. Zettl, "Boron Nitride Substrates for High Mobility Chemical Vapor Deposited Graphene", *Applied Physics Letters* **98**, n° 24, 242105 (2011).

[44] C. R. Dean, A. F. Young, I. Meric, C. Lee, L. Wang, S. Sorgenfrei, K. Watanabe, T. Taniguchi, P. Kim, K. L. Shepard and J. Hone, "Boron nitride substrates for high-quality graphene electronics", *Nature Nanotechnology* **5**, 722–726 (October 2010).

[45] A. S. Mayorov, R. V. Gorbachev, S. V. Morozov, L. Britnell, R. Jalil, L. A. Ponomarenko, P. Blake, K. S. Novoselov, K. Watanabe, T. Taniguchi and et al., "Micrometer-scale ballistic transport in encapsulated graphene at room temperature.", *Nano Letters* **11**, n° 6, 2396–2399 (2011).

[46] E. McCann, Abergel and V. I. Fal'ko, "The low energy electronic band structure of bilayer graphene", *The European Physical Journal - Special Topics* **148**, n° 1, 91–103 (September 2007).

[47] J.-C. Charlier, X. Blase and S. Roche, "Electronic and transport properties of nanotubes", *Rev. Mod. Phys.* **79**, 677–732 (May 2007).

[48] K. Watanabe, T. Taniguchi and H. Kanda, "Direct-bandgap properties and evidence for ultraviolet lasing of hexagonal boron nitride single crystal", *Nature Materials* **3**, 404–409 (June 2004).

[49] "Symmetry constraints on phonon dispersion in graphene", *Physics Letters A* **372**, n° 31, 5189 – 5192 (2008).

[50] A. Barreiro, M. Lazzeri, J. Moser, F. Mauri and A. Bachtold, "Transport Properties of Graphene in the High-Current Limit", *Phys. Rev. Lett.* **103**, 076601 (Aug 2009).

[51] Y. Blanter and M. Büttiker, "Shot noise in mesoscopic conductors", *Physics Reports* **336**, n° 12, 1 – 166 (2000).

[52] J. B. Johnson, "Thermal Agitation of Electricity in Conductors", *Phys. Rev.* **32**, 97–109 (Jul 1928).

[53] H. Nyquist, "Thermal Agitation of Electric Charge in Conductors", *Phys. Rev.* **32**, 110–113 (Jul 1928).

[54] S. Kogan, Cambridge University Press (1996).

[55] G. C. Wick, "The Evaluation of the Collision Matrix", *Phys. Rev.* **80**, 268–272 (Oct 1950).

[56] G. Fève, A. Mahé, J.-M. Berroir, T. Kontos, B. Plaçais, D. C. Glattli, A. Cavanna, B. Etienne and Y. Jin, "An On-Demand Coherent Single-Electron Source", *Science* **316**, n° 5828, 1169–1172 (2007).

[57] F. D. Parmentier, E. Bocquillon, J.-M. Berroir, D. C. Glattli, B. Plaçais, G. Fève, M. Albert, C. Flindt and M. Büttiker, "Current noise spectrum of a single-particle emitter: Theory and experiment", *Phys. Rev. B* **85**, 165438 (Apr 2012).

[58] J. Chaste, *Transistors à nanotube de carbon unique: propriétés dynamiques et résolution d'électrons uniques*, PhD thesis, Université Paris 6 (2009).

[59] T. Ihn, J. Gttinger, F. Molitor, S. Schnez, E. Schurtenberger, A. Jacobsen, S. Hellmller, T. Frey, S. Drscher, C. Stampfer and K. Ensslin, "Graphene single-electron transistors", *Materials Today* **13**, n° 3, 44 – 50 (2010).

[60] H. Brenning, S. Kafanov, T. Duty, S. Kubatkin and P. Delsing, "An ultrasensitive radio-frequency single-electron transistor working up to 4.2 K", *Journal of Applied Physics* **100**, n° 11, 114321 (2006).

[61] E. Grémion, D. Niepce, A. Cavanna, U. Gennser and Y. Jin, "Evidence of a fully ballistic one-dimensional field-effect transistor: Experiment and simulation", *Applied Physics Letters* **97**, n° 23, 233505 (2010).

[62] S. Gustavsson, R. Leturcq, B. Simovič, R. Schleser, T. Ihn, P. Studerus, K. Ensslin, D. C. Driscoll and A. C. Gossard, "Counting Statistics of Single Electron Transport in a Quantum Dot", *Phys. Rev. Lett.* **96**, 076605 (Feb 2006).

[63] M. C. Cassidy, A. S. Dzurak, R. G. Clark, K. D. Petersson, I. Farrer, D. A. Ritchie and C. G. Smith, "Single shot charge detection using a radio-frequency quantum point contact", *Applied Physics Letters* **91**, n° 22, 222104 (2007).

[64] J. Chaste, E. Pallecchi, P. Morfin, G. Fève, T. Kontos, J.-M. Berroir, P. Hakonen and B. Plaçais, "Thermal shot noise in top-gated single carbon nanotube field effect transistors", *Applied Physics Letters* **96**, n° 19, 192103 (2010).

[65] Y. Wu, K. A. Jenkins, A. Valdes-Garcia, D. B. Farmer, Y. Zhu, A. A. Bol, C. Dimitrakopoulos, W. Zhu, F. Xia, P. Avouris and Y.-M. Lin, "State-of-the-Art Graphene High-Frequency Electronics", *Nano Letters* **0**, n° 0, null (0).

[66] J. Tworzydło, B. Trauzettel, M. Titov, A. Rycerz and C. W. J. Beenakker, "Sub-Poissonian Shot Noise in Graphene", *Phys. Rev. Lett.* **96**, 246802 (Jun 2006).

[67] C. H. Lewenkopf, E. R. Mucciolo and A. H. Castro Neto, "Numerical studies of conductivity and Fano factor in disordered graphene", *Phys. Rev. B* **77**, 081410 (Feb 2008).

[68] A. Allain, Z. Han and V. Bouchiat, "Electrical control of the superconducting-to-insulating transition in graphenemetal hybrids", *Nature Materials* **11**, 590 – 594 (2012).

[69] B. M. Kessler, i. m. c. O. Girit, A. Zettl and V. Bouchiat, "Tunable Superconducting Phase Transition in Metal-Decorated Graphene Sheets", *Phys. Rev. Lett.* **104**, 047001 (Jan 2010).

[70] S. Mouras, A. Hamm, D. Djurado and J.-C. Cousseins, "Synthesis of first stage graphite intercalation compounds with fluorides", *Revue de chimie minérale* **24**, n° 5 (1987).

[71] C. Berger, Z. Song, X. Li, X. Wu, N. Brown, C. Naud, D. Mayou, T. Li, J. Hass, A. N. Marchenkov, E. H. Conrad, P. N. First and W. A. de Heer, "Electronic Confinement and Coherence in Patterned Epitaxial Graphene", *Science* **312**, n° 5777, 1191–1196 (2006).

[72] J. Hass, R. Feng, T. Li, X. Li, Z. Zong, W. A. de Heer, P. N. First, E. H. Conrad, C. A. Jeffrey and C. Berger, "Highly ordered graphene for two dimensional electronics", *Applied Physics Letters* **89**, n° 14, 143106 (2006).

[73] A. Balan, R. Kumar, M. Boukhicha, O. Beyssac, J.-C. Bouillard, D. Taverna, W. Sacks, M. Marangolo, E. Lacaze, R. Gohler, W. Escoffier, J.-M. Poumirol and A. Shukla, "Anodic bonded graphene", *Journal of Physics D: Applied Physics* **43**, n° 37, 374013 (2010).

[74] T. Moldt, A. Eckmann, P. Klar, S. V. Morozov, A. A. Zhukov, K. S. Novoselov and C. Casiraghi, "High-Yield Production and Transfer of Graphene Flakes Obtained by Anodic Bonding", *ACS Nano* **5**, n° 10, 7700–7706 (2011).

[75] V. Huc, N. Bendiab, N. Rosman, T. Ebbesen, C. Delacour and V. Bouchiat, "Large and flat graphene flakes produced by epoxy bonding and reverse exfoliation of highly oriented pyrolytic graphite", *Nanotechnology* **19**, n° 45, 455601 (2008).

[76] Telephone interview with Konstantin Novoselov following the announcement of the 2010 Nobel Prize in Physics, 5 October 2010. The interviewer is Adam Smith, Editor-in-Chief of Nobelprize.org.

[77] Q. Yu, J. Lian, S. Siriponglert, H. Li, Y. P. Chen and S.-S. Pei, "Graphene segregated on Ni surfaces and transferred to insulators", *Applied Physics Letters* **93**, n° 11, 113103 (2008).

[78] X. Li, W. Cai, J. An, S. Kim, J. Nah, D. Yang, R. Piner, A. Velamakanni, I. Jung, E. Tutuc, S. K. Banerjee, L. Colombo and R. S. Ruoff, "Large-Area Synthesis of High-Quality and Uniform Graphene Films on Copper Foils", *Science* **324**, n° 5932, 1312–1314 (2009).

[79] *Handbook of chemical vapor deposition*, Noyes Publications (1999).

[80] N. Petrone, C. R. Dean, I. Meric, A. M. van der Zande, P. Y. Huang, L. Wang, D. Muller, K. L. Shepard and J. Hone, "Chemical Vapor Deposition-Derived Graphene with Electrical Performance of Exfoliated Graphene", *Nano Letters* In press.

[81] P. Blake, E. W. Hill, A. H. C. Neto, K. S. Novoselov, D. Jiang, R. Yang, T. J. Booth and A. K. Geim, "Making graphene visible", *Applied Physics Letters* **91**, n° 6, 063124+ (2007).

[82] J. C. Charlier, P. Eklund, J. Zhu and A. Ferrari, *Carbon Nanotubes* **111**, n° 2008, 673–709 (2008).

[83] L. Malard, M. Pimenta, G. Dresselhaus and M. Dresselhaus, "Raman spectroscopy in graphene", *Physics Reports* **473**, n° 56, 51 – 87 (2009).

[84] C. R. Dean, A. F. Young, I. Meric, C. Lee, L. Wang, S. Sorgenfrei, K. Watanabe, T. Taniguchi, P. Kim, K. L. Shepard and J. Hone, "Boron nitride substrates for high-quality graphene electronics - supInfo", *Nature Nanotechnology* pages 1–5 (August 2010), ISSN 1748-3387.

[85] M. Ishigami, J. H. Chen, W. G. Cullen, M. S. Fuhrer and E. D. Williams, "Atomic Structure of Graphene on SiO2", *Nano Letters* **7**, n° 6, 1643–1648 (2007).

[86] *Nanometer CMOS*, Pan Stanford Publishing (2010).

[87] *Radio Frequency Integrated Circuits and Technologies*, Springer-Verlag (2008).

[88] N. Meng, F.-J. Ferrer, D. Vignaud, G. Dambrine and H. Happy, "60 GHz current gain cut-off frequency graphene nanoribbon FET", *International Journal of Microwave and Wireless Technologies* **2**, 441–444 (2010).

[89] J. F. V. D. D. G. H. H. Meng, Nan; Fernandez, "Fabrication and Characterization of an Epitaxial Graphene Nanoribbon-Based Field-Effect Transistor", *IEEE Transactions on Electron Devices* **58**, n° 6, 1594–1596 (2011).

[90] B. N. Szafranek, D. Schall, M. Otto, D. Neumaier and H. Kurz, "Electrical observation of a tunable band gap in bilayer graphene nanoribbons at room temperature", *Applied Physics Letters* **96**, n° 11, 112103 (2010).

[91] B. N. Szafranek, D. Schall, M. Otto, D. Neumaier and H. Kurz, "High On/Off Ratios in Bilayer Graphene Field Effect Transistors Realized by Surface Dopants", *Nano Letters* **11**, n° 7, 2640–2643 (2011).

[92] B. N. Szafranek, G. Fiori, D. Schall, D. Neumaier and H. Kurz, "Current Saturation and Voltage Gain in Bilayer Graphene Field Effect Transistors", *Nano Letters* **12**, n° 3, 1324–1328 (2012).

[93] N. Vandecasteele, A. Barreiro, M. Lazzeri, A. Bachtold and F. Mauri, "Current-voltage characteristics of graphene devices: Interplay between Zener-Klein tunneling and defects", *Phys. Rev. B* **82**, 045416 (2010).

[94] I. Meric, M. Y. Han, A. F. Young, B. Ozyilmaz, P. Kim and K. L. Shepard, "Current saturation in zero-bandgap, top-gated graphene field-effect transistors.", *Nature Nanotechnology* **3**, n° 11, 654–659 (2008).

[95] J. Martin, N. Akerman, G. Ulbricht, T. Lohmann, J. H. Smet, K. Von Klitzing and A. Yacoby, "Observation of Electron-Hole Puddles in Graphene Using a Scanning Single Electron Transistor", *Nature Physics* **4**, n° 2, 144–148 (2008).

[96] I. Meric, C. Dean, A. Young, J. Hone, P. Kim and K. L. Shepard, "Graphene field-effect transistors based on boron nitride gate dielectrics", in "2010 INTERNATIONAL ELECTRON DEVICES MEETING - TECHNICAL DIGEST", International Electron Devices Meeting (2010), ISBN 978-1-4244-7419-6, International Electron Devices Meeting (IEDM), San Francisco, CA, DEC 06-08, 2010.

[97] K. Gloos, P. J. Koppinen and J. P. Pekola, "Properties of native ultrathin aluminium oxide tunnel barriers", *Journal of Physics: Condensed Matter* **15**, n° 10, 1733 (2003).

[98] J. Robertson, "High dielectric constant oxides", *The European Physical Journal Applied Physics* **291**, n° 3, 265–291 (2004).

[99] J. Lee, H.-J. Chung, J. Lee, H. Shin, J. Heo, H. Yang, S.-H. Lee, S. Seo, J. Shin, U. I. Chung and et al., "RF Performance of Pre-patterned Locally-embedded-Back-Gate Graphene Device", *Tech. Digest Int. Electron Devices Meeting* **2**, n° 10, 568–571 (2010).

[100] Z. Y. Zhang, S. Wang, L. Ding, X. L. Liang, H. L. Xu, J. Shen, Q. Chen, R. L. Cui, Y. Li and L. M. Peng, "High-performance n-type carbon nanotube field-effect transistors with estimated sub-10-ps gate delay", *Applied Physics Letters* **92**, n° 13, 133117 (2008).

[101] Y.-m. Lin, S. Member, D. B. Farmer, K. A. Jenkins, Y. Wu, J. L. Tedesco, R. L. Myers-ward, C. R. Eddy, D. K. Gaskill, C. Dimitrakopoulos and et al., "Enhanced Performance in Epitaxial Graphene FETs With Optimized Channel Morphology", *IEEE Electron Device Letter* **32**, n° 10, 1343–1345 (2011).

[102] L. Liao, J. Bai, R. Cheng, Y.-C. Lin, S. Jiang, Y. Qu, Y. Huang and X. Duan, "Sub-100 nm Channel Length Graphene Transistors", *Nano Letters* **10**, n° 10, 3952–3956 (2010).

[103] A. Inhofer, *Etude des propríetés électroniques du graphène CVD*, master thesis, Ecole Normale Supèrieure (2011).

[104] S. Halas, "100 years of work function", *Materials Science - Poland* **24**, n° 4 (2006).

[105] D. I. S. J.-S. R. J. P. J. O. P. B. Jagannathan, D. Greenberg and G. Freeman, "Speed and power performance comparison of state-of-the-art CMOS and SiGe RF transistors", in "2004 Topical Meeting on Silicon Monolithic Integrated Circuits in RF Systems", .

[106] H. Wang, J. W. Chung, X. Gao, S. Guo and T. Palacios, "High Performance InAlN / GaN HEMTs on SiC Substrate", in "The International Conference on Compound Semiconductor Manufacturing Technology 2010 Digest", .

[107] Y.-W. Tan, Y. Zhang, K. Bolotin, Y. Zhao, S. Adam, E. H. Hwang, S. Das Sarma, H. L. Stormer and P. Kim, "Measurement of Scattering Rate and Minimum Conductivity in Graphene", *Phys. Rev. Lett.* **99**, 246803 (Dec 2007).

[108] Z. H. Ni, L. A. Ponomarenko, R. R. Nair, R. Yang, S. Anissimova, I. V. Grigorieva, F. Schedin, P. Blake, Z. X. Shen, E. H. Hill, K. S. Novoselov and A. K. Geim, "On Resonant Scatterers As a Factor Limiting Carrier Mobility in Graphene", *Nano Letters* **10**, n° 10, 3868–3872 (2010).

[109] M. Monteverde, C. Ojeda-Aristizabal, R. Weil, K. Bennaceur, M. Ferrier, S. Guéron, C. Glattli, H. Bouchiat, J. N. Fuchs and D. L. Maslov, "Transport and Elastic Scattering Times as Probes of the Nature of Impurity Scattering in Single-Layer and Bilayer Graphene", *Phys. Rev. Lett.* **104**, 126801 (Mar 2010).

[110] J. H. Chen, C. Jang, S. Adam, M. S. Fuhrer, E. D. Williams and M. Ishigami, "Charged-impurity scattering in graphene", *Nature Physics* **4**, n° 5, 377–381 (Mai 2008).

[111] T. Heinzel, *Mesoscopic Electronics in Solid State Nanostructures*, Wiley-VCH Verlag GmbH, Weinheim, Germany (2003).

[112] L. A. Ponomarenko, R. Yang, R. V. Gorbachev, P. Blake, A. S. Mayorov, K. S. Novoselov, M. I. Katsnelson and A. K. Geim, "Density of States and Zero Landau Level Probed through Capacitance of Graphene", *Phys. Rev. Lett.* **105**, 136801 (Sep 2010).

[113] T. Fang, A. Konar, H. Xing and D. Jena, "Carrier Statistics and Quantum Capacitance of Graphene Sheets and Ribbons", *Applied Physics Letters* **91**, n° 9 (2007).

[114] J. Ziman, *Principles of the Theory of Solids*, Cambridge University Press, cambridge, England (1999).

[115] J.-N. Fuchs, "Introduction to the electronic properties of graphene", Lecture during the "Graphene School 2010" initiated by the international research group "Graphene and Nanotubes".

[116] K. S. Novoselov, D. Jiang, F. Schedin, T. J. Booth, V. V. Khotkevich, S. V. Morozov and A. K. Geim, "Two-dimensional atomic crystals.", *Proceedings of the National Academy of Sciences of the United States of America* **102**, n° 30, 10451–3 (2005).

[117] N. H. Shon and T. Ando, "Quantum Transport in Two-Dimensional Graphite System", *Journal of the Physical Society of Japan* **67**, n° 7, 2421–2429 (1998).

[118] I. L. Aleiner and K. B. Efetov, "Effect of Disorder on Transport in Graphene", *Phys. Rev. Lett.* **97**, 236801 (Dec 2006).

[119] K. Nomura and A. H. MacDonald, "Quantum Hall Ferromagnetism in Graphene", *Phys. Rev. Lett.* **96**, 256602 (Jun 2006).

[120] L. A. Ponomarenko, R. Yang, T. M. Mohiuddin, M. I. Katsnelson, K. S. Novoselov, S. V. Morozov, A. A. Zhukov, F. Schedin, E. W. Hill and A. K. Geim, "Effect of a High-κ Environment on Charge Carrier Mobility in Graphene", *Phys. Rev. Lett.* **102**, 206603 (May 2009).

[121] T. O. Wehling, S. Yuan, A. I. Lichtenstein, A. K. Geim and M. I. Katsnelson, "Resonant Scattering by Realistic Impurities in Graphene", *Phys. Rev. Lett.* **105**, 056802 (Jul 2010).

[122] T. Stauber, N. M. R. Peres and F. Guinea, "Electronic transport in graphene: A semiclassical approach including midgap states", *Phys. Rev. B* **76**, 205423 (Nov 2007).

[123] M. Katsnelson and A. Geim, "Electron scattering on microscopic corrugations in graphene", *PHIL.TRANS.R.SOC.A* **366**, 195 (2008).

[124] M. Ishigami, J. H. Chen, W. G. Cullen, M. S. Fuhrer and E. D. Williams, "Atomic Structure of Graphene on SiO2", *Nano Letters* **7**, n° 6, 1643–1648 (2007).

[125] F. Guinea, B. Horovitz and P. L. Doussal, "Gauge fields, ripples and wrinkles in graphene layers", *Solid State Communications* **149**, n° 2728, 1140 – 1143 (2009).

[126] V. V. Cheianov, O. Syljusen, B. L. Altshuler and V. I. Fal'ko, "Sublattice ordering in a dilute ensemble of monovalent adatoms on graphene", *EPL (Europhysics Letters)* **89**, n° 5, 56003 (2010).

[127] D. Haberer, L. Petaccia, M. Farjam, S. Taioli, S. A. Jafari, A. Nefedov, W. Zhang, L. Calliari, G. Scarduelli, B. Dora, D. V. Vyalikh, T. Pichler, C. Wöll, D. Alfè, S. Simonucci, M. S. Dresselhaus, M. Knupfer, B. Büchner and A. Grüneis, "Direct observation of a dispersionless impurity band in hydrogenated graphene", *Phys. Rev. B* **83**, 165433 (Apr 2011).

[128] B. Huard, N. Stander, J. A. Sulpizio and D. Goldhaber-Gordon, "Evidence of the role of contacts on the observed electron-hole asymmetry in graphene", *Phys. Rev. B* **78**, 121402 (Sep 2008).

[129] C. Ojeda-Aristizabal, M. Monteverde, R. Weil, M. Ferrier, S. Guéron and H. Bouchiat, "Conductance Fluctuations and Field Asymmetry of Rectification in Graphene", *Phys. Rev. Lett.* **104**, 186802 (May 2010).

[130] J. C. Meyer, A. K. Geim, M. I. Katsnelson, K. S. Novoselov, T. J. Booth and S. Roth, "The structure of suspended graphene sheets", *Nature* **446**, n° 7131, 14 (2007).

[131] K. Xu, P. Cao and J. R. Heath, "Scanning Tunneling Microscopy Characterization of the Electrical Properties of Wrinkles in Exfoliated Graphene Monolayers", *Nano Letters* **9**, n° 12, 4446–4451 (2009), pMID: 19852488.

[132] Q. Wilmart, *Propriétés dynamiques des Fermions de Dirac dans le graphène*, master thesis, Ecole Normale Superieure (2012).

[133] D. K. Efetov and P. Kim, "Controlling Electron-Phonon Interactions in Graphene at Ultrahigh Carrier Densities", *Phys. Rev. Lett.* **105**, 256805 (Dec 2010).

[134] J. S. Bunch, S. S. Verbridge, J. S. Alden, A. M. van der Zande, J. M. Parpia, H. G. Craighead and P. L. McEuen, "Impermeable Atomic Membranes from Graphene Sheets", *Nano Letters* **8**, n° 8, 2458–2462 (2008).

[135] V. Perebeinos and P. Avouris, "Inelastic scattering and current saturation in graphene", *Phys. Rev. B* **81**, 195442 (May 2010).

[136] K. M. Borysenko, J. T. Mullen, E. A. Barry, S. Paul, Y. G. Semenov, J. M. Zavada, M. B. Nardelli and K. W. Kim, "First-principles analysis of electron-phonon interactions in graphene", *Phys. Rev. B* **81**, 121412 (Mar 2010).

[137] S. S. Kubakaddi, "Interaction of massless Dirac electrons with acoustic phonons in graphene at low temperatures", *Phys. Rev. B* **79**, 075417 (Feb 2009).

[138] R. Bistritzer and A. H. MacDonald, "Electronic Cooling in Graphene", *Phys. Rev. Lett.* **102**, 206410 (May 2009).

[139] X. Hong, A. Posadas, K. Zou, C. H. Ahn and J. Zhu, "High-Mobility Few-Layer Graphene Field Effect Transistors Fabricated on Epitaxial Ferroelectric Gate Oxides", *Phys. Rev. Lett.* **102**, 136808 (Apr 2009).

[140] J.-H. Chen, C. Jang, S. Xiao, M. Ishigami and M. S. Fuhrer, "Intrinsic and extrinsic performance limits of graphene devices on SiO2", *Nat Nano* **3**, nº 4, 206–209 (April 2008).

[141] K. I. Bolotin, K. J. Sikes, J. Hone, H. L. Stormer and P. Kim, "Temperature-Dependent Transport in Suspended Graphene", *Phys. Rev. Lett.* **101**, 096802 (Aug 2008).

[142] K. Kaasbjerg, K. S. Thygesen and K. W. Jacobsen, "Unraveling the acoustic electron-phonon interaction in graphene", *Phys. Rev. B* **85**, 165440 (Apr 2012).

[143] L. A. Falkovsky, "Optical properties of graphene", *Journal of Physics: Conference Series* **129**, nº 1, 012004 (2008).

[144] F. Wu, P. Virtanen, S. Andresen, B. Plaçais and P. J. Hakonen, "Electron-phonon coupling in single-walled carbon nanotubes determined by shot noise", *Applied Physics Letters* **97**, nº 26, 262115 (2010).

[145] W. Schottky, "ber spontane Stromschwankungen in verschiedenen Elektrizittsleitern", *Annalen der Physik* **362**, nº 23, 541–567 (1918), ISSN 1521-3889.

[146] A. H. Steinbach, J. M. Martinis and M. H. Devoret, "Observation of Hot-Electron Shot Noise in a Metallic Resistor", *Phys. Rev. Lett.* **76**, 3806–3809 (May 1996).

[147] C. W. J. Beenakker and M. Büttiker, "Suppression of shot noise in metallic diffusive conductors", *Phys. Rev. B* **46**, 1889–1892 (Jul 1992).

[148] K. E. Nagaev, "Influence of electron-electron scattering on shot noise in diffusive contacts", *Phys. Rev. B* **52**, 4740–4743 (Aug 1995).

[149] Y. V. Nazarov and J. J. R. Struben, "Universal excess noise in resonant tunneling via strongly localized states", *Phys. Rev. B* **53**, 15466–15468 (Jun 1996).

[150] E. H. Hwang, S. Adam and S. Das Sarma, "Carrier Transport in Two-Dimensional Graphene Layers", *Phys. Rev. Lett.* **98**, 186806 (May 2007).

[151] R. Danneau, F. Wu, M. F. Craciun, S. Russo, M. Y. Tomi, J. Salmilehto, A. F. Morpurgo and P. J. Hakonen, "Shot Noise in Ballistic Graphene", *Phys. Rev. Lett.* **100**, 196802 (May 2008).

[152] W. H. Press, "Flicker Noises in Astronomy and Elsewhere", *Comments on Astrophysics* **7**, n° 4, 103–119 (1978).

[153] J. B. Johnson, "The Schottky Effect in Low Frequency Circuits", *Phys. Rev.* **26**, 71–85 (Jul 1925).

[154] F. N. Hooge, T. G. M. Kleinpenning and L. K. J. Vandamme, "Experimental studies on 1/f noise", *Reports on Progress in Physics* **44**, n° 5, 479 (1981).

[155] G. Liu, S. Rumyantsev, M. Shur and A. A. Balandin, "Graphene thickness-graded transistors with reduced electronic noise", *Applied Physics Letters* **100**, n° 3, 033103 (2012).

[156] G. Liu, W. Stillman, S. Rumyantsev, Q. Shao, M. Shur and A. A. Balandin, "Low-frequency electronic noise in the double-gate single-layer graphene transistors", *Applied Physics Letters* **95**, n° 3, 033103 (2009).

[157] Y. Zhang, E. E. Mendez and X. Du, "Mobility-Dependent Low-Frequency Noise in Graphene Field-Effect Transistors", *ACS Nano* **5**, n° 10, 8124–8130 (2011).

[158] *Electron-Phonon Interaction in Low-Dimensional Structures*, chapter 2, Oxford University Press (2003).

[159] M. R. Arai, "A fundamental noise limit for biased resistors at low temperatures", *Applied Physics Letters* **42**, n° 10, 906–908 (1983).

[160] F. C. Wellstood, C. Urbina and J. Clarke, "Hot-electron effects in metals", *Phys. Rev. B* **49**, 5942–5955 (Mar 1994).

[161] M. Henny, H. Birk, R. Huber, C. Strunk, A. Bachtold, M. Krüger and C. Schönenberger, "Electron heating effects in diffusive metal wires", *Applied Physics Letters* **71**, n° 6, 773–775 (1997).

[162] P. J. Price, "Hot electrons in a GaAs heterolayer at low temperature", *Journal of Applied Physics* **53**, n° 10, 6863–6866 (1982).

[163] Y. Ma, R. Fletcher, E. Zaremba, M. D'Iorio, C. T. Foxon and J. J. Harris, "Energy-loss rates of two-dimensional electrons at a GaAs/Al_x Ga_{1-x}As interface", *Phys. Rev. B* **43**, 9033–9044 (Apr 1991).

[164] A. Mittal, R. Wheeler, M. Keller, D. Prober and R. Sacks, "Electron-phonon scattering rates in GaAs/AlGaAs 2DEG samples below 0.5 K", *Surface Science* **361362**, n° 0, 537 – 541 (1996).

[165] N. J. Appleyard, J. T. Nicholls, M. Y. Simmons, W. R. Tribe and M. Pepper, "Thermometer for the 2D Electron Gas using 1D Thermopower", *Phys. Rev. Lett.* **81**, 3491–3494 (Oct 1998).

[166] M. Reznikov, M. Heiblum, H. Shtrikman and D. Mahalu, "Temporal Correlation of Electrons: Suppression of Shot Noise in a Ballistic Quantum Point Contact", *Phys. Rev. Lett.* **75**, 3340–3343 (Oct 1995).

[167] A. Kumar, L. Saminadayar, D. C. Glattli, Y. Jin and B. Etienne, "Experimental Test of the Quantum Shot Noise Reduction Theory", *Phys. Rev. Lett.* **76**, 2778–2781 (Apr 1996).

[168] J.-Y. Park, S. Rosenblatt, Y. Yaish, V. Sazonova, H. stnel, S. Braig, T. A. Arias, P. W. Brouwer and P. L. McEuen, "ElectronPhonon Scattering in Metallic Single-Walled Carbon Nanotubes", *Nano Letters* **4**, n° 3, 517–520 (2004).

[169] X. Zhou, J.-Y. Park, S. Huang, J. Liu and P. L. McEuen, "Band Structure, Phonon Scattering, and the Performance Limit of Single-Walled Carbon Nanotube Transistors", *Phys. Rev. Lett.* **95**, 146805 (Sep 2005).

[170] L. G. Herrmann, T. Delattre, P. Morfin, J.-M. Berroir, B. Plaçais, D. C. Glattli and T. Kontos, "Shot Noise in Fabry-Perot Interferometers Based on Carbon Nanotubes", *Phys. Rev. Lett.* **99**, 156804 (Oct 2007).

[171] F. Wu, P. Queipo, A. Nasibulin, T. Tsuneta, T. H. Wang, E. Kauppinen and P. J. Hakonen, "Shot Noise with Interaction Effects in Single-Walled Carbon Nanotubes", *Phys. Rev. Lett.* **99**, 156803 (Oct 2007).

[172] S. E. S. Andresen, F. Wu, R. Danneau, D. Gunnarsson and P. J. Hakonen, "Highly sensitive and broadband carbon nanotube radio-frequency single-electron transistor", *Journal of Applied Physics* **104**, n° 3, 033715 (2008).

[173] L. DiCarlo, J. R. Williams, Y. Zhang, D. T. McClure and C. M. Marcus, "Shot Noise in Graphene", *Phys. Rev. Lett.* **100**, 156801 (Apr 2008).

[174] R. Danneau, F. Wu, M. Y. Tomi, J. B. Oostinga, A. F. Morpurgo and P. J. Hakonen, "Shot noise suppression and hopping conduction in graphene nanoribbons", *Phys. Rev. B* **82**, 161405 (Oct 2010).

[175] A. Fay, R. Danneau, J. K. Viljas, F. Wu, M. Y. Tomi, J. Wengler, M. Wiesner and P. J. Hakonen, "Shot noise and conductivity at high bias in bilayer graphene: Signatures of electron-optical phonon coupling", *Phys. Rev. B* **84**, 245427 (Dec 2011).

[176] M. Freitag, M. Steiner, Y. Martin, V. Perebeinos, Z. Chen, J. C. Tsang and P. Avouris, "Energy Dissipation in Graphene Field-Effect Transistors", *Nano Letters* **9**, n° 5, 1883–1888 (2009).

[177] N. M. Gabor, J. C. W. Song, Q. Ma, N. L. Nair, T. Taychatanapat, K. Watanabe, T. Taniguchi, L. S. Levitov and P. Jarillo-Herrero, "Hot CarrierAssisted Intrinsic Photoresponse in Graphene", *Science* **334**, n° 6056, 648–652 (2011).

[178] H. Vora, P. Kumaravadivel, B. Nielsen and X. Du, "Bolometric response in graphene based superconducting tunnel junctions", *Applied Physics Letters* **100**, n° 15, 153507 (2012).

[179] J. Yan, M. H. Kim, J. A. Elle, A. B. Sushkov, G. S. Jenkins, H. M. Milchberg, M. S. Fuhrer and H. D. Drew, "Dual-gated bilayer graphene hot electron bolometer", *Nature Nanotechnology* (June 2012), advance online publication.

[180] K. Chung Fong and K. Schwab, "Ultra-sensitive and Wide Bandwidth Thermal Measurements of Graphene at Low Temperatures", *ArXiv e-prints* (Feb 2012).

[181] F. Wu, L. Roschier, T. Tsuneta, M. Paalanen, T. Wang and P. Hakonen, "Setup for shot noise measurements in carbon nanotubes", *Aip Conference Proceedings* **850**, n° 1, 1482–1483 (2006).

[182] A. A. Balandin, "Thermal Properties of Graphene, Carbon Nanotubes and Nanostructured Carbon Materials", *Nature Materials* **10**, n° 8, 569–581 (2011).

[183] B. N. J. Persson and H. Ueba, "Heat transfer between graphene and amorphous SiO2.", *Journal of physics: Condensed matter* **22**, n° 46, 462201 (2010).

[184] B. N. J. Persson and H. Ueba, "Heat transfer between weakly coupled systems: Graphene on a-SiO 2", *EPL (Europhysics Letters)* **91**, n° 5, 56001 (2010).

[185] I. Calizo, F. Miao, W. Bao, C. N. Lau and A. A. Balandin, "Variable temperature Raman microscopy as a nanometrology tool for graphene layers and graphene-based devices", *Applied Physics Letters* **91**, n° 7, 071913 (2007).

[186] S. V. Dmitriev, J. A. Baimova, A. V. Savin and Y. S. Kivshar, "Ultimate strength, ripples, sound velocities, and density of phonon states of strained graphene", *Computational Materials Science* **53**, n° 1, 194 – 203 (2012).

[187] M. W. Graham, S.-F. Shi, D. C. Ralph, J. Park and P. L. McEuen, "Photocurrent measurements of supercollision cooling in graphene", *ArXiv e-prints* (July 2012).

[188] L. Britnell, R. V. Gorbachev, R. Jalil, B. D. Belle, F. Schedin, A. Mishchenko, T. Georgiou, M. I. Katsnelson, L. Eaves, S. V. Morozov, N. M. R. Peres, J. Leist, A. K. Geim, K. S. Novoselov and L. A. Ponomarenko, "Field-Effect Tunneling Transistor Based on Vertical Graphene Heterostructures", *Science* **335**, n° 6071, 947–950 (2012).

[189] H. Yang, J. Heo, S. Park, H. J. Song, D. H. Seo, K.-E. Byun, P. Kim, I. Yoo, H.-J. Chung and K. Kim, "Graphene Barristor, a Triode Device with a Gate-Controlled Schottky Barrier", *Science* **336**, n° 6085, 1140–1143 (2012).

[190] H. A. Nilsson, T. Duty, S. Abay, C. Wilson, J. B. Wagner, C. Thelander, P. Delsing and L. Samuelson, "A Radio Frequency Single-Electron Transistor Based on an InAs/InP Heterostructure Nanowire", *Nano Letters* **8**, n° 3, 872–875 (2008).

[191] S. J. Angus, A. J. Ferguson, A. S. Dzurak and R. G. Clark, "A silicon radio-frequency single electron transistor", *Applied Physics Letters* **92**, n° 11, 112103 (2008).

[192] S. Gustavsson, R. Leturcq, T. Ihn, K. Ensslin and A. C. Gossard, "Electrons in quantum dots: One by one", *Journal of Applied Physics* **105**, n° 12, 122401 (2009).

[193] J. Güttinger, C. Stampfer, S. Hellmüller, F. Molitor, T. Ihn and K. Ensslin, "Charge detection in graphene quantum dots", *Applied Physics Letters* **93**, n° 21, 212102 (2008).

[194] E. Bocquillon, private communication, laboratoire Pierre Aigrain, ENS, Paris.

[195] J. Gabelli, G. Fève, T. Kontos, J.-M. Berroir, B. Plaçais, D. C. Glattli, B. Etienne, Y. Jin and M. Büttiker, "Relaxation Time of a Chiral Quantum *R-L* Circuit", *Phys. Rev. Lett.* **98**, 166806 (Apr 2007).

[196] A. Pierret, private communication, office national d'études et recherches aérospatiales.